Summer 8-17-2018

FOXM1 Expression and Contribution to Genomic Instability and Chemoresistance in High-Grade Serous Ovarian Cancer

Carter J. Barger
University of Nebraska Medical Center

FOXM1 EXPRESSION AND CONTRIBUTION TO GENOMIC INSTABILITY AND CHEMORESISTANCE IN HIGH-GRADE SEROUS OVARIAN CANCER

by

Carter J Barger

A DISSERTATION

Presented to the Faculty of
the University of Nebraska Graduate College
in Partial Fulfillment of the Requirements
for the Degree of Doctor of Philosophy

Cancer Research Graduate Program

Under the Supervision of Professor Adam R. Karpf

University of Nebraska Medical Center
Omaha, Nebraska

June 2018

Supervisory Committee:

Gargi Ghosal, Ph.D.

Nicholas Woods, Ph.D.

Joyce Solheim, Ph.D.

DEDICATION

To Sandy and Willow

ACKNOWLEDGMENTS

First and foremost, I would like to thank my advisor, Dr. Adam R. Karpf, for his support and guidance during my graduate school career. His mentoring allowed me to develop into an independent scientist, which greatly improved my success during graduate school and this will continue to have a positive impact on my career in science. I would like to acknowledge past and present members of the Karpf laboratory; Wa Zhang, Ashok Sharma, Linda Chee and Connor Branick. I benefited greatly from our fruitful discussions as they related to science and life. I am especially grateful to Linda and Connor for their support and hard work on the FOXM1-RHNO1 project, but more importantly, their patience and willingness to follow my lead, and their ability to work independently as this project developed. I would also like to thank Dr. Dave Klinkebiel and Mustafa Albahrani for their technical assistance with bioinformatic analyses.

I would also like to thank my past and present supervisory committee members: Dr. Gargi Ghosal, Dr. Rene Opavsky, Dr. Joyce Solheim, Dr. Kay-Uwe Wanger, and Dr. Nicholas Woods for their support and guidance over the years. Furthermore, I would like to thank Dr. Keith Johnson and Dr. Greg Oakley for serving on my comprehensive exam committee. I am also very grateful to Dr. Joyce Solheim and Dr. Jenny Black for the support they provided in the preparation of my NIH F99/K00 fellowship application.

I would also like to thank all collaborators for their contribution of reagents and experimental data, and this includes Dr. Kunle Odunsi, Dr. Ronny Drapkin, Dr. Michael Higgins, Dr. Shyam Sharan, Dr. Kajal Biswas, Dr. Lee Zou, Dr. Barbara Vanderhyden, Dr. Nelly Auersperg, Dr. Francis Balkwill, Dr. Anirban Mitra, Dr. Larry Karnitz, Dr. Scott Kaufmann, Dr. Jeremy Stark, Dr. Tadayoshi Bessho, Dr. Frank Graham, Dr. Philip Ng, Dr. Stephen Elledge and Dr. Pradip Raychaudhuri. This work would not have been possible without their generous support.

I would also like to thank the UNMC Core Facilities, especially the DNA Sequencing Core Facility and the Flow Cytometry Core Facility for their support. Furthermore, I would like to thank the Eppley Institute, Cancer Research Program and Graduate Studies for their support.

Lastly, I would like to thank my family, especially my wife, Sandy, not only for providing emotional and moral support during my PhD training, but for being patient and allowing me to dedicate a significant amount of time to my research.

FOXM1 EXPRESSION AND CONTRIBUTION TO GENOMIC INSTABILITY AND CHEMORESISTANCE IN HIGH-GRADE SEROUS OVARIAN CANCER

Carter J Barger, Ph.D.

University of Nebraska Medical Center, 2018

Supervisor: Adam R. Karpf, Ph.D.

High-grade serous ovarian cancer (HGSC) is the most common and deadly subtype of epithelial ovarian cancer. Understanding the molecular basis of HGSC will improve diagnosis and treatment approaches. The Cancer Genome Atlas (TCGA) discovered that Forkhead Box M1 (FOXM1) transcription factor activation is the second most frequent molecular alteration in HGSC (84% of cases), second only to mutations of TP53 (100%). We subsequently defined several genetic mechanisms that underlie increased FOXM1 expression in HGSC, including genomic amplifications and RB-E2F deregulation, and showed that FOXM1 promotes cell cycle progression in cell models relevant to HGSC.

TCGA analyses revealed that genomic instability, consisting of frequent copy number alterations, as key defining molecular features of HGSC and basal breast, more than any other TCGA cancer type. DNA replication stress results from uncoupling of the replicative helicase and polymerase and is a key mechanism of genomic instability. FOXM1 expression is linked to genomic instability but the underlying mechanism is unclear; induction of DNA replication stress could explain this association. In this context, we revealed novel functions of FOXM1 using fallopian tube epithelial (FTE) cells, an HGSC precursor cell model. We showed that FOXM1 increased DNA fork rate, origin firing, and DNA damage. Furthermore, Cyclin E1 cooperated with FOXM1 to increase its transcriptional activity, which promoted cell cycle progression and genomic instability. In

agreement, TCGA HGSC tumors with both FOXM1 and CCNE1 copy number gain show increased FOXM1 and CCNE1 expression and genomic instability.

FOXM1 shares a bidirectional promoter with RHNO1 but this genetic interaction has never been studied in any context. Knowledge of this interaction is important for understanding the molecular mechanism of HGSC. We investigated FOXM1 and RHNO1 expression using large-scale genomic datasets from normal and pan-cancer tissues and validated these findings with HGSC cell lines and tissues. FOXM1 and RHNO1 showed a highly significant correlation in all comparisons suggesting a potential for cooperativity. Importantly, we showed that FOXM1 and RHNO1 cooperate to promote cell survival and chemoresistance in HGSC cells. Collectively, these studies support *in vivo* studies focusing on the cooperativity of FOXM1 and RHNO1 bidirectional gene partners, to further understand their contribution to HGSC development and progression.

TABLE OF CONTENTS

LIST OF FIGURES

LIST OF TABLES

LIST OF ABBREVIATIONS

ATR	Ataxia Telangiectasia and Rad3-Related Protein
BER	Base excision repair
CCNB1	Cyclin B1
CCLE	Cancer Cell Line Encyclopedia
CCNE1	Cyclin E1
ChIP	Chromatin immunoprecipitation
CIN	Chromosomal instability
CNA	Copy number alteration
CpG	Cytidine-guanine dinucleotides
DDR	DNA damage response
DNA	Deoxyribonucleic acid
Dox	Doxycycline
DRS	DNA replication stress
EOC	Epithelial ovarian cancer
FDA	U.S. Food and Drug Administration
FOXM1	Forkhead box M1
FTE	Fallopian tube epithelial
GSEA	Gene set enrichment analysis
GTEx	Genotype-Tissue Expression
HGSC	High-grade serous ovarian cancer
HR	Homologous recombination
IP	Immunoprecipitation
KRAB	Krüppel associated box
mRNA	Messenger ribonucleic acid
MT	Mutant
NHEJ	Non-homologous end-joining
OSE	Ovarian surface epithelium
PARP	Poly (ADP-ribose) polymerase
PCR	Polymerase chain reaction
PLK1	Polo-like kinase-1
RB	Retinoblastoma protein
RHNO1	RAD9-RAD1-HUS1 interacting nuclear orphan 1
RNA	Ribonucleic acid

RNA-seq	RNA sequencing
RPPA	Reverse phase protein array
RT-qPCR	Reverse transcription quantitative polymerase chain reaction
scRNA-seq	Single-cell RNA sequencing
sgRNA	Single guide RNA
shRNA	Small hairpin RNA
siRNA	Small interfering RNA
STIC	Serous tubal intraepithelial carcinoma
TCGA	The Cancer Genome Atlas
TCPA	The Cancer Protein Atlas
TF	Transcription factor
TSS	Transcriptional start site
UCSC	University of California, Santa Cruz
WT	Wild type

CHAPTER 1: INTRODUCTION

Human Ovarian Cancer

Ovarian cancers

Ovarian cancer is the most lethal gynecological malignancy and is the fifth leading cause of cancer-related deaths in women in the United States, accounting for 14,070 estimated deaths and 22,240 estimated new cases in 2018 (6). The 5-year survival rate for women diagnosed with cancer localized to the ovary exceeds 90%; however, more than 60% of cases are diagnosed after cancer cells have metastasized from the primary tumor to distant sites, and the 5-year survival rate for these patients is less than 30% (7). These dire statistics reflect the lack of an effective screening test for early stage diagnosis of ovarian cancer and highlight difficulties in the successful treatment of advanced-stage disease (8).

Ovarian cancer is a generic term that can be used for any cancer involving the ovaries. Ovarian cancers can be divided into 3 major categories based on cell of origin: epithelial, germ cell, and stromal cell tumors. Epithelial cancers are most common and account for at least 90% of ovarian cancer. Epithelial tumors can be further categorized based on histological subtype. Histology-based classification of ovarian cancer was developed by the World Health Organization (WHO) system (9,10). Based on these criteria, epithelial ovarian cancers (EOC) are currently divided into five main types: high-grade serous (70%), endometrioid (10%), mucinous (3%), clear-cell (10%), and low-grade serous (3%) (Figure 1) (11).

Staging and grading of epithelial ovarian cancer

According to the International Federation of Obstetricians and Gynecologists (FIGO) system, ovarian cancer can be classified into Stage I to Stage IV (11). Stage I ovarian cancer is defined as tumors confined to the ovaries and peritoneal fluid/washings (11). Stage II ovarian cancer is defined as extension or metastasis to pelvic organs and may include curable tumors that have directly extended to adjacent organs but have not yet metastasized (11). Stage III ovarian cancer is defined as tumors characteristically spread along peritoneal surfaces involving both pelvic and abdominal peritoneum including the omentum, surfaces of the small and large bowel, mesentery, paracolic gutters, diaphragm, and peritoneal surfaces of the liver and spleen (11). Stage IV ovarian cancer is defined as distant metastasis and includes patients with parenchymal liver/splenic metastases and extra-abdominal metastases (11).

According to the FIGO grading system, ovarian cancers can also be classified into three grades to indicate the degree of tumor cell differentiation (12). Grade 1 is most like normal ovarian tissue; Grade 2 is moderately differentiated tumors; and Grade 3 cancer cells are poorly differentiated or undifferentiated (13). This three-grade system can be applied to all ovarian carcinomas. Low grade serous ovarian cancer is typically grade 1 and high-grade serous ovarian cancer is grade 2 and 3 (13-15).

Prognosis of ovarian cancer is strongly associated with the stage at diagnosis, but the histologic grade also plays a prognostic role, particularly in predicting recurrence (16). Poor prognostic factors include age older than 65 years, clear cell or mucinous tumors (histology), extensive disease (advanced stage), large residual tumor volume, lower global quality-of-life score, and poor cell differentiation (high grade) (16). Even though the overall 5-year survival rate of women with ovarian cancer indicates some recent improvement for women diagnosed between 2002 to 2008, compared to the 1970s and 1980s, these gains

are rather modest (17). Due to difficulties in early detection, most ovarian cancers are diagnosed at an advanced stage, and most of the patients show a poor prognosis because of recurrence after chemotherapy.

Diagnosis of epithelial ovarian cancer

Although the 5-year survival rate of women with localized ovarian tumors exceeds 90%, only as few as 15% of ovarian cancers are confined to the ovaries at diagnosis (17). Furthermore, the diagnosis of ovarian cancer may be difficult because of nonspecific symptoms (16). Patients with ovarian cancer may have abdominal pain, swelling, or nonspecific gastrointestinal symptoms for more than six months before diagnosis (16). When a patient presents with these symptoms, a pelvic examination should be performed. However, the physical examination is not sensitive for detecting ovarian masses (16,18). Additionally, physical examinations are often nonspecific for ovarian cancer, further testing should be performed in women older than 40 of age who have persistent unexplained gynecologic or gastrointestinal symptoms (16). Laboratory tests in these patients should include a complete blood count, comprehensive metabolic panel, and measurement of serum CA125 levels (16). CA125 (MUC16) is a high-molecular mass (1 MDa) glycosylated transmembrane mucin that is expressed in 80% of ovarian cancers (8,19). CA125 is shed from ovarian cancers and circulates in serum allowing for detection without invasive procedures (8,20). It is the first useful biomarker for monitoring the response of ovarian cancer to chemotherapy (8,20). CA125 levels are elevated in 90% of patients with advanced disease, but in only 50% of those with stage I tumors (16,21).

High-Grade Serous Ovarian Cancer

Origins of high-grade serous ovarian cancer

Until recently, the ovarian surface epithelium (OSE) was the assumed origin of the majority of HGSC (Figure 1) (13).The OSE is a single layer of epithelial cells that line the surface of the ovary (22). The OSE was thought to be the origin of HGSC based on the incessant ovulation hypothesis: the extravagant ovulations in the human female, which involves repeated rupture and repair of the ovarian surface following exposure to the estrogen-rich follicular fluid (23). The incessant ovulation hypothesis was further supported by epidemiological studies that demonstrated a relationship between the number of ovulations and a woman's probability of developing ovarian cancer (23).

A recent paradigm shift based on new clinical and molecular evidence suggests that a majority of HGSC cases originate in the fallopian tube epithelium (FTE) (Figure 1). Initial evidence for this theory is based on a study done in 2001, when tubal segments were removed from women undergoing a risk-reducing bilateral salpingo-oophorectomy or the removal of the fallopian tube and ovaries (24). In this study, 12 specimens were examined, and six showed areas of cellular dysplasia in the tubal epithelium, and five displayed hyperplastic lesions, compared to normal fallopian tubes (24). Remarkably, both the hyperplastic and dysplastic lesions histologically resembled high-grade serous ovarian cancer, but without invasion (24). In addition, BRCA mutations were found in both ovarian cancers and fallopian tube malignancies (25). Based on these data, it was hypothesized that most hereditary serous carcinomas originated from the FTE (26) (Figures 1 and 2). Gene expression and DNA methylome analyses have since shown that HGSC is more similar to FTE than OSE (27,28). More recently, evolutionary genomic analyses were performed on tissues isolated from HGSC precursor lesions in the fallopian tube lesions, p53 signatures and serous tubal intraepithelial carcinomas (STICs), as well as primary

HGSC tumors and metastases from nine patients (Figure 2) (29). Genomic analysis showed that STIC lesions had overlap in tumor-specific alterations (TP53, BRCA1, BRCA2 or PTEN) that were present in primary and metastatic ovarian cancers, thus providing further evidence that HGSC originates in the fallopian tube (Figure 2).

Genomic features of high-grade serous ovarian cancer

HGSC is broadly characterized by genomic instability, specifically high copy number abnormalities but few recurrent somatic mutations. Defects in the homologous repair pathway occur in ~50% of tumors due to frequent *BRCA1/2* mutations (30,31). *TP53* mutations are present in 100% of tumors and these occur early in HGSC based on the detection of p53 signatures in the fallopian tube (Figure 2) (30,31). Additionally, RB-E2F deregulation occurs in ~70% of HGSC through loss of *CDKN2A* and *RB1*, and activation of cyclin D and E, and agrees with the increased proliferation that is observed in STICs and HGSC tumors as shown by increased Ki67 staining (Figure 2) (30).

TCGA analyses revealed that genomic instability is a key defining molecular feature of HGSC and basal breast cancer, more than any other TCGA cancer type (32,33). One mechanism is deficient homologous recombination DNA repair (HR), exemplified by BRCA1/2 mutations and promoter methylation, which occur in ~33% of HGSC cases (30). However, all HGSC cases show genomic instability, therefore additional factors contribute to this phenotype. One potential example is cyclin E1 (CCNE1) amplifications, which occur in ~20% of HGSC and are mutually exclusive with HR deficiency (34). CCNE1 induces DNA replication stress and CNA in some cell models, suggesting it could contribute to genomic instability in the context of HGSC (35). Furthermore, FOXM1 pathway activation occurs in ~84% of HGSC (30,36). Notably, FOXM1 is a member of a 25 gene signature for chromosomal instability in a pan-cancer analysis (CIN25 signature) (37). In addition,

FOXM1 is a top biomarker for poor prognosis in solid tumors, potentially consistent with a protein promoting genomic instability (38,39). However, the mechanistic basis for the link between FOXM1 and genomic instability is unknown (40). Genomic instability contributes to tumor evolution and treatment resistance; thus, it is critical to reveal causative factors that drive genomic instability in HGSC (41,42).

Treatment of high-grade serous ovarian cancer

Conventional therapy for ovarian cancer is surgical tumor debulking followed by combination chemotherapy (16). Ovarian cancer is one of the few malignancies where surgeons will perform cytoreductive operation to eliminate macroscopic tumor before chemotherapy (8,43). Surgery can be performed after neoadjuvant chemotherapy if optimal cytoreduction is not considered feasible at initial diagnosis (8,44). However, there is no reliable evidence that chemotherapy before debulking surgery is superior to conventional treatment in women with advanced epithelial ovarian cancer (16). Primary chemotherapy for newly diagnosed ovarian cancer after cytoreductive surgery consists of six cycles of combination carboplatin/paclitaxel chemotherapy (8). Carboplatin is an alkylating agent that binds covalently to DNA, creating adducts that form intrachain and interchain cross-links (8). Paclitaxel binds non-covalently to microtubules and increases their stability, interfering with mitotic spindle formation (8). Despite the initial response of first-line chemotherapy in HGSC patients, more than 70% of patients will experience disease recurrence, and become candidates for second-line chemotherapy within 12 to 18 months (8). Persistent elevation of CA125 after chemotherapy indicates residual disease with more than 90% accuracy (8). Retreatment with carboplatin and paclitaxel is associated with a 20-50% response when platinum-sensitive disease recurs more than 6 months after primary chemotherapy (8). Although recurrent disease is not curable, drug

combinations, such as liposomal doxorubicin and etoposide, can prolong survival in these patients (8).

The discovery of BRCA1/2 mutations and HR deficiency in HGSC led to the first clinical trials of poly (ADP-ribose) polymerase (PARP) inhibitors (45). PARP inhibitors have been found to induce synthetic lethality in BRCA-mutated HGSC (45,46). Synthetic lethality occurs between two genes when cells with mutation or loss of either gene alone are viable but mutation or loss of both genes leads to cell death (47). PARP1 is a DNA repair enzyme that is involved in the base excision repair (BER) pathway (45,46). It is believed that PARP inhibitors induce DNA replication stress by trapping PARP on genomic DNA and/or inhibiting BER, which creates a dependency on BRCA1/2 for cell survival (45,48,49). Studies have shown that loss of both HR and BER forces cells to use non-homologous end-joining (NHEJ) DNA repair, which is error-prone, thus causing an accumulation of DNA damage and cell death (45). In clinical trials, PARP inhibitors have shown selective toxicity toward tumor cells with BRCA1/2 germline mutations as well as some without germline BRCA1/2 mutations, which is likely due to somatic defects in other components of the HR pathway (50-52). In 2014, the PARP inhibitor olaparib received FDA approval for the treatment of germline BRCA-mutated ovarian cancers after third-line therapy based on a non-randomized study of olaparib monotherapy in BRCA-mutated cancer (53,54). Furthermore, PARP inhibitors have shown selectivity for BRCA1/2-mutated cancers, however, only a fraction of BRCA1/2 mutant cancers respond to PARPi therapy and responders typically develop resistance (48,55-57). Thus, a strategy to overcome PARPi resistance in BRCA-mutant cancers is needed to improve this otherwise promising targeted therapy.

FOXM1

Genomic configuration, protein domains and regulation

FOXM1 was previously known in the literature as Trident (in mouse), WIN or INS-1 (in rat), FKHL-16, MPP-2 (partial human cDNA) or HFH-11 (in human). FOXM1 was initially identified as MPP-2 during a cDNA screen as a protein phosphorylated during the mitotic phase of the cell cycle (58). A subsequent publication by Han Clevers group reported that the team had cloned FOXM1 and determined it had a sequence motif similar to the conserved DNA binding domain of the Forkhead family of transcription factors (59). FOXM1 is now recognized as a member of the Forkhead box (FOX) transcription factor family, which is unified by a conserved winged helix DNA binding domain (DBD, Figure 3) (60). In addition to the DNA binding domain, FOXM1 protein contains a transactivation domain at the C terminus, which is important for activating target gene expression (Figure 3) (61). The binding specificity of FOXM1 relative to other family members is in part achieved via an atypical chromatin interaction mechanism in which FOXM1 is bridged to DNA by the Myb-MuvB (MMB) transcriptional activator complex (62). Human *FOXM1* is located at 12p13.33 and has ten exons, nine of which are coding. Alternative splicing of exons Va (A1) and VIIa (A2) give rise to three FOXM1 variants: FOXM1a, FOXM1c, and FOXM1b (figure 3). FOXM1a contains exons Va and VIIa with the latter disrupting the transactivation domain, making this isoform transcriptionally inactive (Figure 3) (63). However, the addition of alternative exon A1 does not alter the binding of FOXM1c and FOXM1a (64).

FOXM1 is expressed in a cell cycle-dependent manner and regulated by post-translational modifications throughout the cell cycle via phosphorylation by many different kinases (60). Phosphorylation by ERK on Ser331 and Ser704 in the Pro-Gly-Ser-Pro (PGSP) motif regulates the nuclear translocation downstream of mitogen signaling. This

is highlighted by the observation that non-phosphorylated FOXM1 localizes to the cytoplasm, but phosphorylated FOXM1 is primarily located in the nucleus (65). Additionally, FOXM1b lacks exon A1, which contains an ERK1/2 target sequence (Ser331). In contrast FOXM1a/c contain exon A1 and Ser331 must be phosphorylated before they can translocate to the nucleus. Therefore, FOXM1b is thought to be constitutively active because it is proficient for nuclear translocation independent of this phosphorylation event.

FOXM1 function and expression in normal cells

FOXM1 protein was first identified because it was phosphorylated during mitosis and expressed in cycling cells. Further studies determined FOXM1 to be a transcription factor important for cell cycle progression through the G1/S and G2/M checkpoints in normal cells (58). Early studies showed FOXM1 to be critical for mitotic progression, whereby FOXM1-knockout MEFs had slower proliferation, failed to properly enter mitosis, accumulated mitotic defects, and eventually underwent progressive cellular senescence (66,67). Consistent with these phenotypes, FOXM1 has been demonstrated to play an essential role in the maintenance of appropriate chromosomal segregation and its loss resulted in genomic instability and accumulation of polyploid cells (68,69). Numerous studies have reported transcriptional targets of FOXM1 that allow mitotic progression, proper assembly of the mitotic spindles, accurate chromosome segregation and cytokinesis (66,70,71). Cell cycle regulation (G1-S and G2-M transitions) is the most characterized pathway that is influenced by the transcriptional activity of FOXM1 (40,60).

The expression and the transcriptional activity of FOXM1 are highly dependent on the cell cycle phase (72). FOXM1 mRNA and protein levels are low in quiescent cells, but are upregulated when cells enter the S-phase of the cell cycle and persist throughout the

G2 and M-phases (59). The transcriptional activity of FOXM1 correlates with its phosphorylation level. Both gradually increase as cells progress through the cell cycle reaching maximum levels at the G2/M transition. FOXM1 is initially phosphorylated in G1 and then further phosphorylated in a sequential order by multiple protein kinases, including Cdk-cyclin complexes and mitogenic kinases in the S and G2/M phases of the cell cycle, generating the hyperphosphorylated and fully active form of FOXM1 by the G2/M-phase (72). Moreover, FOXM1 is overexpressed and activated in many human cancers and possesses oncogenic activity *in vitro* and *in vivo* (40). Mechanisms accounting for FOXM1 expression in cancer are diverse and include p53 (73,74), Rb (74) and FOXO3 loss (2,75), Myc, HIF-1, Gli1, SP1, STAT3 and E2F activation (76-81), and genomic amplification (82).

Oncogenic features of FOXM1

FOXM1 has been linked to many hallmarks of cancer through its role as a transcription factor, activating target genes that functionally promote oncogenic phenotypes (40). By far, the most common phenotype associated with FOXM1 is the deregulation of the cell cycle to promote cellular proliferation. FOXM1 is necessary for tumor formation, which would be expected since it is an essential gene in normal cells; therefore, mice with FOXM1 knockout in all tissue types are not viable (69,83). This lethal phenotype agrees with the *in vitro* studies showing that loss of FOXM1 results in mitotic defects and eventually cellular senescence (66,68). Conversely, transgenic models show that FOXM1 expression alone is not sufficient for tumor formation (84). When FOXM1 is overexpressed in spontaneous and genetically engineered models of cancer, it results in shorter time to tumor formation and larger tumor size, supporting its oncogenic role in cellular proliferation (84).

FOXM1 associates with many hallmarks of cancer, but its link to genomic instability is not fully understood (40). The first association between FOXM1 expression and genomic instability is highlighted by its inclusion in the CIN25 signature, a gene expression profile predictive of chromosomal instability in cancer and patient clinical outcome (37). Surprisingly, many of the CIN25 genes are targets of FOXM1. FOXM1 was among the top-ranking genes whose expression correlated with chromosomal instability in in a pan-cancer analysis. Furthermore, FOXM1 overexpression in human keratinocytes induced genomic instability in the form of CNAs, and upregulated the protein levels of phospho-p38, phospho-p53, p21 and cleaved PARP1, suggesting induction of DNA damage by an unknown mechanism (85). In this context, FOXM1 is a transcriptional regulator of genes involved in DNA replication initiation (86,87), and overexpression of genes involved in DNA replication have been linked to DNA replication stress (88). Furthermore, FOXM1 enabled the accumulation of genomic instability by promoting cell cycle progression downstream of DNA damage induced by nicotine or UVB exposure (85,89). Similarly, FOXM1 was shown to function downstream of DNA damaged induced by MYC activation in human keratinocytes, which by itself impaired cell division due to mitotic defects (90). However, overexpression of FOXM1 rescued the proliferative capacity of MYC cells exhibiting high levels of DNA damage, thus promoting genomic instability (90). Together, these data suggest that FOXM1 activation could alter DNA replication dynamics inducing DNA replication stress but also enable cells with damaged DNA to evade the G2/M checkpoint, resulting in genomic instability. Lastly, FOXM1 is implicated in DNA repair via direct transcriptional regulation of genes involved the repair process (91). However, based on the literature described above, it seems that aberrant FOXM1 expression promotes genomic instability rather than reduces it (85,89).

DNA Replication Stress

Sources, cellular response and implications for cancer

DNA replication stress is caused by impediments in DNA replication, leading to fork stalling and/or collapse. DNA replication stress results from the uncoupling of the replicative helicase and polymerase, and leads to generation of ssDNA and, potentially, DNA damage (92-94). Both extrinsic and intrinsic mechanisms can cause DNA replication stress, and the latter includes oncogene-induced DNA replication stress. Oncogene-induced DNA replication stress is a major driver of cancer genomic instability, including copy number changes such as genomic duplications (95,96). The normal cellular response to DNA replication stress involves activation of cell cycle checkpoints that promote fork stabilization, fork restart, and DNA repair. Landmark studies over a decade ago showed that circumvention of the DNA replication stress response leads to dsDNA breaks and is a critical early event in oncogenesis (97). ATR activates CHK1 in response to damaged DNA generated from the resection of DNA double strand breaks (DSBs) and DNA replication stress, resulting in cell cycle arrest at S and G2/M checkpoints, inhibition of DNA replication and initiation of DNA repair (98,99). Although ATR responds to single stranded DNA (ssDNA) at sites of DSBs, it has a more extensive role in responding to DNA replication stress (99). The initial step in the activation of ATR in response to DNA damage occurs when ssDNA is coated with replication protein A (RPA), which allows for the independent recruitment of ATR by ATRIP (ATR interacting protein) and loading of the 9-1-1 (Rad9, Rad1, Hus1) checkpoint clamp by Rad17 (Figure 4) (99). Once the 9-1-1 complex is loaded onto DNA, TOPBP1 and RHNO1 interact with Rad9 and ATR, bringing TOPBP1 in close proximity to ATR allowing for its activation (Figure 4) (5,100). Once activated, ATR phosphorylates and activates CHK1 to mediate this signaling cascade through phosphorylation of numerous downstream targets (101,102). CHK1 regulates the

G2/M checkpoint by phosphorylating CDC25A, targeting it for proteasomal degradation (101). Since CDC25A activates the CDK1-CCNB1 complex to facilitate mitotic entry, cells arrest in the G2 phase upon CDC25A degradation (101).

In addition to serving as a barrier to transformation, numerous studies have now shown that tumor cells have elevated levels of constitutive DNA replication stress. These observations provide the rationale for therapies that target the DNA replication stress response, as the DNA replication stress response contributes to DNA repair and cancer cell survival (103,104). In particular, given the frequent impairment of ATM-p53 in cancer cells, tumor cells have heightened dependence on ATR-CHK1, the main DNA replication stress response pathway, for survival (105). In this regard, several emerging approaches that target the DNA replication stress response have entered clinical testing. These strategies include inhibitors of the ATR, CHK1, and WEE1 kinases (94,104,106). Inhibitors of ATR and CHK1 have anti-cancer activity, including in ovarian cancer, by inducing cell death and sensitizing cells to chemotherapeutic agents such gemcitabine, etoposide, topotecan, veliparib, and cisplatin (107,108). ATR inhibitors, AZD6738 and VE-822, are currently undergoing Phase I clinical trials (NCT02223923 and NCT02157792, respectively). VE-822 was the first ATR inhibitor to enter clinical development and is an analogue of VE-821, which was the first potent and selective inhibitor of ATR (109). Loss of p53, a frequent event in cancer and ubiquitous in HGSC, disrupts the G1 checkpoint, forcing cells to be dependent on ATR-CHK1 signaling and the G2/M checkpoint for DNA repair (110). It is proposed that tumors with p53 loss select for functional ATR-CHK1 signaling to sustain survival and proliferation (97,111).

Bidirectional Promoters

Genomic configuration and features

Bidirectional promoters are flanked by two genes arranged in a head to head orientation on opposite strands of genomic DNA with less than 1,000 bp between their transcription start sites (112). However, nearly 67% of head-to-head promoters have intervening sequences that are less than 300 bp in length (113). Trinklein *et al* conducted the first genome-wide computational analysis of bidirectional promoters (114). Of a total of 23,752 annotated genes, >10% were found to be in a bidirectional configuration sharing common promoter regions that were less than 1,000 bp apart. Ortholog mapping of bidirectional promoters in human and mouse showed that most bidirectional promoter arrangements are conserved across human and mouse genomes, which suggests this orientation supports a critical function (115). Mapping of gene orthologues across nine vertebrates species showed selective pressure for the retention of bidirectional gene pairs (head-to-head genes) compared to tail-to-tail genes spaced within 1,000 bp of each other, supporting a possible regulatory and functional need for this arrangement (116). Genomic features of a bidirectional promoter include the presence of a CpG island and lack of a TATA box (112,114,117). It was recently shown that bidirectional promoters are enriched with histone modifications H3K4me3, H3K9ac, H3K27ac, and H3K4me2 (118). Bidirectional promoters are overrepresented with the following transcription factor motifs: GABPA, MYC, E2F1, E2F4, NRF-1, CCAAT, and YY1 (119). Bidirectional promoters are devoid of repetitive elements, further suggesting that gene partners often play a functional role as housekeeping genes (113). Bidirectional genes are often co-expressed, and their function is enriched in processes such as cell cycle and DNA repair (114,117,120).

RHNO1

Genomic configuration and protein domains

Human *RHNO1* is located at 12p13.33 and consists of three exons, two of which are coding (Figure 5). Protein blast analysis indicates that RHNO1 orthologs exist only in vertebrates with the highest conservation being in the N- and C-termini of the protein (100), which agrees with conservation of the FOXM1-RHNO1 bidirectional promoter in vertebrates (115,116). RHNO1 protein contains a conserved APSES (Asm1p, Phd1p, Sok2p, Efg1p and StuAp) DNA binding domain at the N-terminus, which is necessary for interaction with the 9-1-1 complex (100) (Figure 5). Additionally, the C-terminus is required for binding the 9-1-1 complex and TopBP1, localizing to sites of DNA damage and promoting efficient HR (100). RHNO1 was previously identified to be a substrate of ATM/ATR kinases in a high-throughput proteomics screen following treatment with ionization radiation (121). This hit was followed up after the function of RHNO1 was identified and mutation of the potential ATM/ATR sites did not affect its localization to sites of DNA damage or disrupt protein-protein interactions (100).

Contribution to ATR-CHK1 signaling and homologous recombination

Prior to 2011, RHNO1 was classified as an ORF with unknown function, formerly known as C12orf32 (chromosome 12 open reading frame 32) and information on this molecule was limited to a single publication (122). In 2011, RHNO1 was identified in a high-throughput siRNA screen investigating the DNA damage response (100). Loss of RHNO1 abrogated the G2/M checkpoint, allowing cells to enter mitosis with damaged DNA. Further biochemical studies established its interaction with the 9-1-1 complex, required for the full activation of ATR, hence the name change from C12orf32 to RHNO1

(Rad9, Rad1, Hus1 interacting nuclear orphan). The activation of ATR is dependent on the direct interaction of TOPB1 and RHNO1, which ultimately bridges the protein-protein interaction between ATR and the 9-1-1 checkpoint clamp (Figure 4) (5,123). Furthermore, the loss of RHNO1 also decreased HR proficiency although to a lesser extent than what was observed with ATR loss, which agrees with its role as a modifier to ATR activation (100). In agreement, depletion of RHNO1 and Rad17, a protein that recruits the 9-1-1 checkpoint clamp to chromatin after DNA damage, had similar impairment of HR proficiency which suggests that RHNO1 primarily promotes HR through the ATR-CHK1 pathway (100). The observation that the RHNO1 gene is only present in vertebrate genomes indicates it is a unique regulatory factor of the ATR-CHK1 pathway (100).

Oncogenic phenotypes of RHNO1

The study of RHNO1 in cancer is limited to a single publication that found the mRNA to be overexpressed in breast cancer and protein was localized to the nucleus (122). Subsequent knockdown of RHNO1 in two different breast cancer cell lines decreased colony formation and increased the number of sub-G1 cells, suggesting RHNO1 depletion promotes cell death (122). These data suggest that RHNO1 is an oncogene that is important for cancer cell survival. Although these studies were done prior to the discovery of its functional role in ATR-CHK1 signaling, the phenotypes associated with RHNO1 loss agree with its more recently identified function.

DISSERTATION OBJECTIVES

Since the initial discovery of FOXM1 in 1994, it has been reported to contribute to many normal and cancer phenotypes. However, a role for FOXM1 in HGSC was not proposed until 2012 when TCGA reported that FOXM1 transcription factor activation as the second most frequent molecular alteration in HGSC (84% of cases), second only to mutations of TP53 (100%). Therefore, further study of FOXM1 is critical to define its potential role in HGSC biology and to address the following knowledge gaps: 1) FOXM1 transcriptional pathway is activated in HGSC, but genetic mechanisms that contribute to FOXM1 expression in HGSC are not known; 2) FOXM1 expression is associated with genomic instability and genomic instability is a defining feature of HSGC, yet this relationship has not been explored in HGSC nor is the mechanism known in any context; and 3) FOXM1 shares a bidirectional promoter with RHNO1, but the cooperativity between these gene partners has never been explored. To address these knowledge gaps, we propose the following specific aims:

SPECIFIC AIM 1: Determine the genetic contribution to FOXM1 expression in high-grade serous ovarian cancer.

SPECIFIC AIM 2: Determine the relationship between FOXM1 expression and genomic instability in high-grade serous ovarian cancer.

SPECIFIC AIM 3: Determine the functional contribution of FOXM1 and RHNO1 to survival and chemoresistance in high-grade serous ovarian cancer.

Figures

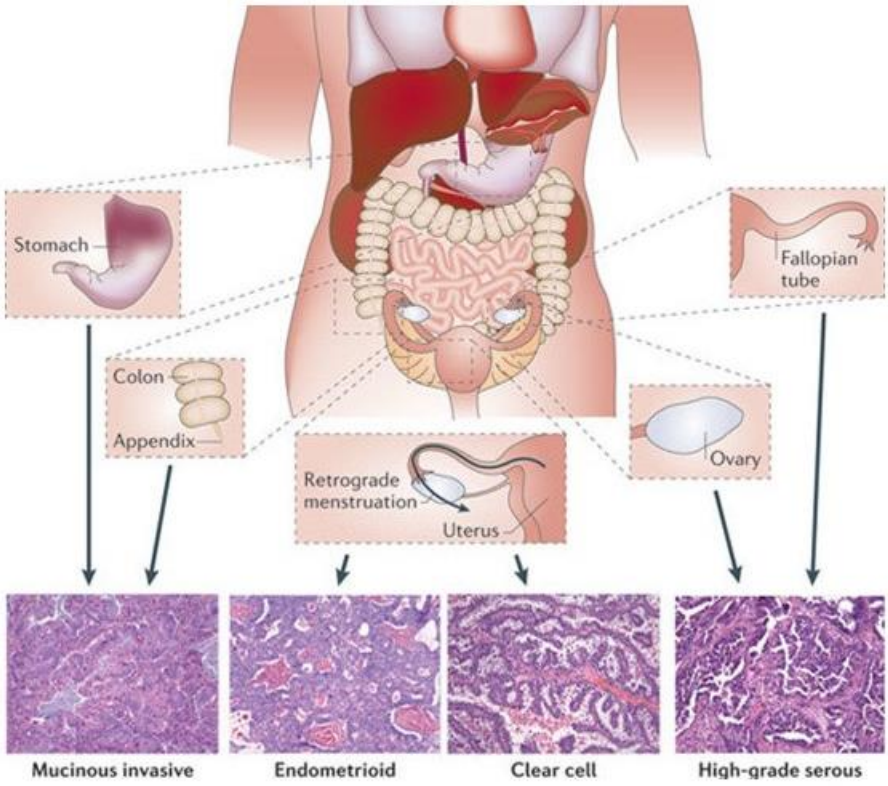

Figure 1. Epithelial ovarian cancer (EOC) histological subtypes. The upper panels show the presumed tissues of origin for EOC histological subtypes. The lower panels show images of H&E staining for the different histological subtypes. Adapted from: (1).

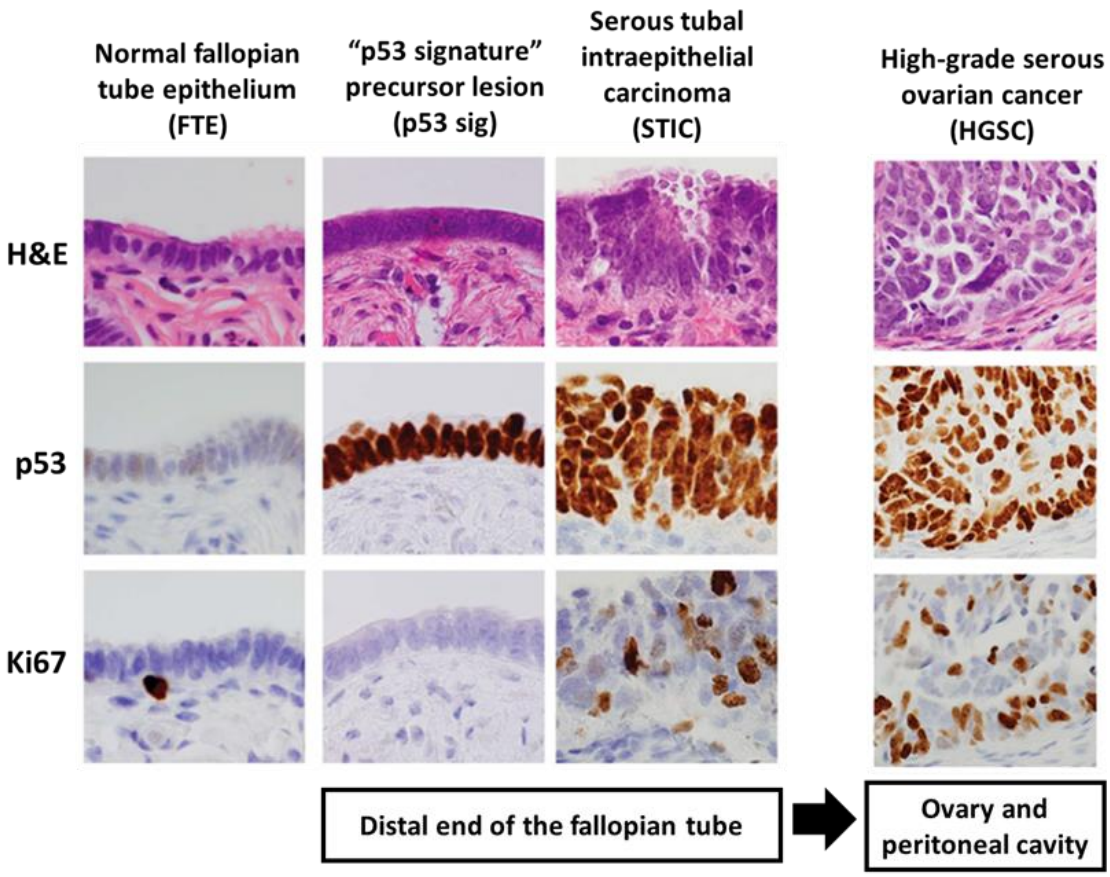

Figure 2. HGSC precursor lesions in the fallopian tube. Images represent H&E or IHC staining of tissues from different lesions as indicated on the left and top of the figure. HGSC = invasive cancer or primary tumor on the ovary, not within the fallopian tube. Precursor lesions start with normal FTE to the left and proceed to the right with the acquisition of additional malignant features. Lesions are detected in the distal end of the fallopian tube. Adapted from: (2).

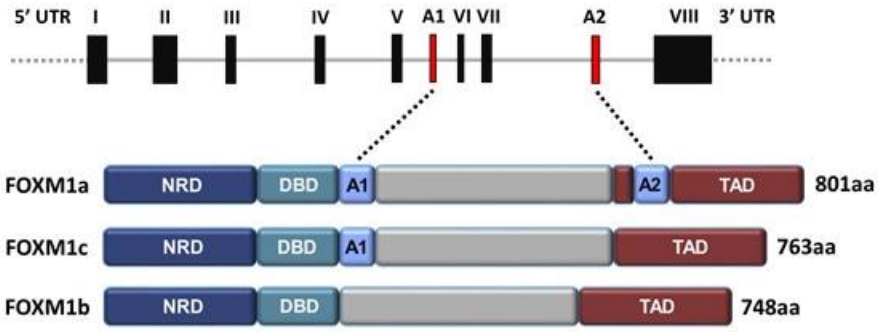

Figure 3. FOXM1 mRNA and protein. *FOXM1* mRNA is displayed at top showing 10 exons with intervening introns. The red boxes highlight the alternative exons, A1 and A2, which give rise to the different exons shown below. FOXM1 isoforms are shown below along with their protein domains. The N-terminus has a repression domain (NRD). The forkhead DNA binding domain, DBD, immediately following the NRD. FOXM1a and FOXM1c possess alternative exon A1. The C terminus contains the transactivation domain (TAD). FOXM1a possesses alternative exon A2, which disrupts the function of the TAD.

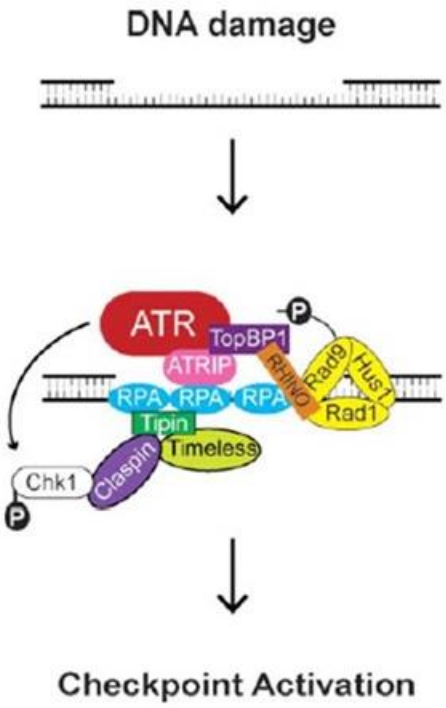

Figure 4. ATR-CHK1 activation in response to DNA damage. DNA damage generates single stranded which serves as a scaffold for the recruitment of the 9-1-1 checkpoint clamp. Through protein-protein interactions, the 9-1-1 checkpoint clamp recruits ATR allowing for its activation. ATR kinase then phosphorylates downstream effector proteins to signal the DNA damage response and promote cell cycle arrest and DNA repair. Adapted from: (5).

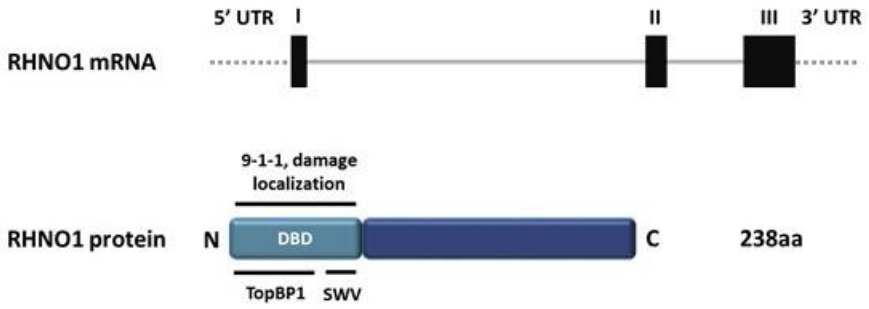

Figure 5. RHNO1 mRNA and protein. *RHNO1* mRNA is displayed at top showing three exons with intervening introns. The N-terminus, in light blue, contains the DBD, which has a sequence similar to the APSES (ASM-1, Phd1, StuA, EFG1, and Sok2) domain, a DNA binding domain found in fungi and homologous to the KilA-N domain found in eukaryotic viruses. The N-terminus interacts with 9-1-1 checkpoint proteins including TOPB1. The SWV region, when mutated, impairs RHNO1 for interaction with 9-1-1 checkpoint proteins. The C-terminus, in dark blue, is not essential for these interactions.

CHAPTER 2: MATERIALS AND METHODS

Human Tissue Samples

Bulk normal ovary (NO) tissues and EOC samples (n=143) were obtained from patients undergoing surgical resection at Roswell Park Comprehensive Cancer Center (RPCCC) under Institutional Review Board-approved protocols, as described previously. Pathology specimens were reviewed at RPCCC, and tumors were classified according to World Health Organization criteria (124) Flash-frozen bulk tumor tissue samples were crushed using liquid nitrogen pre-chilled mortar and pestles. Genomic DNA was isolated from approximately 20 mg of powdered tissue using the Puregene Tissue Kit (Qiagen). Upon the addition of cell lysis buffer, the tissue powder was immediately homogenized using VWR Pellet Mixer (VWR International) with disposable microtube pestles (Argos Technologies). Total RNA was extracted by TRIzol reagent (Invitrogen) from approximately 20 mg of powdered tissue. The tissue was immediately homogenized in TRIzol by an electric homogenizer with disposable microtube pestles. Total protein was extracted using radioimmunoprecipitation assay (RIPA) buffer (25 mM Tris HCl pH 7.6, 150 mM NaCl, 1% NP-40, 1% sodium deoxycholate, 0.1% SDS) containing Protease Inhibitor Cocktail (SIGMA), Phosphatase Inhibitor Cocktail 1 (SIGMA) and Phosphatase Inhibitor Cocktail 2 (SIGMA). Upon the addition of RIPA buffer, the frozen tissue powder was immediately homogenized using an electric homogenizer with disposable microtube pestles. The solution was further sonicated with a Bioruptor (Diagenode).

Cell Lines

COV362 and COV318 cell lines (Sigma) were cultured in DMEM (Corning) supplemented with 10% fetal bovine serum (FBS, Invitrogen), 2 mM glutamine (Life

Technologies), and 1% penicillin-streptomycin (pen-step, Life Technologies). KURAMOCHI and OVSAHO (Japanese Collection of Research Bioresources Cell Bank) and SNU-119 (Korean Cell Line Bank) cell lines were cultured in RPMI-1640 (Hyclone) supplemented with 10% FBS and 1% pen-strep. The OVCAR4 cell line (National Cancer Institute Division of Cancer Treatment and Diagnosis Cell Line Repository) was cultured in RPMI-1640 supplemented with 10% FBS and 1% pen-strep. The OVCAR8 cell line (National Cancer Institute Division of Cancer Treatment and Diagnosis Cell Line Repository) was cultured in DMEM (Corning) supplemented with 10% FBS, and 1% penicillin-streptomycin (pen-step, Life Technologies). The OVCAR3 cell line (American Type Culture Collection) was cultured in DMEM with 10% FBS and 1% pen-strep. Caov3 and OVCAR5 cell lines were generous gifts from Professor Anirban Mitra (Indiana University) and were cultured in DMEM with 10% FBS and 1% pen-strep. UWB1.289, UWB1-SyR12 and UWB1-SyR13 cell lines were generous gifts from Professor Lee Zou (Massachusetts General Hospital Cancer Center) and were cultured in RPMI 1640/Mammary Epithelial Growth Media (1:1; Hyclone/PromoCell) supplemented with 3% FBS, MEGM growth factors and 1% pen-step. Primary hOSE cells (ScienCell) were cultured in Ovarian Epithelial Cell Medium (ScienCell, 7311). HGSC precursor cells or immortalized fallopian tube epithelial (FTE; FT190, FT282-E1 and FT282) cells were a generous gift from Professor Ronny Drapkin (University of Pennsylvania) and were cultured in DMEM-Ham's F12 50/50 (Corning) supplemented with 2% USG (Pall Corporation) or 10% FBS and 1% pen-strep (Figure 6). IOSE-T (IOSE-21, hOSE immortalized with hTERT) cells (125) were a generous gift from Professor Francis Balkwill (Cancer Research UK) and were cultured in Medium 199/MCDB105 (1:1, Sigma) supplemented with 15% FBS, 1% pen-strep, 10 ng/mL human epidermal growth factor (Life Technologies), 0.5 µg/mL hydrocortisone (Sigma), 5 µg/mL bovine insulin (Cell Applications), and 34 µg protein/mL bovine pituitary extract (Life Technologies). IOSE-SV

(IOSE-121, hOSE immortalized with SV40 Large T antigen) were a generous gift from Professor Nelly Auersperg (University of British Columbia) and were cultured in Medium 199/MCDB105 (1:1) supplemented with 10% FBS and 25 µg/ml gentamicin (Life Technologies). mOSE cells and floxed p53 and Rb variants (126) were a generous gift from Professor Barbara Vanderhyden (Ottawa Hospital Research Institute) and were cultured in Alpha Modified MEM (Corning) containing 10% FBS, 0.05% pen-strep, 1 µg/ml gentamicin, and 1% insulin–transferrin–sodium–selenite solution (ITSS, Roche). HEK293T cells (American Type Culture Collection) was cultured in DMEM with 10% FBS and 1% pen-strep. U2OS-DR-GFP (282C) cells were a kind gift from Professor Jeremy Stark (City of Hope) and grown in McCoy's 5A (Corning), 10% FBS and 1% pen-strep (127,128). OVCAR8-DR-GFP cells were a kind gift from Professor Larry Karnitz and Professor Scott Kaufmann (Mayo Clinic) and grown in the same conditions as the OVCAR8 parental cells as described above (108). All cell lines were maintained at 37 °C in a humidified incubator with 5% CO_2. Cell culture medium was changed every 3-5 days depending on cell density. For routine passage, cells were split at a ratio of 1:3-10 when they reached 85% to 90% confluence. Cell lines were authenticated by short tandem repeat (STR) analysis at the DNA Services Facility, University of Illinois at Chicago, and confirmed to be for Mycoplasma free by RT-qPCR at the Epigenetics Core Facility, University of Nebraska Medical Center. Doxycycline inducible cells were treated every 48 hours with doxycycline (Sigma, solubilized in water) unless otherwise noted.

Pharmacologic Inhibitors

Cells were treated with the following inhibitors: PARPi (olaparib, ABT-888, solubilized in DMSO) from SelleckChem, ATRi (VE-822, VX970) from SelleckChem,

hydroxyurea (HU) from Sigma or etoposide (Etop, E1383, solubilized in DMSO) from Sigma.

DNA, RNA and Protein Extracts from Cell Lines

Genomic DNA was isolated from cell lines using the Puregene Tissue Kit (Qiagen). Total RNA was purified using TRIzol (Invitrogen). Total protein was extracted with RIPA buffer. Nuclear and cytosolic proteins were extracted from cell samples using the NE-PER Nuclear and Cytoplasmic Extract kit (Pierce Biotechnology). Protease Inhibitor Cocktail (Sigma), Phosphatase Inhibitor Cocktail 1 (Sigma) and Phosphatase Inhibitor Cocktail 2 (Sigma) were added to protein lysis buffers.

Bulk RNA Sequencing (RNA-seq) Analysis

RNA was isolated from cell lines according to the method described above. The RNA samples were transported to the UNMC DNA Sequencing Core Facility. RNA samples were analyzed with respect to purity and potential degradation. Purity and concentration were assessed by measurement of the A260/280 ratios using a Nanodrop instrument (Thermo Scientific, Nanodrop Products, Wilmington, DE) instrument and only those samples with values of 1.8 to 2.0 underwent further processing. Potential degradation of the samples was assessed by analysis of 200 ng of the RNA with an Advanced Analytical Technical Instruments Fragment Analyzer (AATI, Ames, IA) and only intact RNA samples were used to generate sequencing libraries. Sequencing libraries were generated by the UNMC NGS Core beginning with 1 µg of total RNA from each sample using the TruSeq V2 RNA sequencing library kit from Illumina following recommended procedures (Illumina Inc., San Diego, CA). Resultant libraries were

assessed for size of insert by analysis of an aliquot of each library on a Bioanalyzer instrument (Agilent Technologies, Santa Clara, CA). Each library had a unique indexing identifier barcode allowing the individual libraries to be multiplexed together for efficient sequencing. Multiplexed libraries (12 samples per pool) were sequenced across 2 lanes of the HiSeq 2500 DNA Analyzer (Illumina) to generate a total of approximately 20 million 75 bp single reads for each sample. During sequencing the quality was continually monitored regarding cluster number and fluorescence intensity and percentages of reads passing filter with a Q30 score. Following sequencing, samples were demultiplexed to produce FASTQ files. The UNMC Epigenomics Core Facility processed the resulting sequence files based on the following steps. Adaptor sequences and low quality (Phred score: 20) ends were trimmed from sequences using the Trim Galore software package (http://www.bioinformatics.babraham.ac.uk/projects/trim_galore/). Resulting FASTQ files were aligned to the human genome (NCBI37/hg19) using the software TopHat (v2.0.8) (http://ccb.jhu.edu/software/tophat/index.shtml). The software Cufflinks (v2.1.1) http://cole-trapnell-lab.github.io/cufflinks/ was used to estimate the expression values, and Cuffdiff (v2.1.1) was used to determine differential expression. Geneset enrichment analysis (GSEA) was performed using the GSEA software version 3, build 0160, available from the BROAD Institute (http://www.broadinstitute.org/gsea/index.jsp) (129). Bulk RNA-seq datasets, with genes ranked by log2 fold-change, were compared against the Hallmark Signature genesets (http://software.broadinstitute.org/gsea/msigdb/genesets.jsp?collection=H) or a custom CIN70 geneset based on the CIN70 gene expression signature (37). Output data included normalized enrichment score (NES) and FDR (q-value). Statistical significance was set at an FDR < 0.25. NES was used for comparing enrichment because it accounts for differences in gene set size and in correlations between gene sets and the expression dataset.

Single-Cell RNA Sequencing (scRNA-seq) Analysis

FT282 and OVCAR8 cells were seeded at day 0 at ~50% and ~30% confluency, respectively, then harvested at day 2 at ~80% confluence. Cells were trypsinized and suspensions were pipetted several times and passed through a 40 µm cell strainer to ensure a single cell suspension. Cell viability (Trypan blue exclusion) was confirmed to be greater than 90% using the TC20 Automated Cell Counter (Bio-Rad). Cell pellets were washed twice in PBS containing 0.04% BSA, then resuspended in PBS and 0.04% BSA to ~500,000 cells/ml and transported to the UNMC DNA Sequencing Core Facility for single cell capture, library preparation and scRNA-sequencing. As per manufacturer instructions, approximately ~2,750 cells were loaded per channel to achieve a target of ~1,500 captured cells. Single cells were loaded on a Chromium Single Cell Instrument (10x Genomics) to generate single cell Gel Bead in Emulsions (GEMs) for the partitioning of samples and reagents into droplets. GEMs contain oligos, lysed cell components and Master Mix. GEMs were processed as following: briefly, cells were lysed, RNA extracted, and reverse transcribed to generate full-length, barcoded cDNA from the poly A-tailed mRNA transcripts. Barcoded cDNA molecules from every cell were PCR-amplified in bulk followed by enzymatic fragmentation. The Qubit was then used to measure and optimize the insert size of the double-stranded cDNA prior to library construction. Single cell cDNA and RNA-Seq libraries were prepared using the Chromium Single Cell 3' Library and Gel Bead Kit v2 (10x Genomics) and the products were quantified on the 2100 Bioanalyzer DNA High Sensitivity Chip (Agilent). Each fragment contains the 10x Barcode, UMI and cDNA insert sequence used in data analysis. During library construction Read 2 is added by Adapter ligation. Both single cell libraries were sequenced using the Illumina NextSeq 550 system using the following parameters: pair-end sequencing with single indexing, 26 cycles for Read1 and 98 cycles for Read2. FT282 cells produced a total of 85.6 million reads and OVCAR8 produced 82 million reads, and both had an overall Q30 for the run

of 87.6%. Sequencing data were transferred to the Bioinformatics and Systems Biology Core Facility for analysis. The Cell Ranger Single Cell Software (10X Genomics) was used to process raw bcl files to perform sample demultiplexing, barcode processing and single cell 3' gene counting (https://software.10xgenomics.com/single-cell/overview/welcome). Each dataset was aligned to a combined human (hg19) reference and only cells that were identified as aligned to human in the "filtered" output of the Cell Ranger count module were used in the analysis.

Statistical Impute of Transcript Dropouts in Single-Cell RNA Sequencing Datasets

The statistical method scImpute was used to accurately and robustly impute the transcript dropouts (zero values) that exist in scRNA-seq data from sequencing small amount of RNA (130). The scImpute R package was downloaded from https://github.com/Vivianstats/scImpute and was run in R with default settings. FT282 and OVCAR8 scRNA-seq raw gene expression matrix files (.mtx) were converted into dense expression matrices using `cellRanger mat2csv` command. The scImpute input data consisted of a scRNA-seq matrices with rows representing genes and columns representing cells, and output data consisted of an imputed count matrix with the same dimension.

Reverse Phase Protein Array (RPPA)

RPPA was performed at the RPPA Core Facility at MD Anderson Cancer Center (https://www.mdanderson.org/research/research-resources/core-facilities/functional-proteomics-rppa-core.html). The protein lysates were prepared according to the Core's instructions and sent to them for the profiling. Briefly, immortalized fallopian cell lines engineered for doxycycline inducible expression were grown in the presence of

doxycycline for 72 hours then harvested for protein. Proteins were extracted by adding RIPA buffer to monolayer cultures on ice. Protein concentrations were measured by the BCA assay then normalized to 1 µg/ml in 1X sample loading buffer containing beta-mercaptonethanol. Samples were incubated 95 °C for 5 minutes then stored at -80 °C until they were submitted to the Core for the analysis. All samples were run in biological triplicate. The Core stained the slides with 304 unique antibodies (RPPA antibody set 145-Present). Stained slides were analyzed on Array-Pro then by supercurve R ×64 2.15.1. There were 14 sets of replicated antibodies and 3 negative controls for secondary antibodies among 243 slides. QC tests were performed for each antibody staining (slide). All the data points were normalized for protein loading, transformed to linear values and subsequently transformed to log2 values (NormLog2) and then median-centered for hierarchical clustering analysis (NormLog2_MedianCentered). Heat maps were generated using the online software Morpheus (http://broadinstitute.org) as hierarchical clusters with normalized log2, median centered RPPA data using the one minus Pearson Correlation metric and average linkage method.

Cell Viability Measurements

Cells were seeded at a density of 500-1,000 cells per well in quadruplicate into sterile 96-well plates and treated with the indicated drug for 96 hours. AlamarBlue (BioRad) was used to assess cell viability. Background values from empty wells were subtracted and data were normalized to vehicle-treated control.

Homologous Recombination (HR) Reporter Assay

U2OS and OVCAR8 cells were previously generated for stable integration of DR-GFP, an HR substrate that generates a functional green fluorescent protein (GFP) upon successful HR after I-SceI cutting (108,128,131). U2OS and OVCAR8 cells were grown in the presence of doxycycline for 48 hours to induce shRNA expression. U2OS cells were transfected with pCBASceI (Addgene; #26477) in the presence of 1 µg/ml doxycycline. Media containing doxycycline was changed 3 hours post transfection and cells were kept in culture for an additional 48 hours. OVCAR8 cells were transduced for 8 hours with AdNGUS24i, an adenovirus expressing I-SceI (Drs. Frank Graham and Phillip Ng). Cells were harvested and fixed with 10% formaldehyde, washed and analyzed by FACS to determine the fraction of GFP positivity.

***In Vitro* Clonogenic Survival Assay**

To assess colony formation, cells were trypsinized, counted and seeded at a density of 500-1,000 cells per well in 6-well dishes in single-cell suspension and allowed to form colonies for 8-12 days. Following incubation, cells were simultaneously fixed and stained in PBS containing 10% methanol and 0.5% crystal violet for 30 minutes at room temperature, rinsed with water and air dried overnight. Colonies containing over 50 cells were manually counted with an inverted light microscope.

Comet Assay

The Comet Assay Kit (Trevigen) was used according to the manufacturer's instructions. Briefly, cells were suspended in low melt agarose, layered onto treated slides to promote attachment (500 cells per slide), lysed, and subjected to electrophoresis (1

V/cm) under alkaline conditions using the Comet Assay Electrophoresis System II (Trevigen). Samples were then fixed, dried, and stained with SYBR Gold. Images were acquired with a 10X objective lens using the EVOS FL Cell Imaging System (ThermoFisher). Comet tail size was quantified using Comet Analysis Software (Trevigen).

Flow Cytometry

Cells were fixed in 70% ethanol overnight for cell cycle and γ-H2AX expression analysis. Fixed cells were washed with PBS and incubated overnight in PBS containing 1% BSA, 10% goat serum and pS139-H2AX antibody (Millipore), washed and incubated in goat anti-mouse Alexa Fluor 647 antibody for 30 minutes at RT. Cells were incubated in 50 µg/mL propidium iodide and 100 µg/mL RNase A for 30 minutes, and 10,000 cells per sample were analyzed on a BD FACSarray (BD Biosciences) using 532- and 635-nm excitations and collecting fluorescent emissions with filters at 585/42 nm and 661/16 nm (yellow and red parameters, respectively).

Production of Lentiviral Particles and *In Vitro* Lentiviral Transduction

Replication-deficient lentivirus was produced by transient transfection of psPAX2 (Addgene; 12260), pDM2G (Addgene: 12259) and transfer plasmid into HEK293T cells. Viral supernatant was collected at 48 hours and filtered. Select cell lines were transduced with serially diluted viral supernatant followed by antibiotic selection for functional titration. Cells were expanded from the viral dilution well that resulted in 30% survival following antibiotic selection.

MOSE Cell *In Vitro* Adenoviral Transduction

Recombinant adenovirus expressing enhanced GFP (Ad-eGFP, control) or both eGFP and Cre recombinase (AdCre-eGFP) were purchased from the University of Iowa Gene Transfer Vector Core. mOSE cells were transduced at a MOI of 200.

MOSE Cell Genotyping and Detection of Recombination

Genomic DNA was isolated using the Puregene Tissue Kit (Qiagen). DNA was resuspended in Tris-EDTA (50 mM, pH 6.8). Genotyping was performed as previously described (30). PCR was performed with an annealing temperature of 60 °C and 30 cycles for all primer pairs. Primer sequences are listed in Table 2.

Plasmid Constructs and RNA Interference

Tables 2 and 3 contains a list of all plasmids, siRNAs, shRNAs, and sgRNAs. All cloning was sequence verified. Plasmids were transfected with Lipofectamine 2000 (Life Technologies), according to the manufacturer's instructions. siRNAs were transfected with Lipofectamine RNAiMax reagent (Life Technologies), according to the manufacturer's instructions.

Site-Directed Mutagenesis

FOXM1c DNA binding domain was mutated as following, R286A, H267A, and S290A, rendering FOXM1 deficient in DNA binding (132). All plasmids were sequence verified. Primers were designed using QuikChange Primer Design software (Agilent Technologies) and are listed in Table 2.

Murine Ovarian Tumor Model

Trp53$^{loxP/loxP}$/*Rb1*$^{loxP/loxP}$ mice (floxed *Trp53* and *Rb1*) were a kind gift from Professor Kenneth Gross (RPCCC). All mice were maintained identically, following recommendations of the Institutional Laboratory Animal Use and Care Committee (at RPCCC). Intrabursal injections of recombinant adenovirus expressing both enhanced GFP and Cre recombinase (AdCre-eGFP) or eGFP alone (Ad-eGFP) as the contralateral control (University of Iowa Gene Transfer Vector Core) were performed on adult mice in estrus as previously described (133). Mice were determined to be in estrus by vaginal cytology. The original viral stock solution was diluted with PBS to $3.5x10^9$ pfu/mL immediately before injection of 10 µL. Mice were euthanized and subjected to necropsy when tumor mass exceeded 1 cm or the animal exhibited other signs of sickness, such as abdominal distension and moribund behavior. Tumor samples were dissected and snap frozen in liquid nitrogen and stored at -80 °C. Frozen tumor samples were ground into a powder with a mortar and pestle over liquid nitrogen and immediately processed for RNA (mRNAeasy Mini Kit, Qiagen) and whole cell protein cell extracts were prepared with RIPA buffer (1X PBS, 1% NP40, 0.5% sodium deoxycholate, 0.1% SDS) supplemented with protease and phosphatase inhibitors, and centrifuged at 4 °C for 10 minutes at 14,000 *g*. RNA was treated for contaminating DNA using the TURBO DNA-free Kit (Ambion), and integrity was determined using a bioanalyzer (Agilent). One µg of DNase treated RNA was converted to cDNA using the iScript cDNA Synthesis Kit (Bio-Rad).

Immunohistochemistry of Mouse Tumor Tissue Samples

Formalin-fixed paraffin blocks were cut into 4 µm sections, placed on charged slides, and dried at 60 °C for one hour. Slides were cooled to room temperature, deparaffinized in three changes of xylene, and rehydrated using graded alcohols. For

antigen retrieval, slides were heated in a steamer for 20 minutes in citrate buffer pH=6 (BioCare Medical, B910) for Smooth Muscle Actin or target retrieval solution pH=9 (Dako, S2367) for Cytokeratin and allowed to cool for 20 minutes, endogenous peroxidase was quenched with aqueous 3% H_2O_2 for 10 minutes, and the slides were washed with PBS/T. Slides were loaded on a Dako autostainer and serum-free protein block (Dako, X0909) was applied for 5 minutes, blown off and the corresponding antibody was applied. Smooth Muscle Actin antibody (Abcam, ab5694) was applied at 1:125 (Rabbit IgG) for one hour. Powervision poly HRP anti-rabbit IgG (Leica; catalog #PV6119) was then applied for 30 minutes. L- DAB (Leica; catalog #PV6126), applied for 5 minutes, was used for chromogen visualization. Pan-Cytokeratin antibody (Dako, Z0622) was applied at 1:1750 (Rabbit IgG) for one hour. Rabbit Envision/ labeled polymer HRP anti -rabbit (Dako; catalog #K4003) was then applied for 30 minutes. DAB (Dako; catalog #K3468), applied for 10 minutes, was used for chromogen visualization. Lastly, the slides were counterstained with hematoxylin, rinsed, and cover slipped.

Reverse Transcription Quantitative PCR (RT-qPCR)

Total RNA was purified using TRIzol (Invitrogen) and quality was determined by RNA denaturing gel. Briefly, one µg of RNA was DNase-treated using the DNA-free kit (Ambion) or treated in column during purification with the Zymo Pure RNA Isolation Kit. RNA was converted to cDNA using the iScript cDNA Synthesis Kit (BioRad). One µl of 1:5 cDNA sample dilutions were used for qPCR reactions. Standard curves were prepared using gel-purified end-point RT-PCR products. All samples were run in triplicate using the CFX Connect Real-Time System (Bio-Rad Laboratories) and all gene expression data were normalized to 18s rRNA. PCR was performed with an annealing temperature of 60 °C and a total of 45 cycles for all primer pairs. Dissociation curves were performed to

confirm specific product amplification. RT-qPCR standards for each gene were generated from a mixture of human or mouse cell cDNA via end-point RT-PCR then gel purification, using the appropriate primer pair. Gradient PCR reactions were performed with the C1000 Touch Thermal cycler (Bio-Rad Laboratories) to determine the annealing temperatures for each primer set. Primer sequences are listed in Table 2. Primer sequences corresponding to each gene for the mRNA expression analysis were designed using NCBI Primer Blast (134) or selected from those previously reported in the literature.

Microarray Analysis of FOXM1 and E2F1 Expression

Affymetrix HG 1.0ST arrays were used to determine the expression of FOXM1 and E2F1 in EOC. Probe generation, array hybridization, and expression analyses were performed by the Next Generation Sequencing and Expression Analysis Core Facility at the University at Buffalo Center for Excellence in Bioinformatics. Samples included 40 primary EOC tissues.

Western Blot

Whole cell protein extracts were prepared with RIPA buffer [1X PBS, 1% NP40, 0.5% sodium deoxycholate, 0.1% sodium dodecyl sulfate (SDS)] supplemented with protease and phosphatase inhibitors (Sigma) and centrifuged at 4 °C for 10 minutes at 14,000 *g*. Nuclear extracts were prepared using the NE-PER Nuclear and Cytoplasmic Extraction Kit (Thermo Scientific) supplemented with protease and phosphatase inhibitors. Protein concentration was determined by the BCA protein assay (Thermo Scientific). Equal amounts of protein (30-50 µg) were fractionated on 4-12% gradient SDS-polyacrylamide gel electrophoresis gels (Invitrogen) and transferred to PVDF membranes (Roche). Membranes were stained with Ponceau S to confirm efficient transfer and equal

loading then blocked with 5% nonfat dry milk in Tris-buffered saline Tween-20 (TBST) for 1 hour at room temperature. The membranes were incubated with primary antibodies in 5% nonfat dry milk in TBST at 4 °C overnight followed by incubation with secondary antibody in 5% nonfat dry milk in TBST for 1 hour at room temperature. Primary antibodies are listed in Table 4. Enhanced chemiluminescence (Thermo Fisher Scientific) was used for protein detection. Quantification of protein expression was performed using ImageJ software (Image Processing and Analysis in Java, National Institute of Health) (135).

Co-Immunoprecipitation

Cells expressing empty vector, and Flag- or HA-tagged ORFs were lysed with M-PER (Pierce) containing Halt Protease and Phosphatase Cocktail (Pierce), and Nuclease S1. Lysates were mixed end over end at 4 ºC for 30 minutes then centrifuged at 4 °C for 10 minutes at 14,000 *g* to eliminate cellular debris. Protein concentration was determined by the BCA protein assay (Thermo Scientific). Immunoprecipitation was performed with anti-Flag or HA magnetic beads and 500 µg total protein. Samples were incubated overnight at 4 ºC with end over end mixing. The next day the magnetics beads were washed, and protein eluted with sample loading buffer. The entire sample was loaded on the Western blot along with 5% total protein as input.

Illumina Infinium Human Methylation 450K Datasets

The TCGA pan-cancer DNA methylation (HumanMethylation450K) dataset was downloaded from UCSC Xena (http://xena.ucsc.edu), consisting of 9,753 samples. The TCGA pan-cancer dataset contains the DNA methylation 450K array beta values, compiled by combining available data from all TCGA cohorts. The GDSC1000 collection (The Genomics of Drug Sensitivity in Cancer Project, Welcome Sanger Institute) was

downloaded from NCBI GEO (GSE68379) (136). The NCI-60 cell line DNA methylation 450K dataset (NCBI GEO: GSE66872) was downloaded from CellMiner (137,138). For all datasets, the DNA methylation profile was measured experimentally using the Illumina Infinium HumanMethylation450 platform and Infinium HumanMethylation450 BeadChip Kit. The method consists of approximately 450,000 probes querying the methylation status of CpG sites within and outside CpG islands. The DNA methylation score of each CpG is represented as a beta value, which is a normalized value between 0 (fully-unmethylated) and 1 (fully-methylated).

Sodium Bisulfite DNA Sequencing

Sodium bisulfite DNA sequencing was used to determine the methylation status of the FOXM1/RHNO1 bidirectional promoter (139). Sanger sequencing analysis was performed by the University of Nebraska Medical Center DNA Sequencing Core Facility. Genomic DNA was isolated using the Puregene Tissue Kit (Qiagen) as described above, and then were chemically converted with sodium bisulfite using the EZ DNA Methylation Kit (Zymo Research Corp.). The FOXM1 and RHNO1 bidirectional promoter containing a CpG island was amplified from the bisulfite-converted DNA using methylation PCR specific primers, designed using MethPrimer (Table 2) (140). Gradient PCR reactions were analyzed using a C1000 Touch Thermal cycler (Bio-Rad) to optimize annealing temperatures for the primer set. After gel purification using the QIAquick Gel Extraction Kit (QIAGEN), PCR products were cloned using either the TOPO TA Cloning Kit (Invitrogen). Between 9 and 15 individual clones were sequenced for each sample. DNA sequence information was analyzed using the Lasergene SeqMan Pro program (DNASTAR, Inc.).

5’ RNA Ligase-Mediated Rapid Amplification of cDNA Ends (RLM-RACE) Mapping

The transcription start site of FOXM1 and RHNO1 in different cell lines was determined using the FirstChoice RLM-RACE Kit (Ambion), according to the manufacturer's instructions. RNA for RLM-RACE analysis was isolated using TRIzol reagent (Invitrogen) followed by purification with Direct-zol RNA MiniPrep with in column genomic DNA digestion. RLM-RACE assay allows for the specific amplification of 5' capped RNA, which is found only on full-length mRNA transcripts. The specific outer and inner (nested) primers in combination with adaptor-specific primers were used for amplifying the 5’ ends of *FOXM1* and *RHNO1* mRNA. The 5’ end specific primers are listed in Table 2. As negative controls, non-tobacco alkaline phosphatase (TAP)-treated aliquots from each RNA source were utilized; in all cases, this did not yield any specific product amplification (data not shown). In contrast, FOXM1- and RHNO1-specific PCR products of various sizes were yielded from TAP-containing reactions. PCR products were separated on 2% agarose gels, excised, and subsequently purified using the QIAquick gel extraction kit (Qiagen). Gel-purified PCR products were cloned using the TOPO TA Cloning Kit (Invitrogen), and individual clones were sequenced using standard methods.

Promoter Activity Luciferase Reporter Assay

Firefly and Renilla luciferase activities were measured between 24 hours after transfection using the Dual-Luciferase® Reporter Assay System (Promega) and luminometer. Bidirectional promoter studies were normalized with secreted embryonic alkaline phosphatase (SEAP) activity present in the culture medium was measured at the same time using the Phospha-Light System (Applied Biosystems). All transfections were performed in triplicate within each individual experiment. Firefly and Renilla luciferase activities were expressed in arbitrary units as displayed on the luminometer after a 10

second integration time and normalized against SEAP production in the individual transfected 24-well dishes.

University of California Santa Cruz (UCSC) Genome Browser

The genomic region of FOXM1 and RHNO1 was retrieved from UCSC Genome Browser (http://genome.ucsc.edu) (141) using the human genome build hg19 with genomic coordinates chr12:2,966,265-2,999,264. The following tracks were selected and displayed in the Genome Browser: *FOXM1* and *RHNO1* mRNA, CpG island, Encode E2F1, H3K4Me3 and H3K27Ac ChIP-seq tracks, and conserved genome tracks from 100 vertebrates and mammalian genomes. The Genome Browser screen shot tool was used to obtain images.

DNA Fiber Assay

DNA fiber analysis was performed as previously described with minor modifications (142,143). Briefly, FTE cells were seeded at 50% confluency. The next day, cells were first pulsed with 8 μg/ml chlorodeoxyuridine (CldU) for 30 minutes, washed 3X with pre-warmed 1X PBS, and then pulsed with 90 μg/ml iododeoxyuridine (IdU) for 30 minutes. Three microliters of cell suspension containing approximately 3×10^5 cells were mixed with 7 μl lysis buffer (200 mM Tris-HCl pH 7.4, 50 mM EDTA, 0.5% SDS) on glass slides and incubated at room temperature for 8 minutes. The slide was then tilted to allow spreading of fibers at approximately a 45^o angle to allow the drop to slowly run down the slide. Fibers were air dried for 2-3 hours and then fixed in methanol/acetic acid (3:1) at 4 °C overnight, rehydrated by PBS and denatured in 2.5 M HCL for 1 hour. After rinsing away HCL by PBS, slides were blocked in PBS with 5% BSA for 1 hour and incubated

overnight at 4 ºC overnight with anti-BrdU antibody (Mouse, #347580, Becton Dickinson, 1:100 dilution) to detect IdU and anti-BrdU antibody (Rat, ab6326, Abcam, 1:500 dilution) to detect CldU. Slides were rinsed with PBS with 0.1% Tween-20 (PBST) and incubated with AlexaFluor488-conjugated (green) anti-mouse IgG secondary antibody and AlexaFluor594-conjugated (red) anti-rat IgG secondary antibody for 1 hour at room temperature. Slides were rinsed with PBST and mounted by mounting media (Prolong Gold, Invitrogen). Images were taken in Zeiss Axio Imager Z1 microscope and fiber length was measured by ImageJ software (NIH). For data analysis, the length of each labeled DNA tract (IdU and CldU) determined by ImageJ was then converted to kb using a conversion factor of 2.59 kb/μm. Fork rate was calculated by dividing the length of the tract by the labeling time (kb/min). Percentage of origins fired was calculated by counting DNA fibers with the following with the following staining pattern (G = green and R = red), GRG, G, GRG, G, and RG, then using this equation: (GRG + G) / (GRG + G + RG). See Figures 7 and 8 for the interpretation of the data.

The Cancer Genome Atlas (TCGA), Cancer Cell Line Encyclopedia (CCLE), Genotype-Tissue Expression (GTEx), and RIKEN Fantom5 Datasets

TCGA, CCLE and GTEx genomic profiled datasets were retrieved from cBioPortal or UCSC Xena Browser. TCGA and CCLE RPPA data were obtained from UCSC Xena (https://xenabrowser.net) or The Cancer Proteome Atlas (144,145). TCGA Provisional datasets were used for analyses because they contain published data plus data from new samples that have since been profiled, thus increasing the sample size. FOXM1 mutation and somatic copy-number alterations were analyzed in pan-cancer datasets. The genomic profile of *FOXM1* and *RHNO1* were further analyzed in the HGSC (Ovarian Serous Cystadenocarcinoma-TCGA Provisional) dataset for putative somatic copy-number

alterations from GISTIC (146) using Onco Query Language (OQL) and mRNA expression (RNA seq V2 RSEM). In brief, GISTIC predicts gene copy number alterations according to sample specific thresholds generated by comparing chromosomal segments with median chromosomal arm copy numbers. High gains (Amp) are segments with copy number that exceed the maximum median chromosomal arm copy number for that sample by at least 0.1; low gains (Gain) are segments with copy numbers from 2.1 to the high gain threshold; neutral segments (Diploid) have copy numbers between 1.9 and 2.1; shallow losses (Hetloss) have copy numbers between 1.9 and the deep deletion threshold; and deep deletions (Homdel) have copy numbers that are below the minimum median chromosomal arm copy number for that sample by at least 0.1. Overall patient survival was graphed in Kaplan-Meier survival curves. Fraction of genome altered by copy number data was downloaded from cBioPortal and was previously calculated as following: length of segments with log2 CNA value larger than 0.2 or less than -0.2 divided by the length of all segments measured. Mutation burden is the sum of all mutations detected from the exome-seq data. These values were used as a basic measurement of genomic instability in the form of CNA and mutations. CAGE (Cap Analysis of Gene Expression) analysis of mouse tissues in RIKEN FANTOM5 project (RNA-seq) dataset was retrieved from www.ebi.ac.uk.

FOXM1 and RHNO1 Correlation in Public Single-Cell RNA Sequencing Datasets

Single-cell RNA-sequencing datasets from mouse normal colon epithelium (GSE92332) (147) and human melanoma (GSE72056) (148) were downloaded from NCBI GEO. Single-cell RNA sequencing data for human high-grade serous ovarian cancer tissue was obtained from a published dataset (149). Single-cell RNA sequencing data were normalized with sclmpute (150).

Genome-Wide Correlation of FOXM1 and ORC2 Occupancy

ORC2 (GSE70165) and FOXM1 ChiP-seq (GSE105524) datasets were retrieved from NCBI GEO (151,152). Both ChiP-seq experiments were performed using K562 cells and mapped to human genome build hg19. The StereoGene C++ source code was downloaded from http://stereogene.bioinf.fbb.msu.ru/. StereoGene was run to determine the statistical overlap of genome-wide co-occupancy between FOXM1 and ORC2 in the publicly available ChiP-seq datasets (153). FOXM1 ChIP-seq bed files and ORC2 significant Broadpeak files were input into the StereoGene program and analysis performed with the contig settings set at default. Final data output consists of the following correlations: 1) foreground distribution, which is calculated from a set of paired windows with the same genome positions and the matched windows are compared, and 2) background distribution, which is a shuffling procedure that is randomly match windows on one profile to the windows on another profile.

Statistical Analyses

Student's t-test was used to compare differences between means of two groups. Mann-Whitney test was used to compare differences between medians of two groups. One-way analysis of variance (ANOVA) with a post-test for linear trend was used to compare two or more groups. For all analyses, significance was inferred at $P < 0.05$ and P values were two-sided. GraphPad Prism statistical software (GraphPad Software, Inc) was used for statistical analysis.

Figures

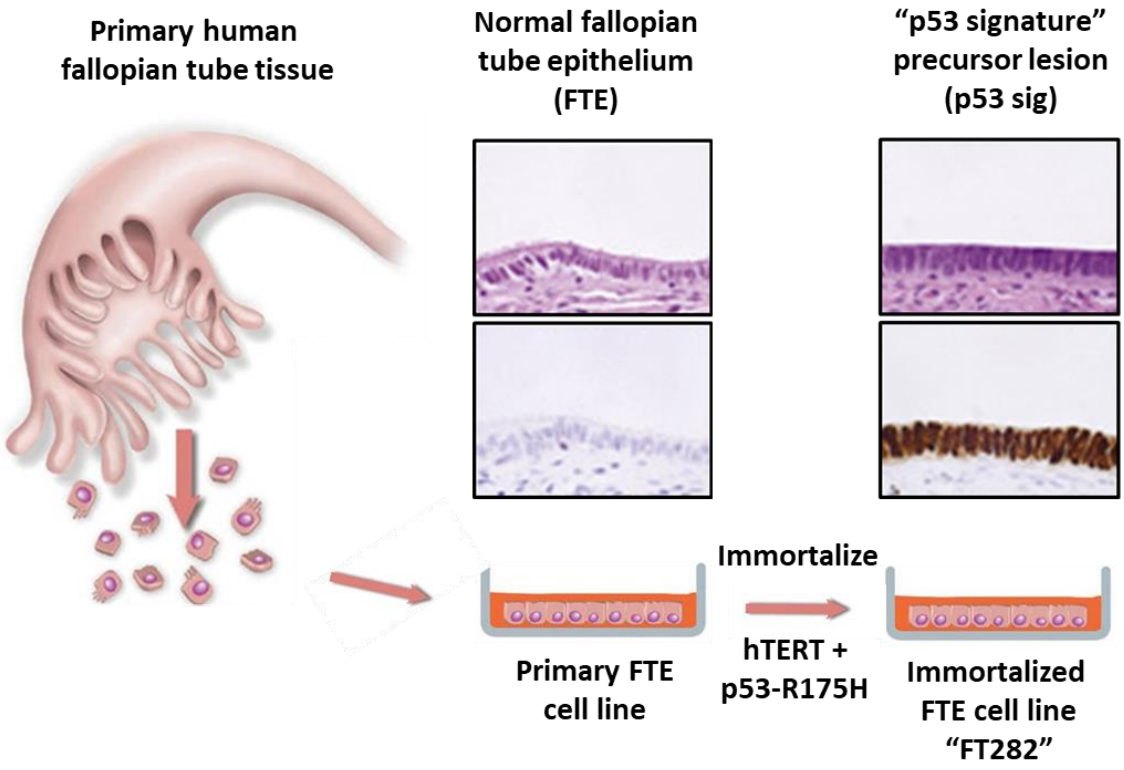

Figure 6. Generation of immortalized fallopian tube epithelial cells (FTE; FT282). Fallopian tube epithelial cells were dissociated from the lining of the fallopian tube. Fallopian tube secretory cells (FTE) were immortalized by transduction with lentivirus expressing mutant p53 and retrovirus expressing hTERT. These cells can grow long term on plastic but are not transformed and model the p53 signature lesion found within the distal end of the fallopian tube. Adapted from: (4).

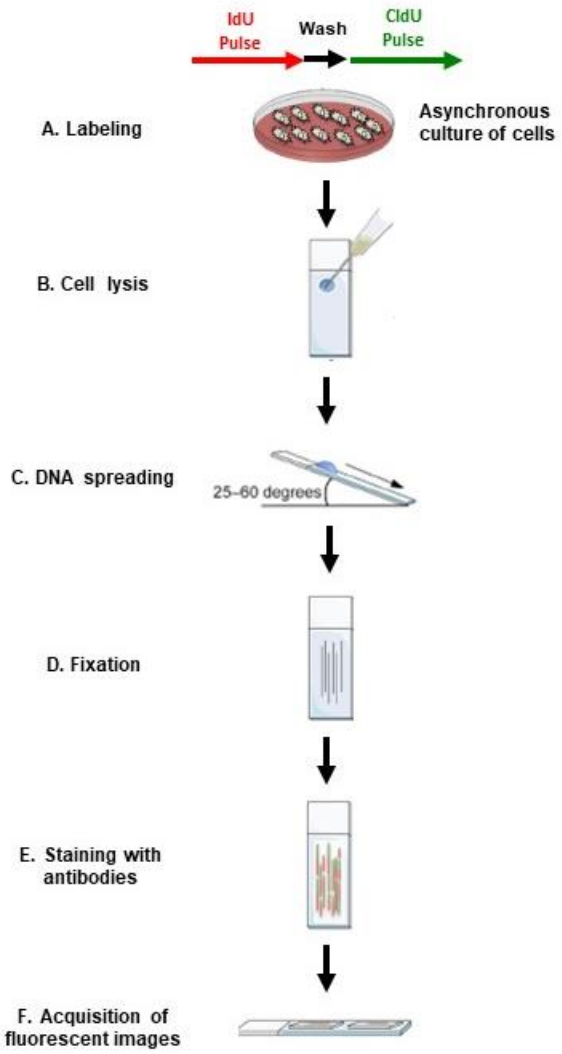
IdU
Pulse
Wash
CldU
Pulse
A. Labeling
Asynchronous
culture of cells
B. Cell lysis
C. DNA spreading
25–60 degrees
D. Fixation
E. Staining with
antibodies
F. Acquisition of
fluorescent images

Figure 7.

Figure 7. DNA fiber assay using DNA spreading. A. Asynchronous culture of cells is labeled in two pulses with washing between. The first pulse in this example is with IdU (red) and the second pulse is with CldU (green). **B.** A drop of prelabeled cells is transferred to a positively coated microscope slide and lysed. **C.** The slide is then tilted at a 25–60-degree angle to allow DNA spreading down the slide. **D.** DNA is then fixed with methanol/acetic acid**. E.** The slide containing fixed DNA is first immunostained with primary antibodies that recognize CldU and IdU then immunostained with fluorescently conjugated secondary antibodies. **F.** DNA fibers are visualized through a fluorescent microscope and data analysis can be performed with ImageJ. Adapted from: (3).

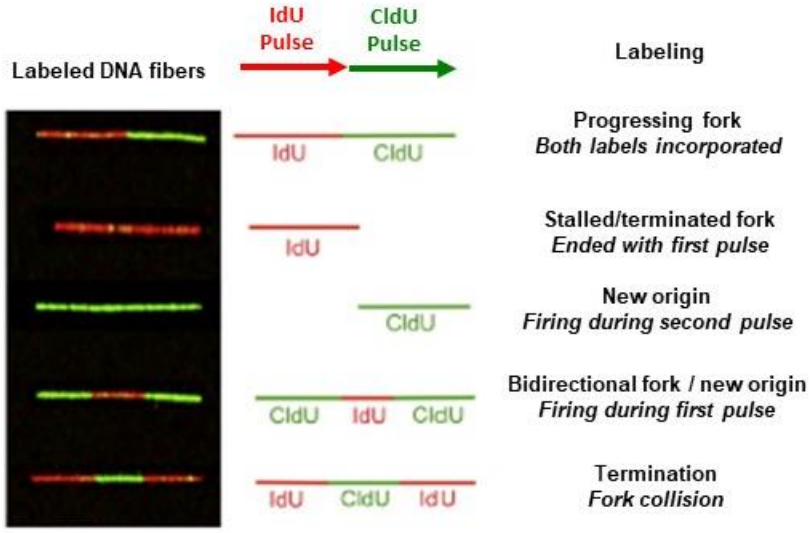

Figure 8. Schematic showing the different replication events that can be detected with DNA fiber analysis. Nucleotide analog labeling scheme according DNA fiber in Figure 7. IdU is incorporated as the first nucleotide analog followed by CldU incorporated as the second analog. Representative DNA fibers are shown on the left and their interpretations on the right. The color of the DNA fibers corresponds to the fluorescence emission from the secondary antibody that recognizes either IdU or CIdU. Adapted from: (3).

Vector Type	Vector type	Expression	Mammalian selection marker	Insert type cloned	Insert name
pCMV6 AN-HA empty	Episomal	Transient	Neomycin	ORF	Empty
pCW57-GFP-P2A-MCS-(Puro)	Lentiviral	Dox inducible	Puromycin	ORF or mir30 shRNA	Empty
pCW57-GFP-P2A-MCS-(Neo)	Lentiviral	Dox inducible	Neomycin	ORF or mir30 shRNA	Empty
pCW57-GFP-P2A-MCS-(Hygro)	Lentiviral	Dox inducible	Hygromycin	ORF or mir30 shRNA	Empty
pCW57-GFP-P2A-MCS-(Blast)	Lentiviral	Dox inducible	Blasticidin	ORF or mir30 shRNA	Empty
pCW57-RFP-P2A-MCS-(Puro)	Lentiviral	Dox inducible	Puromycin	ORF or mir30 shRNA	Empty
pCW57-RFP-P2A-MCS-(Neo)	Lentiviral	Dox inducible	Neomycin	ORF or mir30 shRNA	Empty
pCW57-RFP-P2A-MCS-(Hygro)	Lentiviral	Dox inducible	Hygromycin	ORF or mir30 shRNA	Empty
pCW57-RFP-P2A-MCS-(Blast)	Lentiviral	Dox inducible	Blasticidin	ORF or mir30 shRNA	Empty
pCW57-MCS1-P2A-MCS2-(Puro)	Lentiviral	Dox inducible	Puromycin	ORF or mir30 shRNA	Empty
pCW57-MCS1-P2A-MCS2-(Neo)	Lentiviral	Dox inducible	Neomycin	ORF or mir30 shRNA	Empty
pCW57-MCS1-P2A-MCS2-(Hygro)	Lentiviral	Dox inducible	Hygromycin	ORF or mir30 shRNA	Empty
pCW57-MCS1-P2A-MCS2-(Blast)	Lentiviral	Dox inducible	Blasticidin	ORF or mir30 shRNA	Empty
pCW57-MCS1-P2A-MCS2-(Puro)	Lentiviral	Dox inducible	Puromycin	ORF or mir30 shRNA	Empty
pCW57-MCS1-P2A-MCS2-(Neo)	Lentiviral	Dox inducible	Neomycin	ORF or mir30 shRNA	Empty
pTRIPZ	Lentiviral	Dox inducible	Puromycin	mir30 shRNA	
pGL4 Luc Rluc Empty	Episomal	Transient	N/A	Promoter	Empty
pGL4.7 Renilla-empty	Episomal	Transient	N/A	Promoter	Renilla
pGL4.1 Firefly-empty	Episomal	Transient	N/A	Promoter	Firefly
pCMV6-SEAP	Episomal	Transient	N/A	Promoter	pCMV6
pRL-TK (Renilla control)	Episomal	Transient	N/A	Promoter	Renilla
pTurboGFP-PRL vector, no promoter	Episomal	Transient	N/A	Promoter	no
pCW57-GFP-P2A-MCS	Lentiviral	Dox inducible	Puromycin	ORF	P2A
pLentiCRISPRv2	Lentiviral	Constitutive	Puromycin	sgRNA	Lenti
PX458-WT-Cas9-empty	Episomal	Transient	N/A	sgRNA	Cas9
N174-MCS Puro	Lentiviral	Constitutive	Puromycin	ORF	MCS
N174-MCS Neo	Lentiviral	Constitutive	Neomycin	ORF	MCS
TLCV2	Lentiviral	Dox inducible	Puromycin	sgRNA	Cas9-2A-GFP
lenti-SAMv2-Puro	Lentiviral	Constitutive	Puromycin	sgRNA	SAMv2
lenti-MPHv2-Neo	Lentiviral	Constitutive	Neomycin	N/A	MPHv2
pCAGGS empty	Episomal	Transient	N/A	N/A	pCAGGS
pCBA-SceI	Episomal	Transient	N/A	N/A	I-SceI
pLV hU6-sgRNA hUbC-dCas9-KRAB-T2A-Puro (KRAB)	Lentiviral	Constitutive	Puromycin	sgRNA	empty

Table 1: List of plasmids.

Gene	Species	Assay type	Sequnce 5' to 3'
Foxm1 F	Mouse	RT-qPCR	AGCGTTAAGCAGGAACTGGA
Foxm1 R	Mouse	RT-qPCR	GGAAGTGGTCCTCAATCCAA
18s rRNA F	Mouse	RT-qPCR	ATGGCCGTTCTTAGTTGGTG
18s rRNA R	Mouse	RT-qPCR	GAACGCCACTTGTCCCTCTA'
p53_int1_new_F	Mouse	PCR Genotype	CACAAAAAACAGGTTAAACCCAG'
p53_int1 R	Mouse	PCR Genotype	AGCACATAGGAGGCAGAGAC
p53_int10 F	Mouse	PCR Genotype	AAGGGGTATGAGGGACAAGG
p53_int10 R	Mouse	PCR Genotype	GAAGACAGAAAAGGGGAGGG
Rb212 F2	Mouse	PCR Genotype	GAAAGGAAAGTCAGGGACATTGGG
Rb18 R	Mouse	PCR Genotype	GGCGTGTGCCATCAATG
18s rRNA F	Human	RT-qPCR	CAGCCACCCGAGATTGAGCA
18s rRNA R	Human	RT-qPCR	TAGTAGCGACGGGCGGTGTG
FOXM1a F	Human	RT-qPCR	TGGGGAACAGGTGGTGTTTGG
FOXM1a R	Human	RT-qPCR	GCTAGCAGCACTGATAAACAAAG
FOXM1c F	Human	RT-qPCR	CAATTGCCCGAGCACTTGGAATCA
FOXM1c R	Human	RT-qPCR	TCCTCAGCTAGCAGCACCTTG
FOXM1b F	Human	RT-qPCR	CCAGGTGTTTAAGCAGCAGA
FOXM1b R	Human	RT-qPCR	TCCTCAGCTAGCAGCACCTTG
FOXM1 F	Human	RT-qPCR	GCAGGCTGCACTATCAACAA
FOXM1 R	Human	RT-qPCR	TCGAAGGCTCCTCAACCTTA
PLK1 F	Human	RT-qPCR	GGACTATTCGGACAAGTACG
PLK1 F	Human	RT-qPCR	CGGAAATATTTAAGGAGGGTGA
SKP2 F	Human	RT-qPCR	GGTGTTTGTAAGAGGTGGTATCGC
SKP2 R	Human	RT-qPCR	CACGAAAAGGGCTGAAATGTTC
CCNB1 F	Human	RT-qPCR	AACTTTCGCCTGAGCCTATTTT
CCBN1 R	Human	RT-qPCR	TTGGTCTGACTGCTTGCTCTT'
RAD51 F	Human	RT-qPCR	CGCTGCGGACCGAGTAAT
RAD51 R	Human	RT-qPCR	GGCAACAGCCTCCACAGTAT
RHNO1 145 F	Human	RT-qPCR	AGCAAGCCCATTGACCACAG
RHNO1 145 R	Human	RT-qPCR	TTCGACTTGAGTGTCTCGCC
RHNO1 1245 F	Human	RT-qPCR	TCATTCACCGGTTGATGCCT
RHNO1 1245 R	Human	RT-qPCR	CACCTGTCGAGTGTGAGTGA
ATR F	Human	RT-qPCR	TGATATGGTGGAAATTCTTGCTTC
ATR R	Human	RT-qPCR	TCTCTTCTACGAGACTCTGCATC
CDC25B	Human	RT-qPCR	CCTCCGAATCTTCTGATGCAG
CDC25B	Human	RT-qPCR	GCGTCTGATGGCAAACTGC
BRCA2	Human	RT-qPCR	CAAGCAGATGATGTTTCCTGTCC
BRCA2	Human	RT-qPCR	AGAACTAAGGGTGGGTGGTGTAGC
CCNA1	Human	RT-qPCR	TGTCTGTTCTGAGAGGGAAACTGC
CCNA1	Human	RT-qPCR	AAGGAGAAACTGGTTGGTGGTTGG
CCNA2	Human	RT-qPCR	CTGGAAAGTCTTAAGCCTTGTCTCA
CCNA2	Human	RT-qPCR	GTTGAGGAGAGAAACACCATGATACT
FOXM1c_ T868G _QC_F	Human	Site directed mutagenesis	CCATCCGCCACAACCTTGCCCTGCACGAC
FOXM1c_ T868G _QC_R	Human	Site directed mutagenesis	GTCGTGCAGGGCAAGGTTGTGGCGGATGG
FOXM1c_ TC856/7GC_CA859/60GC _QC_F	Human	Site directed mutagenesis	GCTGGAAGAACTCCATCGCCGCCAACCTTGCCCTGCACG
FOXM1c_ TC856/7GC_CA859/60GC _QC_R	Human	Site directed mutagenesis	CGTGCAGGGCAAGGTTGGCGGCGATGGAGTTCTTCCAGC
FOXM1-RHNO1 BS	Human	Bisulfite PCR	TTTTTTAGTGAGGAAATTAATTAAAGT
FOXM1-RHNO1 BS	Human	Bisulfite PCR	CAAACCAAACCTAAAACTCCATTAC
RHNO1-5'RACE-outer_+424-R1	Human	5' RACE	CTGACATGTTCCCACAGCTTTG
RHNO1-5"RACE-inner_+270 R2	Human	5' RACE	CTTGGAGGTGGTAGGTTTTCGA
RHNO1-5'RACE-outer +349-R1	Human	5' RACE	TGGAAGATTGCGGACTCTCAAA
FOXM1-5'RACE-outer_+400 R1	Human	5' RACE	TCCTTTTGGCATCATAGCTGGT
FOXM1-5'RACE-inner_+242 R2	Human	5' RACE	TTGTTGGGGATGGCCACTAC
FOXM1_ 5'RACE-+36 R3	Human	5' RACE	TTTGAGAATCAGTGGCCGAC
5' RACE Outer	Human	5' RACE	GCTGATGGCGATGAATGAACACTG
5' RACE Inner	Human	5' RACE	CGCGGATCCGAACACTGCGTTTGCTGGCTTTGATG

Table 2: List of primers.

Gene	Species	Name	Type	Sequnce 5' to 3'
N/A	N/A	NS - Nonsilencing control	mir30-shRNA	CTCGCTTGGGCGAGAGTAA
RHNO1	Human	403203	mir30-shRNA	TTTCTATTGAGATTACTGA
RHNO1	Human	324131	mir30-shRNA	TGTTGGTGGAACAGCAGCG
RHNO1	Human	324133	mir30-shRNA	TCGACTTGAGTGTCTCGCC
RHNO1	Human	324130	mir30-shRNA	ATTCCATACTTGTCCTCGG
RHNO1	Human	117443	mir30-shRNA	TCGACTTGAGTGTCTCGCC
RHNO1	Human	117442	mir30-shRNA	TAAGGTAAGCTCTGAAGTG
FOXM1	Human	283849	mir30-shRNA	ATAATTAGAGGATAATTTG
FOXM1	Human	396941	mir30-shRNA	TGATGGTCATGTTCCGGCG
FOXM1	Human	311190	mir30-shRNA	TTCTGCTGCTTAAACACCT
FOXM1	Human	396938	mir30-shRNA	CTAGGAAGATTCACATCCC
FOXM1	Human	396939	mir30-shRNA	ATTGTTGATAGTGCAGCCT
FOXM1	Human	FOXM1 siRNA	siRNA	GGACCACUUUCCCUACUUU
E2F1	Human	E2F1 siRNA	siRNA	GUCACGCUAUGAGACCUCA
Non-targeting	N/A	Non-targeting control	siRNA	UAAGGCUAUGAAGAGAUAC
AAVS1	Human	AAVS1	sgRNA	GGGGCCACTAGGGACAGGAT
FOXM1	Human	462	sgRNA	TGAGAATCAGTGGCCGACGG
FOXM1	Human	464	sgRNA	TAATGAAAACTAGCCCCCGT
RHNO1	Human	413	sgRNA	TTGTTGGTGGAACAGCAGCG
RHNO1	Human	434	sgRNA	GTTCCACCAACAACCACTGG
RB1	Human	RB#1	sgRNA	CACCGGCTCTGGGTCCTCCTCAGGA
FOXM1/RHNO1 Promoter	Human	2877184	sgRNA	GGAGCGTTAAGGTCACGTGA
FOXM1/RHNO1 Promoter	Human	2877199	sgRNA	CGTGACGGAACGTCGCCAAT
FOXM1/RHNO1 Promoter	Human	2877205	sgRNA	GGAACGTCGCCAATCGGCGC
FOXM1/RHNO1 Promoter	Human	2877233	sgRNA	TCTCGGCATTCCGGGCTCGA
FOXM1/RHNO1 Promoter	Human	2877299	sgRNA	TTCCCCCACAAGCCGGCCTG
FOXM1/RHNO1 Promoter	Human	2877363	sgRNA	CCTCGGCTCGCCCACCCACG
FOXM1/RHNO1 Promoter	Human	2877163	sgRNA	CTGTTTGAAATTGGCGCCGG
FOXM1/RHNO1 Promoter	Human	2877130	sgRNA	GCGGAACAAACTGAAAGCTC
FOXM1/RHNO1 Promoter	Human	2877070	sgRNA	TCCCCTCCCGGGATCCCCCG
Non-targeting	N/A	NT1 - non-targeting	sgRNA	GCTGAAAAAGGAAGGAGTTGA
Non-targeting	N/A	NT2- non-targeting	sgRNA	GAAGATGAAAGGAAAGGCGTT

Table 3. List of siRNAs, shRNAs, and sgRNAs.

Antibody	Company	Catalog Number	Application	Dilution
FOXM1	Santa Cruz	sc-271746	Western blot	1:500
FOXM1	Santa Cruz	sc-500	Western blot	1:500
FOXM1	Cell Signaling	5436	Western blot	1:1000
RB1	Millipore	OP66	Western blot	1:300
E2F1	Santa Cruz	sc-251	Western blot	1:250
Cyclin E1	Santa Cruz	sc-247	Western blot	1:1000
β-Actin	Santa Cruz	sc-47778	Western blot	1:5000 - 1:10000
CHEK1	Santa Cruz	sc-8408	Western blot	1:500
P-CHEK1 S345	Cell Signaling	2348	Western blot	1:1000
P-CHEK1 S317	Cell Signaling	12302	Western blot	1:1000
RPA2	Santa Cruz	sc-56770	Western blot	1:5000
P-RPA2 S33	Bethyl	A300-246A	Western blot	1:5000
ATR	GeneTex	GTX70109	Western blot	1:1000
P-ATR T1989	GeneTex	GTX128145	Western blot	1:1000
H2AX	Bethyl	A303-837A	Western blot	1:5000
P-H2AX S139	Cell Signaling	9718	Western blot	1:1000
P-H2AX S139	Millipore	05-636	Flow cytometry	1:1000
Flag	Cell Signaling	14793	Western blot	1:1000
HA	Cell Signaling	3724	Western blot	1:1000-5000
MCM2	Cell Signaling	3619	Western blot	1:1000
ORC2	Cell Signaling	4736	Western blot	1:1000
RHNO1	Novus	NBP1-93694	Western blot	1:250
RHNO1	Sigma	HPA038682	Western blot	1:250
TOPBP1	Cell Signaling	14342S	Western blot	1:1000
RAD9	Santa Cruz	sc-8324	Western blot	1:500
RAD1	Thermo	P1702149	Western blot	1:1000
HUS1	Cell Signaling	16416S	Western blot	1:1000
DNMT1	NEB	RM0231S	Western blot	1:1000
DNMT3A	Novus	NB100-265	Western blot	1:1000
DNM3TB	Novus	N/A	Western blot	1:1000

Table 4. List of antibodies.

CHAPTER 3: GENETIC DETERMINANTS OF FOXM1 OVEREXPRESSION IN HIGH-GRADE SEROUS OVARIAN CANCER[1]

Introduction

TCGA recently reported mRNA and miRNA expression, CNA, promoter methylation, and mutational data for HGSC, which led to classification into sub-groups based on these molecular criteria (30). CNA is prominent in HGSC and occurs at a higher frequency than in any other TCGA-profiled tumor type (30,31,154). It was also notable that *TP53* was mutated in virtually all HGSC, suggesting p53 as a "gatekeeper" for this disease (30). Other tumor suppressors and oncogenes implicated in HGSC include BRCA1/2, Rb, PI3K, Ras, and CCNE1 (30,34,155). Finally, FOXM1 pathway activation is a highly frequent alteration in HGSC, second only to *TP53* mutation (30).

FOXM1 is a member of the Forkhead box (FOX) transcription factor family, which is unified by a conserved winged helix DNA binding motif (60). FOXM1 plays a well-established role in cell cycle progression, promoting G1/S and G2/M transitions by transactivation of genes regulating these checkpoints (40,60). Furthermore, FOXM1 is overexpressed and activated in many human cancers and possesses oncogenic activity *in vitro* and *in vivo* (40). Mechanisms accounting for FOXM1 overexpression in cancer cells and tissues are diverse and include: p53, Rb, and FOXO3 loss (2,73-75), Myc, HIF-1, Gli1, SP1, STAT3 and E2F activation (76-81), and gene amplification (82).

[1] Part of the data presented in this chapter were previously published: 36. Barger CJ, Zhang W, Hillman J, Stablewski AB, Higgins MJ, Vanderhyden BC*, et al.* Genetic determinants of FOXM1 overexpression in epithelial ovarian cancer and functional contribution to cell cycle progression. Oncotarget **2015**;6:27613-27

The goal of the current study was to begin to define the genetic determinants of FOXM1 overexpression in HGSC, to analyze its expression across cancer types and during EOC disease progression, and to investigate its role in EOC cell cycle progression. For this task, we utilized publicly available TCGA datasets, primary human EOC tissues, immortalized ovarian surface epithelial (OSE) cell models (murine and human), immortalized human fallopian tube epithelial (FTE) cell models, a transgenic murine ovarian cancer model, and human HGSC cell lines.

Results

FOXM1 shows highest expression in HGSC compared to other TCGA tumor types

FOXM1 is overexpressed and activated in many human cancers. However, the expression of FOXM1 protein has not been characterized in HGSC nor has it been compared across other cancer types. To determine the level of FOXM1 protein expression in TCGA cohorts, we retrieved the level 4 TCGA RPPA dataset from The Cancer Proteome Atlas (TCPA) (145). This dataset was a reprocess of raw TCGA RPPA data using a novel approach, called ‘replicates-based normalization’ (RBN) to correct for batch effects and ultimately allow for the merging of samples across 19 different cancer types for pan-cancer analyses (156). We then analyzed this dataset for FOXM1 protein expression across 19 TCGA cancer cohorts. Notably, we observed that FOXM1 protein expression was the highest in HGSC as compared to all other TCGA cohorts (Figure 9). This suggests that HGSC has distinct genomic features that gives rise to increased FOXM1 expression.

FOXM1 gene amplification correlates with increased FOXM1 expression and reduced survival in HGSC

HGSC exhibits more frequent copy number alterations than other TCGA cancer types. *FOXM1* is located at chromosome 12p13.33, a known amplified region in cancer (53,99,100). Therefore, we hypothesized that *FOXM1* is altered in copy number in HGSC thus contributing to its increased expression. To determine if 12p13.33 is a genomic region with significant copy number increase in HGSC, we downloaded the TCGA HGSC copy number analysis (GISTIC2) data from the Broad TCGA Genomic Data Analysis Center (GDAC)-Firehose data portal. Upon review of the TCGA HGSC GISTIC data, we observed that 12p13.33 is one of the 33 significant focal amplifications in HGSC as highlighted with the black arrow (Figure 10) and *FOXM1* was among the 33 genes in this amplicon (Table 5). We then determined the frequency of *FOXM1* amplification among the different cancer types using TCGA datasets. Notably, amongst all tumor types with TCGA data, *FOXM1* was most frequently amplified in HGSC, with ~12% of tumors affected (Figure 11A). Together, 57% of HGSC cases showed either copy number gain or amplification, suggesting FOXM1 as an HGSC oncogene (Figure 11B). To determine if *FOXM1* copy number status correlates with expression, we compared FOXM1 mRNA and protein expression versus *FOXM1* copy number in TCGA HGSC data. We observed a progressive increase in FOXM1 mRNA and protein expression with copy number status that was highly statistically significant (Figure 11C-D). Furthermore, we compared FOXM1 mRNA and protein expression and observed a strong correlation (Figure 11E), suggesting that copy number contributes to increased *FOXM1* mRNA expression thus resulting in a corresponding increase in protein expression. Together these data support our pan-cancer analysis of FOXM1 expression, which showed that HGSC had the highest level of FOXM1 protein expression. We additionally compared overall survival (OS) to *FOXM1*

CNA and FOXM1 mRNA and protein expression and observed that only the former showed a significant correlation with OS (Figure 11F-H). This finding suggests that additional genes located at the amplified region of 12p13.33 may contribute to OS in HGSC, and/or that FOXM1 activation levels may be more relevant than expression levels for impacting OS. Finally, our analysis of TCGA mutational data did not reveal *FOXM1* mutations in HGSC (data not shown).

TCGA HGSC and basal breast cancer exhibit similar *FOXM1* copy number status and level of expression for FOXM1

The TCGA report and subsequent pan-cancer analyses have shown that HGSC and basal breast subtype have very similar genomic features including *TP53* mutations in the majority of cases and more genomic instability, in the form of copy number alterations, than other subtypes of breast and ovarian cancer or most other TCGA cancer types (32,33). Therefore, we hypothesized that basal breast cancer and HGSC would show similar *FOXM1* copy number status and expression. In our earlier TCGA pan-cancer comparisons (Figure 9 and11A), breast cancer showed lower frequency of FOXM1 amplification and lower protein expression as compared to HGSC. A caveat to this comparison was that it did not differentiate between breast cancer molecular subtypes. To address the possible differences between molecular subtypes, we retrieved the TCGA PAM50 expression subtype data for TCGA breast cancer and categorized samples based on molecular subtype. We compared *FOXM1* copy number and expression between subtypes in respect to HGSC. Our analysis of *FOXM1* amplification showed that basal breast and HGSC have an increased frequency of *FOXM1* amplification, while the other breast molecular subtypes showed infrequent *FOXM1* amplification (Figure 12A). Because HGSC and basal breast showed very similar frequency of *FOXM1* amplification,

we next compared *FOXM1* copy number status. We observed a striking similarity in copy number status between these two cancer types (Figure 12B). To determine if breast molecular subtypes and HGSC have similar FOXM1 expression, we compared FOXM1 mRNA and protein expression among normal breast, breast molecular subtypes and HGSC. Again, in agreement with the copy number data, HGSC and basal breast showed the highest level of FOXM1 mRNA and protein expression compared to the other breast subtypes and normal breast tissue (Figure 12C-D). These data validate our observation that *FOXM1* copy number status contributes to its frequent expression in HGSC and agree with previous reports that HGSC and basal breast subtype have similar genomic features. Most importantly, these data further support our hypothesis that HGSC has unique genomic features that contribute to the frequent overexpression of FOXM1 that we have observed.

FOXM1 expression in relation to EOC type and progression status, and FOXM1 isoform expression in HGSC

The FOXM1 transcriptional factor pathway was initially reported to be activated in HGSC by the TCGA (30). The reported FOXM1 pathway activity in HGSC was based on the degree of overlap between FOXM1 expression and the expression of its reported transcriptional targets. However, the extent of FOXM1 overexpression in HGSC as compared to a normal control, such as FTE or OSE, was not determined. To address this, we retrieved the provisional TCGA HGSC microarray mRNA expression dataset and compared *FOXM1* expression in normal ovary tissue, primary and recurrent HGSC tumors. We observed a significant increase in *FOXM1* expression for primary and recurrent tumor as compared to normal ovary tissue, showing that *FOXM1* is overexpressed in HGSC (Figure 13A). *FOXM1* mRNA expression data was then

compared by stage and grade. We found that *FOXM1* expression was increased in high grade (grade 2 and 3; HGSC) but we did not observe a significant difference by stage (Figure 13B-C). *FOXM1* has three known splice variants: FOXM1a, b, and c, which encode proteins with varying activities (10). Furthermore, current knowledge of *FOXM1* isoform expression in different cancer types is inconsistent and the isoform expression is not known in HGSC. To address these issues and determine *FOXM1* isoform expression in HGSC, we then retrieved the TOIL TCGA RNA-seq dataset from UCSC Xena. The TOIL dataset was a reprocess of raw TCGA RNA-sequencing data to correct for batch effects and to allow for the merging of samples across all TCGA datasets for pan-cancer analyses (157). We then analyzed the TOIL HGSC RNA-seq dataset and compared *FOXM1* isoform expression in primary tumors samples and found that *FOXM1c* is the predominant isoform expressed in HGSC, followed by *FOXM1b* and *FOXM1a* (Figure 13D). Furthermore, we analyzed TOIL TCGA pan normal and cancer tissue RNA-seq dataset to determine if *FOXM1* isoforms are differentially expressed across pan-normal and -cancer tissues and, more importantly, how the expression compares with HGSC tissues. In agreement with the HGSC isoform expression data, pan-normal and -cancer tissues show that *FOXM1c* is the predominant isoform expressed, followed by *FOXM1b* and *FOXM1a* (Figure 13E). These data suggest that *FOXM1* isoform ratios are relatively similar in normal and cancer tissues; therefore, the observed increase in FOXM1 expression in cancer is not the result of the differential expression of only a single isoform.

We next validated the TCGA HGSC FOXM1 expression using our own independent set of EOC tissues with diverse histology, stage, and grade (158,159). RT-qPCR analysis demonstrated that *FOXM1* is frequently overexpressed in different EOC histological subtypes relative to normal ovary (NO), and furthermore shows increased expression in both late-stage and high-grade EOC (Figure 14A-C). To validate the

expression of FOXM1 isoforms we observed in TCGA HGSC, we used FOXM1 isoform-specific primers and performed RT-qPCR to quantify their expression, and in agreement with the TCGA HGSC data, we found that *FOXM1c* is the predominant isoform expressed in HGSC, followed by *FOXM1b* and *FOXM1a* (Figure 14D). Similarly to the mRNA, FOXM1 protein expression was elevated in EOC as compared to NO (Figure 14E). Together, these data agree with our TCGA analysis, showing that EOC and HGSC exhibits frequent overexpression of FOXM1.

FOXM1 **expression in HGSC cell models**

Thus far, our analyses have been performed with HGSC tumors which are subject to genetic heterogeneity. We next used clinically relevant cell models of human HGSC to examine genetic influences on *FOXM1* expression (160). All cell lines used have *TP53* mutations as well as additional genetic alterations relevant to HGSC (Figure 15A). We found that *FOXM1* mRNA expression was elevated in all but one cancer cell line as compared to hOSE cells and was heterogeneous in the HGSC cell types (Figure 15B). Notably, highest *FOXM1* expression was observed in the two cell lines (SNU-119, COV362) in which the *FOXM1* locus is amplified. Isoform-specific RT-qPCR revealed highest expression of *FOXM1c*, moderate expression of *FOXM1b*, and low expression of *FOXM1a* in HGSC cell lines. *FOXM1c* expression was highest in the SNU-119 and COV362 lines, in which *FOXM1* is amplified (Figure 15C). The relative expression of the three *FOXM1* isoforms agrees with our data using primary HGSC tumors (Figure 13C). In further agreement, FOXM1 protein expression was highest in cell lines with increased copy number status (Figure 15D).

Disruption of Rb and p53 induces FOXM1 expression in murine and human OSE cells

The OSE is a potential tissue of origin for EOC, and primary OSE cells are useful for exploring EOC relevant processes (161,162). We first used established murine OSE (mOSE) cell models to examine mechanisms regulating FOXM1 expression. We focused on *TP53* and *RB1*, as these disruptions are recurrent in HGSC (30). *Trp53* and *Rb1* knockout was achieved through Ad-Cre infection of mOSE cells as described previously (Figure 16A) (163). While loss of either tumor suppressor gene (TSG) alone resulted in a modest upregulation of *Foxm1*, combined p53 and Rb loss led to a robust induction (Fig 16B). Similar effects were observed for FOXM1 protein expression (Figure 16C). We next investigated the potential role of p53 and Rb in FOXM1 regulation in human OSE (hOSE) cells by measuring FOXM1 expression in hOSE cells immortalized with either SV40 Large T antigen (IOSE-SV), which leads to potent inactivation of p53 and Rb, or hTERT (IOSE-T), which leaves both proteins intact (125). IOSE-SV cells showed significantly higher levels of expression of both FOXM1 mRNA and protein as compared to IOSE-T or primary (non-immortalized) human OSE cells (Figure 16D-E). These data reveal that Rb and p53 play a major role in regulating FOXM1 expression in OSE cells.

FOXM1 is overexpressed in murine ovarian cancer driven by combined p53/Rb1 disruption

To complement the OSE cell studies described above, we measured FOXM1 expression in murine ovarian tumors developing after dual disruption of p53 and Rb in the OSE. As shown in Figure 17A-B, FOXM1 mRNA and protein expression were significantly increased in ovarian tumors as compared to the mouse normal ovary control. These *in vivo* data provide further support that loss of p53 and Rb contribute to FOXM1

overexpression in ovarian cancer. Notably, immunohistochemistry (IHC) analyses of the ovarian tumors arising in this model indicated that the tumors were negative for cytokeratin expression and positive for smooth muscle actin (Figure 17C). This finding suggests that cancer in this model may represent leiomyosarcoma, and not EOC, as was reported previously (163).

E2F1 and FOXM1 expression in OSE cells and EOC

Transcriptional activation of *FOXM1* following Rb loss suggests that E2F transcription factors may contribute to FOXM1 overexpression. To test this, we used IOSE-SV and COV362 cells, which have high FOXM1 expression as well as alterations in p53 and Rb. Following E2F1 knockdown by siRNA (Figure 18A), *FOXM1* mRNA expression in both cell types was significantly reduced, as compared to the non-targeting siRNA control (Figure 18B). To validate this finding in the primary disease setting, we tested whether *FOXM1* correlates with *E2F1* expression in human EOC. As shown in Figure 18C-D, in both the TCGA HGSC dataset and in our independent set of EOC tissues, expression of *FOXM1* and E2F1 were highly correlated. Together, these data implicate E2F1 in promoting FOXM1 expression in EOC.

Deregulation of the Rb-E2F pathway contributes to FOXM1 overexpression in fallopian tube epithelial cells

Thus far we determined that FOXM1 expression was increased with loss of p53 and Rb in OSE models, while FOXM1 expression was decreased with knockdown of E2F1. We next validated these findings in a more relevant HGSC precursor cell model system (Figure 6), TERT-immortalized fallopian tube epithelial cells, engineered to

overexpress mutant p53-R175H (FT282), large T antigen (FT190) or Cyclin E1 (FT282-E1). Similarly to our data in IOSE-T, the large T-expressing FTE cells showed increased FOXM1 mRNA and protein expression, as compared to FTE cells expressing mutant p53 alone (Figure 19A-B). Interestingly, the Cyclin E1 expressing cells showed the highest expression of FOXM1 and thus revealed a new upstream regulator of FOXM1 (Figure 19A-B). To improve upon these models, we used the TERT-immortalized FTE-expressing mutant p53 as a model to introduce temporal genetic modifications to the Rb-E2F pathway to further understand upstream regulators of FOXM1 expression. To determine the impact of RB loss, we modified the widely used lenti-CRISPR vector into an inducible system and engineered FTE cells for RB1 knockout using a previously characterized guide RNA to human RB1 (164,165). We doxycycline treated FTE cells engineered with inducible CRISPR-Cas9 targeted to *RB1* for 72 hours then sorted cells based on positive GFP expression to enrich for knockout. These cells were then expanded in the absence of doxycycline for one week and harvested for RNA and protein. We then characterized the mRNA and protein expression for RB1 and FOXM1, and we observed a significant increase in FOXM1 expression with RB knockout (Figure 19C-D). Similarly, we overexpressed E2F1 in FTE cells using a doxycycline inducible lentiviral vector to complement our prior results when we knocked down E2F1 with a siRNA. FTE cells engineered for E2F1 inducible expression were doxycycline treated for 72 hours then analyzed for E2F1 and FOXM1 mRNA and protein expression. In agreement with previous data, we observed increased FOXM1 expression when E2F1 was overexpressed (Figure 19E-F). Cyclin E1 is frequently amplified in HGSC, resulting in its overexpression (155). Furthermore, when Cyclin E1 interacts with its kinase, CDK2, this complex phosphorylates RB to release E2F1. Since we observed in increase in FOXM1 expression in the FTE cells engineered for constitutive Cyclin E1 expression, we next overexpressed Cyclin E1 in fallopian cells in an inducible manner and observed that it increased FOXM1 expression

in a dose-dependent manner (Figure 19G-H). Collectively, these data indicate that deregulation of the Rb-E2F pathway contributes to the frequent overexpression of FOXM1 in HGSC precursor lesions and primary tumors.

Functional contribution of FOXM1 to EOC cell cycle progression and target gene expression

To determine if FOXM1 plays a functional role in EOC cells, we explored its canonical function in cell cycle progression using knockdown and overexpression approaches. Knockdown of FOXM1 was efficient in IOSE-SV cells and led to accumulation of cells in G2-M, with concomitant decreases in both G1 and S (Figure 20A and C). Interestingly, in COV362 cells, FOXM1 knockdown also led to decreased cells in S phase but caused accumulation of cells in G1 with no significant alteration of G2-M (Figure 20B and D). These data suggest that FOXM1 regulates both the G1/S and G2/M checkpoints, but in a cell context-dependent manner. To determine whether the observed effect of FOXM1 knockdown on cell cycle progression coincided with altered expression of relevant FOXM1 target genes, we analyzed *SKP2*, *PLK1*, and *CCNB1* expression. SKP2 promotes G1-S transition, while PLK1 and CCNB1 promote G2-M transition, both downstream of FOXM1 (66,68,166). In agreement with our cell cycle data, FOXM1 knockdown in IOSE-SV and COV362 downregulated these genes, with the lone exception of *PLK1* in COV362 (Figure 20E-F).

In addition to FOXM1 knockdown, we overexpressed FOXM1b or FOXM1c using a stable doxycycline inducible system in primary hOSE cells. Interestingly, while the mRNA expression levels were identical, the FOXM1c protein appeared to be more stable than FOXM1b in these cells (Figure 21B). FOXM1c overexpression in hOSE led to increased cells in S and G2/M, with a decrease in G1 (Figure 21C). In contrast,

overexpression of FOXM1b did not alter cell cycle (data not shown). To determine whether the effect of FOXM1c overexpression on cell cycle coincided with altered expression of relevant FOXM1 target genes, we again analyzed *SKP2*, *PLK1*, and *CCNB1*. Overexpression of FOXM1c in hOSE cells led to upregulation of *PLK1* and *CCNB1*, while *SKP2* was unaffected (Figure 21D). These data are consistent with the functional impact of FOXM1 in EOC cell cycle regulation and suggest that this activity may be mediated by FOXM1's function as a transcriptional regulator. Although the effects of FOXM1c on cell cycle was modest, this could be due to the primary hOSE cell model used, which is assumed to have a functional p53 pathway. In agreement, the specific effect of FOXM1 overexpression on cell cycle progression in primary hOSE are reminiscent of that reported in cancer cells, although the effects were more robust in cancer cells (167,168).

Summary

Together, our data implicate gene amplification, p53 inactivation, and Rb-E2F deregulation in FOXM1 overexpression in HGSC. *FOXM1* amplification and expression are highest in HGSC compared to other TCGA cancer types but comparable to basal breast subtype. Among *FOXM1* isoforms, *FOXM1c* showed highest expression in HGSC cells and tumors. FOXM1 was overexpressed in late-stage, high-grade disease, and *FOXM1* gene amplification, but not expression, correlated with reduced HGSC survival. Finally, we demonstrate that FOXM1 activates target genes that positively regulate progression through the G1/S and G2/M checkpoints, and this functionally contributes to cell cycle progression in OSE and HGSC cell models. Finally, we identified CCNE1 as a new upstream activator of FOXM1 expression.

Figures and Tables

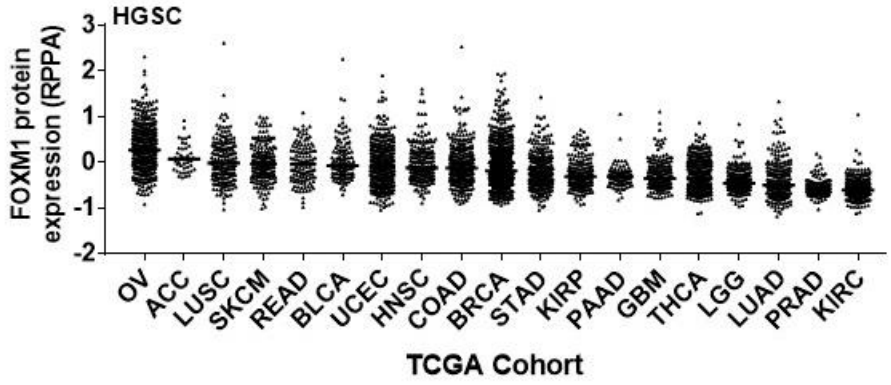

Figure 9. FOXM1 protein expression (RPPA, RBN normalized) across TCGA cancer types. TCGA cancer cohorts are listed on the x-axis and ranked according to median FOXM1 expression with the highest expression on the left. Median lines are shown for each cancer cohort. HGSC = OV.

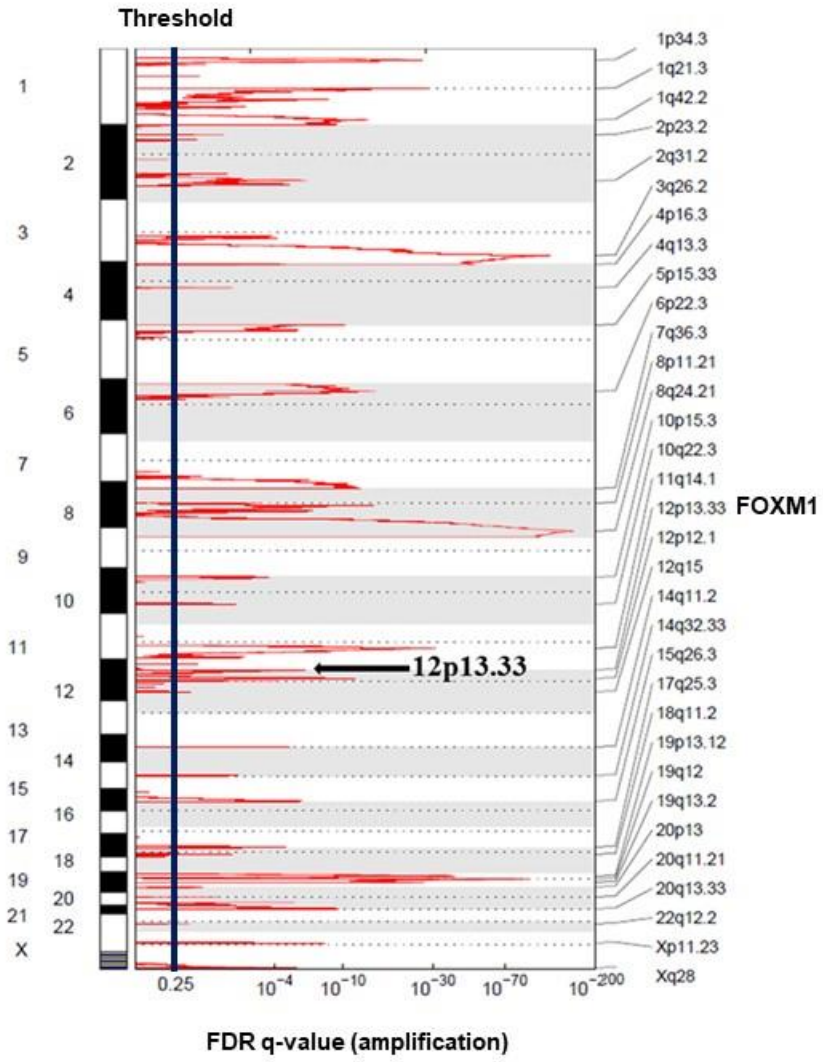
Threshold
1
2
3
4
5
6
7
8
9
10
11
12
13
14
15
16
17
18
19
20
21
22
X
12p13.33
1p34.3
1q21.3
1q42.2
2p23.2
2q31.2
3q26.2
4p16.3
4q13.3
5p15.33
6p22.3
7q36.3
8p11.21
8q24.21
10p15.3
10q22.3
11q14.1
12p13.33 FOXM1
12p12.1
12q15
14q11.2
14q32.33
15q26.3
17q25.3
18q11.2
19p13.12
19q12
19q13.2
20p13
20q11.21
20q13.33
22q12.2
Xp11.23
Xq28
0.25
10^-4
10^-10
10^-30
10^-70
10^-200
FDR q-value (amplification)

Figure 10.

Figure 10. Recurrent sites of DNA copy number amplification in HGSC determined by GISTIC. The GISTIC plot shows 33 recurrent sites of DNA copy number amplification in 579 TCGA HGSC samples**.** The x-axis displays statistical significance as FDR q-value. The black vertical line indicates the threshold for significance, which is set with an FDR q-value less than 0.25. Chromosomes listed on the left are arranged from chromosome 1 on top to chromosome X on the bottom. Significantly amplified cytobands are listed on the right. The 12p13.33 peak is highlighted on the plot. The GISTIC data was retrieved on 8/21/2015 from the Broad Institute TCGA Genome Data Analysis Center. TCGA HGSC SNP6 Copy number analysis (GISTIC2).

Cytoband	12p13.33
FDR q-value	0.000001374
Peak boundaries	chr12:1-3550659
Genes in peak	**FOXM1**
	FKBP4
	CBX3P4
	CACNA1C
	LINC00940
	LINC00942
	RN7SL852P
	RNU4ATAC16P
	FAM138D
	NINJ2
	RAD52
	KDM5A
	SLC6A12
	SLC6A13
	TEAD4
	TULP3
	TSPAN9
	ERC1
	ITFG2
	PRMT8
	WNK1
	ADIPOR2
	WNT5B
	RHNO1
	NRIP2
	CCDC77
	CACNA2D4
	FBXL14
	DCP1B
	B4GALNT3
	IQSEC3
	LRTM2
	MIR3649

Table 5: List of genes contained at the TCGA HGSC 12p13.33 amplicon.

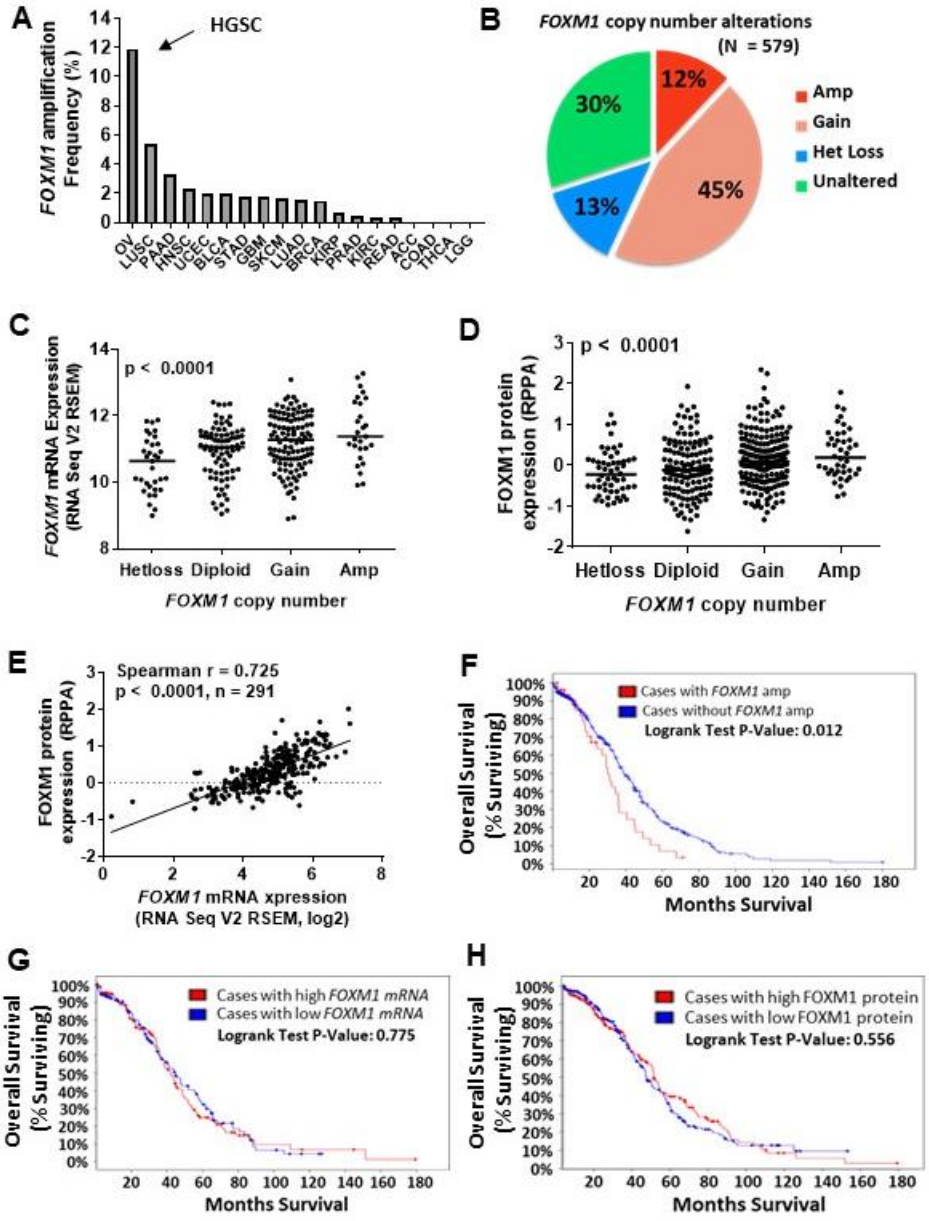
A
FOXM1 amplification Frequency (%)
HGSC
OV LUSC PRAD HNSC UCEC BLCA STAD GBM SKCM LUAD BRCA KIRP PRAD KIRC READ ACC COAD THCA LGG
B
FOXM1 copy number alterations (N = 579)
12%
45%
13%
30%
Amp
Gain
Het Loss
Unaltered
C
FOXM1 mRNA Expression (RNA Seq V2 RSEM)
p < 0.0001
Hetloss Diploid Gain Amp
FOXM1 copy number
D
FOXM1 protein expression (RPPA)
p < 0.0001
Hetloss Diploid Gain Amp
FOXM1 copy number
E
FOXM1 protein expression (RPPA)
Spearman r = 0.725
p < 0.0001, n = 291
FOXM1 mRNA xpression (RNA Seq V2 RSEM, log2)
F
Overall Survival (% Surviving)
Cases with FOXM1 amp
Cases without FOXM1 amp
Logrank Test P-Value: 0.012
Months Survival
G
Overall Survival (% Surviving)
Cases with high FOXM1 mRNA
Cases with low FOXM1 mRNA
Logrank Test P-Value: 0.775
Months Survival
H
Overall Survival (% Surviving)
Cases with high FOXM1 protein
Cases with low FOXM1 protein
Logrank Test P-Value: 0.556
Months Survival

Figure 11.

Figure 11. *FOXM1* copy number alterations (CNA) and overall survival in HGSC. **A.** *FOXM1* amplification frequency in TCGA datasets, showing the 19 cancer types from Figure 7. Arrow indicates HGSC. **B.** *FOXM1* CNA in HGSC TCGA datasets as determined by GISTIC. **C.** *FOXM1* mRNA expression (RNA Seq V2 RSEM, log2) compared to *FOXM1* copy number in HGSC TCGA datasets. **D.** FOXM1 protein expression (RPPA) compared to *FOXM1* copy number in HGSC TCGA datasets**. E**. *FOXM1* mRNA expression (RNA Seq V2 RSEM, log2) correlated with FOXM1 protein expression (RPPA) in HGSC TCGA datasets. **F-H.** Overall survival as a function of **F.** *FOXM1* amplification, **G**. *FOXM1* mRNA expression (dichotomized by group median) and **H.** FOXM1 protein expression (RPPA) (dichotomized by group median) in HGSC TCGA datasets. The *p* value for Logrank test is shown. The p value for ANOVA with post-test for linear trend is shown. Lines represent group medians.

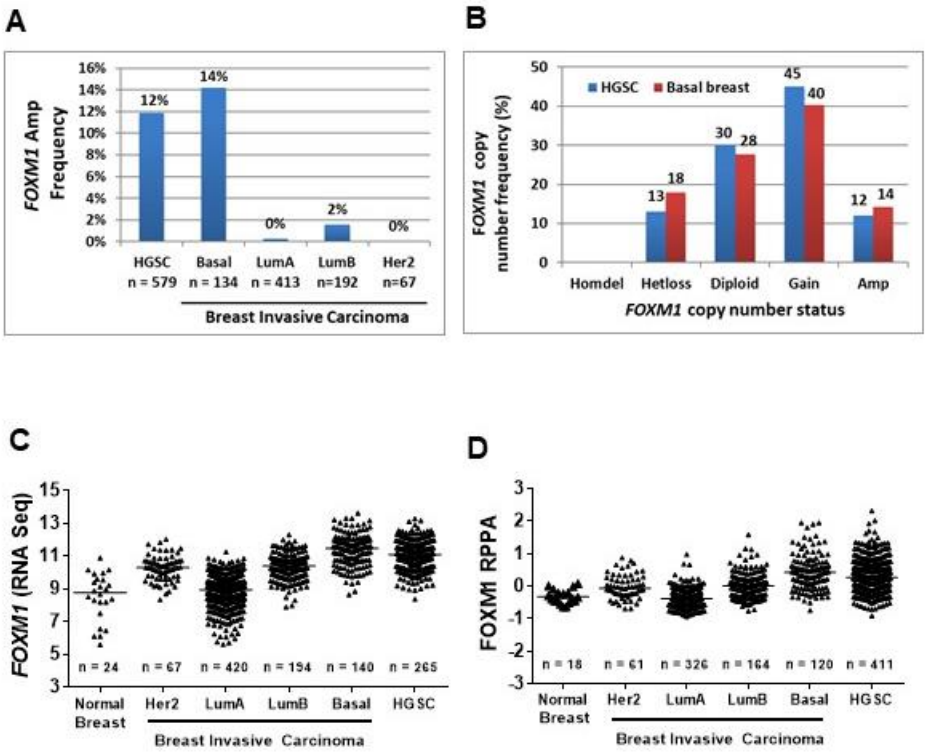

Figure 12. *FOXM1* copy number alterations (CNA) and expression in TCGA HGSC vs breast tissues. A. *FOXM1* amp frequency in HGSC vs breast molecular subtypes. **B**. *FOXM1* copy number status in HGSC vs basal breast**. C-D**. FOXM1 expression in HGSC vs breast molecular subtypes **C.** mRNA expression (RNA-seq) and **D.** protein expression (RPPA). Lines represent group medians.

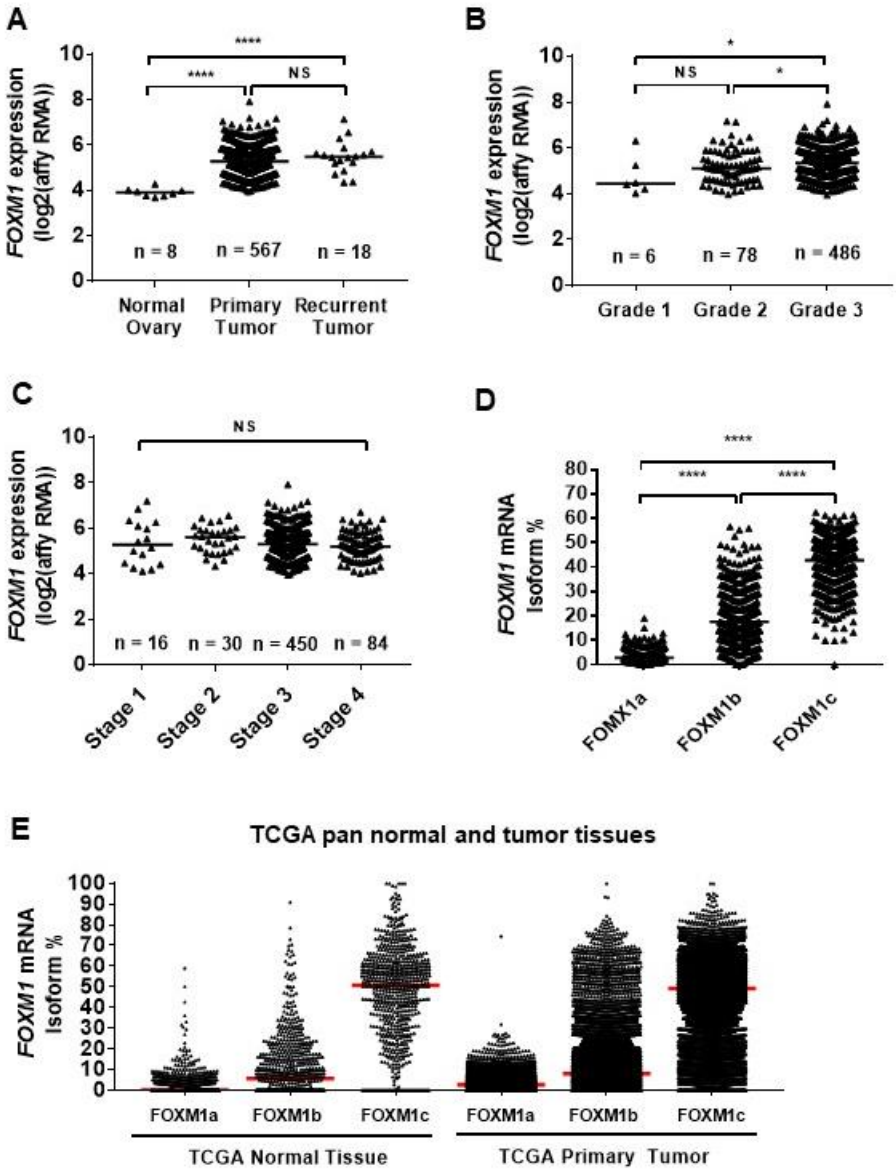
A
FOXM1 expression (log2(affy RMA))
****
****
NS
n = 8
n = 567
n = 18
Normal Ovary
Primary Tumor
Recurrent Tumor
B
FOXM1 expression (log2(affy RMA))
*
NS
*
n = 6
n = 78
n = 486
Grade 1
Grade 2
Grade 3
C
FOXM1 expression (log2(affy RMA))
NS
n = 16
n = 30
n = 450
n = 84
Stage 1
Stage 2
Stage 3
Stage 4
D
FOXM1 mRNA Isoform %
****
****
****
FOMX1a
FOXM1b
FOXM1c
E
TCGA pan normal and tumor tissues
FOXM1 mRNA Isoform %
FOXM1a
FOXM1b
FOXM1c
FOXM1a
FOXM1b
FOXM1c
TCGA Normal Tissue
TCGA Primary Tumor

Figure 13.

Figure 13. *FOXM1* expression in TCGA high-grade serous ovarian cancer. A. *FOXM1* mRNA expression HGSC primary and recurrent tumor as compared to normal ovary (RNA-seq) **B.** *FOXM1* mRNA expression in serous ovarian cancer as function of pathological grade. **C.** *FOXM1* mRNA expression in serous ovarian cancer as a function of disease stage (RNA-seq). **D-E.** *FOXM1* isoform expression in **D.** TCGA HGSC tissues and **E.** TCGA pan-normal and -cancer tissues is represented as percentage of total *FOXM1* transcript levels measured by RNA-seq. Lines represent group medians. The Mann-Whitney test P value is shown. P value designation: **** < 0.0001, *** < 0.001, ** < 0.01, * < 0.05.

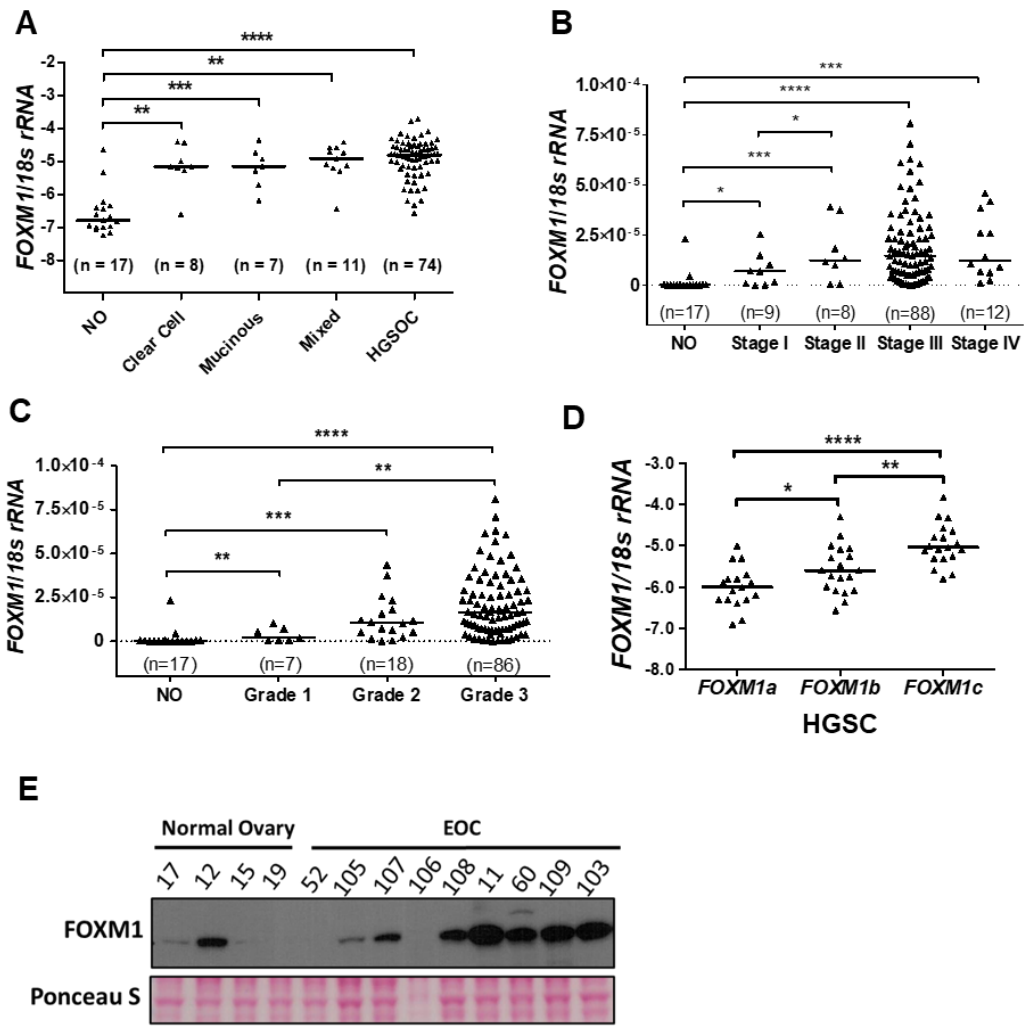

Figure 14. FOXM1 expression in EOC tissues. A. *FOXM1* expression measured with RT-qPCR (log10) in EOC histological subtypes as compared to normal ovary (NO). *FOXM1* expression was normalized to *18s rRNA*. **B.** *FOXM1* expression in NO and in EOC as a function of disease stage. **C.** *FOXM1* expression in NO and in EOC as a function of pathological grade. Lines represent group medians. Mann-Whitney test *p* values are shown. **D.** *FOXM1* isoform specific RT-qPCR (log10) measured in HGSC tissues. **E.** FOXM1 Western blot analysis in NO and EOC. Ponceau S staining is shown as a loading control. Lines represent group medians. The Mann-Whitney test *P* value is shown. *P* value designation: **** < 0.0001, *** < 0.001, ** < 0.01, * < 0.05.

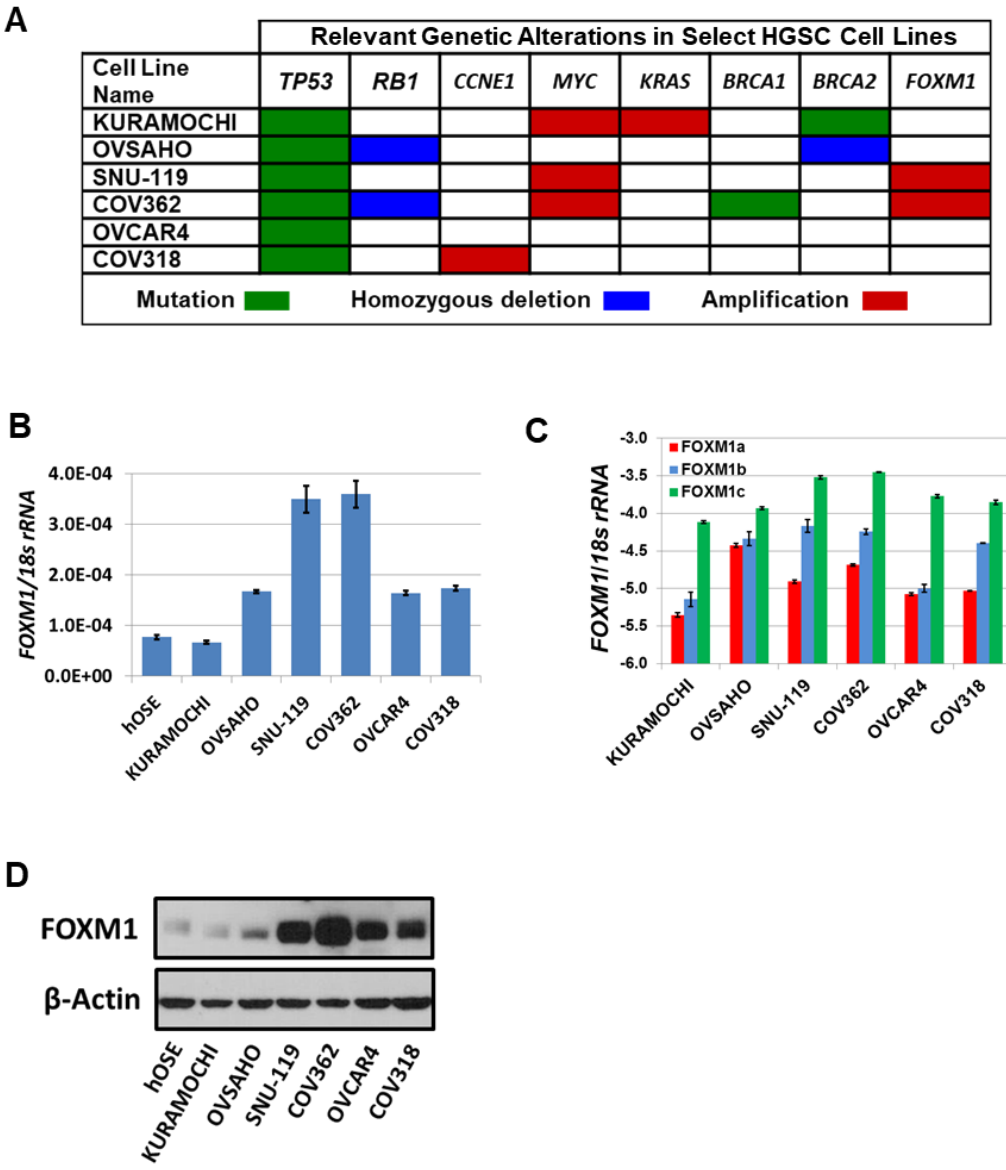

Figure 15. FOXM1 expression in HGSC cell lines. A. Relevant genetic alterations in HGSC cell lines. Data were retrieved from the CCLE dataset and copy number alterations were visualized with IGV as described in *Methods*. **B.** *FOXM1* mRNA expression in HGSC cell lines and hOSE cells (control) was measured by RT-qPCR. **C.** Isoform specific *FOXM1* mRNA expression in HGSC cell lines was measured by RT-qPCR (log10). **D.** FOXM1 protein expression in HGSC cell lines and hOSE (control) was measured by Western blot. For **B**-**C**, bars represent mean ± SD.

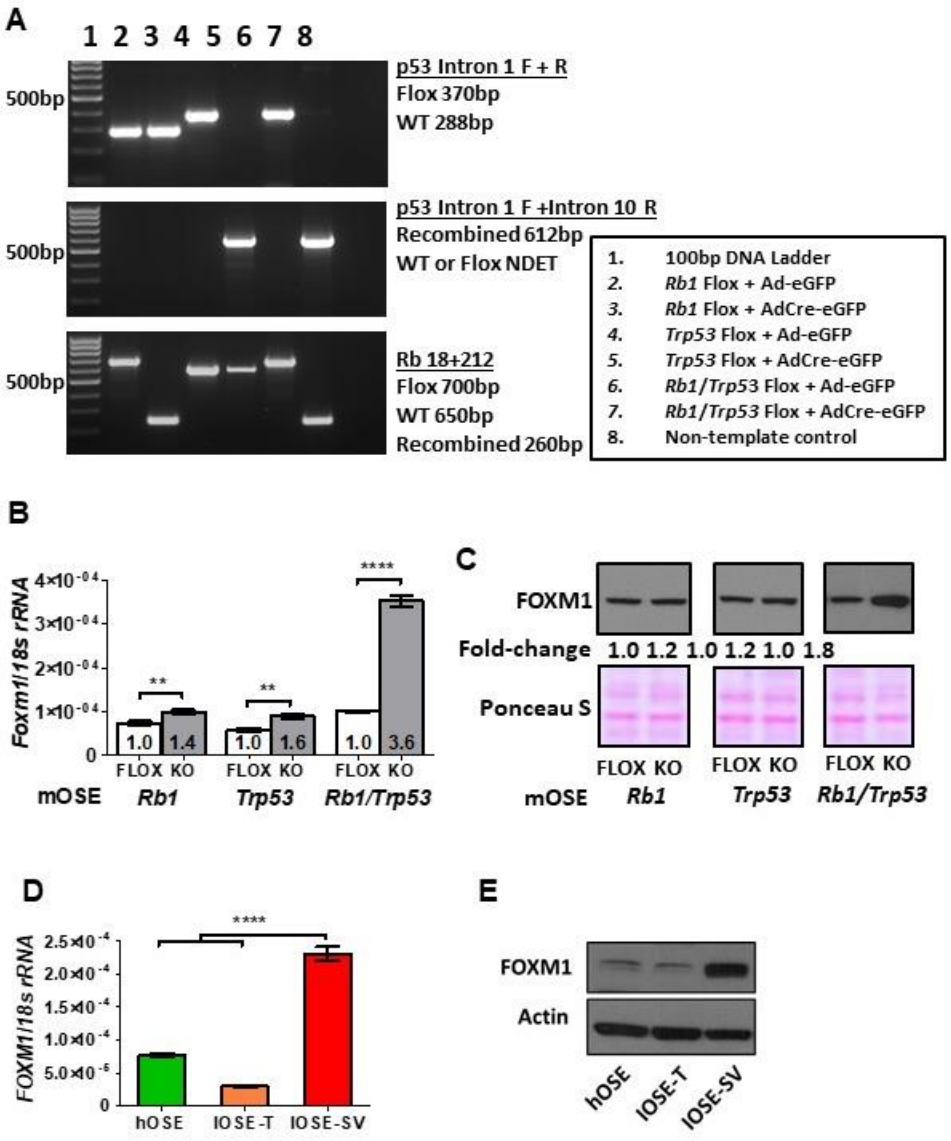
A
1 2 3 4 5 6 7 8
500bp
p53 Intron 1 F + R
Flox 370bp
WT 288bp
500bp
p53 Intron 1 F +Intron 10 R
Recombined 612bp
WT or Flox NDET
500bp
Rb 18+212
Flox 700bp
WT 650bp
Recombined 260bp
1. 100bp DNA Ladder
2. Rb1 Flox + Ad-eGFP
3. Rb1 Flox + AdCre-eGFP
4. Trp53 Flox + Ad-eGFP
5. Trp53 Flox + AdCre-eGFP
6. Rb1/Trp53 Flox + Ad-eGFP
7. Rb1/Trp53 Flox + AdCre-eGFP
8. Non-template control
B
Foxm1/18s rRNA
4×10-04
3×10-04
2×10-04
1×10-04
0
**
**
****
1.0 1.4 1.0 1.6 1.0 3.6
FLOX KO FLOX KO FLOX KO
mOSE Rb1 Trp53 Rb1/Trp53
C
FOXM1
Fold-change 1.0 1.2 1.0 1.2 1.0 1.8
Ponceau S
FLOX KO FLOX KO FLOX KO
mOSE Rb1 Trp53 Rb1/Trp53
D
FOXM1/18s rRNA
2.5×10-4
2.0×10-4
1.5×10-4
1.0×10-4
5.0×10-5
0
****
hOSE IOSE-T IOSE-SV
E
FOXM1
Actin
hOSE IOSE-T IOSE-SV

Figure 16.

Figure 16. FOXM1 expression in murine and human OSE cells following Rb and/or p53 abrogation. A. PCR genotyping of mOSE cells following infection with recombinant adenovirus expressing enhanced GFP (Ad-eGFP, control) or Cre recombinase + eGFP (AdCre-eGFP). **B-C.** FOXM1 expression in Rb and/or p53 floxed (control) and knockout (post-Cre infection) mOSE cells. **B.** *Foxm1* RT-qPCR with respective fold-change relative to the floxed control. Data represent mean ± SD. Students *t*-test *p* value is shown. **C.** FOXM1 Western blot with respective fold change relative to the floxed control, performed with nuclear lysates. Ponceau S staining is shown as a loading control. **D-E**. FOXM1 expression in primary and immortalized human OSE cells (hOSE and IOSE-T or IOSE-SV). Cell line descriptions are provided in the *Methods*. **D.** *FOXM1* RT-qPCR. Data represent mean ± SD. **E.** FOXM1 Western blot. β-actin is shown as a loading control. Students *t*-test *p* values: **** < 0.0001, *** < 0.001, ** < 0.01, * < 0.05.

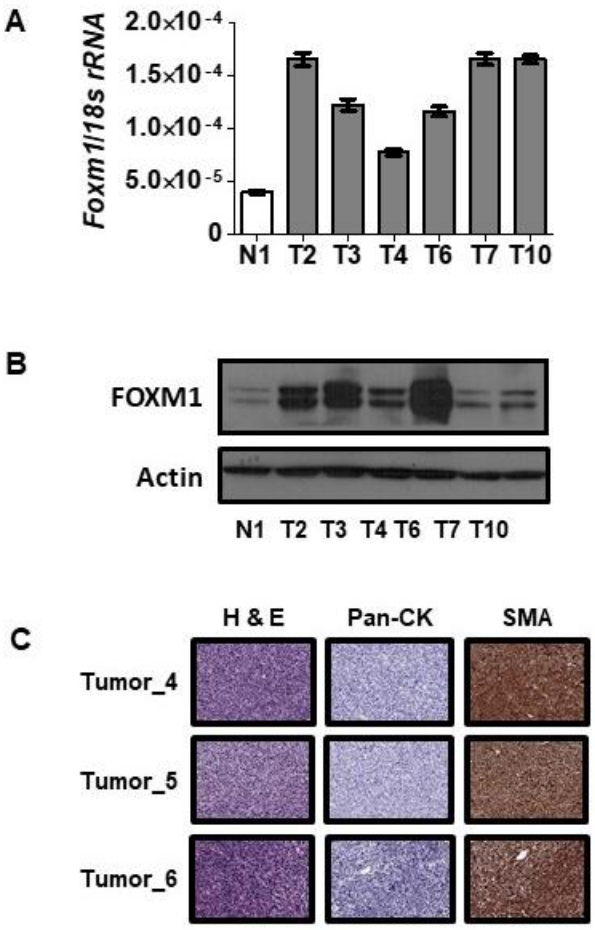

Figure 17. FOXM1 expression in Rb1/Trp53 knockout-driven murine ovarian cancer. **A-B.** FOXM1 expression in *Rb1*/*Trp53* knockout murine ovarian tumor tissues (T) and murine normal ovary control tissue (N). The mouse model is described in *Methods*. **A.** *Foxm1* RT-qPCR. Data represents means ± SD. **B.** FOXM1 Western blot. β-actin is shown as a loading control. **C.** Ovarian tumor histology in Rb/p53 knockout mice. Paraffin sections of the tumors were stained with H&E or specific antibodies to pan-cytokeratin (Pan-CK) or smooth muscle actin (SMA). Images were captured using 20X objective. Antigen detection is indicated by the presence of a brownish-red stain.

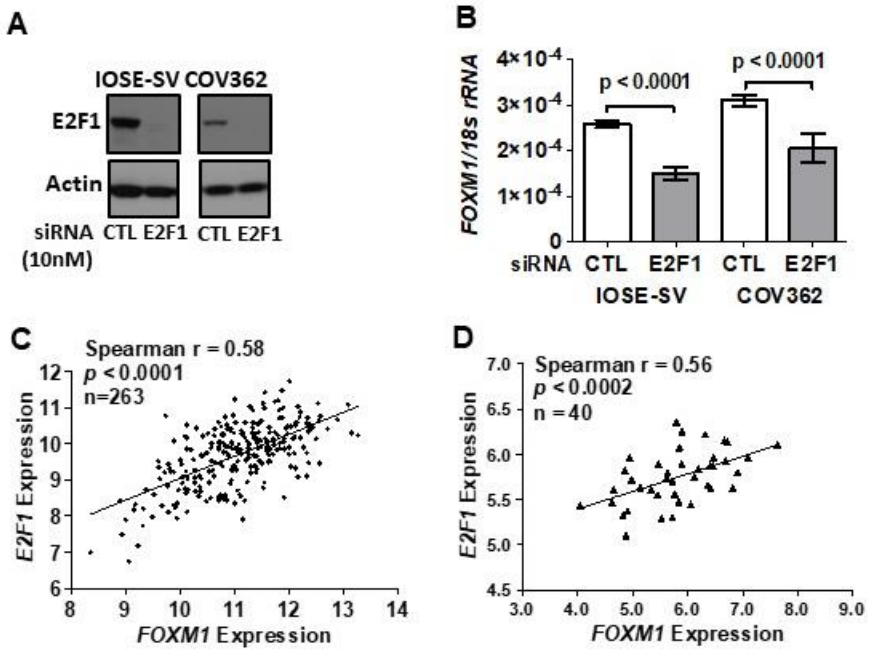

Figure 18. E2F1 and *FOXM1* expression in IOSE-SV, EOC cells, and EOC tissues. A-B. siRNA knockdown of E2F1 (10nM) in IOSE-SV and COV362 cells for 72 hours. **A.** E2F1 Western blot. β-actin is shown as a loading control. **B.** *FOXM1* RT-qPCR, normalized to *18s rRNA*. Data represent mean ± SD. Student's *t*-test *p* value is shown. **C-D.** *E2F1* and *FOXM1* expression correlation in human EOC tissues. **C.** Correlation in 263 HGSC tissues from TCGA datasets (gene expression determined by RNA seq V2, log2). **D.** Correlation in an independent set of 40 EOC tissues (gene expression determined by Affymetrix HG 1.0ST microarray, log2).

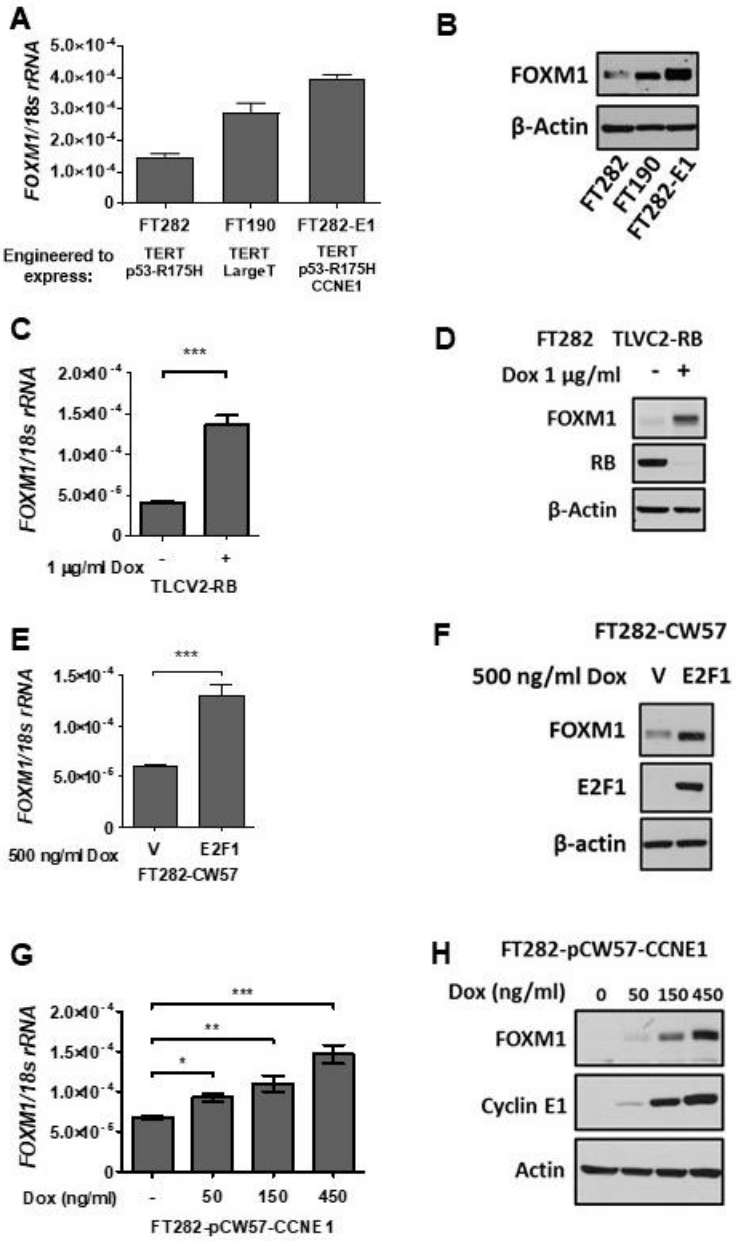
A
FOXM1/18s rRNA
5.0×10⁻⁴
4.0×10⁻⁴
3.0×10⁻⁴
2.0×10⁻⁴
1.0×10⁻⁴
0
FT282
FT190
FT282-E1
Engineered to express:
TERT p53-R175H
TERT LargeT
TERT p53-R175H CCNE1
B
FOXM1
β-Actin
FT282
FT190
FT282-E1
C
FOXM1/18s rRNA
***
2.0×10⁻⁴
1.5×10⁻⁴
1.0×10⁻⁴
5.0×10⁻⁵
0
1 µg/ml Dox
-
+
TLCV2-RB
D
FT282 TLVC2-RB
Dox 1 µg/ml - +
FOXM1
RB
β-Actin
E
FOXM1/18s rRNA
***
1.5×10⁻⁴
1.0×10⁻⁴
5.0×10⁻⁵
0
500 ng/ml Dox
V
E2F1
FT282-CW57
F
FT282-CW57
500 ng/ml Dox V E2F1
FOXM1
E2F1
β-actin
G
FOXM1/18s rRNA
***
**
*
2.0×10⁻⁴
1.5×10⁻⁴
1.0×10⁻⁴
5.0×10⁻⁵
0
Dox (ng/ml)
-
50
150
450
FT282-pCW57-CCNE1
H
FT282-pCW57-CCNE1
Dox (ng/ml) 0 50 150 450
FOXM1
Cyclin E1
Actin

Figure 19.

Figure 19. FOXM1 expression in FTE cells engineered for deregulation of the Rb-E2F pathway. A-B. FOXM1 mRNA and protein expression were measured by RT-qPCR and Western blot, respectively, in FTE cells. β-actin is shown as a loading control. **C-D.** FOXM1 expression by RT-qPCR and Western blot, respectively, in RB1 CRISPR KO FT282 cells. **E-F.** FOXM1 expression by RT-qPCR and Western blot, respectively, in E2F1-inducible FTE cells. **G-H.** FOXM1 expression by RT-qPCR and Western blot, respectively, in CCNE1-inducible FTE cells. Bars represent mean ± SD. Student's *t* test *p* values are shown. *P* value designation: **** < 0.0001, *** < 0.001, ** < 0.01, * < 0.05.

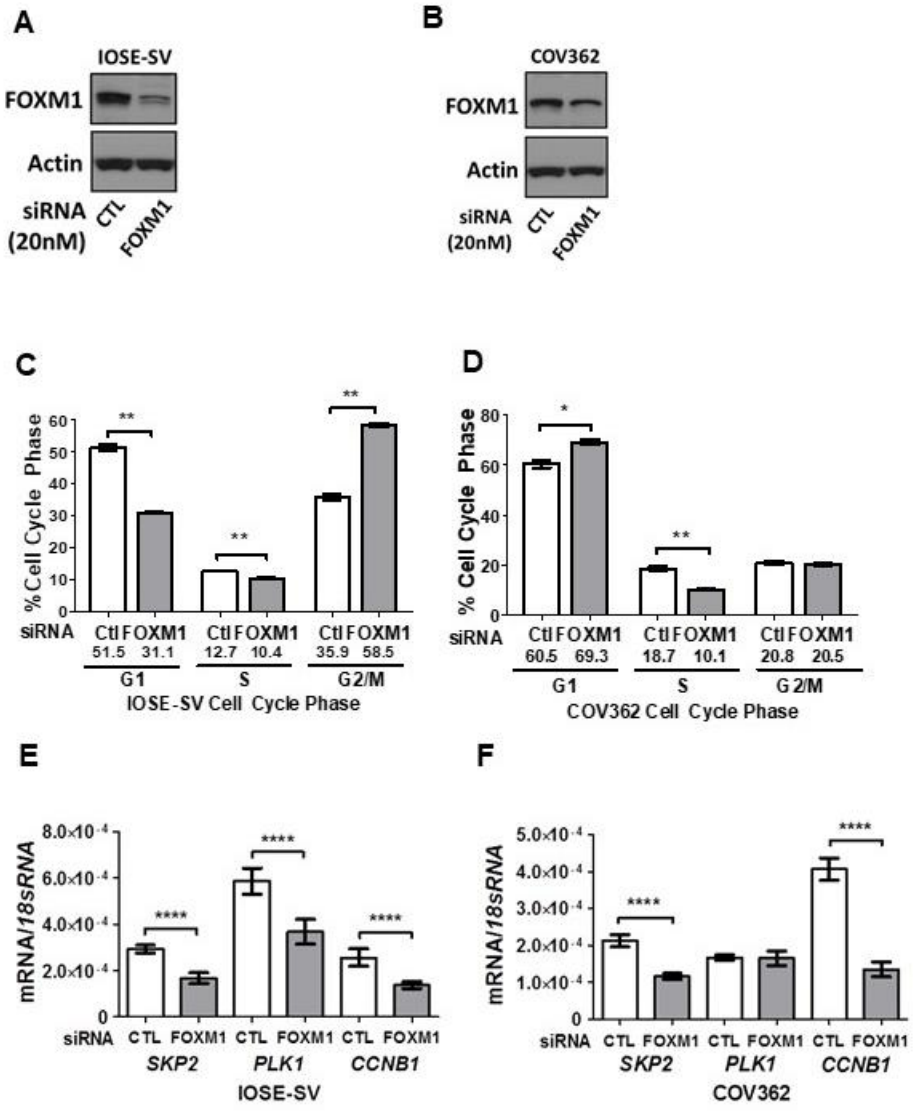
A
IOSE-SV
FOXM1
Actin
siRNA (20nM)
CTL
FOXM1
B
COV362
FOXM1
Actin
siRNA (20nM)
CTL
FOXM1
C
% Cell Cycle Phase
siRNA
Ctl FOXM1
51.5 31.1
12.7 10.4
35.9 58.5
G1
S
G2/M
IOSE-SV Cell Cycle Phase
D
% Cell Cycle Phase
siRNA
Ctl FOXM1
60.5 69.3
18.7 10.1
20.8 20.5
G1
S
G2/M
COV362 Cell Cycle Phase
E
mRNA/18sRNA
siRNA CTL FOXM1 CTL FOXM1 CTL FOXM1
SKP2
PLK1
CCNB1
IOSE-SV
F
mRNA/18sRNA
siRNA CTL FOXM1 CTL FOXM1 CTL FOXM1
SKP2
PLK1
CCNB1
COV362

Figure 20.

Figure 20. Impact of FOXM1 knockdown on cell cycle progression and target gene expression in IOSE-SV and COV362 cells. Transient siRNA-mediated knockdown of FOXM1 (20nM) was completed for 72 hours. **A-B.** Validation of FOXM1 protein knockdown in **A.** IOSE-SV cells and **B.** COV362. FOXM1 protein expression was determined by Western blot, and β-actin is shown as a loading control. **C-D.** Cell cycle analysis of **C.** IOSE-SV and **D.** COV362 cells following FOXM1 or control siRNA treatment. **E-F.** FOXM1 target gene expression determined by RT-qPCR in **E.** IOSE-SV and **F.** COV362 cells, following FOXM1 or control siRNA treatment. Expression data are shown for *SKP2*, *PLK1*, and *CCNB1*, each normalized to *18s rRNA.* Bars represent mean ± SD. Student's *t* test *p* values are shown. *P* value designation: **** < 0.0001, *** < 0.001, ** < 0.01, * < 0.05.

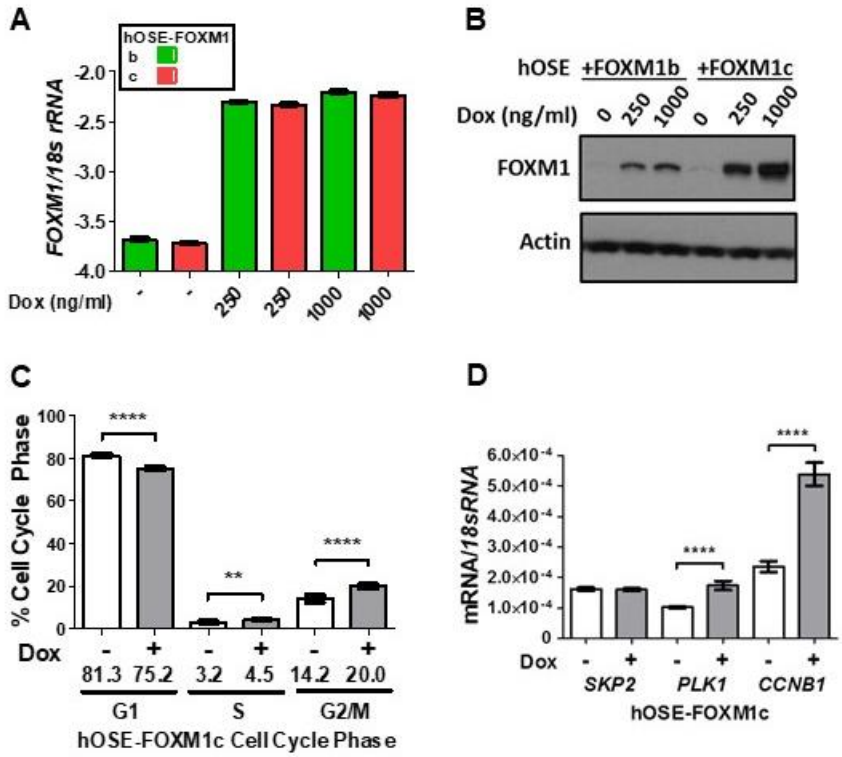

Figure 21. Impact of FOXM1 overexpression on cell cycle progression and target gene expression in hOSE cells. A-B. Doxycycline inducible FOXM1b and FOXM1c overexpression in primary hOSE cells after 72 hours of doxycycline treatment as indicated. **A.** *FOXM1* RT-qPCR (log10). **B**. FOXM1 Western blot. β-actin is shown as a loading control. **C.** Cell cycle analysis following doxycycline inducible FOXM1c overexpression in primary hOSE cells after 72 hours of treatment. Cells treated with 250ng/ml and 1000ng/ml doxycycline were combined for analysis and compared against the control without treatment. **D.** FOXM1 target gene expression was measured by RT-qPCR in hOSE cells following 72 hours of doxycycline treatment to induce FOXM1c. Expression data are shown for *SKP2*, *PLK1*, and *CCNB1*, each normalized to *18s rRNA*. Data represents mean ± SD. Student's *t*-test *p* values are shown. *P* value designation: **** < 0.0001, *** < 0.001, ** < 0.01, * < 0.05.

CHAPTER 4: FOXM1 AND GENOMIC INSTABILITY IN HIGH-GRADE SEROUS OVARIAN CANCER

Introduction

While FOXM1 is linked to several cancer hallmarks, its role in genomic instability has not been explored in HGSC, a disease that exhibits frequent FOXM1 activation and has genomic instability as a key defining molecular feature (30). Additionally, we have shown that HGSC has the highest level of FOXM1 expression among TCGA cancer types and an early pan-cancer analysis observed that FOXM1 expression is associated with genomic instability (37). FOXM1 is a transcriptional activator of genes involved in DNA replication initiation and cell cycle progression (68,86,130,166), and when dysregulated, such genes may promote DNA replication stress and genomic instability (88). These observations suggest that aberrant FOXM1 expression and transcriptional activity may induce DNA replication stress and promote genomic instability in HGSC. The objective of the current study was to determine the functional consequence of aberrant FOXM1 expression on DNA replication stress and genomic instability in HGSC. For this task, we utilized publicly available TCGA datasets, immortalized human FTE cell models, and human HGSC cell lines.

Results

FOXM1 associates with markers of DNA replication stress and genomic instability in HGSC tissue and cell lines

FOXM1 expression has been associated with genomic instability (37,85), but it is unclear whether FOXM1 causes this phenotype and, if so, by what mechanism.

Oncogene-induced DNA replication stress is linked to genomic instability (88,92,97,169). We hypothesized that FOXM1 expression promotes DNA replication stress, providing a mechanistic link to genomic instability. To test the possibility that FOXM1 induces DNA replication stress, we first analyzed TCGA HGSC cancer datasets to determine the association of FOXM1 expression with the expression of P-CHK1-S345, an established marker of DNA replication stress (58). Notably, *FOXM1* mRNA significantly correlated with P-CHK1-S345 protein expression (Figure 22A). The comparison between FOXM1 protein and P-CHK1-S345 protein expression did not show a significant correlation but it did show a direct correlation (Figure 22B). The discrepancy in correlation for FOXM1 mRNA and protein expression may be due to technical differences in the assays (e.g. RNA-seq vs RPPA) or differences in samples and sample size. We next analyzed TCGA HGSC datasets to determine if FOXM1 expression showed a relationship with genomic instability in the form of total mutation count in coding regions of the genome (mutation burden) or genome wide CNAs as a fraction of the total genome (fraction of copy number altered genome). Analysis of TCGA HGSC data showed a signification correlation between FOXM1 mRNA and protein expression and genome wide copy number alterations, a marker of genomic instability (Figure 22E-F). In contrast, FOXM1 expression did not show a significant correlation with the mutation burden (Figure 22C-D), suggesting FOXM1 may promote global copy number alterations but not mutations. Controlling for *FOXM1* copy number, which we have shown contributes to FOXM1 expression in HGSC (36), we made similar comparisons using samples with diploid *FOXM1* copy number status and again we observed a significant correlation between FOXM1 protein expression and genome wide copy number alterations (Figure 22H). The correlation of CNA with *FOXM1* mRNA showed a direct relationship but did not reach statistical significance, possibly due to smaller sample size (Figure 22G). These data suggest that FOXM1 may promote DNA replication stress and genomic instability in HGSC.

To expand and independently confirm these observations, we analyzed the Cancer Cell Line Encyclopedia (CCLE) pan-cancer and ovarian cancer cell line datasets. Notably, FOXM1 protein significantly correlated with P-CHK1-S345 protein expression in both CCLE pan-cancer and ovarian cancer cell lines (Figure 23A-B). We then measured total FOXM1 protein along with canonical DNA replication stress response markers in a panel of HGSC cell lines as compared to an immortalized FTE cell line which represents the p53 signature precursor lesion in HGSC (Figures 2 and 6). We observed that HGSC cells showed increased basal levels of phosphorylated CHK1 and RPA2 as compared to the FTE cells (Figure 24A). We also observed that FOXM1 protein expression was increased in HGSC cells as compared to FTE (Figure 24A). We next overexpressed FOXM1 in FTE cells then measured the expression of P-CHK1-S345 to determine the relationship in their expression. We found a dose dependent response between FOXM1 and P-CHK1 expression (Figure 24B). These data support the idea that FOXM1 induces DNA replication stress in HGSC, potentially contributing to genomic instability.

FOXM1 transcriptional activity is required for the induction of DNA replication stress and DNA damage in FTE cells

Our central hypothesis is that FOXM1 induces DNA replication stress thereby promoting genomic instability. To test whether FOXM1-induced DNA replication stress is dependent on its transcriptional activity, we generated a FOXM1 DBD mutant where three key residues in the FOXM1 DNA binding domain (DBD) were changed to alanine. These amino acid residues were shown to be essential for FOXM1 to bind DNA based on previous reports using X-crystallography and ChIP-seq (132,170). We next overexpressed FOXM1 wild-type and DBD mutant in FTE cells using a doxycycline inducible system to determine if FOXM1-induced DNA replication stress is linked to its transcriptional activity.

We first validated the functional activity of FOXM1 wild-type and DBD mutant by measuring the endogenous expression of a canonical target gene, *CCNB1*, and by the widely used 6X FOXM1 luciferase reporter assay (171). Following doxycycline induction of wild-type FOXM1 in FTE cells and transfection of the the 6X FOXM1 reporter construct, we observed a significant increase in luciferase activity, but not for the DBD mutant (Figure 25A). In agreement, we observed a dose dependent increase in *CCNB1* mRNA expression, but we did not see a significant increase in *CCNB1* mRNA with the induction of FOXM1 DBD mutant (Figure 25B). Most importantly, following doxycycline induction, we observed that wild-type FOXM1 increased P-CHK1-S317 and -S345 but the FOXM1 DBD mutant did not (Figure 25C). These data demonstrate that FOXM1 transcriptional activity is related to its ability to induce DNA replication stress in a relevant HGSC precursor cell model.

The above data show that FOXM1 is capable of inducing a DNA replication stress response in FTE cells. Therefore, we hypothesized that FOXM1 not only induces DNA replication stress but also induces DNA damage. To test this, we asked whether FOXM1 expression in human immortalized FTE cells leads to detectable levels of DNA damage measured at single cell resolution with the Comet assay. Following doxycycline induction, we observed an increased percentage of Comet tail DNA in FTE cells expressing wild-type FOXM1, as compared to FTE cells expressing FOXM1 DBD mutant, suggesting that transcriptional activity is required for this phenotype as well (Figure 25D).

FOXM1 and CCNE1 produce comparable levels of DNA damage in FTE cells

FOXM1 is associated with genomic instability but the mechanistic link has not been demonstrated. Oncogene-induced DNA replication stress is linked to genomic instability in many various cell types (88). Thus far, we observed that FOXM1 expression shows a

direct relationship with markers of DNA replication stress and genomic instability in TCGA HGSC. In addition, FOXM1 expression induced the expression of DNA replication stress markers and increased DNA damage as measured with the Comet assay. We extended these studies by comparing the DNA damage phenotypes between FTE cells expressing FOXM1 or CCNE1, an oncogene known to induce DNA replication stress and DNA damage in FTE cells (155). We observed that both FOXM1 and Cyclin E1 showed increased and comparable levels of γ-H2AX and percentage of Comet tail DNA, but CCNE1 showed a greater increase in P-CHK1 (Figure 26A-C). Furthermore, we used Flow Cytometry as an independent readout of DNA damage by measuring the levels of γ-H2AX in S-phase cells, or the DNA damage occurring during DNA replication. In agreement with the Comet data, we observed that FOXM1 expressing cells showed increased expression of γ-H2AX in S-phase as compared to vector control (Figure 26D). These results agree with the DNA replication stress phenotype we observed for wild-type and DBD mutant FOXM1, suggesting that DNA replication stress links FOXM1 to genomic instability.

FOXM1 promotes cell cycle progression in fallopian tube epithelial cells

Thus far in our cell models, FOXM1 overexpression in FTE cells activated ATR-CHK1 signaling with a corresponding increase in DNA damage, indicative of DNA replication stress. When cells experience DNA replication stress, the ATR-CHK1 signaling pathway is activated, thereby promoting fork stabilization and restart, and inducing cell cycle arrest in the S and G2 phases allowing time for damaged DNA to be repaired prior to entering mitosis (88). Therefore, the FTE cells with FOXM1-induced DNA replication stress and DNA damage might have increased cells in the S and G2/M phases although FOXM1 is known to promote G2-M progression. To test this, we overexpressed FOXM1 wild-type, FOXM1 DBD mutant, and Cyclin E1 in FTE cells and performed cell cycle

analysis after 72 hours of doxycycline induction (Figure 27A). Unexpectedly, the FTE cells expressing the FOXM1 DBD mutant showed an increased number of cells in the G2/M phase of the cell cycle (Figure 27B). In contrast, FTE cells expressing wild-type FOXM1 showed an increase in G1 and S phases but a decrease in the G2/M phase, suggesting FOXM1 promoted cell cycle progression through the G2/M checkpoint, which agrees with its canonical function in cell cycle regulation (Figure 27B). In agreement with previous reports using other cell types, we observed that FTE cells expressing Cyclin E1 showed a decreased G1 phase with increased S and G2/M phases (Figure 27B). This suggests that Cyclin E1 promoted cell cycle progression though the G1/S checkpoint but the resulting DNA replication stress leads to cell cycle arrest in S and G2/M phases (172). Finally, the failure of FOXM1-expressing FTE cells to arrest in S and G2/M either suggests that FOXM1 does not induce a traditional DNA replication stress phenotype or the canonical function of FOXM1 has an opposing force on the ATR-CHK1-mediated cell cycle arrest, and thus the cells fail to arrest and instead progress into mitosis.

FOXM1 promotes replication fork progression in fallopian tube epithelial cells

We observed that wild-type FOXM1 expression activates markers of DNA replication stress while promoting cell cycle progression. To determine how FOXM1 associates with these phenotypes, we performed DNA fiber analysis, which is the gold standard for measuring DNA replication stress and the most comprehensive method for assessing the DNA replication dynamics among a population of mammalian cells (169,173). We performed DNA fiber spreading with FTE cells engineered for doxycycline inducible expression of empty vector (control), wild-type FOXM1, DBD mutant FOXM1, and Cyclin E1, an oncogene shown to cause DNA replication stress in other cell types by DNA fiber analysis (172,174,175). Inducible FTE cells were grown in the presence of

doxycycline for 72 hours prior to labeling them with nucleotide analogues for DNA fiber analysis. Cells were harvested for DNA fiber and we measured fork rate and the number of origins fired. As expected, based on previous reports for other cell types, Cyclin E1 expression in FTE cells decreased fork rate and increased origin firing (Figure 28A-C) (120,122,123). Unexpectedly, we observed that wild-type FOXM1 not only promoted increased fork rate in FTE cells, but it increased origin firing (Figure 28A-C). Also surprising, but in agreement with the cell cycle data, the FOXM1 DBD mutant decreased fork movement (Figure 28A-C), the phenotype that results from cells experiencing DNA replication stress. DNA replication stress is more generally defined by the replication fork dynamics where there is an observed slowing or stalling of the replication forks (169). This is also the accepted definition for oncogene-induced DNA replication stress and this type of phenotype is often reported in the literature for most oncogenes (88). However, based on this recent review, not all oncogenes that promote DNA replication stress promote fork stalling (88). In fact, some oncogenes increase fork speed while inducing DNA damage although the activation of ATR-CHK1 signaling in these studies was not characterized (176-179). Given this knowledge and our recent data, we hypothesized that FOXM1 may activate target genes involved in DNA replication or chromatin remodeling that facilitate fork movement.

FOXM1 activates target genes involved in the regulation of the G2/M cell cycle checkpoint

Oncogenes, such as Ras, Myc, and Cyclin E, deregulate E2F-dependent G1/S transcription to drive progression into S phase and promote DNA replication (180,181). Specifically, Cyclin E1 expression enhanced a global transcriptional program, causing increased DNA replication stress, and this phenotype was rescued by either transcription

or CDK inhibition (175,180). However, the mechanism for how Cyclin E1 causes DNA replication stress in FTE cells is not known. Furthermore, DNA replication can be affected by the expression and interplay between different chromatin factors and histone modifications to promote rapid replisome progression (182). In this context, FOXM1 can bind DNA and activate target gene expression, but the FOXM1 DBD mutant is deficient in this function. Additionally, FOXM1 wild-type increases DNA fork rate and FOXM1 DBD mutant decreases DNA fork rate. Therefore, FOXM1 wild-type might activate the expression of genes involved in DNA replication initiation and elongation, and chromatin remodeling, thus facilitating fork movement.

To identify a possible mechanism for FOXM1-induced fork movement, as well as Cyclin E1-induced fork stalling, we performed RNA-seq analysis with FTE cells expressing empty vector (control), FOXM1 and Cyclin E1 (Figure 29A-B). GSEA analysis for Cyclin E1-expressing FTE cells showed an enriched gene expression signature for DNA replication and initiation (Figure 30A). This suggests that Cyclin E1 expression promotes increased DNA replication initiation or origin firing, a condition which can lead to depletion of nucleotide pools, and eventually fork stalling and DNA replication stress (169). Interestingly, we observed that the FTE cells expressing Cyclin E1 show a significantly enriched FOXM1 pathway gene expression signature (Figure 30B) and this is consistent with our prior data (Figure 19G-H). Gene Set Enrichment Analysis (GSEA) of FTE cells expressing FOXM1 showed an enriched expression signature for FOXM1 target genes, specifically those involved in the regulation of the G2/M checkpoint and mitosis, rather than a gene expression signature of DNA replication or chromatin remodeling (Figure 30C-D). We validated the FOXM1 target gene expression by RT-qPCR and found that FTE cells expressing FOXM1 or Cyclin E1 both showed increased mRNA expression for FOXM1 target genes (Figure 31A-C). Although *BRCA2* mRNA was not differentially

expressed in our RNA-seq analysis for FTE cells expressing FOXM1, we measured the expression of *BRCA2* mRNA by RT-qPCR because it has been reported to be a FOXM1 target gene (91). Furthermore, RNA-seq analysis showed that *BRCA2* mRNA expression was increased in FTE cells expressing CCNE1. These data support a functional role for FOXM1 in the G2/M checkpoint downstream of Cyclin E1 and suggest that FOXM1 transcriptional activity does not directly explain the increase in fork movement.

Analysis of RPPA functional proteomics data confirms the involvement of FOXM1 in the G2/M checkpoint

Our RNA-seq analysis did not identify gene expression changes that may contribute to the FOXM1-induced fork movement, therefore, we decided to investigate proteomic changes as the possible cause of this phenotype. Reverse phase protein arrays (RPPA) provide a large-scale measurement of a defined number of total proteins, and phosphorylated and cleaved proteins that can provide insight into post-transcriptional changes in multiple signaling pathways, including receptor tyrosine kinases, PI3K-AKT and MAPK cascades, as well as DNA repair, cell cycle and apoptosis/autophagy regulators (156,183). We performed RPPA to characterize the proteomic profile in the FTE cells expressing FOXM1 and Cyclin E1 to determine if there are differences in these select signaling pathways, potentially providing insight for the increased fork rate in FTE cells expressing wild-type FOXM1. We overexpressed FOXM1 wild-type, FOXM1 DBD mutant, and Cyclin E1 in an inducible manner by growing cells FTE cells in the presence of doxycycline for a period of 72 hours. Proteins were harvested and sent to the RPPA Core at MD Anderson for analysis. We used the normalized log2, median centered RPPA data to generate heat maps for visualization of the data. Vector control, FOXM1 wild-type, FOXM1 DBD mutant and Cyclin E1-expressing FTE cells were compared by using

unsupervised hierarchical clustering. Interestingly, FOXM1 wild-type and DBD mutant clustered together and were more similar to FTE-expressing V control than FTE cells expressing Cyclin E1 (Figure 32A). The clustering of FOXM1 wild-type and DBD mutant is surprising, considering that FOXM1 DBD does not appear to be transcriptionally active and should therefore be more similar to V control. This clustering suggests that the FOXM1 DBD mutant retains functions independent of FOXM1 transcriptional activity. Furthermore, Cyclin E1-expressing FTE cells did not cluster with the other cell types suggesting it has a signaling profile that is distinct. Next, the heatmaps were sorted based on ranked expression by either FOXM1 wild-type, FOXM1 DBD mutant or Cyclin E1, and the top 10 proteins were compared (Figure 32B-D). We observed that Cyclin E1 showed very dramatic changes in the expression of proteins involved in regulation of the G1/S and G2/M checkpoints (Figure 32D). FOXM1 wild-type showed very few changes in cell cycle-associated proteins except for Cyclin B1, which promotes G2/M progression (Figure 32B). Lastly, the FOXM1 DBD mutant did not show changes in the expression of proteins that promote G2/M progression (Figure 32C).

FOXM1 directly interacts with proteins involved in DNA replication and epigenetic modification

Our analysis of FOXM1 RNA-seq and RPPA did not identify obvious changes in gene or protein expression that could explain the increased fork movement and origin firing in FTE cells expressing FOXM1. This suggests that this phenotype is independent of FOXM1 transcriptional activity or changes in defined downstream protein levels or signaling pathways. We next hypothesized that FOXM1 may interact with chromatin or proteins involved in DNA replication or chromatin modification, potentially facilitating fork

movement. In this context, a recent high-throughput proteomics study characterized protein-protein interactions for several transcription factors, including FOXM1 (184). Intriguingly, FOXM1 was shown to interact with MCM and ORC proteins, proteins involved in DNA replication initiation and elongation, along with known interactions related to its canonical function in the activation of target gene expression (184). Furthermore, pathway analysis showed that FOXM1 protein interactions were enriched in processes such as chromatin modification, DNA replication and transcription (184). FOXM1 protein interacts with proteins that modify chromatin such as DNMT3b (185), and besides this recent report, its interaction with proteins involved in DNA replication has not been explored. FOXM1 could interact with DNA replication proteins and thus alter fork movement as we observed (Figure 28). To this this hypothesis, we performed co-immunoprecipitation (co-IP) studies with HA-tagged FOXM1 wild-type isoforms (a, b and c) and FOXM1 DBD mutant constructs expressed in 293T *FOXM1* knockout cells (Figure 33A-B). Surprisingly, all FOXM1 isoforms, including the DBD mutant, similarly interacted with DNA replication proteins (Figure 33C). Our studies were performed with total cell protein so it's possible that the interactions exist within different compartments of the nucleus such as soluble and chromatin fractions. More so, the FOXM1 DBD mutant could be interacting with these proteins but the protein complexes are not able to bind DNA, thus interfering with their functions at chromatin. In an independent experiment, we previously investigated the interaction between FOXM1 and DNA methyltransferases (DNMTs) based on a previous report showing the interactions of these proteins (185). We indeed observed that FOXM1 interacts with DNMT1, DNMT3A and DNMT3B, further supporting the protein-protein interactions between FOXM1 and proteins involved in DNA replication (Figure 33D). However, we do not know yet if these protein-protein interactions occur in the nucleus, on chromatin, or at sites of DNA replication. In agreement with these data and support for the localization of the protein-protein interactions, we retrieved publicly available FOXM1 and

ORC2 ChiP-seq datasets generated from K562 cells and determined the genome-wide correlation in their DNA binding. We observed that FOXM1 and ORC2 show a highly significant correlation in their DNA binding, indicated by the shifted foreground peak compared to background for both replicates (Figure 34A-B). Together, these data suggest that FOXM1 interacts with ORC2 on chromatin and possibly at sites of DNA replication.

FOXM1 functions downstream of Cyclin E1 to promote cell cycle progression

Thus far, our data shows that Cyclin E1 promotes progression through the G1/S checkpoint, which contributes to DNA replication stress and DNA damage, ultimately leading to arrest in G2. Furthermore, FOXM1 target genes are activated downstream of Cyclin E1 in FTE cells. Based on the FOXM1 gene expression signature and cell cycle data, we hypothesized that FOXM1 may cooperate with Cyclin E1 to overcome G2 blockage and allow unscheduled entry into mitosis with damaged DNA, thus contributing to genomic instability. To test this, we expressed FOXM1 wild-type or DBD mutant in the backdrop of Cyclin E1 expression in FTE cells (Figure 35A). These cells were doxycycline induced for a period of 72 hours then harvested for cell cycle analysis (Figure 35A-B). Importantly, we observed that FOXM1 wild-type promoted cell cycle progression through the G2/M checkpoint, as shown by the increase in G1 phase and decrease in G2/M phase compared to the empty vector control (Figure 35B). Conversely, the FOXM1 DBD mutant compounded the Cyclin E1-mediated G2/M arrest as shown by the increased G2/M cells (Figure 35B). Notably, these data suggest that FOXM1 functions downstream of Cyclin E1 in a cooperative fashion to promote cell cycle progression in cells experiencing oncogene-induced DNA replication stress, allowing premature mitotic entry with damaged DNA, promoting genomic instability.

FOXM1 transcriptional activity is enhanced by Cyclin E1 in FTE cells

We previously observed that FOXM1 is expressed downstream of Cyclin E1 in FTE cells (Figure 19G-H). Furthermore, FOXM1 and many of its targets were shown to be overexpressed in our RNA-seq analyses of FTE cells expressing Cyclin E1, and GSEA showed the FOXM1 pathway to be a significantly enriched gene expression signature (Figure 30A-B). Therefore, based on previous reports showing that Cyclin E1-CDK2 phosphorylates FOXM1, increasing its transcriptional activity (186-188), we hypothesized that FOXM1 would be more transcriptionally active in the FTE cells when co-expressed with Cyclin E1. To test this, we engineered FTE cells for doxycycline inducible expression of Cyclin E1 and vector control, or Cyclin E1 and FOXM1 wild-type. We grew cells in the presence of doxycycline for 48 hours then proceeded with RNA-seq analysis to determine if Cyclin E1 enhances FOXM1 transcriptional activity (Figure 36A-B). We then compared the top differentially expressed genes that clustered together in the heat map to determine if there was visual difference in overall transcriptional activity between FTE cells expressing FOXM1 or Cyclin E1 alone, or FOXM1 and Cyclin E1 together. We observed that FTE cells expressing both FOXM1 and Cyclin E1 have a striking gene expression pattern showing increased transcriptional activity compared to FOXM1 or Cyclin E1 alone (Figure 37A). To validate these findings, we performed RT-qPCR to measure the expression of FOXM1 canonical target genes. We observed that FTE cells expressing both wild-type FOXM1 and Cyclin E1 showed the highest expression for FOXM1 target genes, but the expression of Cyclin E1 with FOXM1 DBD mutant did not show a difference when compared to Cyclin E1 alone (Figure 37B-D). These data and the cell cycle data suggest that Cyclin E1 increases the transcriptional activity of FOXM1, thus promoting increased cell cycle progression.

Dual FOXM1 and Cyclin E1 expression induces an enriched genomic instability gene expression signature in FTE cells

FOXM1 expression has been linked to genomic instability by its inclusion in the CIN25/CIN70 expression signature (37). However, the mechanistic relationship between FOXM1 and genomic instability is not known. Furthermore, the CIN70 expression signature contains many of the FOXM1 target genes and has been used as a readout for genomic instability. Therefore, we hypothesized the FTE cells expressing FOXM1 may show an enriched gene expression signature for CIN70, which is an extended version of the CIN25 gene expression signature. To test this, we generated a GSEA CIN70 geneset and performed GSEA analysis with the RNA-seq data from FTE cells expressing FOXM1. We observed a significantly enriched CIN70 gene expression signature when FOXM1 was expressed in FTE cells (Figure 38A). Our data show that Cyclin E1 expression in FTE cells induced DNA replication stress, DNA damage and showed an enriched FOXM1 pathway gene expression signature. We next performed GSEA analysis to determine if FTE cells expressing Cyclin E1 have an enriched CIN70 gene expression signature. We observed that Cyclin E1 expression showed a significantly enriched CIN70 gene expression, and the enrichment was greater than FOXM1 (Figure 38B). We have shown that Cyclin E1 enhances the transcriptional activity of FOXM1, thus promoting increased cell cycle progression. Therefore, we hypothesized that FTE cells expressing both FOXM1 and Cyclin E1 would have the greatest enrichment in the CIN70 gene expression signature. We performed GSEA analysis and observed that FTE cells expressing both FOXM1 and Cyclin E1 had greater enrichment in the CIN70 gene expression as compared to Cyclin E1 or FOXM1 alone (Figure 38C). We next generated a heatmap to compare the overall expression of the CIN70 genes among FTE cells expressing FOXM1, Cyclin E1 or both FOXM1 and Cyclin E1. Visually, FTE cells expressing both FOXM1 and Cyclin E1

showed the greatest expression of CIN70 genes followed by Cyclin E1 and FOXM1 (Figure 38D).

HGSC tumors with overexpression of both FOXM1 and Cyclin E1 show increased genomic instability

Our data show that Cyclin E1 induces FOXM1 expression and enhances its transcriptional activity, promoting cell cycle and genomic instability. This phenotype is stronger when FOXM1 is overexpressed together with Cyclin E1. To determine this relationship in HGSC, we compared the frequency of *FOXM1* and *CCNE1* copy number gains in TCGA HGSC to determine if they tend to co-exist. We found that FOXM1 and CCNE1 copy number gain and amplification have a highly significant tendency to co-occur in HGSC (Figure 39A). We then tested if the co-occurring copy number gain contributed to increased FOXM1 and Cyclin E1 protein expression. We found that HGSC tumors with both *FOXM1* and *Cyclin E1* copy number gain and amplification showed the highest level of FOXM1 and Cyclin E1 protein expression (Figure 39B) compared to either one alone. Furthermore, FOXM1 and Cyclin E1 protein expression showed a highly significant direct correlation thus providing additional support for cooperativity in HGSC (Figure 39C). FTE cells expressing both FOXM1 and Cyclin E1 showed increased enrichment in the CIN70 gene expression signature (Figure 38C-D). We hypothesized that HGSC tumors with both *FOXM1* and *CCNE1* copy number gain would have increased genomic instability as compared to either one alone. To test this, we compared the fraction of the copy number altered genome among HGSC tumors that had copy number amp/gain for both *FOXM1* and *CCNE1*, *FOXM1* or *CCNE1* alone, or neither. In agreement with the GSEA analysis for CIN70 enrichment in FTE cells, we found that HGSC tumors with both *FOXM1* and *CCNE1* copy number increase had a significantly higher level of genomic instability,

followed by Cyclin E1 alone then FOXM1 alone and neither (Figure 39D). Collectively, these data suggest that FOXM1 and Cyclin E1 may cooperate to promote genomic instability in HGSC.

Summary

In this study we compared the expression of FOXM1 and markers of genomic instability and DNA replication stress. We found that FOXM1 expression correlates with genomic instability and DNA replication stress markers, thus providing a mechanism link between FOXM1 and genomic instability. We next overexpressed FOXM1 in fallopian tube cells and found increased expression of P-CHK1, a marker of DNA replication stress. Furthermore, FOXM1 expression in FTE cells resulted in increased DNA damage measured with γ-H2AX expression and Comet assays. Cell cycle analysis revealed a phenotype that suggested cell cycle progression, not DNA replication stress. However, the expression of the FOXM1 DBD mutant showed a cell cycle profile indicative of DNA replication stress. Therefore, we next performed DNA fiber analysis in fallopian tube engineered for doxycycline inducible expression of FOXM1 wildtype and DBD mutant, and Cyclin E1 to characterize the DNA replication dynamics. We unexpectedly observed that FOXM1 expression in FTE cells increased fork rate and origin firing, but even more surprising, the FOXM1 DBD mutant decreased fork rate. To determine how FOXM1 may increase fork rate, we performed RNA-seq analysis to identify gene expression signatures contributing to this phenotype. We found that FOXM1 showed enriched gene expression for canonical FOXM1 target genes, specifically that promote G2-M progression and mitosis, but we did identify enriched genesets for DNA replication or chromatin modification. FOXM1 has recently been reported to interact with proteins involved in DNA

replication, suggesting the increased fork rate and origin firing that we observed might be independent of FOXM1's canonical role as a transcription factor. We tested if FOXM1 interacted with proteins involved in DNA replication initiation and found that it not only interacted with these proteins, but it also interacted with other chromatin modifying proteins, DNA methyltransferases.

RNA-seq analysis revealed that the FOXM1 pathway is activated downstream of Cyclin E1 overexpression in FTE cells. Cyclin E1 expression showed a strong DNA replication stress phenotype and increased DNA damage. Taken together, this suggests that FOXM1 might play dual oncogenic roles downstream of Cyclin E1: 1) to promote DNA fork movement; and 2) to promote cell cycle progression and genomic instability. We found that co-expression of FOXM1 with Cyclin E1 partially rescued the cell cycle abrogation but both FOXM1 and Cyclin E1 expression promote DNA damage. These findings suggest that FOXM1 promotes genomic instability downstream of Cyclin E1 by promoting mitotic entry. In support, we found that co-expression of FOXM1 and Cyclin E1 produced a gene expression signature that had a significant overlap with the CIN70 gene expression signature. In agreement, TCGA HGSC tumors with copy number gain for both FOXM1 and CCNE1 showed increased genomic instability.

Figures

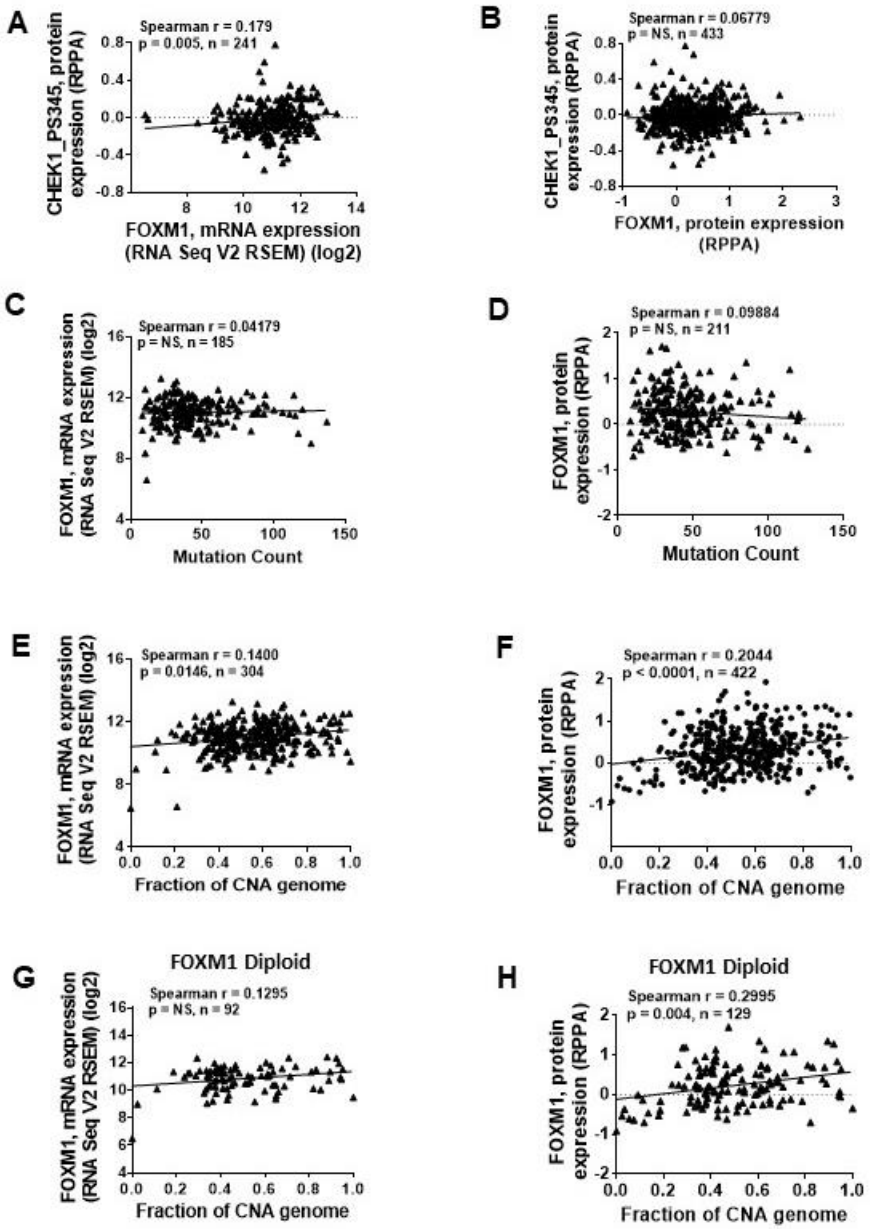
A
Spearman r = 0.179
p = 0.005, n = 241
CHEK1_PS345, protein expression (RPPA)
FOXM1, mRNA expression (RNA Seq V2 RSEM) (log2)
B
Spearman r = 0.06779
p = NS, n = 433
CHEK1_PS345, protein expression (RPPA)
FOXM1, protein expression (RPPA)
C
Spearman r = 0.04179
p = NS, n = 185
FOXM1, mRNA expression (RNA Seq V2 RSEM) (log2)
Mutation Count
D
Spearman r = 0.09884
p = NS, n = 211
FOXM1, protein expression (RPPA)
Mutation Count
E
Spearman r = 0.1400
p = 0.0146, n = 304
FOXM1, mRNA expression (RNA Seq V2 RSEM) (log2)
Fraction of CNA genome
F
Spearman r = 0.2044
p < 0.0001, n = 422
FOXM1, protein expression (RPPA)
Fraction of CNA genome
G
FOXM1 Diploid
Spearman r = 0.1295
p = NS, n = 92
FOXM1, mRNA expression (RNA Seq V2 RSEM) (log2)
Fraction of CNA genome
H
FOXM1 Diploid
Spearman r = 0.2995
p = 0.004, n = 129
FOXM1, protein expression (RPPA)
Fraction of CNA genome

Figure 22.

Figure 22. FOXM1 relationship with DNA replication stress and genomic instability in TCGA HGSC. A-B. FOXM1 **A.** mRNA (RNA-seq) and **B.** protein (RPPA) correlation with P-CHK1-S345 protein (RPPA) in TCGA HGSC. **C-D.** FOXM1 **C.** mRNA (RNA-seq). and **D.** protein (RPPA) correlation with mutation burden in TCGA HGSC. **E-F.** FOXM1. **E.** mRNA (RNA-seq) and **F.** protein (RPPA) correlation with fraction of the copy number altered genome in TCGA HGSC. **G-H.** FOXM1 **G.** mRNA (RNA-seq) and **H.** protein (RPPA) correlation with fraction of the copy number altered genome in TCGA HGSC *FOXM1* diploid samples.

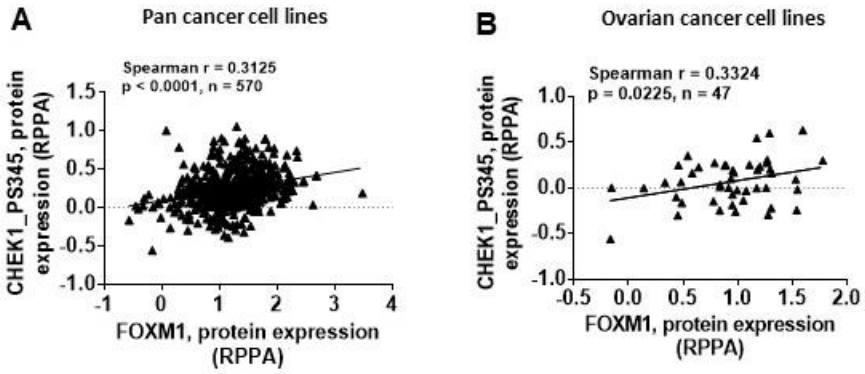

Figure 23. FOXM1 relationship with markers of DNA replication stress in CCLE pan-cancer and ovarian cancer cell lines. A. FOXM1 protein expression (RPPA) correlation with P-CHK1-S345 protein expression (RPPA) in CCLE pan-cancer cell lines. **B.** FOXM1 protein expression (RPPA) correlation with P-CHK1-S345 protein expression (RPPA) in CCLE ovarian cancer cell lines.

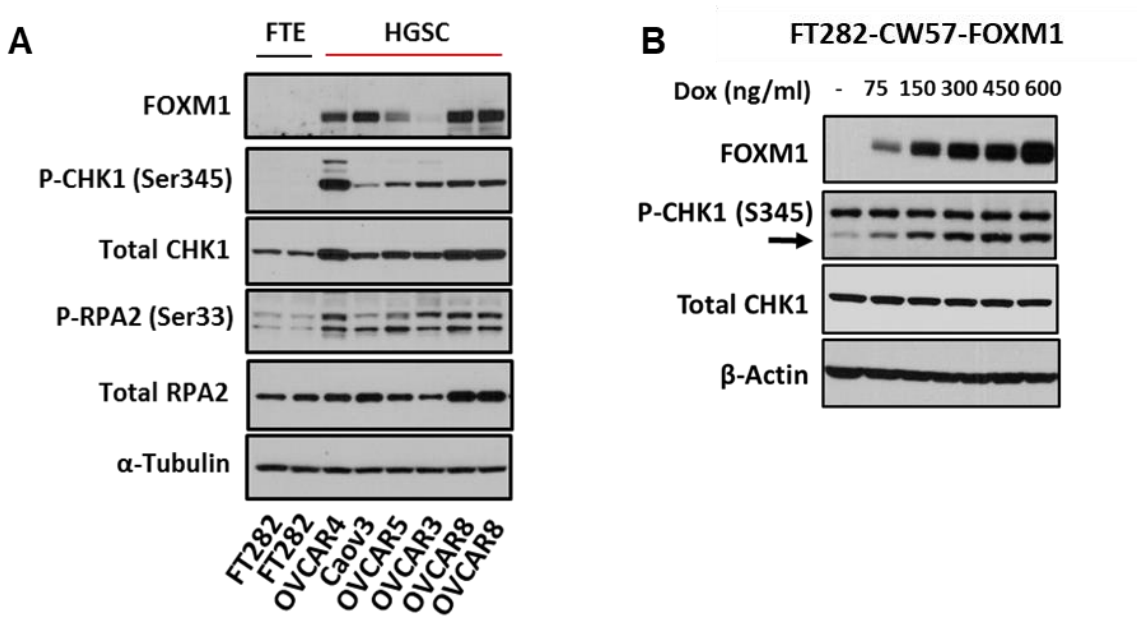

Figure 24. FOXM1 expression correlates with DNA replication stress markers in FTE and HGSC cells. A. Western blot analysis of canonical markers of DNA replication stress among a panel of HGSC cells compared to FTE cells. **B.** Western blot analysis of P-CHK1-S345 for FTE cells with increasing FOXM1 expression.

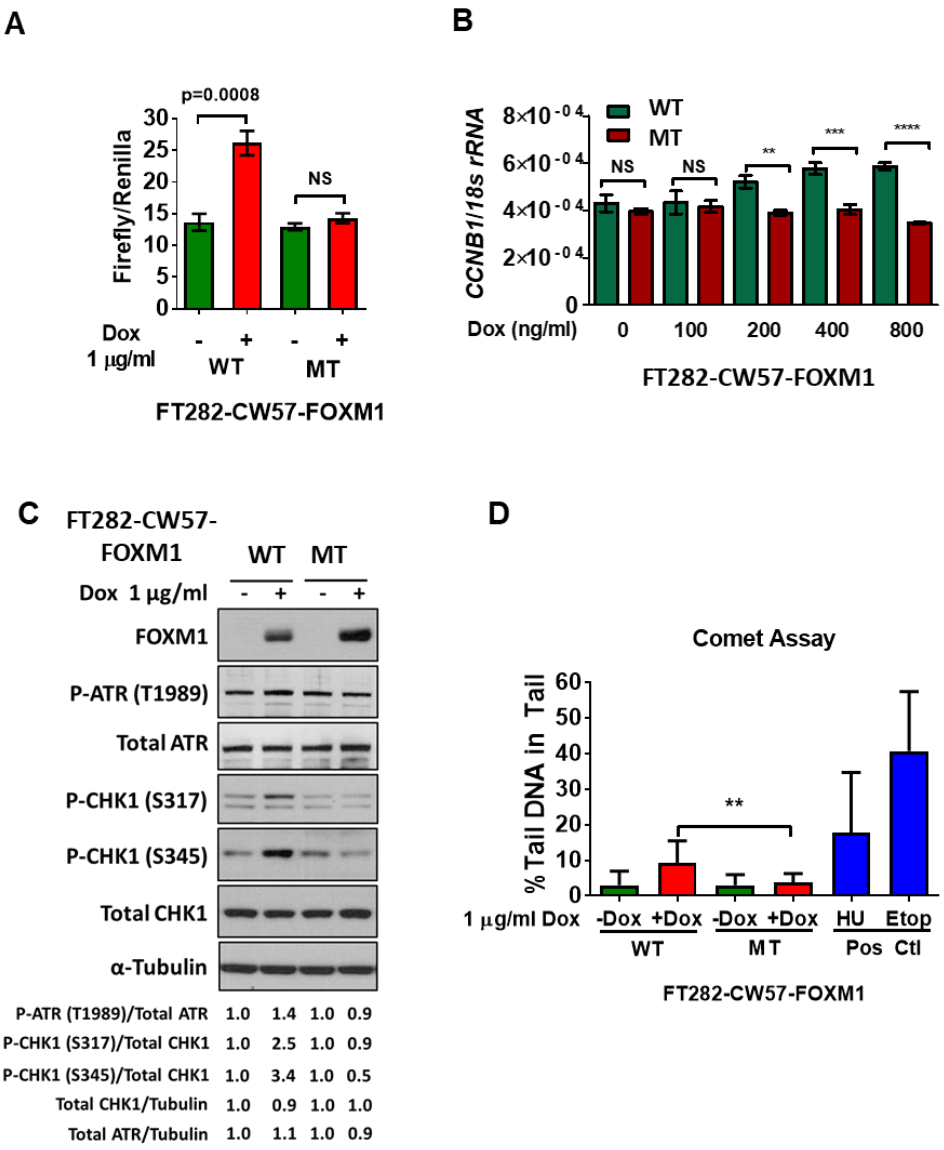

Figure 25. FOXM1 transcriptional activity is required for DNA replication stress and DNA damage in FTE cells. A. 6X FOXM1 reporter activity with FTE cells expressing FOXM1 wild-type (WT) or FOXM1 DBD mutant (MT). **B.** *CCNB1* mRNA expression measured by RT-qPCR for FTE cells expressing FOXM1 wild-type (WT) or FOXM1 DBD mutant (MT). **C.** Western blot analysis of canonical DNA replication stress markers for FTE cells expressing FOXM1 wild-type (WT) or FOXM1 DBD mutant (MT). **D.** Comet assay comparing percent DNA in tail for FTE cells expressing FOXM1 wild-type (WT) or FOXM1 DBD mutant (MT)**.** t-test *P* value is shown. *P* value designation: **** < 0.0001, *** < 0.001, ** < 0.01, * < 0.05.

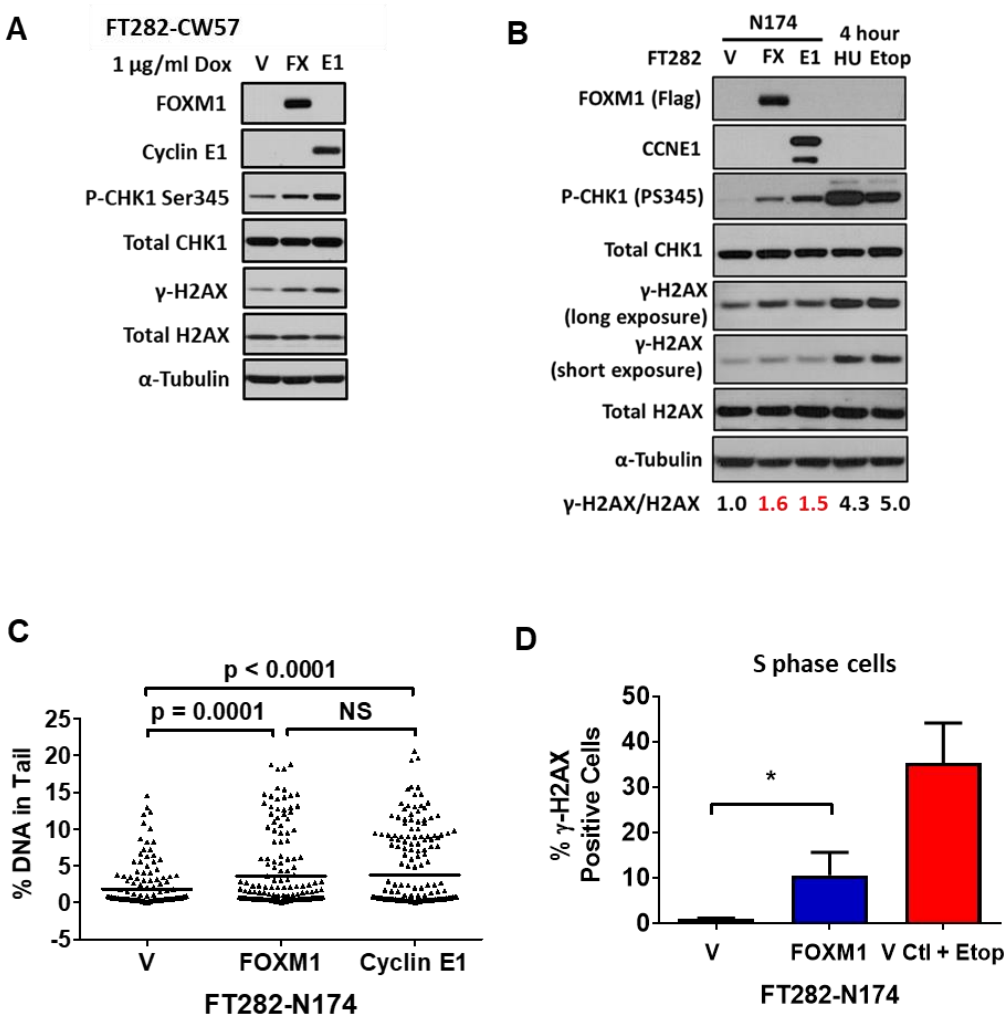

Figure 26. FOXM1 promotes DNA replication stress and DNA damage in FTE cells. **A.** Western blot analysis for markers of DNA damage and replication stress in FTE cells engineered for doxycycline inducible V control, FOXM1 and Cyclin E1 expression and grown for 72 hours in presence of 1 µg/ml of doxycycline. **B.** Western blot analysis for markers of DNA damage and replication stress with FTE cells engineered for constitutive expression of V control, FOXM1 and Cyclin E1. 2 mM Hydroxyurea (HU) and 20 µM etoposide were used as positive controls to induce DNA replication stress and DNA damage. **C.** Comet Analysis for cells in panel B. **D.** FACS analysis of γ-H2AX positivity in S phase for FTE cells engineered for constitutive expression of V and FOXM1. 20 µM etoposide was used as positive control to induce DNA damage. t-test *P* value is shown. *P* * < 0.05.

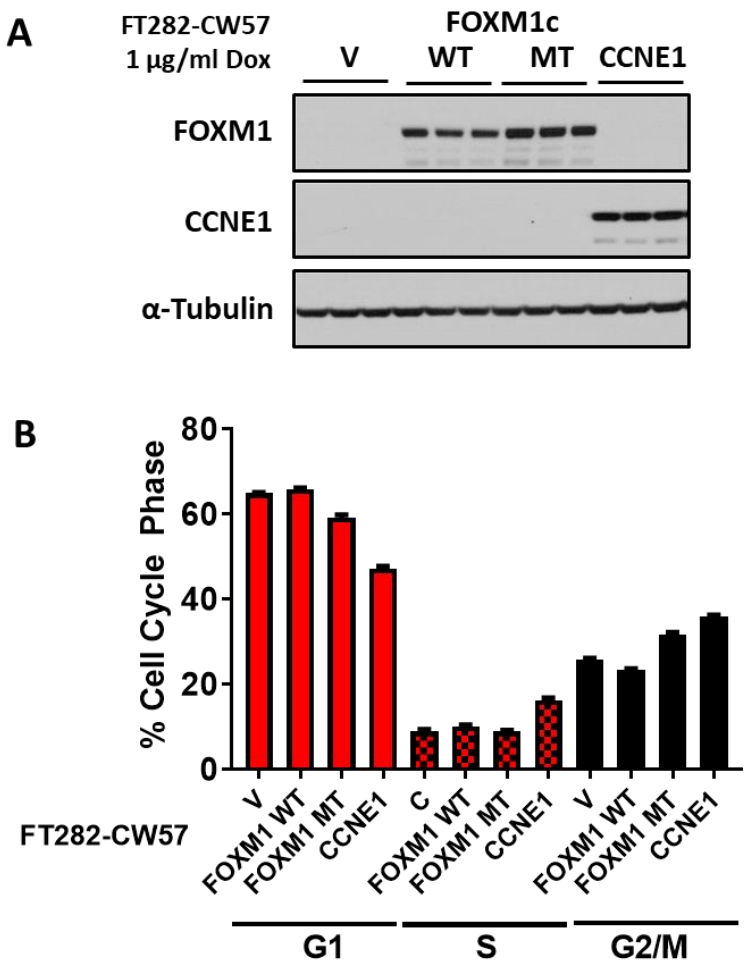

Figure 27. Cell cycle analysis of FTE cells expressing FOXM1 or Cyclin E1. A. Western blot analysis of FTE cells engineered for inducible expression of V, FOXM1 wild-type (WT), FOXM1 DBD mutant (MT), and Cyclin E1, and grown in the presence of doxycycline for 72 hours. **B.** Cell cycle analysis of FTE cells engineered for inducible expression of V, FOXM1 wild-type (WT), FOXM1 DBD mutant (MT), and Cyclin E1, and grown in the presence of doxycycline for 72 hours.

A

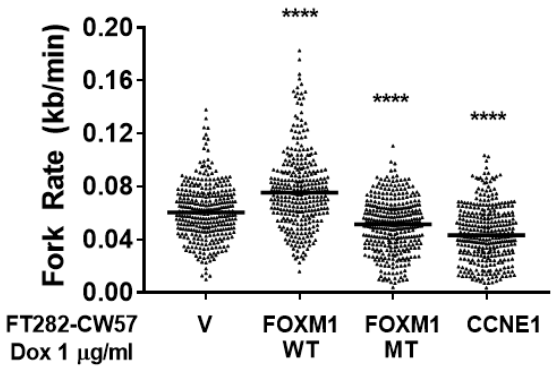

B

Fork Rate (kb/min)				
282-57	V	FOXM1 WT	FOXM1 MT	CCNE1
N	337	328	360	345
Median	0.060	0.075	0.051	0.043

C

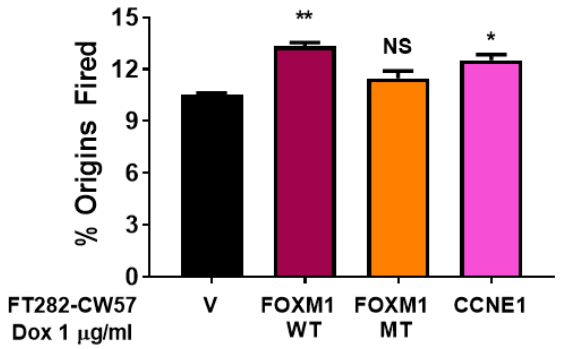

Figure 28. DNA fiber analysis in FTE cells. A. Fork velocity for inducible FTE cells expressing V control, FOXM1 wild-type (WT), FOXM1 DBD mutant (MT) or Cyclin E1 grown in the presence of doxycycline for 72 hours. Data represents a composite of two independent experiments. Median lines shown for all samples. **B.** The median fork velocity for the above data. **C.** Origin firing for inducible FTE cells expressing V control, FOXM1 wild-type (WT), FOXM1 DBD mutant (MT) or Cyclin E1 grown in the presence of doxycycline for 72 hours. Data represents the average of two experiments with at least 150 fibers analyzed for each group. P value designation: **** < 0.0001, *** < 0.001, ** < 0.01, * < 0.05.

A

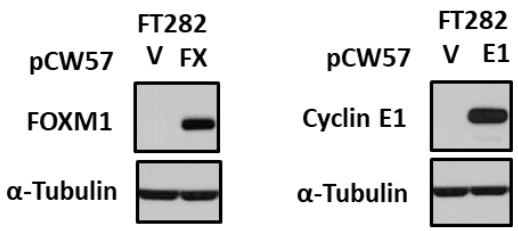

B

HiSeq 2500 DNA Analyzer (Illumina)
Triplicate replicates with 75 bp single reads

Sample name	Means reads ± SD (millions)
FT282-57-V	20.2 ± 2.9
FT282-57-FOXM1	20.1 ± 1.2
FT282-57-CCNE1	21.5 ± 2.3

Figure 29. RNA-sequencing with FTE cells expressing V control, FOXM1 or CCNE1. Inducible FTE cells expressing V control, FOXM1, or CCNE1 were grown in the presence doxycycline for 48 hours and cells were harvested for RNA or protein. Sample were prepared in triplicate for each group. **A.** Western blot analysis of FOXM1 and CCNE1 protein expression. **B.** RNA sequencing performance characteristics.

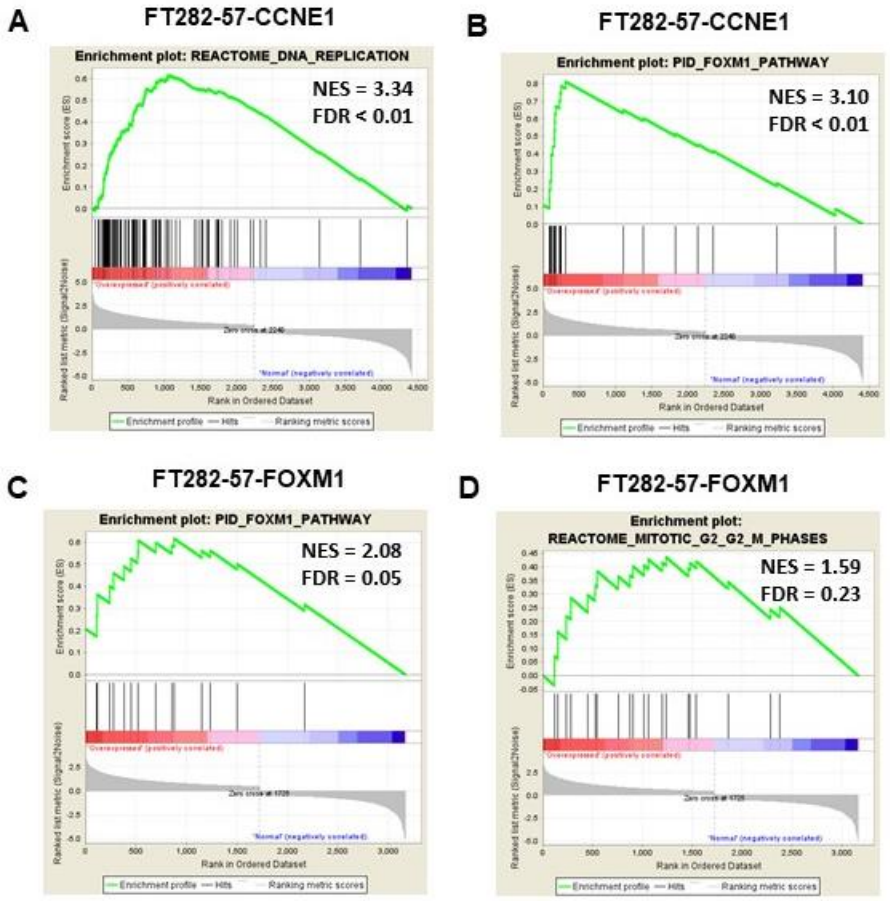

Figure 30. FOXM1 and Cyclin E1 enriched pathway signatures. A-B. GSEA analysis of the top two hallmark pathways for FTE cells expressing CCNE1. **A.** DNA replication and **B.** FOXM1 pathway. **C-D.** GSEA analysis of the top two hallmark pathways for FTE cells expressing FOXM1. **C.** FOXM1 pathway and **D.** G, G2/M phases. Enrichment as a function of FTE cells expressing FOXM1 or CCNE1 using RNA-seq expression data. Normalized enrichment score (NES), and false discovery rate q values (FDR) are shown.

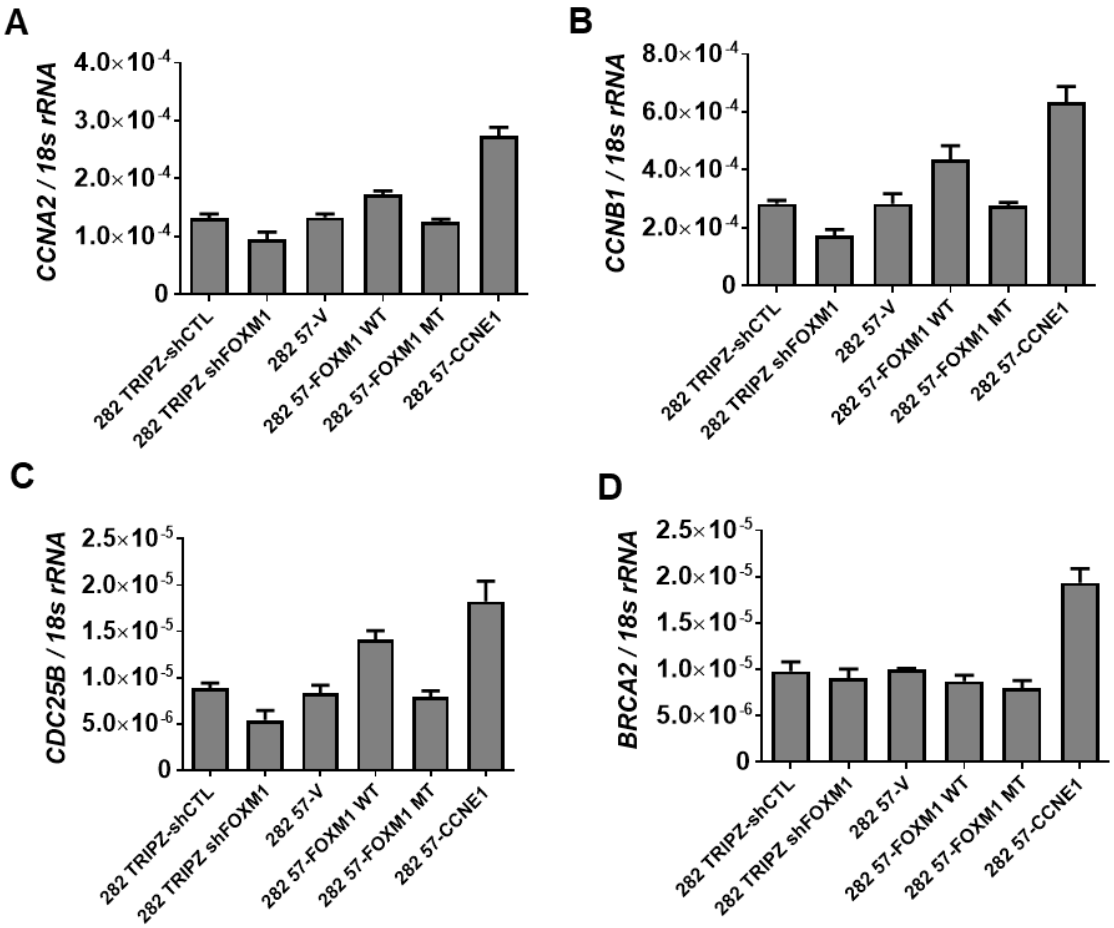

Figure 31. Validation of top differentially expressed genes from the RNA-seq analysis for FTE cells expressing FOXM1 compared to FOXM1 knockdown and CCNE1 expression. A-D. A. *CCNA2* **B.** *CCNB1* **C.** *CDC25B* and **D.** *BRCA2* mRNA expression measured by RT-qPCR from FTE cells expressing control or FOXM1 targeting shRNA, empty vector, FOXM1 wild-type (WT), FOXM1 DBD mutant (MT) or Cyclin E1. *BRCA2* mRNA did not show differential expression in the RNA-seq analysis, but instead was included used as a negative control.

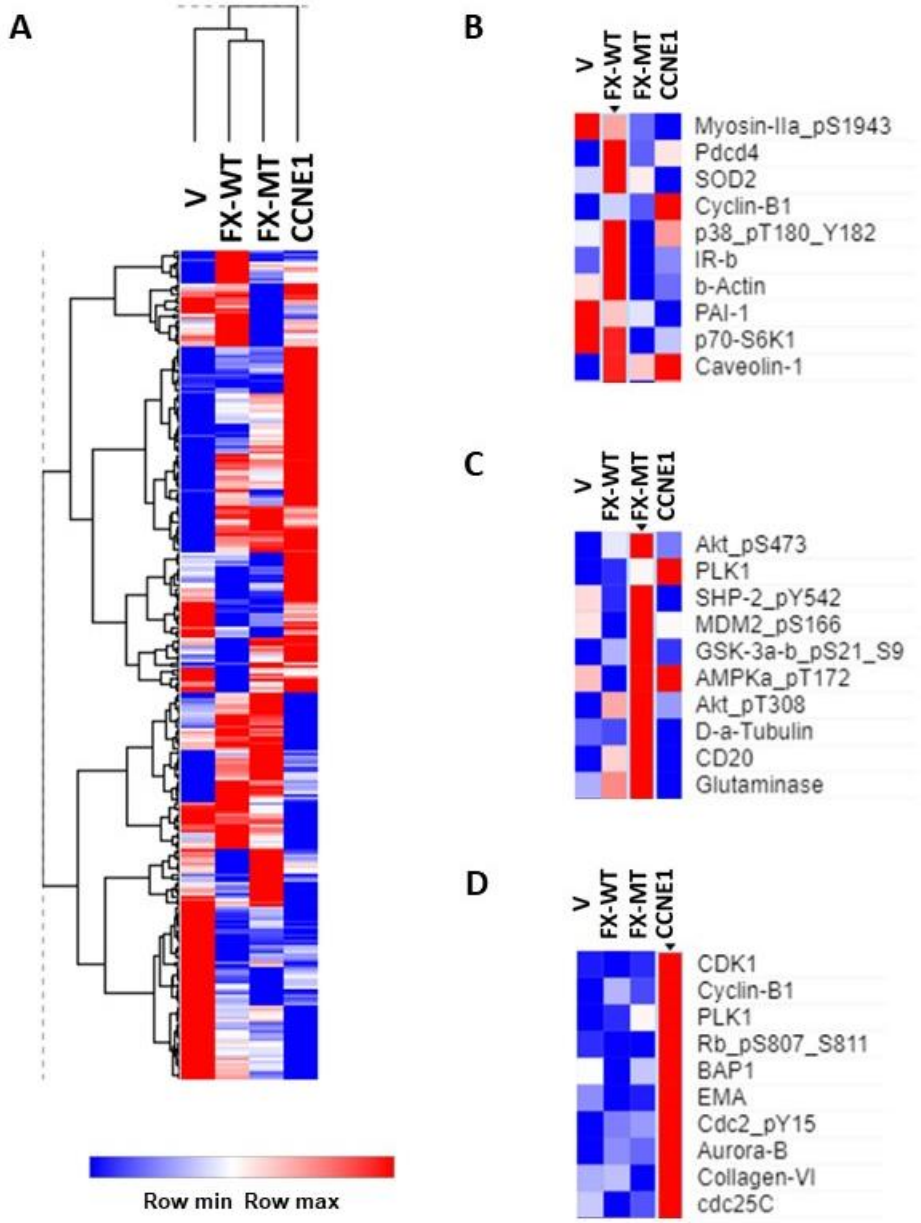

Figure 32. Heat-maps of RPPA data for FTE cells expressing V, FOXM1 wild-type, FOXM1 DBD mutant, and Cyclin E1. A. Heat map showing unsupervised hierarchical clustering of log2 normalized median centered RPPA from FTE cells grown in the presence of 1 µg/ml doxycycline for 72 hours. Samples were performed in triplicate and averaged. **B-D.** Top 10 proteins for FOXM1-wild-type (WT), FOXM1-DBD-mutant (MT) and Cyclin E1, respectively.

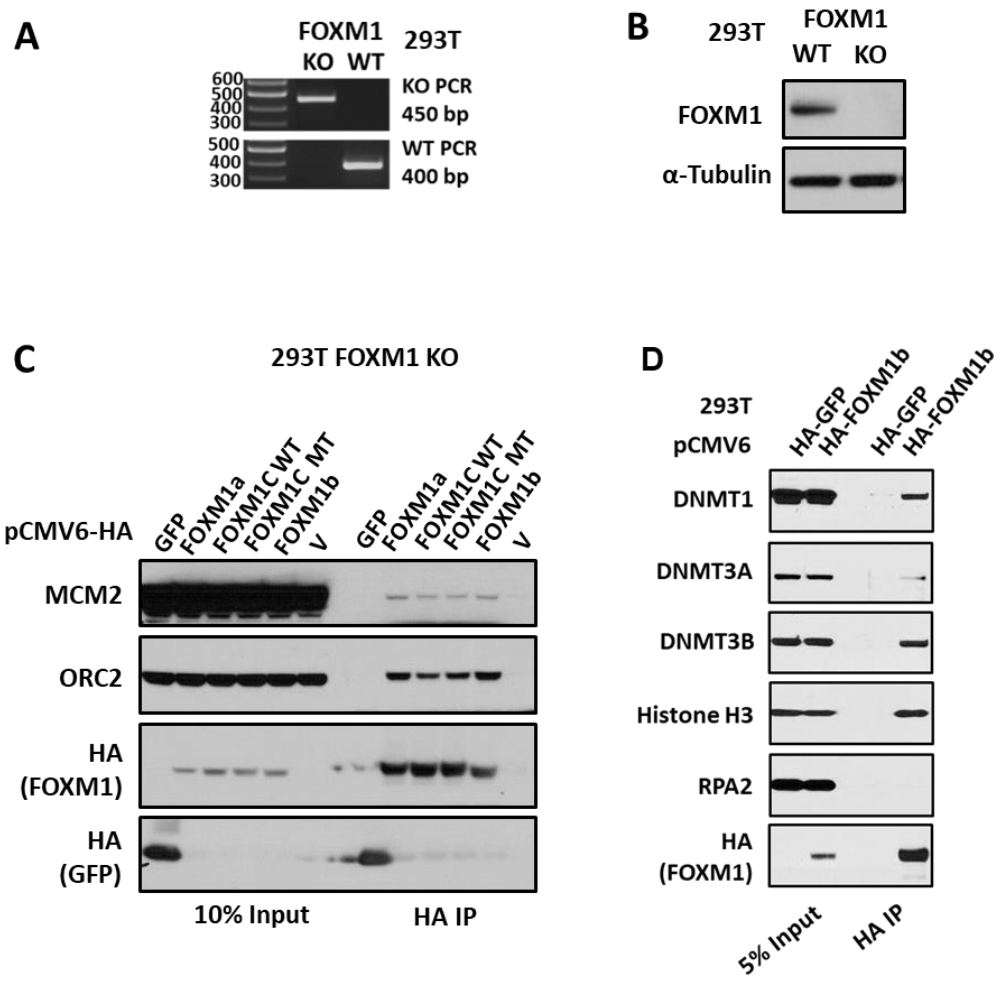

Figure 33. FOXM1 interacts with protein involved in DNA replication and chromatin modification in 293T cells. A-B. 293T cells with CRISPR-mediated homozygous deletion of *FOXM1* using guide RNAs that targeted near the start and stop codons. Homozygous deletion of *FOXM1* was confirmed by **A.** PCR genotype and **B.** Western blot analysis. **C.** 293T *FOXM1* knockout cells were transfected with empty vector, vector expressing HA tagged GFP, FOXM1 isoforms a, b, c or FOXM1c DBD mutant (MT). Protein was harvested 24 hours post transfection for co-IP and Western blot analysis. **D.** Parental 293T cells were transfected with HA tagged GFP or FOXM1b. Protein was harvested 24 hours post transfection for co-IP and Western blot analysis.

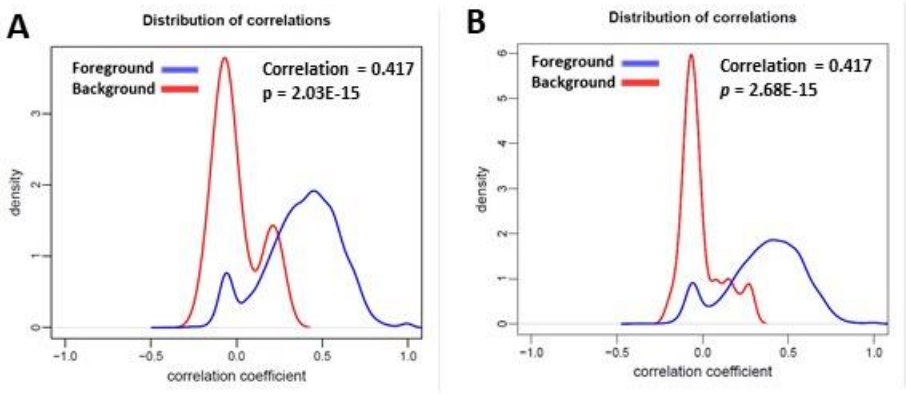

Figure 34. Genome-wide correlation of FOXM1 and ORC2 DNA binding. A-B. StereoGene plots showing correlation between FOXM1 and ORC2 DNA binding across the genome using K562 ChIP-seq data retrieved from NCBI GEO. The x axis shows the correlation value and y axis shows the density of genomic regions. The blue line represents the foreground correlation or correlation between FOXM1 and ORC2 binding the same genomic location. The red line represents background shuffling or correlation of random genomic windows. The p value represents the difference between the foreground and background distribution. ORC2 ChIP-seq vs FOXM1 ChIP-seq **A.** replicate 1 and **B.** replicate 2.

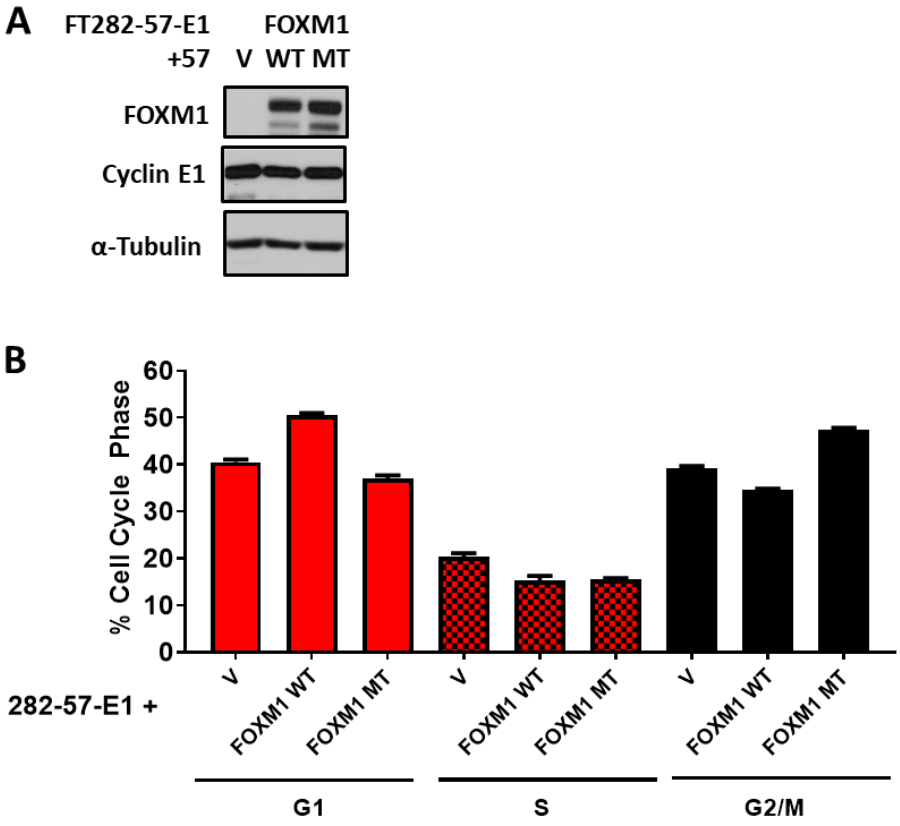

Figure 35. Cell cycle analysis of FTE cells expressing Cyclin E1 and/or FOXM1 wild-type and FOXM1 DBD mutant. A-B. Inducible FTE cells expressing CCNE1 and empty vector control, CCNE1 and FOXM1 wild-type (WT) or CCNE1 and FOXM1 DBD mutant (MT) were grown in the presence of doxycycline for 72 hours before harvesting cells for protein or for cell cycle. **A.** Western blot analysis. **B.** Cell Cycle analysis. Data was performed in duplicate replicates and repeated three times.

A

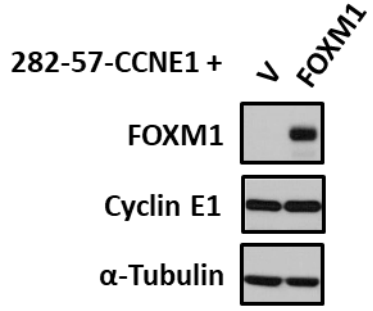

B

HiSeq 2500 DNA Analyzer (Illumina)
Triplicate replicates with 75 bp single reads

Sample name	Means reads ± SD (millions)
FT282-57-CCNE1-V	11.8 ± 0.9
FT282-57-CCNE1+FOXM1	12.9 ± 0.9

Figure 36. RNA-sequencing with FTE cells expressing CCNE1 and V control or CCNE1 and FOXM1 wild-type. Inducible FTE cells expressing CCNE1 and V control or CCNE1 and FOXM1 were grown in the presence doxycycline for 48 hours and cells were harvested for RNA or protein. Sample were prepared in triplicate for each group. **A**. Western blot analysis of FOXM1 and CCNE1 protein expression. **B.** RNA sequencing performance characteristics.

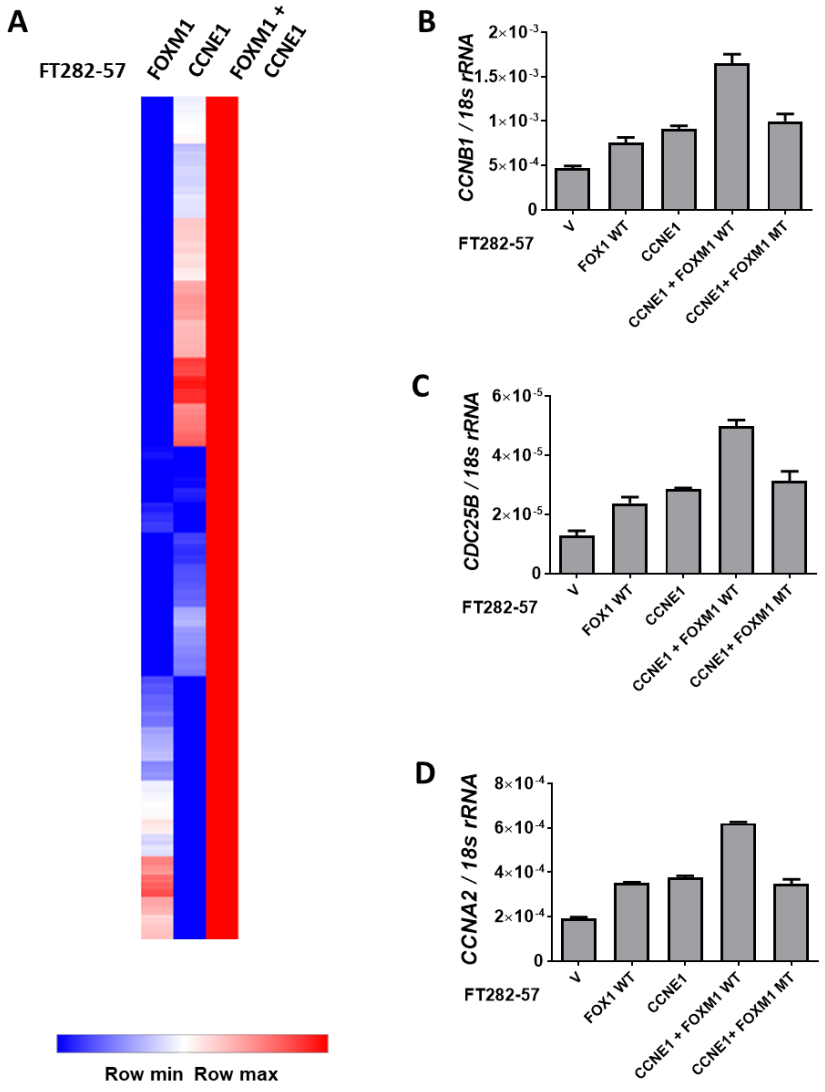

Figure 37. Cyclin E1 enhances FOXM1 transcriptional activity. A. Heat map shows 647 genes with significant upregulation in FTE cells expressing FOXM1, CCNE1, or FOXM1 and CCNE1. Heat map values represent log2 fold change from triplicate replicates normalized to v control. Heat map color is normalized to the row. **B**. Validation of top differentially expressed genes in the RNA-seq analysis **B-D. B.** *CCNB1* **C.** *CDC25B* and **D.** *CCNA2* mRNA expression measured by RT-qPCR with FTE cells expressing empty vector, FOXM1 wild-type, CCNE1 and FOXM1 wild-type (WT) or Cyclin E1 and FOXM1 DBD mutant (MT).

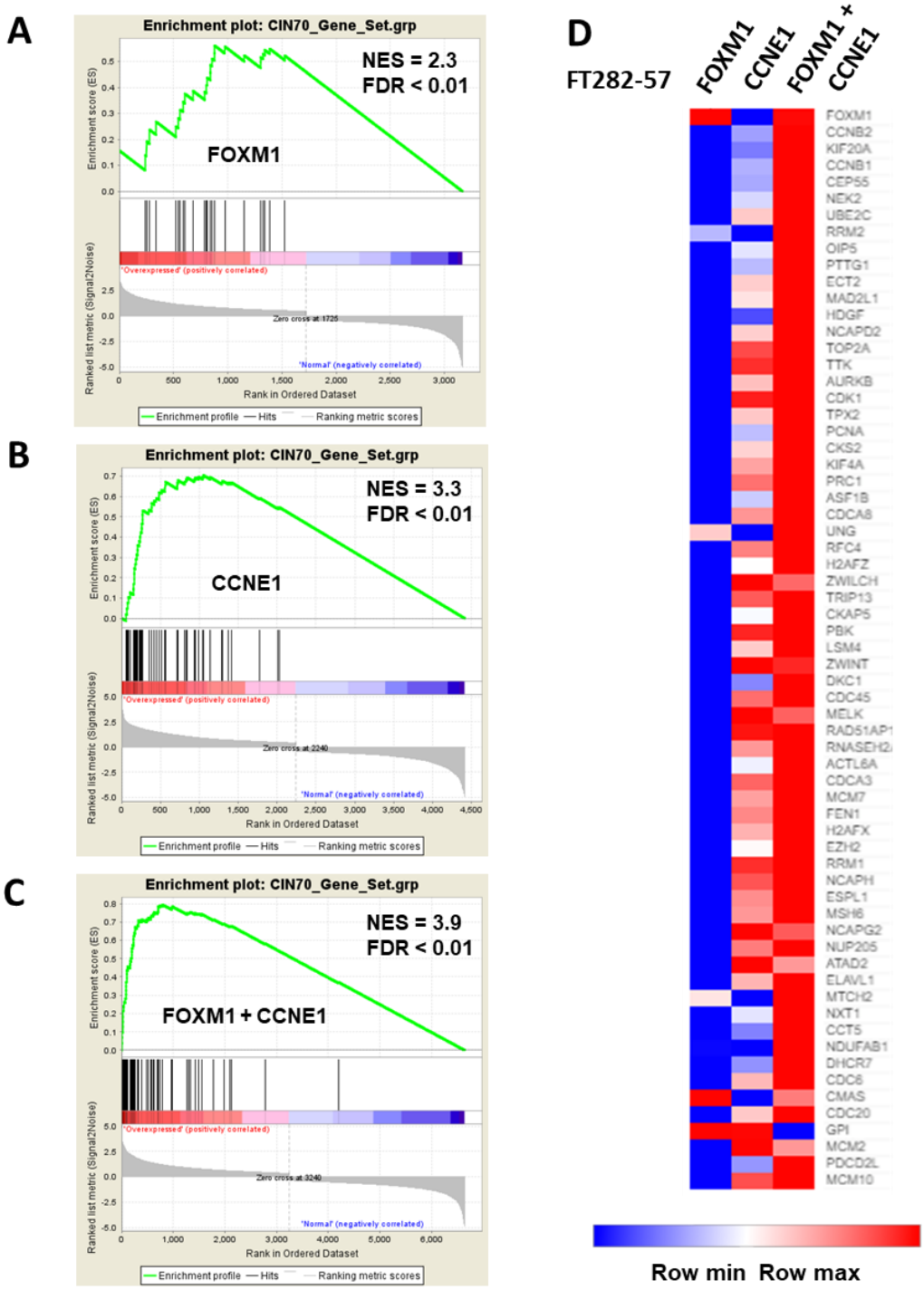
A
Enrichment plot: CIN70_Gene_Set.grp
NES = 2.3
FDR < 0.01
FOXM1
B
Enrichment plot: CIN70_Gene_Set.grp
NES = 3.3
FDR < 0.01
CCNE1
C
Enrichment plot: CIN70_Gene_Set.grp
NES = 3.9
FDR < 0.01
FOXM1 + CCNE1
Enrichment score (ES)
Ranked list metric (Signal2Noise)
'Overexpressed' (positively correlated)
'Normal' (negatively correlated)
Rank in Ordered Dataset
Enrichment profile
Hits
Ranking metric scores
D
FT282-57
FOXM1
CCNE1
FOXM1 + CCNE1
FOXM1
CCNB2
KIF20A
CCNB1
CEP55
NEK2
UBE2C
RRM2
OIP5
PTTG1
ECT2
MAD2L1
HDGF
NCAPD2
TOP2A
TTK
AURKB
CDK1
TPX2
PCNA
CKS2
KIF4A
PRC1
ASF1B
CDCA8
UNG
RFC4
H2AFZ
ZWILCH
TRIP13
CKAP5
PBK
LSM4
ZWINT
DKC1
CDC45
MELK
RAD51AP1
RNASEH2A
ACTL6A
CDCA3
MCM7
FEN1
H2AFX
EZH2
RRM1
NCAPH
ESPL1
MSH6
NCAPG2
NUP205
ATAD2
ELAVL1
MTCH2
NXT1
CCT5
NDUFAB1
DHCR7
CDC6
CMAS
CDC20
GPI
MCM2
PDCD2L
MCM10
Row min
Row max

Figure 38.

Figure 38. CIN70 enriched gene signatures in FTE cells expressing FOXM1 and CCNE1. A-C. GSEA analysis of CIN70 geneset with RNA sequencing expression data from FTE cells expressing **A.** FOXM1, **B.** CCNE1 or **C.** FOXM1 and CCNE1, normalized to FTE cells expressing V control. Normalized enrichment score (NES), and false discovery rate q values (FDR) are shown. **D.** Heat map for CIN70 genes comparing the overall expression among FTE cells expressing FOXM1, CCNE1, or FOXM1 and CCNE1. Heat map values represent log2 fold change from triplicate replicates normalized to vector control. Heat map color is normalized to the row.

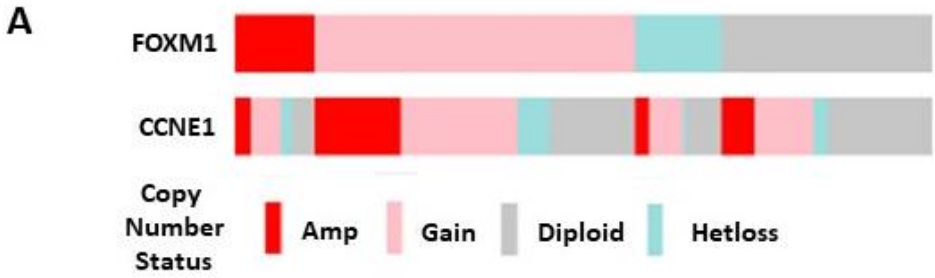

A	B	Neither	A Not B	B Not A	Both	Log Odds Ratio	p-Value	Tendency
CCNE1 AMP GAIN	FOXM1 AMP GAIN	130	117	126	206	0.597	<0.001	Co-occurrence

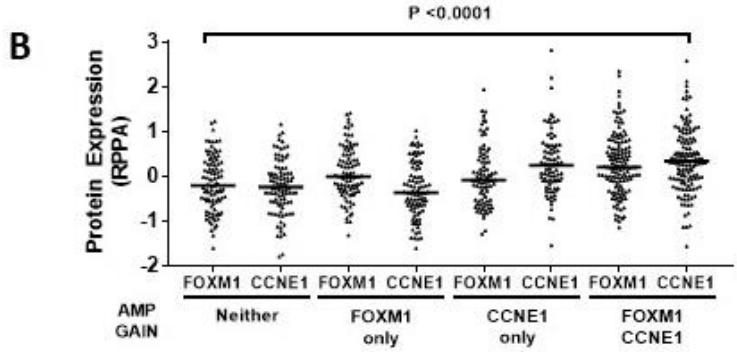

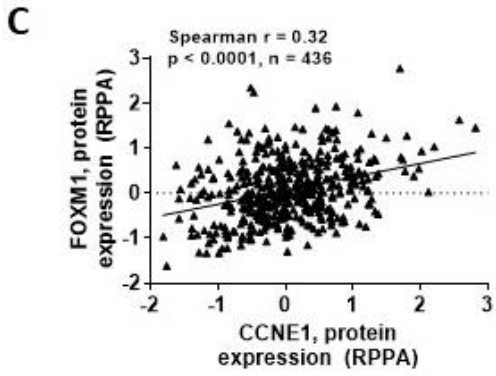

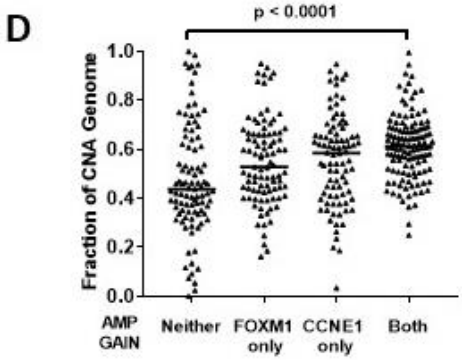

Figure 39.

Figure 39. Frequent *FOXM1* and *CCNE1* copy number gain and expression associate with genomic instability in HGSC. A. *FOXM1* and *CCNE1* number status in TCGA HGSC tissues. Log odds ratio for tumors with both *FOXM1* and *CCNE1* Amp/Gain vs F*OXM1* or *CCNE1* alone, or neither. **B.** FOXM1 and CCNE1 protein expression (RPPA) compared HGSC tumors with both *FOXM1* and *CCNE1* Amp/Gain, *FOXM1* Amp/Gain only, *CCNE1* Amp/Gain only or neither. The p value for ANOVA with post-test for linear trend is shown. Lines represent group medians. **D.** FOXM1 protein expression (RPPA) vs CCNE1 protein expression (RPPA) in TCGA HGSC tissues. **D.** Fraction of the copy number altered genome compared in HGSC tumors with both *FOXM1* and *CCNE1* Amp/Gain, *FOXM1* Amp/Gain only, *CCNE1* Amp/Gain only and neither. The p value for ANOVA with post-test for linear trend is shown. Lines represent group medians.

CHAPTER 5: FOXM1 AND RHNO1 BIDIRECTIONAL GENE PARTNERS PROMOTE SURVIVAL AND CHEMORESISTANCE IN HIGH-GRADE SEROUS OVARIAN CANCER

Introduction

Bidirectional gene partners make up approximately 10% of human genes and they often function in similar pathways such as cell cycle and DNA repair (117). *FOXM1* shares an intergenic space with *RHNO1*, a protein that interacts with the 9-1-1 checkpoint clamp to promote efficient ATR-CHK1 signaling in response to DNA replication perturbations and contributes to the homologous recombination DNA repair pathway (100). FOXM1 has a well-established role in cell cycle progression and proliferation but it has also been linked to DNA repair and drug resistance via its ability to transactivate genes involved in these phenotypes. However, our RNA-seq analysis of FTE cells engineered for FOXM1 overexpression did not show altered expression of genes involved in the DNA damage response. Interestingly, we observed that FOXM1 promotes increased DNA replication fork rate and interacts with proteins involved in DNA replication and chromatin modification, suggesting that FOXM1 might promote fork movement via protein-protein interactions. Furthermore, FOXM1 might promote fork progression in the presence of endogenous or exogenous DNA damage, thus promoting proliferation in the presence of damaged DNA. Together, considering our new findings for FOXM1 and the reported function of RHNO1, we hypothesized that FOXM1 may play cooperative roles with RHNO1 in cell survival and chemotherapy resistance in HGSC. The objective of this study was 1) to demonstrate that the intergenic space between *FOXM1* and *RHNO1* functions as a bidirectional promoter; 2) to determine the relationship in expression between these FOXM1 and RHNO1; and 3) to determine the functional contribution of *FOXM1* and

RHNO1 bidirectional gene partners to clonogenic survival, homologous recombination DNA repair, and chemoresistance in HGSC cells.

Results

Genomic arrangement of *FOXM1* and *RHNO1* bidirectional partners at 12p13.33

We previously showed that *FOXM1* is located at 12p13.33 and that this genomic region is frequently amplified in HGSC. This region contains 32 other genes (Table 5), so we performed analysis of the 12p13.33 region using UCSC Genome Browser and observed that *FOXM1* and *RHNO1* are positioned in a head-to-head orientation with a putative bidirectional promoter (Figure 40). This genomic configuration is observed in approximately 10% of the human genes and is a feature of bidirectional genes pairs which are frequently co-regulated and function in similar pathways (114,117,120). This suggested that *FOXM1* and *RHNO1* have a bidirectional promoter and may be co-regulated. The *FOXM1/RHNO1* promoter region contains a CpG island which is a feature of bidirectional promoters (Figure 40) (113,117,189). It was recently shown that bidirectional promoters are enriched with histone modifications H3K4me3, H3K9ac, H3K27ac, and H3K4me2 (118). Our analysis of ENCODE data revealed that transcriptionally active histone marks, including H3K27Ac and H3K4me3, are enriched for both *FOXM1* and *RHNO1*, showing bimodal peaks, suggesting the bidirectional promoter is active in both directions (Figure 40). In addition, the ENCODE data revealed the presence of an E2F1 ChIP-seq peak in this region, which is consistent with E2F1's known involvement in bidirectional promoter regulation and our previous studies of *FOXM1* (Figure 18-19) (81,190,191). These data suggest that *FOXM1* and *RHNO1* gene partners share an active bidirectional promoter and therefore may be co-expressed.

FOXM1 and *RHNO1* expression in normal and cancer tissues

Based on the genomic arrangement of *FOXM1* and *RHNO1* bidirectional gene partners, we hypothesized that their mRNA expressions would correlate in normal tissues and cancer types. We first analyzed RNA-seq datasets from RIKEN normal mouse tissues, GTEx normal human tissues, and TCGA pan-cancer tissues. We observed a highly significant correlation between *FOXM1* and *RHNO1* mRNA expression in all comparisons, showing this relationship is not restricted to normal or cancer tissues and is conserved in mammals (Figure 41A-C). We next performed correlation of *FOXM1* and *RHNO1* mRNA expression using the CCLE human pan-cancer cell line microarray dataset to validate the correlation we observed in tissue samples. In agreement, the CCLE human cancer cell lines showed a strong correlation between *FOXM1* and *RHNO1* mRNA expression, and similar to normal and cancer tissues (Figure 41D).

We next used the TOIL TCGA dataset to compare the levels of *FOXM1* and *RHNO1* mRNA expression in normal tissue versus primary, metastatic and recurrent pan-cancer tissues. We observed that *FOXM1* and *RHNO1* were overexpressed in primary, metastatic and recurrent tumor as compared to normal tissue (Figure 42A). Furthermore, we found that *FOXM1* expression was lower than *RHNO1* expression in normal tissues, but the inverse was true in tumor tissues (Figure 42A). To follow-up this observation, we used the TOIL TCGA GTEx dataset to compare the ratio of *FOXM1* and *RHNO1* mRNA expression in normal and tumor tissues. In agreement, we observed that the expression ratio was shifted toward *RHNO1* in normal tissues but toward *FOXM1* in tumor tissues (Figure 42B). Based on these data, we hypothesized that tumors have an increased proliferative index compared to normal tissue and FOXM1 is a proliferation associated transcription factor; therefore, this ratio shift could be related to a difference in proliferative

states. To test this, we normalized *FOXM1* and *RHNO1* mRNA expression to *Ki67*, a canonical marker of proliferation, in TCGA normal and tumor tissues. In agreement with our hypothesis, we observed that normalizing the *FOXM1* and *RHNO1* mRNA expression to *Ki67* resulted in similar expression ratios in normal and tumor tissues (Figure 42B). These data suggest that increased proliferation, as indicated by Ki67 expression, has a greater influence on *FOXM1* expression than *RHNO1* expression.

FOXM1 **and** ***RHNO1*** **expression in single cells from normal and cancer tissues**

Our analysis of *FOXM1* and *RHNO1* mRNA expression has been limited to the bulk RNA-sequencing data, which averages gene expression over a population of cells and masks potential heterogeneity in expression. Our data thus far and previous studies have shown bidirectional gene partners are frequently co-expressed (117,118,120); however, it remains unknown if this correlation exists within single cells. Therefore, measuring RNA expression at the single cell level would further the overall understanding of bidirectional gene partners and, more importantly, provide data to test potential cooperativity between FOXM1 and RHNO1. To test this, we analyzed publicly available single cell RNA-seq datasets consisting of cells isolated from normal mouse intestinal epithelium (Figure 43A), human melanoma (Figure 43B), and human high-grade serous tumors (Figure 43C) (147-149). We observed a significant correlation between *FOXM1* and *RHNO1* mRNA expression at a single cell level (Figure 43A-C). Furthermore, the correlation we observed among both bulk and single cell population was very similar (Spearman r = 0.4 to 0.6) (Figures 41 and 43). These data show that *FOXM1* and *RHNO1* are expressed at the same time within a cell, thus providing additional support for potential cooperativity.

DNA methylation analysis of the *FOXM1-RHNO1* bidirectional promoter

We observed that *FOXM1* and *RHNO1* expression were increased in cancer compared to normal, and *FOXM1* expression tended to show a more dramatic increase in tumor samples. The *FOXM1*/*RHNO1* promoter region contains a CpG island, and promoter methylation has been shown to regulate other bidirectional promoters (192). We hypothesized that differential methylation might contribute to these expression differences. To test this, we performed *in silico* analysis of publicly available Illumina Infinium HumanMethylation450 BeadChip Arrays performed on human cancer cell lines (the GDSC1000 collection), as well as human normal and cancer tissues (TCGA). We found the CpG island within the *FOXM1*/*RHNO1* bidirectional promoter was hypomethylated in all datasets (Figure 44). The 450K methylation array has a technical limitation on the number of CpGs interrogated at a gene promoter, specifically within a CpG island, so we next performed a comprehensive measurement of DNA methylation at the *FOXM1*/*RHNO1* bidirectional promoter using bisulfite clonal sequencing of normal and EOC tumor tissues. In agreement with the 450K data, we found the promoter was hypomethylated in both tissue (Figure 45). These data suggest that DNA methylation may not regulate the *FOXM1*/*RHNO1* bidirectional promoter, and that altered methylation does not contribute to the increased *FOXM1* and *RHNO1* mRNA expression in human cancer tissues (Figure 42A).

***FOXM1* and *RHNO1* copy number status and expression in HGSC**

We previously made comparisons in *FOXM1* and *RHNO1* expression across normal and pan-cancer tissue types and found a strong correlation, with increased expression in tumor tissues. We next validated these findings in HGSC and determined if copy number contributes to both *FOXM1* and *RHNO1* overexpression in HGSC. We first

analyzed the TOIL TCGA GTEx RNA-seq dataset to compare *FOXM1* and *RHNO1* expression in normal fallopian tube tissue and primary HGSC tumors. We observed that *FOXM1* and *RHNO1* were overexpressed and showed a strong correlation in their expression (Figure 46A-B). We confirmed this correlation by measuring *FOXM1* and *RHNO1* expression by RT-qPCR among a panel of HGSC tumors in our tumor bank (Figure 46C).

We previously showed that *FOXM1* is amplified in HGSC, contributing to its increased expression. We next determined the copy number status for both genes, to test as a contributing factor to their increased expression. We found that *FOXM1* and *RHNO1* copy number status was 100% concordant in HGSC tissues, suggesting that copy number might contribute to their frequent overexpression (Figure 46D). To test if *FOXM1* and *RHNO1* copy number status correlates with expression, we compared *FOXM1* and *RHNO1* mRNA and copy number in TCGA HGSC data. We observed a progressive increase in *FOXM1* and *RHNO1* expression with copy number status that was highly significant (Figure 46E). This suggests that copy number contributes to the frequent *FOXM1* and *RHNO1* expression in HGSC.

We next measured *FOXM1* and *RHNO1* mRNA in a panel of FTE, OSE, and HGSC cells by RT-qPCR. In agreement with our comparison of GTEx fallopian tube and TCGA HGSC tissues, we found that HGSC cells had significantly higher *FOXM1* and *RHNO1* mRNA expression than FTE and OSE cells (Figure 47A). We tested the relationship between *FOXM1* and *RHNO1* expression in CCLE HGSC cell lines and in agreement, *FOXM1* and *RHNO1* showed a strong correlation (Figure 47B), which we confirmed by RT-qPCR using a panel of HGSC cell lines (Figure 47C). Next, we determined whether *FOXM1* and *RHNO1* exhibit similar copy number status in CCLE HGSC cell lines. We observed 100% concordance in their copy number status (Figure

47D), which agrees with the TCGA HGSC data. Additionally, we observed a striking similarity in the frequency of *FOXM1* and *RHNO1* copy number in HGSC tissues and cell lines (Figures 45D and 47D), which agrees with previous reports showing that these HGSC cell lines are genomically similar to TCGA HGSC primary tumors (160). Further, we found that copy number correlates with increased *FOXM1* and *RHNO1* mRNA expression in cell lines (Figure 47E). To confirm these data, we compared *FOXM1* and *RHNO1* mRNA expression by RT-qPCR using normal FTE and OSE, and HGSC cell lines with differences in copy number status. We found that as *FOXM1* and *RHNO1* mRNA expression increases as copy number increases (Figure 48A). We then measured FOXM1 and RHNO1 protein expression in a subset of these cell lines and, in agreement, protein expression rises with copy number increases (Figure 48B). These data suggest that increased copy number contributes to FOXM1 and RHNO1 overexpression in HGSC.

FOXM1 and RHNO1 expression in single FTE and HGSC cells

We previously made comparisons in *FOXM1* and *RHNO1* expression across publicly available single cell RNA-seq datasets consisting of cells isolated from normal mouse intestinal epithelium, and human melanoma and high-grade serous tumors (147-149). We observed a significant correlation of *FOXM1* and *RHNO1* mRNA expression at a single cell level. To directly test this relationship in FTE and HGSC cells, we performed single cell RNA sequencing using immortalized fallopian tube epithelial cells and OVCAR8, an HGSC cell line. We compared *FOXM1* and *RHNO1* mRNA expression in FTE and OVCAR8 cells at the single cell level and observed a significant correlation (Figure 49A-B), which agrees with the correlation that we observed from measuring *FOXM1* and *RHNO1* mRNA by RT-qPCR from HGSC tissues and cell lines. Additionally, we compared *FOXM1* and *RHNO1* expression between FTE and HGSC cells and, as

expected, OVCAR8 cells had increased expression of both genes compared to FTE (Figure 49C). Together, our expression data provide strong support of co-regulation and potential cooperativity between FOXM1 and RHNO1.

FOXM1 and *RHNO1* promoter shows bidirectional activity

We observed that *FOXM1* and *RHNO1* mRNA showed a strong correlation across many cell and tissue types, in both bulk and single cell populations, including FTE and HGSC; thus, we next tested their relationship in promoter activity in FTE and HGSC cell models. We first performed 5' RACE to determine the transcriptional start sites for both genes, in order to experimentally define the bidirectional promoter, using immortalized FTE and two HGSC cell lines. We found that the transcriptional starts sites and intergenic distance are similar to those predicted by NCBI (Figure 50). Based on these data, we cloned the *FOXM1*/*RHNO1* bidirectional promoter into a reporter construct where FOXM1 drives the expression of Renilla luciferase and RHNO1 drives the expression of Firefly luciferase (Figure 50 and 51A). This reporter construct and control constructs were co-transfected into immortalized FTE and a panel of HGSC cells. We first compared the promoter activity in both directions and observed a direct correlation between *FOXM1* and RHNO1 promoter activities (Figure 51B). We next compared the promoter activity versus endogenous mRNA expression for each gene and found a direct relationship between the two, suggesting that the regulation of promoter activity contributes to the frequent co-expression of FOXM1 and RHNO1 (Figure 51C-D).

Thus far, we have measured activity of the FOXM1-RHNO1 bidirectional promoter using a synthetic reporter construct. The endogenous FOXM1-RHNO1 bidirectional promoter could be regulated differently, based on chromatin modifications and genomic architecture. To overcome this limitation, we used a CRISPR activation system to study

the endogenous bidirectional promoter, which uses a single guide RNA to recruit a catalytically dead Cas9 fused to a transcriptional activator, VP64 (193). We designed multiple guide RNAs to target within the bidirectional promoter and regions flanking it (Figure 52A). We introduced the CRISPR activation system into FTE cells, which have low FOXM1 and RHNO1 expression. Interestingly, we found that guide RNAs targeting outside the bidirectional promoter, regions upstream of the transcriptional start site for one gene and within the gene body for the other gene, induced the expression of the distal gene (Figure 52B). In contrast, the guide RNA targeting within the bidirectional promoter efficiently induced the expression of both *FOXM1* and *RHNO1* (Figure 52B). To complement these findings, we tested if a CRISPR-KRAB system could repress the bidirectional promoter in an HGSC cell line with high endogenous FOXM1 and RHNO1 expression. We selected the guide RNAs that targeted within the bidirectional promoter and showed the strongest induction in gene expression in FTE cells and cloned them into a CRISPR inhibition system, which uses a catalytically dead Cas9 fused to a transcriptional repressor, KRAB (194). We then introduced the CRISPR inhibition system into a high-grade serous cell line, OVCAR8, via lentiviral transduction. Importantly, we found that the guide RNA targeting within the bidirectional promoter efficiently repressed the expression of both *FOXM1* and *RHNO1* (Figure 52C). These data suggest that frequent FOXM1 and RHNO1 expression is driven, in large part, by bidirectional promoter regulation.

FOXM1 and RHNO1 promote HGSC cell clonogenic survival

An oncogenic role for FOXM1 has been reported in many different cancer types including ovarian cancer; however, the contribution of RHNO1 to cancer, and particularly the functional relationship between FOXM1 and RHNO1 has been unknown. We

hypothesized that FOXM1 and RHNO1 contribute to growth and survival of HGSC cells, as FOXM1 promotes cell cycle progression, and RHNO1 participates in the DNA replication stress response (5,100). To test this, we engineered OVCAR8 and CAOV3 for inducible FOXM1 and RHNO1 knockdown and performed clonogenic survival assays. In agreement, either FOXM1 or RHNO1 knockdown suppressed the clonogenic survival of OVCAR8 and CAOV3 HGSC cells (Figure 53A-C). To validate this finding, we conducted CRISPR-Cas9 knockouts of FOXM1 and RHNO1 in two different HGSC cell lines (OVCAR8 and CAOV3). In each case, we observed a significant diminishment in clonogenic survival as compared to the sgRNA control (Figure 54A-C). Furthermore, CRISPR-mediated knockout of FOXM1 or RHNO1 also increased the number of apoptotic cells, supporting a specific role for each protein in cell survival (Figure 54D).

FOXM1 and RHNO1 knockdown and knockout both reduced HGSC cell clonogenic survival. We next hypothesized that their combined loss may have a greater impact on HGSC clonogenic survival than either alone. To test this, we engineered OVCAR8 cells for dual FOXM1 and RHNO1 knockdown and performed clonogenic survival assays in comparison to the individual knockdowns. We found that dual FOXM1 and RHNO1 inhibition had significantly reduced clonogenicity as compared to either single knockdown (Figure 55A-C). These data suggest that FOXM1 and RHNO1 may cooperate to promote cell survival.

To understand how FOXM1 and RHNO1 loss contributes to decreased survival, we investigated the cell cycle dynamics following their loss. We observed that loss of FOXM1 showed an increase of G2/M cells, which agrees with earlier FTE cell cycle data for FOXM1 overexpression (Figure 56). RHNO1 loss showed an increase in S and G2 cells suggesting that its loss slowed progression through S phase (Figure 56). Importantly, FOXM1 and RHNO1 loss together showed a greater increase in G2/M than either one

alone (Figure 56). These data further support FOXM1 and RHNO1 cooperativity in the growth and survival of HGSC cells.

FOXM1 transcriptional activity regulates genes involved in cell cycle and the G2/M checkpoint

Unlike RHNO1, FOXM1 is linked to cell phenotypes through its function as a transcription factor. Therefore, to better understand how the loss of FOXM1 reduced cell survival, we performed RNA-seq analysis with OVCAR8 and CAOV3 cells following FOXM1 knockdown (Figure 57A). We performed GSEA analysis with the RNA-seq expression data, and both CAOV3 and OVCAR8 cells showed a significant enrichment in a cell cycle gene expression signature, along with enriched mitotic and G2/M checkpoint expression signatures, respectively (Figure 58A-D). The enriched G2/M checkpoint signature agrees with our data obtained with FTE cells. Surprisingly, FOXM1 knockdown did not show enriched gene expression signatures for DNA repair, which has been reported for FOXM1 in other cell types, suggesting that FOXM1 has cell context-dependent differences in its transcriptional program (91,130). We validated the FOXM1 target gene expression by RT-qPCR and found that CAOV3 and OVCAR8 cells both showed a decrease in target gene expression following FOXM1 knockdown (Figure 59A-C). Furthermore, in agreement with our FTE data, RNA-seq analysis and RT-qCPR measurement (Figure 59D) for HGSC cells with FOXM1 knockdown confirmed that the DNA repair gene BRCA2 is not a target gene of FOXM1 in these cell models. Together, this suggests that FOXM1 primarily regulates genes involved in cell cycle progression and not DNA repair in HGSC cells.

RHNO1 localizes to chromatin and interacts with the 9-1-1 complex to promote efficient ATR-CHK1 signaling, genomic stability and cell survival in HGSC cells

RHNO1 was previously shown to contribute to the DNA replication stress response by promoting ATR-CHK1 signaling via binding to the 9-1-1 clamp and TOPBP1 (21, 22). Furthermore, we determined that RHNO1 loss in HGSC cells reduces clonogenic survival. Therefore, we next investigated the role of RHNO1 in ATR-CHK1 signaling in FTE and HGSC cells. To test whether RHNO1 augments the DNA replication stress response and impacts DNA damage in FTE and HGSC cells, we knocked down RHNO1 using doxycycline inducible shRNA in FTE and OVCAR8 cells, and measured P-CHK1-S345 by Western blot. We observed ~2-fold reduction of P-CHK1-S345, a canonical readout of the DNA replication stress response (Figure 60A-D). This effect size is similar in magnitude to that reported in previous studies of RHNO1 (21, 22). RHNO1 loss impairs ATR-CHK1 signaling in HGSC cells and potentially impairs their ability to respond to endogenous levels of DNA replication stress, resulting in increased DNA damage. To directly determine whether RHNO1 knockdown impacts DNA damage, we used flow cytometry to measure γ-H2AX as a function of cell cycle phase. We observed a significant increase in γ-H2AX-expressing cells in S and G2 phases. This was to a lesser extent than ATRi, as expected (Figure 60E). In agreement, COMET analyses of DNA breakage revealed significant increases with RHNO1 knockdown (Figure 60F).

RHNO1 interacts with 9-1-1 checkpoint proteins but these interactions have not been investigated in ovarian cancer cells, nor in the context of treatments that specifically cause DNA replication stress. To test if RHNO1 interacts with 9-1-1, we first overexpressed HA-tagged wild-type and SWV mutant RHNO1 in 293T cells then co-immunoprecipitated RHNO1 protein complexes. The RHNO1-SWV, which has mutations within the APSES DNA binding domain, was previously shown to has disrupt the

interaction with 9-1-1 proteins but not TOPBP1 (Figure 61A) (100). As expected, Western blotting of the immunoprecipitated protein complexes and cell lysates showed that wild-type RHNO1 interacts with RAD9 and RAD1 in 293T cells; however, RHNO1-SWV mutant was deficient for these interactions (Figure 61B). We then tested if these interactions, specifically RHNO1-RAD9, may be enhanced under conditions of DNA replication stress. We overexpressed HA-tagged RHNO1 in 293T cells and treated the cells with hydroxyurea (HU) prior to harvesting protein for co-immunoprecipitation, and observed that RHNO1 and RAD9 interaction was enhanced with HU treatment (Figure 61C). Finally, we investigated RHNO1 localization and 9-1-1 protein interactions in HGSC cells. We first tested if endogenous RHNO1 localized to chromatin in OVCAR8 cells following HU treatment. We observed that RHNO1 is present at chromatin without treatment, but HU further enriched chromatin localization (Figure 61D). We then tested if RHNO1 interacts with 9-1-1 proteins in OVCAR8 cells, and if this interaction was dependent on the APSES DNA binding domain. We used an shRNA to knock down endogenous RHNO1 in OVCAR8 cells then reconstituted the expression with HA-tagged wild-type and SWV mutant, shRNA-resistant RHNO1 in a doxycycline inducible manner. Following immunoprecipitation and Western blotting, we observed that wild-type RHNO1 interacts with all 9-1-1 proteins and TOPBP1, but the RHNO1 SWV mutant only interacted with TOPBP1 (Figure 61E). Together, these data provide strong support for RHNO1 as a significant contributor to the DNA replication stress response and DNA damage protection in HGSC cells.

Based on the data presented above, we hypothesized that RHNO1 wild-type, but not SWV mutant, would rescue the decreased clonogenicity following loss of endogenous RHNO1 in HGSC cells. To test this, we knocked down RHNO1 with an shRNA then re-expressed shRNA-resistant RHNO1 wild-type and SWV mutant and measured their ability

to rescue clonogenic survival in OVCAR8 cells (Figure 62A). We found that only wild-type RHNO1 partially rescues the defect in clonogenic survival (Figure 62B). Next, to determine if the reduced survival following RHNO1 loss is retained in non-cancer cells, we used CRISPR to knock out RHNO1 in immortalized FTE cells and measured their viability (Figure 63A-B). RHNO1 knockout and wild-type FTE cells showed no difference in viability, but RHNO1 knockout and knockdown HGSC cells showed significant decrease in survival as compared to control HGSC cells suggesting that HGSC cells have an increased dependency on RHNO1 for growth survival as compared to non-transformed FTE cells (Figure 63C).

FOXM1 and RHNO1 promote homologous recombination-mediated DNA repair

FOXM1 functions as a transcription factor to regulate the expression of genes involved in a variety of essential processes, including cell cycle progression and DNA repair. FOXM1 has also been shown to promote homologous recombination (HR) (195-198). However, we observed that loss of FOXM1 in OVCAR8 cells did not alter the expression of a gene involved in the DNA damage response, and more specifically, BRCA2 which has been reported as a FOXM1 target gene (Figures 58 and 59). RHNO1 interacts with the 9-1-1 checkpoint clamp to promote ATR-CHK1 signaling upon exposure of single stranded DNA resulting from end resection at a DNA double strand break or due to helicase-fork uncoupling during DNA replication stress.

Together, based on their genomic arrangement, co-regulation, reported function, and our novel data, we hypothesized that FOXM1 and RHNO1 may cooperatively promote homologous recombination. To test this hypothesis, we used the well-established, chromosomally integrated HR reporter assay, DR-GFP (direct repeat green fluorescent protein system) in U2OS cells (127,128). These cells were chosen because they are the

most widely used model to study factors that regulate HR. We engineered U2OS cells for inducible FOXM1 and RHNO1 knockdown alone and in combination (Figure 64A). We also engineered these cells for RAD51 knockdown as a positive control for HR impairment (Figure 64B) (100). Upon transient transfection of the I-SceI expressing plasmid, we found that U2OS DR-GFP cells had impaired HR efficiency following RAD51 knockdown, as expected (Figure 64E). RHNO1 knockdown decreased HR efficiency, but surprisingly, FOXM1 knockdown did not (Figure 64E). However, dual knockdown of FOXM1 and RHNO1 showed a greater impairment in HR efficiency as compared to the knockdown of RHNO1 alone, suggesting cooperativity (Figure 64E). We next used OVCAR8 DR-GFP cells to validate these findings in a HGSC-relevant context. OVCAR8 cells have a methylated BRCA1 promoter and show decreased BRCA1 expression but still maintain a minimal level of HR proficiency (108). We engineered OVCAR8 cells for inducible FOXM1 and RHNO1 knockdown alone and in combination (Figure 64C). We also engineered these cells for RAD51 knockdown as a positive control for HR impairment (Figure 64D) (100). Similar to U2OS cells, in OVCAR8 cells, FOXM1 loss slightly reduced HR and RHNO1 loss also reduced HR, but dual loss resulted in a more signification reduction in HR proficiency (Figure 64F). These data indicate that both FOXM1 and RHNO1 promote HR in HGSC cells and further suggest a functional interaction between these two genes.

FOXM1 and RHNO1 loss sensitizes HGSC cells to the PARPi olaparib

Homologous recombination (HR) is defective in about half of the HGSC tumors primarily through BRCA1/2 mutations (30). Furthermore, HR can be impaired by defects in other genes. HR-deficient tumors are highly sensitive to PARP inhibition due to the excess of single strand breaks that ultimately are converted into double strand breaks (DSBs) during DNA replication (45,48). Our data thus far suggests that FOXM1 and

RHNO1 promote the DNA damage response, where we see decreased HR proficiency following their loss. FOXM1 expression and its downstream targets have been linked to the drug resistance for a wide variety of drugs in various cancer types including resistance to platinum, paclitaxel and PARP inhibitors in epithelial ovarian cancer (130,199-201). In addition, RHNO1 functions in the ATR-CHK1 signaling pathway in response to ssDNA and dsDNA breaks, and intriguingly, it was recently reported that ATRi synergizes with PARPi (202). These data suggest that RHNO1 loss may promote PARPi sensitivity potentially in combination with FOXM1. A PARP inhibitor, olaparib, received FDA approval in 2014 for the treatment of germline BRCA-mutated ovarian cancers after third-line therapy (53,54). Furthermore, FOXM1 has been studied for its ability to sensitize ovarian cancer cells to olaparib treatment (130,200). Therefore, we focused on the FOXM1 and RHNO1 bidirectional gene partners to determine if their loss sensitizes HGSC cells to the olaparib. To test this, we engineered OVCAR8 cells for single and dual inducible shRNA mediated knockdown of FOXM1 and RHNO1. To determine the impact of FOXM1 and RHNO1 loss on olaparib sensitivity, we knocked down FOXM1 and RHNO1 in OVCAR8 cells and determined the IC_{50} using AlamarBlue viability assays following 8 days of treatment. We observed that FOXM1 and RHNO1 loss alone sensitized OVCAR8 cells to olaparib treatment, while OVCAR8 cells with loss of both FOXM1 and RHNO1 had a significant increase in sensitivity to olaparib (Figure 65A-B). To address a potential mechanism whereby FOXM1 and RHNO1 loss promotes sensitivity to olaparib, we characterized the cell cycle profile under the same conditions, and loss of both FOXM1 and RHNO1 resulted in an increased number of cells in G2/M as compared to either knockdown alone (Figure 66). Together, our data suggest that FOXM1 and RHNO1 not only play a role in maintaining a basal level of genomic stability, but they also promote genomic stability when challenged with PARPi, suggesting they play cooperative roles in the DNA damage response.

To validate these findings, we next used OVCAR8 cells with KRAB-mediated inhibition of the FOXM1 and RHNO1 bidirectional promoter. We then determined the IC_{50} of olaparib with the AlamarBlue viability assay following 8 days of treatment. In agreement with the shRNA knockdown data, we observed that the combined loss of FOXM1 and RHNO1 sensitized OVCAR8 cells to olaparib treatment (Figure 67A-C). Next, we measured the percentage of apoptotic cells following FOXM1 and RHNO1 loss after PARPi treatment. We found OVCAR8 cells with FOXM1 and RHNO1 depletion had increased apoptotic cells as compared to control (Figure 68A). Moreover, PARPi treatment significantly increased cell death in the FOXM1- and RHNO1-depleted cells as compared to control cells (Figure 68B). We performed cell cycle analysis on FOXM1- and RHNO1-depleted cells following PARPi treatment. In agreement with the apoptosis data, we found that OVCAR8 cells with FOXM1 and RHNO1 depletion had increased G2/M arrest as compared to control when treated with PARPi (Figure 68B).

FOXM1 and RHNO1 loss re-sensitizes PARPi-resistant HGSC cells to olaparib

In vitro and *in vivo* experimental studies have confirmed that BRCA1/2 deficient tumor cells are more sensitive to PARP inhibitors than are BRCA1/2 wild-type tumor cells (45,46,203). However, only a fraction of BRCA1/2 mutation carriers respond to PARPi therapy and even those who respond subsequently develop resistance (48,55-57). Thus, a strategy to overcome PARPi resistance in BRCA-deficient cancers is needed to improve this otherwise promising targeted therapy. In this context, we obtained two isogenic derivatives of UWB1.289, a BRCA1 null HGSC cell line, that were treated *in vitro* with olaparib, and subsequently developed acquired resistance *in vitro* (202). Furthermore, these two PARPi-resistant BRCA1-deficient cell lines, SyR12 and SyR13, are dependent on ATR for cell survival in the presence of PARPi, and GSEA analysis showed enriched

G2/M checkpoints and activation of ATR signaling, respectively (202). We first validated these cell lines by determining the IC_{50} of olaparib with the AlamarBlue viability assay after 8 days of treatment (Figure 69A). As expected, both PARPi resistant clones, SyR12 and SyR13, had resistance to olaparib relative to parental cells. It was reported that the UWB1 clone SyR13 showed an enriched gene expression signature for ATR activation. We measured *ATR* mRNA by RT-qPCR and observed that the SyR13 clone had increased expression of *ATR* as compared to the parental line and resistant clone SyR12 (Figure 69B). These data suggest that FOXM1 and RHNO1 may show increased expression in the PARPi-resistant clones. To test this, we performed RT-qPCR and observed that the SyR13 clone had increased expression of *FOXM1* and *RHNO1* mRNA expression as compared to the parental line and resistant clone SyR12 (Figure 69C).

Based on the reported data and our expression data together, we hypothesized that targeting FOXM1/RHNO1 may re-sensitize these PARPi-resistant clones to olaparib. To test this, we engineered UWB1.289 parental and PARPi-resistance cells for KRAB-mediated inhibition of the FOXM1/RHNO1 bidirectional promoter. We found that the KRAB repressor targeting the FOXM1/RHNO1 bidirectional promoter efficiently silenced *FOXM1* and *RHNO1* mRNA expression in the PARPi-resistant cells (Figure 70A). We then tested the olaparib sensitivity by assessing the IC_{50} after 8 days of treatment. We observed that the loss of FOXM1 and RHNO1 re-sensitized both SyR12 and SyR13 PARPi-resistant cells to olaparib by 3-fold and 4-fold, respectively, but did not completely restore the sensitivity to the level observed in the UWB1 parental cells (Figure 70B-C). In support of the magnitude of IC_{50} shift that we observed for olaparib with FOXM1 and RHNO1 loss in both PARPi-resistant cells, an ATR inhibitor was reported to shift the IC50 by ~3-fold and did not completely restore the sensitivity observed in parental cells (202). These data suggest FOXM1 and RHNO1 targeting as a potential means to combat PARPi resistance.

Furthermore, a FOXM1 inhibitor has very recently been reported to sensitize ovarian cancer cell lines to PARPi treatment (130). Potentially FOXM1 inhibitors could be combined with ATR inhibitors to re-sensitize PARPi-resistant cells to these agents.

Summary

Our analysis of 12p13.33 identified that FOXM1 shares a bidirectional promoter with RHNO1, a gene shown to promote efficient ATR-CHK1 signaling. We hypothesized that FOXM1 and RHNO1 would have frequent co-expression and play cooperative roles in cell survival, HR and chemoresistance. Our analysis of *in silico* genomic data sets showed a strong correlation between *FOXM1* and *RHNO1* mRNA expression in normal, HGSC and pan-cancer tissues. The relationship was validated in our independent HGSC tumor banks and HGSC cell lines and using scRNA analyses. In agreement with the genomic analyses, we found that the *FOXM1* and *RHNO1* intergenic space functions as a bidirectional promoter in immortalized FTE and HGSC cells. We found that depletion of FOXM1 and RHNO1 reduced HR efficiency and survival in HGSC cells. Furthermore, we found that FOXM1 promotes cell cycle progression and RHNO1 promotes ATR-CHK1 signaling, and this is dependent on interactions with the 9-1-1 checkpoint clamp. The depletion of FOXM1 and RHNO1 promoted PARPi sensitivity in HGSC cells. Furthermore, loss of FOXM1 and RHNO1 re-sensitized HGSC PARPi-resistant cells to olaparib. These data support additional studies of FOXM1 and RHNO1 gene partners, specifically, to further the understanding of HGSC biology through *in vivo* modeling of FOXM1 and RHNO1, and to determine if RHNO1 and FOXM1 cooperate in normal and other cancer cells. Broadly, these data support the study of other bidirectional gene partners to determine their cooperativity in normal and cancer biology.

Figures

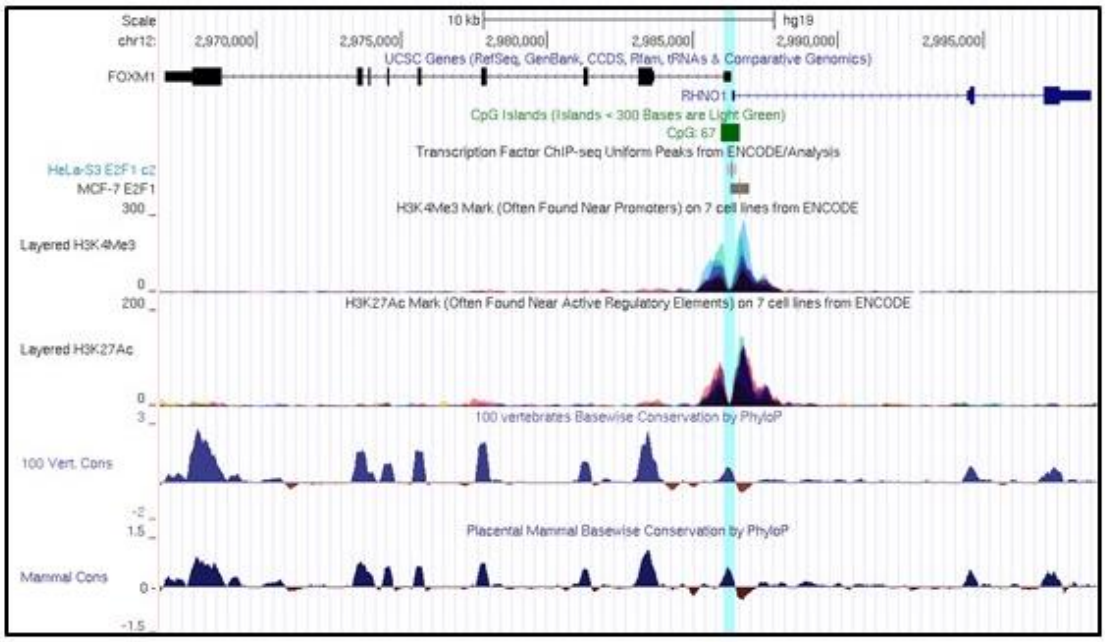

Figure 40. Genomic features of the FOXM1/RHNO1 bidirectional gene partners. UCSC Genome Browser (http://genome.ucsc.edu, human genome build hg19 with genomic coordinates chr12:2,966,265-2,999,264) displaying *FOXM1* and *RHNO1* genes. The following tracks are displayed in the browser: *FOXM1* and *RHNO1* mRNA, CpG island, Encode E2F1, H3K4Me3 and H3K27Ac ChIP-seq track, and conserved genome tracks 100 vertebrates and mammalian. The putative FOXM1/RHNO1 bidirectional is highlighted with the light blue vertical line.

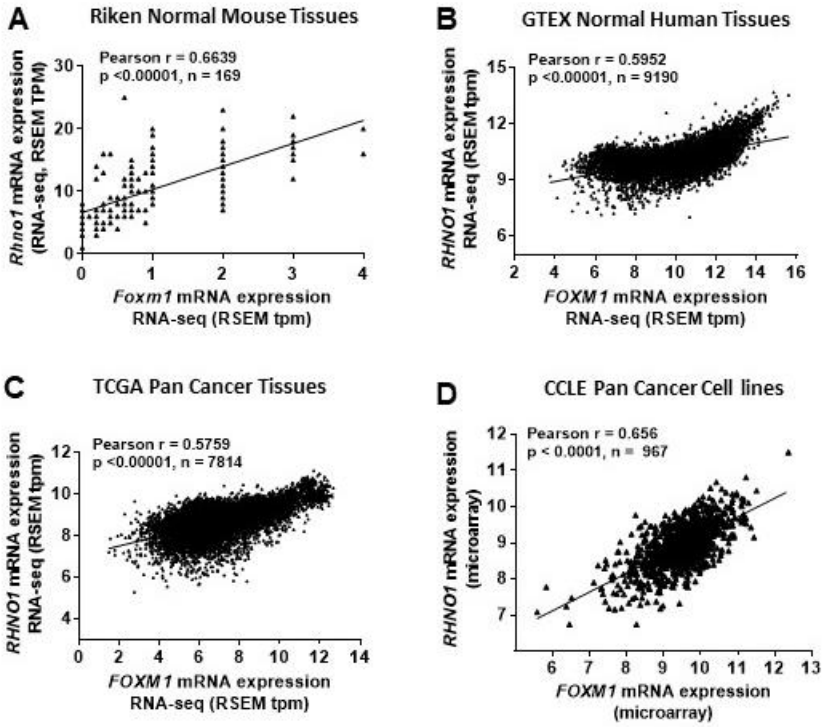

Figure 41. *FOXM1* and *RHNO1* expression correlation in normal and cancer tissues.

A-D. *FOXM1* and *RHNO1* mRNA expression in **A**. Riken normal mouse tissues (RNA-seq), **B.** GTEx normal human tissues (RNA-seq), **C.** TCGA pan-cancer tissues (RNA-seq) and **D.** CCLE pan-cancer cell lines (microarray).

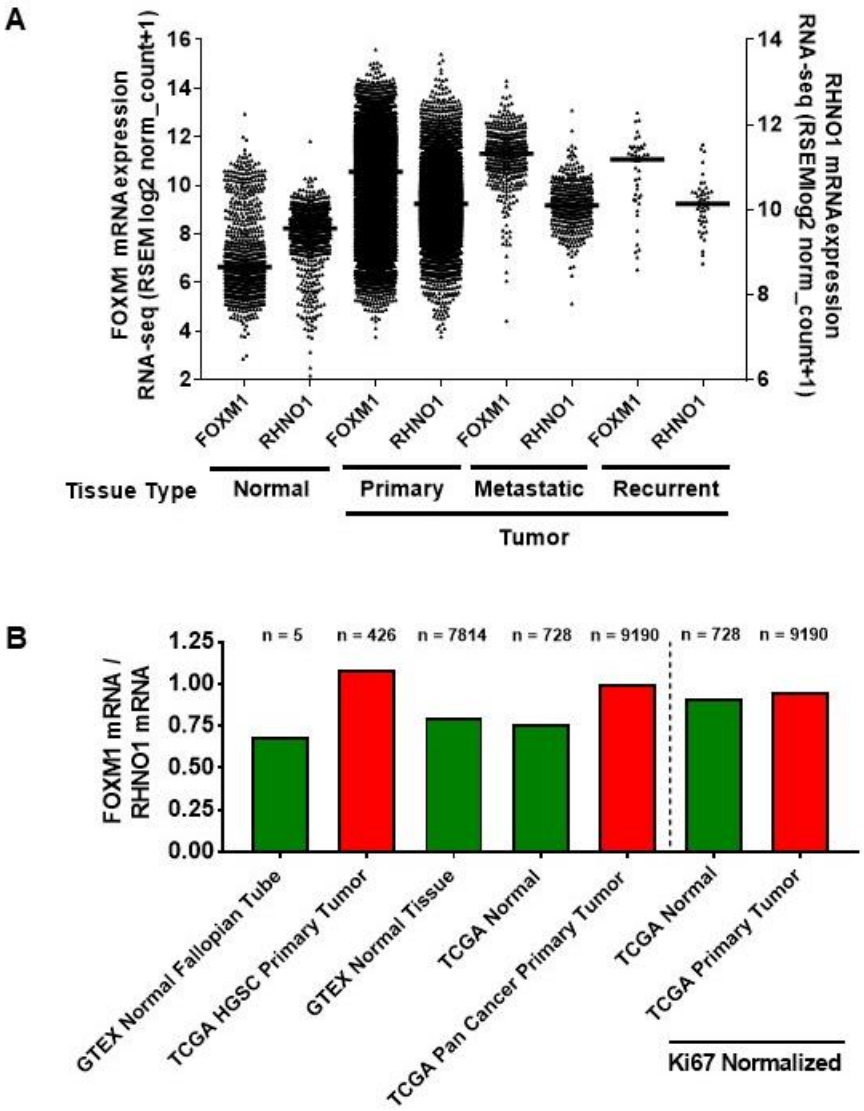

Figure 42. *FOXM1* and *RHNO1* mRNA expression (RNA-seq) in normal and pan-cancer tissues. A. *FOXM1* and *RHNO1* expression (RNA-seq) in GTEx and TCGA normal tissues and TCGA tumor tissues. **B**. *FOXM1* and *RHNO1* expression ratio in normal and cancer, and Ki67 normalized ratio on the far right for TCGA normal and tumor tissues.

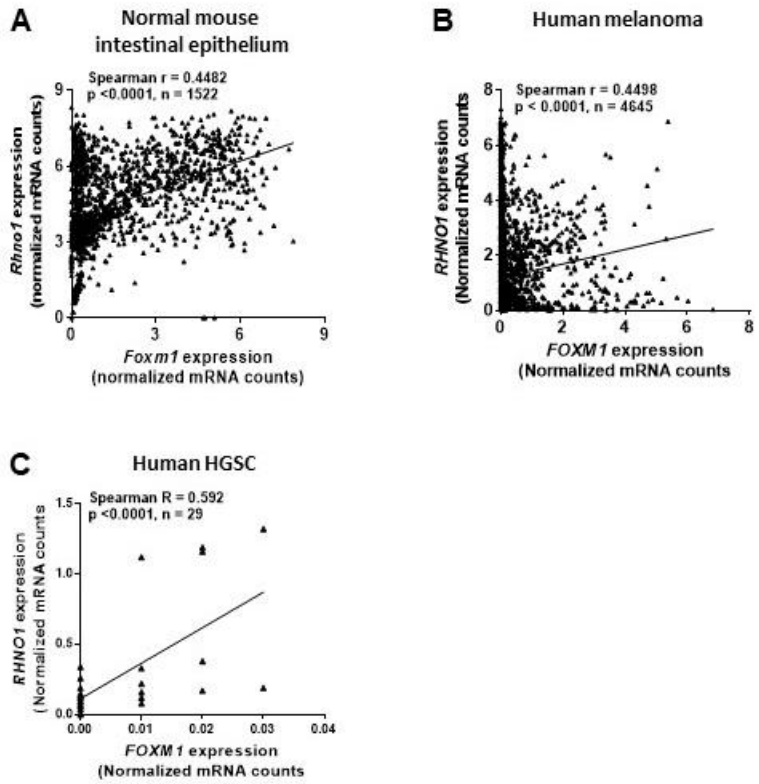

Figure 43. *FOXM1* and *RHNO1* mRNA expression correlation in single cell RNA-seq from normal and cancer tissues. **A.** Single cells isolated from normal mouse epithelium tissue (single cell RNA-sequencing) (GSE92332). **B.** Single cells isolated from human melanoma tissue (single cell RNA-sequencing) (GSE72056). **C.** Single cells isolated from HGSC primary tumors (single cell RNA sequencing) (Winterhoff *et a*l, 2017).

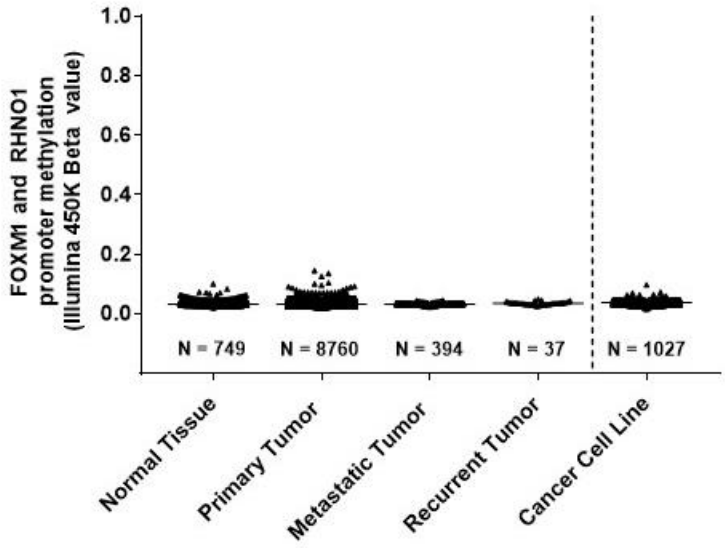

Figure 44. DNA methylation at the FOXM1/RHNO1 bidirectional promoter in TCGA normal and tumor pan-cancer tissues, and CCLE pan-cancer cell lines. Beta values represent the level of DNA methylation, averaged across 7 CpG sites within the FOXM1/RHNO1 CpG island. A value of 1 is the highest level of methylation and 0 is the lowest level of methylation.

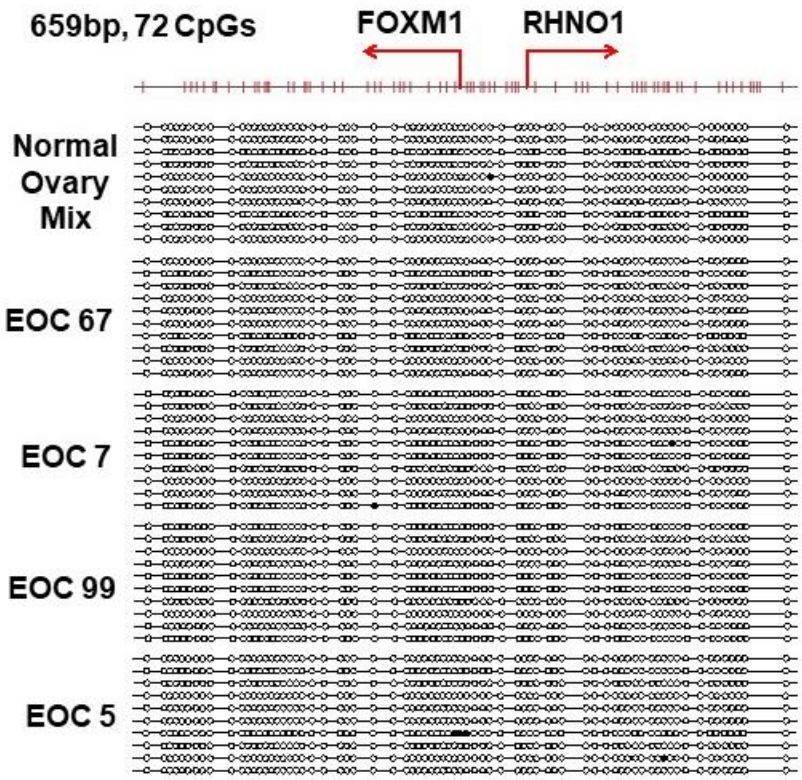

Figure 45. FOXM1/RHNO1 bidirectional promoter methylation analysis by bisulfite sequencing. Sodium bisulfite clonal sequencing of the FOXM1/RHNO1 bidirectional promoter region was performed on the indicated samples. The NCBI predicted TSS is indicated by the red broken arrows. The intergenic space spans between the two arrows. Filled and open circles indicate methylated and unmethylated CpG sites, respectively, and each row represents one sequenced allele.

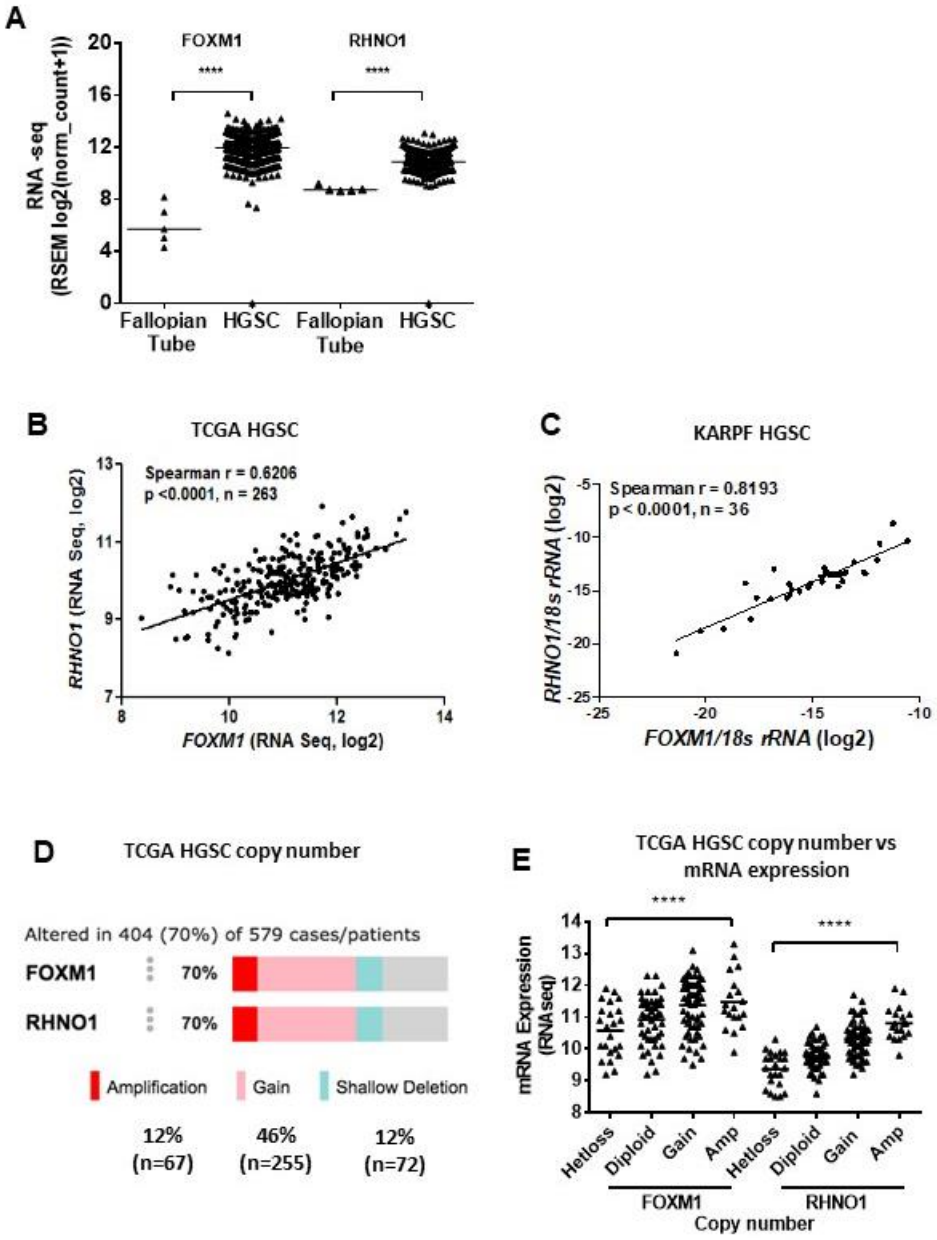
A
FOXM1
RHNO1
****
****
RNA -seq
(RSEM log2(norm_count+1))
20
16
12
8
4
0
Fallopian Tube
HGSC
Fallopian Tube
HGSC
B
TCGA HGSC
Spearman r = 0.6206
p <0.0001, n = 263
RHNO1 (RNA Seq, log2)
FOXM1 (RNA Seq, log2)
C
KARPF HGSC
Spearman r = 0.8193
p < 0.0001, n = 36
RHNO1/18s rRNA (log2)
FOXM1/18s rRNA (log2)
D
TCGA HGSC copy number
Altered in 404 (70%) of 579 cases/patients
FOXM1
RHNO1
70%
70%
Amplification
Gain
Shallow Deletion
12% (n=67)
46% (n=255)
12% (n=72)
E
TCGA HGSC copy number vs mRNA expression
****
****
mRNA Expression (RNAseq)
Hetloss
Diploid
Gain
Amp
Hetloss
Diploid
Gain
Amp
FOXM1
RHNO1
Copy number

Figure 46.

Figure 46. *FOXM1* and *RHNO1* copy number and expression in HGSC tissues. A. *FOXM1* and *RHNO1* expression (RNA-seq) in TCGA HGSC tissue as compared to GTEX normal fallopian tube tissues. **B.** *FOXM1* mRNA expression vs *RHNO1* mRNA expression (RNA-seq) from TCGA HGSC tissues. **C.** *FOXM1* mRNA expression vs *RHNO1* mRNA expression from Karpf lab HGSC tissues. **D.** *FOXM1* vs *RHNO1* copy number from TCGA HGSC tissues **E.** *FOXM1* and *RHNO1* mRNA expression (RNA-seq) correlated with copy number in TCGA HGSC tissues. The p value for ANOVA with post-test for linear trend is shown. Lines represent group medians. t-test *P* value is shown. *P* value designation: **** < 0.0001, *** < 0.001, ** < 0.01, * < 0.05.

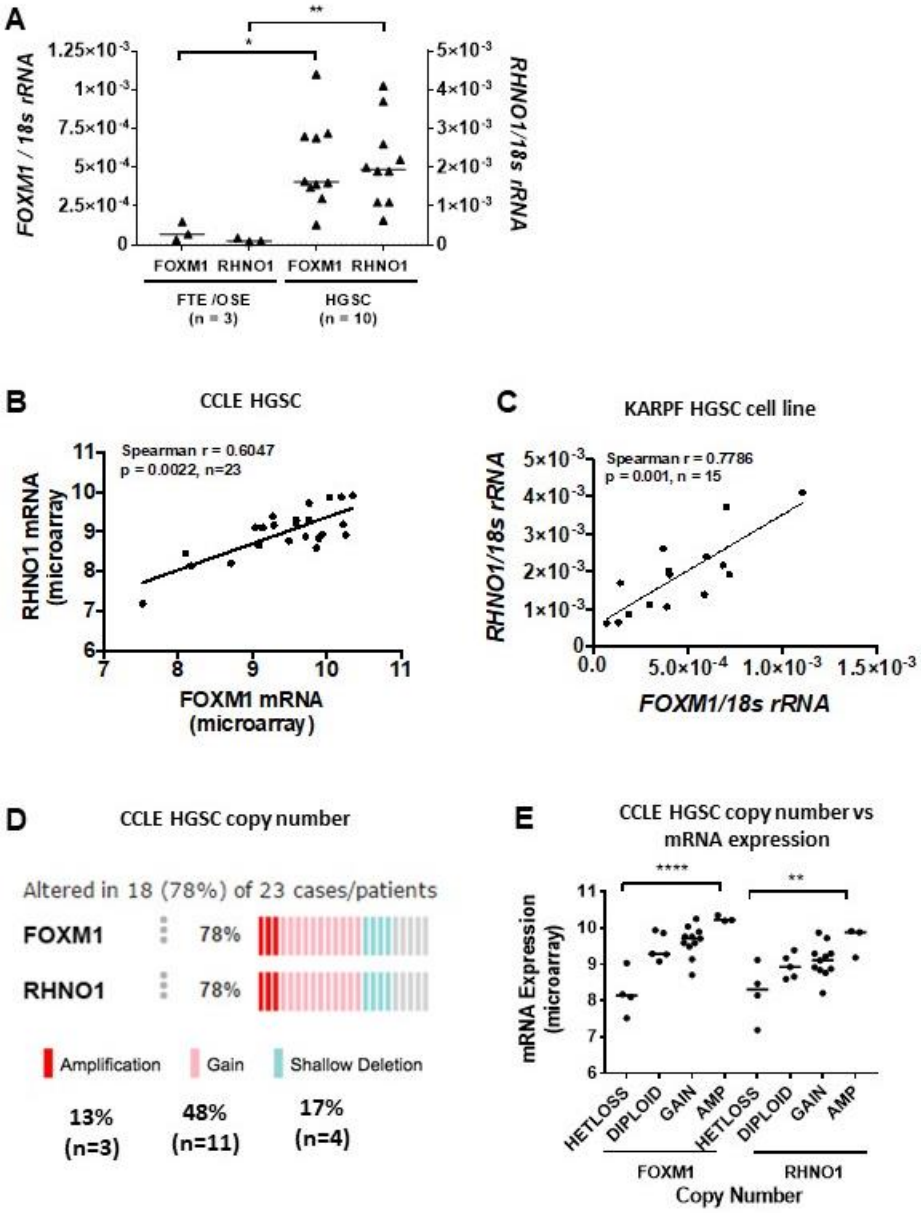
A
FOXM1 / 18s rRNA
RHNO1/18s rRNA
FOXM1 RHNO1 FOXM1 RHNO1
FTE /OSE (n = 3)
HGSC (n = 10)
B
CCLE HGSC
Spearman r = 0.6047
p = 0.0022, n=23
RHNO1 mRNA (microarray)
FOXM1 mRNA (microarray)
C
KARPF HGSC cell line
Spearman r = 0.7786
p = 0.001, n = 15
RHNO1/18s rRNA
FOXM1/18s rRNA
D
CCLE HGSC copy number
Altered in 18 (78%) of 23 cases/patients
FOXM1 78%
RHNO1 78%
Amplification
Gain
Shallow Deletion
13% (n=3)
48% (n=11)
17% (n=4)
E
CCLE HGSC copy number vs mRNA expression
mRNA Expression (microarray)
HETLOSS DIPLOID GAIN AMP HETLOSS DIPLOID GAIN AMP
FOXM1
RHNO1
Copy Number

Figure 47.

Figure 47. FOXM1 and RHNO1 expression in HGSC cell lines. A. *FOXM1* and *RHNO1* mRNA expression from FTE and OSE cell lines compared to HGSC cell lines as measured by RT-qPCR. **B**. *FOXM1* mRNA expression vs *RHNO1* mRNA expression (microarray) from CCLE HGSC cell lines. **C.** *FOXM1* mRNA expression vs *RHNO1* mRNA expression from Karpf lab HGSC cell lines as measured by RT-qPCR. **D.** *FOXM1* vs *RHNO1* copy number among CCLE HGSC cell lines. **E.** *FOXM1* and *RHNO1* mRNA expression (microarray) correlated with copy number in CCLE HGSC cell lines. The p value for ANOVA with post-test for linear trend is shown. Lines represent group medians. t test *P* value is shown. *P* value designation: **** < 0.0001, *** < 0.001, ** < 0.01, * < 0.05.

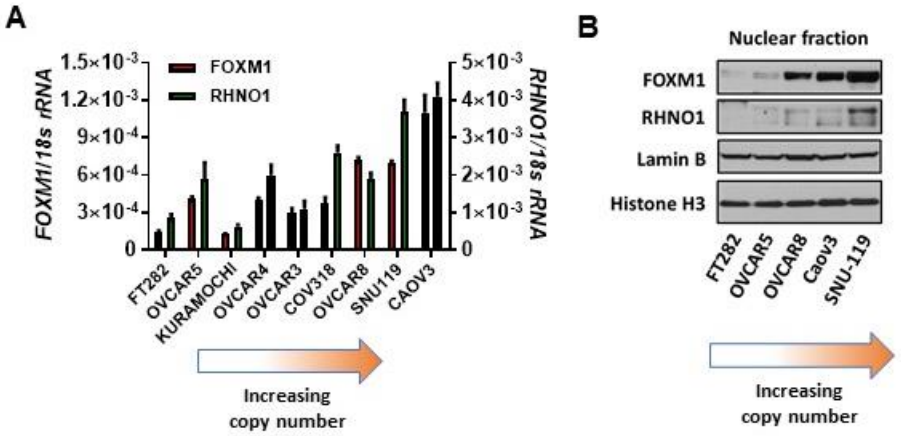

Figure 48. FOXM1 expression comparison in FTE and HGSC cell lines. A. *FOXM1* and *RHNO1* mRNA expression were measured RT-qPCR. **B.** FOXM1 and RHNO1 protein expression were measured by Western blot. Lamin B and Histone H3 are shown as loading controls. The arrow below panels A and B indicates the increasing *FOXM1* and *RHNO1* copy number status from left to right.

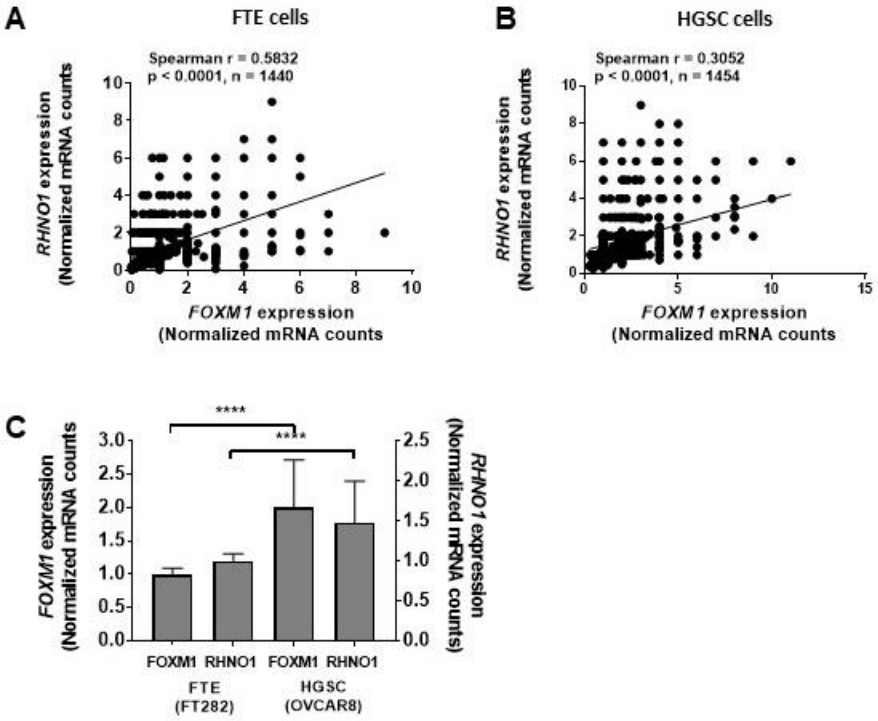

Figure 49. *FOXM1* and *RHNO1* mRNA expression in FTE and HGSC single cells. A. *FOXM1* and *RHNO1* mRNA expression correlation among FTE single cells (single cell RNA sequencing). **B.** *FOXM1* and *RHNO1* mRNA expression correlation among HGSC single cells (single cell RNA sequencing). **C.** *FOXM1* and *RHNO1* mRNA expression comparison in FTE and HGSC single cells. t-test P value is shown. P value designation: **** < 0.0001, *** < 0.001, ** < 0.01, * < 0.05.

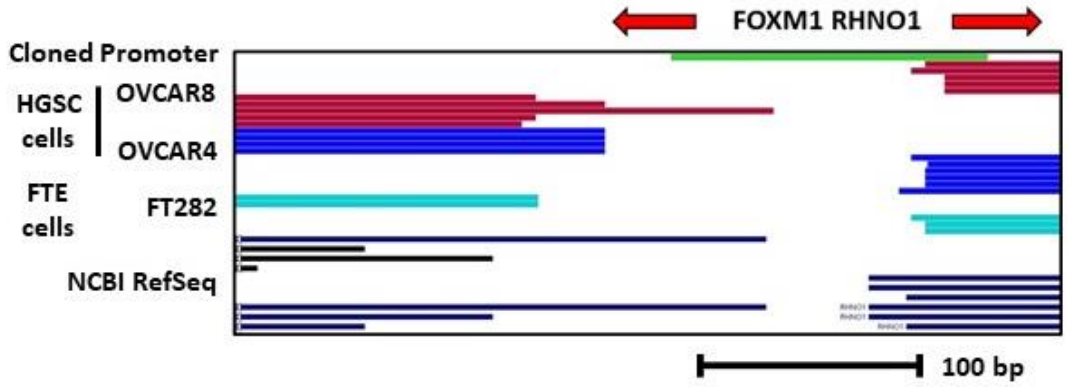

Figure 50. FOXM1 and RHNO1 mapping of transcription start sites (TSS). RLM-RACE mapping the 5' end of *FOXM1* and *RHNO1* mRNA. The red left and right arrows indicate the orientation of each gene. The left y-axis indicates the sequenced clones from the respective HGSC and FTE cell line. NCBI predicted TSS is show on the bottom. The green line at the top indicates the bidirectional promoter cloned for reporter assays in subsequent experiments. The bottom lines represent a scale in bp length.

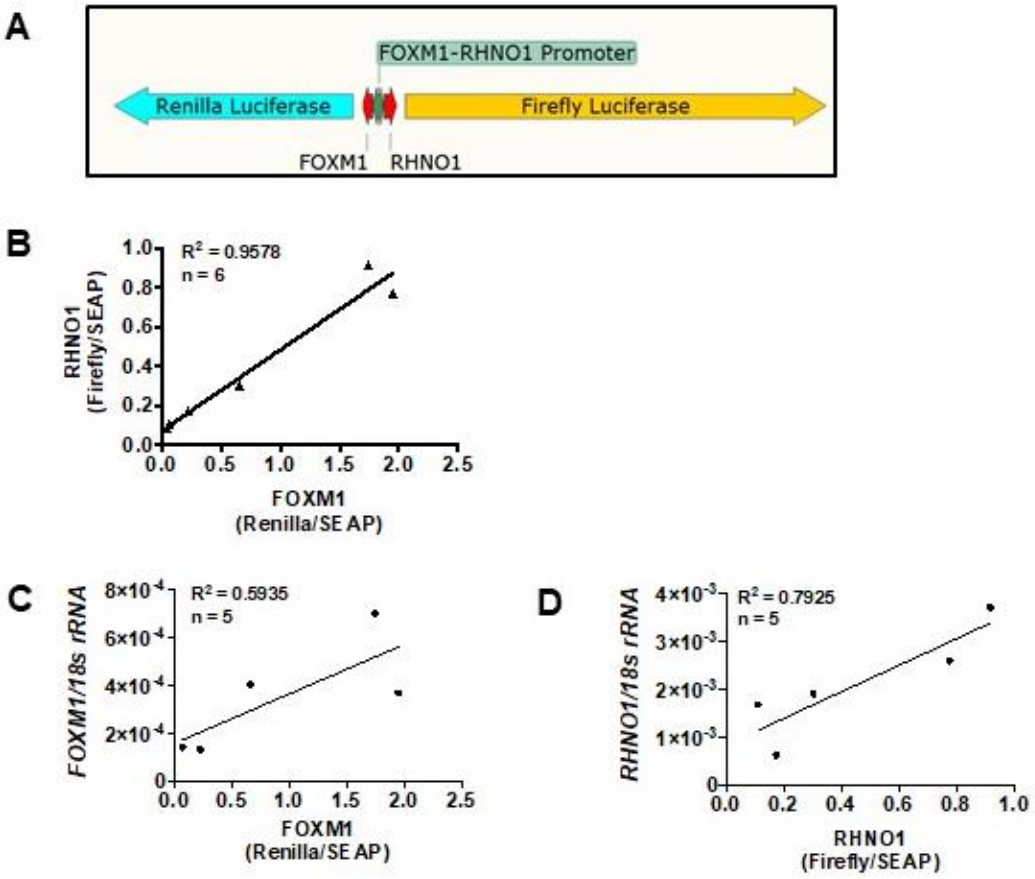

Figure 51. FOXM1/RHNO1 bidirectional reporter assay. A. FOXM1/RHNO1 bidirectional reporter construct with the promoter colored in green. FOXM1 drives Renilla luciferase and RHNO1 drives Firefly. luciferase. Secreted embryonic alkaline phosphatase (SEAP) was co-transfected and used as the internal normalization control. **B.** Correlation of FOXM1 and RHNO1 promoter activity in a panel of FTE and HGSC cells. **C.** Correlation of FOXM1 promoter activity and mRNA measured by RT-qPCR. **D.** Correlation of RHNO1 promoter activity and mRNA measured by RT-qPCR.

80

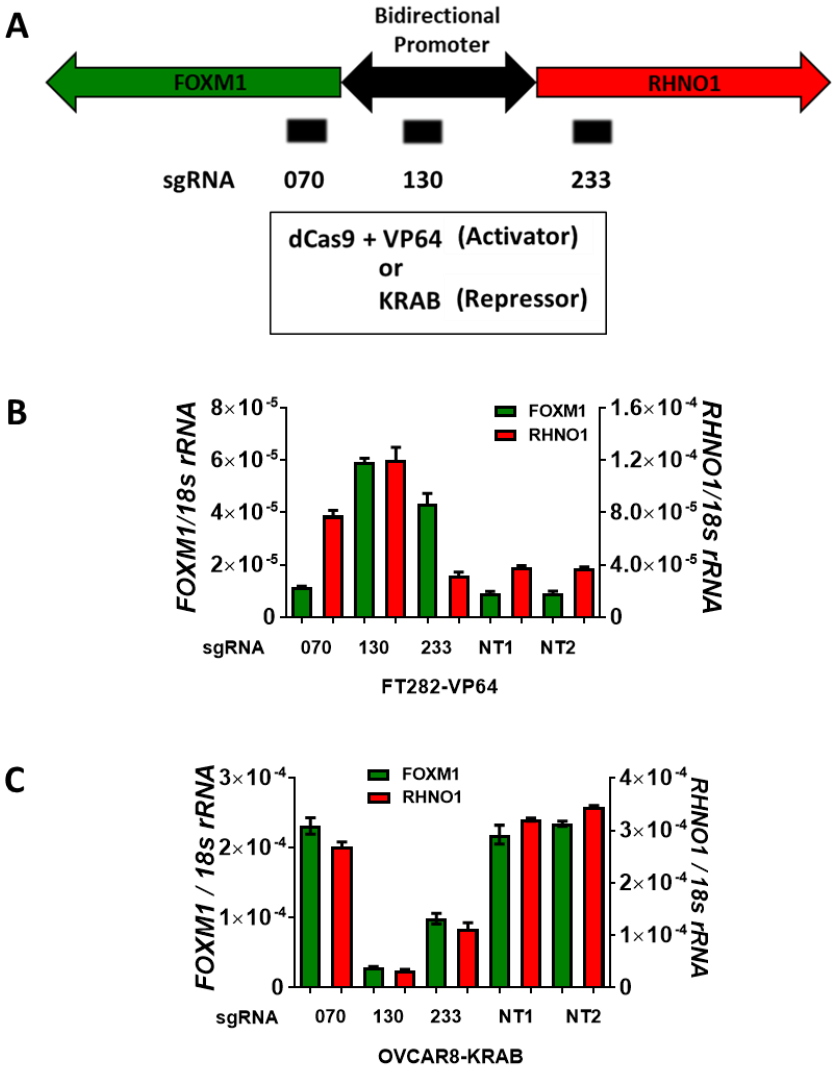
A
Bidirectional
Promoter
FOXM1
RHNO1
sgRNA
070
130
233
dCas9 + VP64 (Activator)
or
KRAB (Repressor)
B
FOXM1/18s rRNA
RHNO1/18s rRNA
FOXM1
RHNO1
8×10-5
6×10-5
4×10-5
2×10-5
0
1.6×10-4
1.2×10-4
8.0×10-5
4.0×10-5
0
sgRNA
070
130
233
NT1
NT2
FT282-VP64
C
FOXM1 / 18s rRNA
RHNO1 / 18s rRNA
FOXM1
RHNO1
3×10-4
2×10-4
1×10-4
0
4×10-4
3×10-4
2×10-4
1×10-4
0
sgRNA
070
130
233
NT1
NT2
OVCAR8-KRAB

Figure 52.

Figure 52. CRISPR mediated activation and repression of the endogenous FOXM1/RHNO1 bidirectional promoter. **A.** FOXM1/RHNO1 bidirectional reporter and guide RNAs indicated below. **B.** CRISPR mediated activation of the FOXM1/RHNO1 bidirectional promoter in FTE cells expressing synergistic activation mediator (VP64) and a guide RNA targeting the bidirectional promoter and the corresponding changes in mRNA expression as measured by RT-qPCR. **C.** CRISPR mediated inhibition of the FOXM1/RHNO1 bidirectional promoter in HGSC cells expressing Krüppel associated box (KRAB) transcriptional repressor and a guide RNA targeting the bidirectional promoter and the corresponding changes in mRNA expression as measured by RT-qPCR. NT1 and NT2 – non-targeting control guide RNAs.

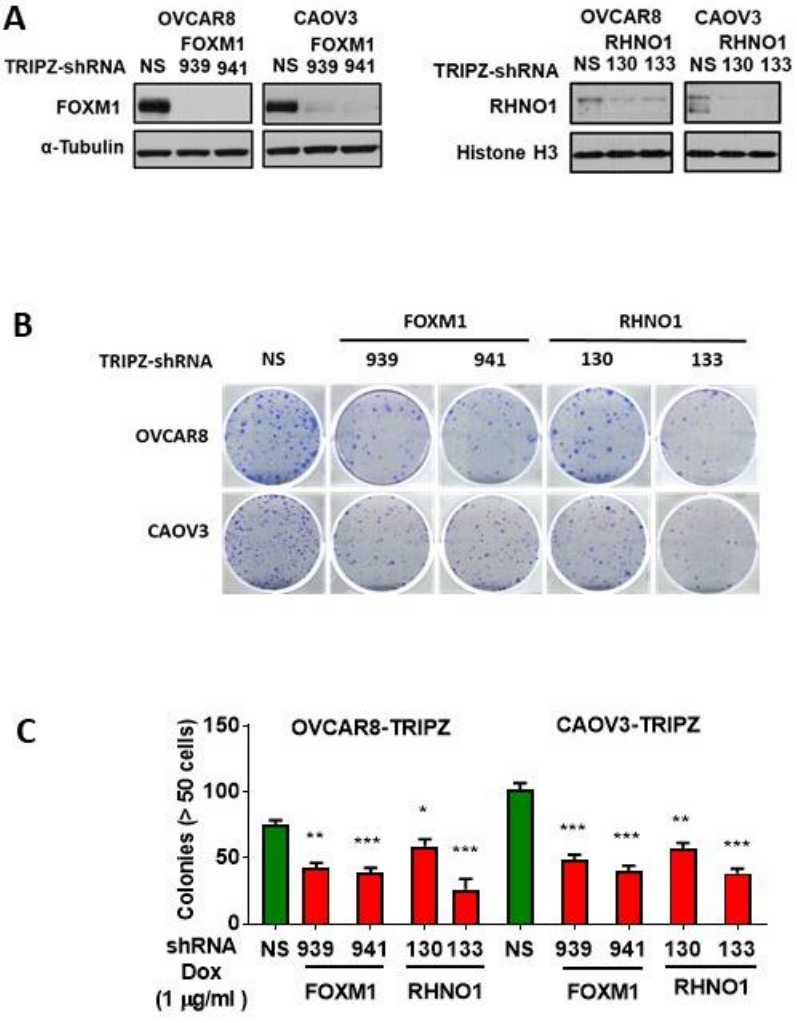
A
OVCAR8
CAOV3
FOXM1
TRIPZ-shRNA NS 939 941 NS 939 941
FOXM1
α-Tubulin
OVCAR8
CAOV3
RHNO1
TRIPZ-shRNA NS 130 133 NS 130 133
RHNO1
Histone H3
B
FOXM1
RHNO1
TRIPZ-shRNA NS 939 941 130 133
OVCAR8
CAOV3
C
OVCAR8-TRIPZ
CAOV3-TRIPZ
Colonies (> 50 cells)
150
100
50
0
shRNA NS 939 941 130 133 NS 939 941 130 133
Dox (1 μg/ml)
FOXM1 RHNO1 FOXM1 RHNO1

Figure 53.

Figure 53. Clonogenic survival for HGSC cells following FOXM1 or RHNO1 knockdown. OVCAR8 and CAOV3 cells engineered for inducible FOXM1 or RHNO1 knockdown were seeded for protein extraction and Western blot or clonogenic survival. **A.** Cells were grown in the presence of doxycycline for 72 hours to harvest protein followed by Western blot analysis to confirm knockdown efficiency. **B.** Cells were seeded into a 6-well dish, in triplicate, at a density of 500 or 1,000 cells, respectively. Doxycycline was added at the time of seeding and media containing doxycycline was replenished every 48 hours. Clonogenic survival was measured at 12 and 14 days, respectively, after the cells were fixed with methanol and stained with crystal violet. **C.** Colonies containing more than 50 cells were counted and clonogenic survival was quantified as an average of the replicates. NS = non-targeting shRNA. t test *P* value is shown. *P* value designation: **** < 0.0001, *** < 0.001, ** < 0.01, * < 0.05.

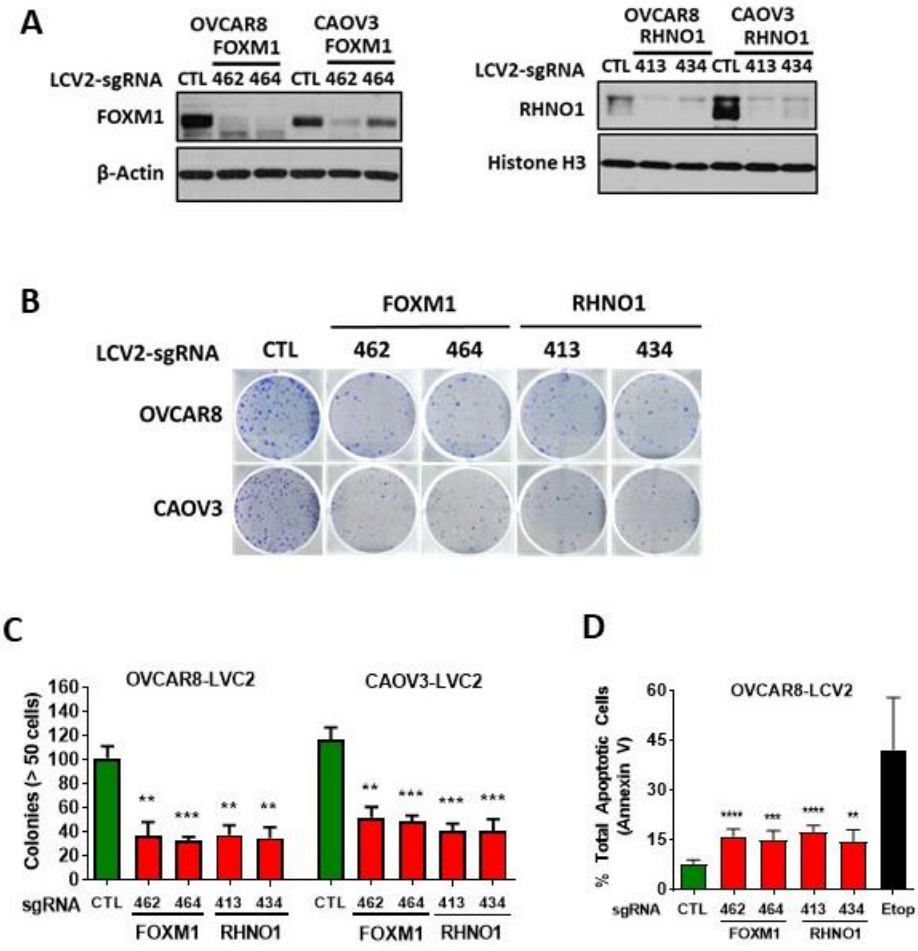
A
OVCAR8 FOXM1
CAOV3 FOXM1
LCV2-sgRNA CTL 462 464 CTL 462 464
FOXM1
β-Actin
OVCAR8 RHNO1
CAOV3 RHNO1
LCV2-sgRNA CTL 413 434 CTL 413 434
RHNO1
Histone H3
B
FOXM1
RHNO1
LCV2-sgRNA CTL 462 464 413 434
OVCAR8
CAOV3
C
OVCAR8-LVC2
CAOV3-LVC2
Colonies (> 50 cells)
sgRNA CTL 462 464 413 434 CTL 462 464 413 434
FOXM1 RHNO1 FOXM1 RHNO1
D
OVCAR8-LCV2
% Total Apoptotic Cells (Annexin V)
sgRNA CTL 462 464 413 434 Etop
FOXM1 RHNO1

Figure 54.

Figure 54. Clonogenic survival for HGSC cells following FOXM1 or RHNO1 knockout. OVCAR8 and CAOV3 cells engineered for FOXM1 or RHNO1 knockout were seeded for protein or clonogenic survival. **A.** Cells were for 72 hours to harvest protein followed by Western blot analysis to confirm knockout efficiency. **B.** Cells were seeded into a 6-well dish, in triplicate, at a density of 500 or 1,000 cells, respectively. Media was replenished every 48 hours. Clonogenic survival was measured at 12 and 14 days, respectively, after the cells were fixed with methanol and stained with crystal violet. **C.** Colonies containing more than 50 cells were counted and clonogenic survival was quantified as an average of the replicates. **D.** Total apoptotic cells for OVCAR8 FOXM1 or RHNO1 knockout cells was determined by Annexin V staining and FACS. Etoposide was used a positive control CTL = non-targeting guide RNA. test *P* value is shown. *P* value designation: **** < 0.0001, *** < 0.001, ** < 0.01, * < 0.05.

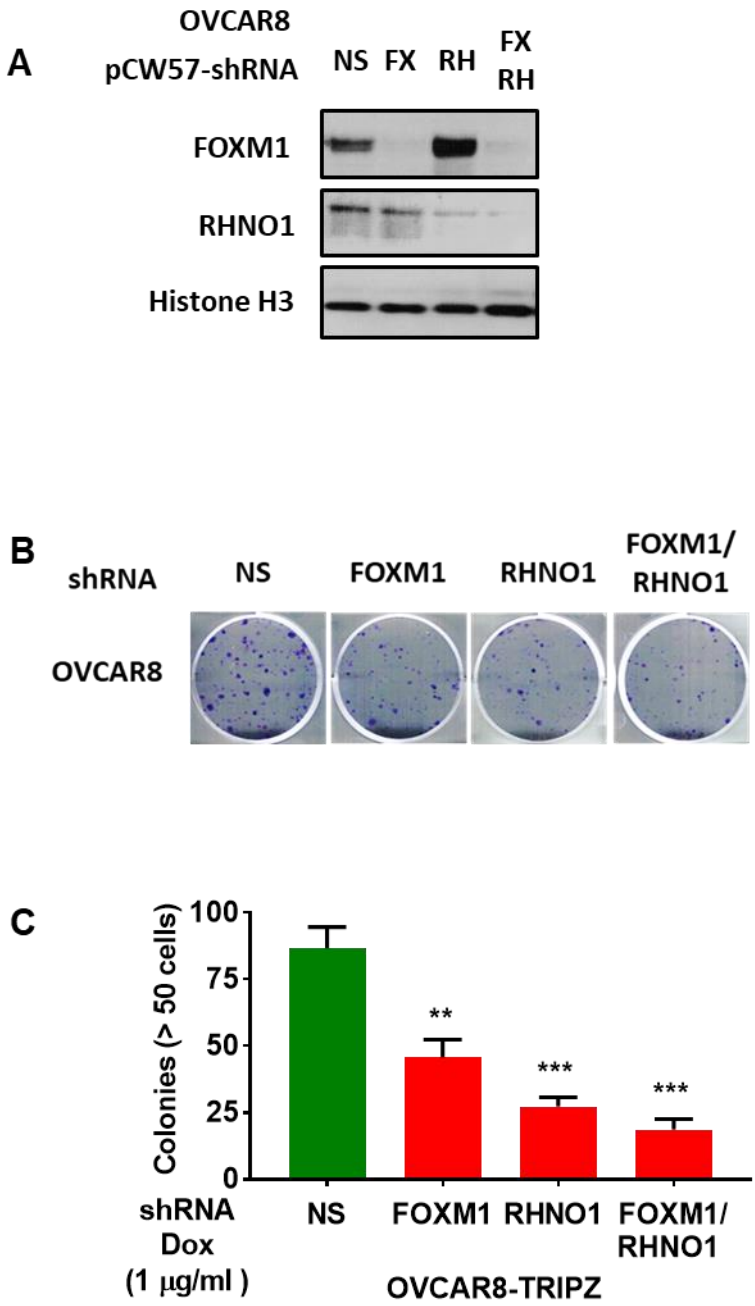
A
OVCAR8
pCW57-shRNA
NS
FX
RH
FX RH
FOXM1
RHNO1
Histone H3
B
shRNA
NS
FOXM1
RHNO1
FOXM1/ RHNO1
OVCAR8
C
Colonies (> 50 cells)
100
75
50
25
0
**
***
***
shRNA
Dox
(1 μg/ml)
NS
FOXM1
RHNO1
FOXM1/ RHNO1
OVCAR8-TRIPZ

Figure 55.

Figure 55. Clonogenic survival for HGSC cells following FOXM1 and/or RHNO1 knockdown. OVCAR8 cells engineered for FOXM1 and/or RHNO1 knockout were seeded for protein or clonogenic survival. **A**. Cells were seeded in the presence of doxycycline and grown for 72 hours to harvest protein followed by Western blot analysis to confirm knockdown efficiency. **B.** Cells were seeded into a 6-well dish, in triplicate, in the presence of doxycycline at a density of 500 cells. Media containing doxycycline was replenished every 48 hours. Clonogenic survival was measured at 12 days after the cells were fixed with methanol and stained with crystal violet. **C.** Colonies containing more than 50 cells were counted and clonogenic survival was quantified as an average of the replicates. NS = non-targeting shRNA. test P value is shown. P value designation: **** < 0.0001, *** < 0.001, ** < 0.01, * < 0.05.

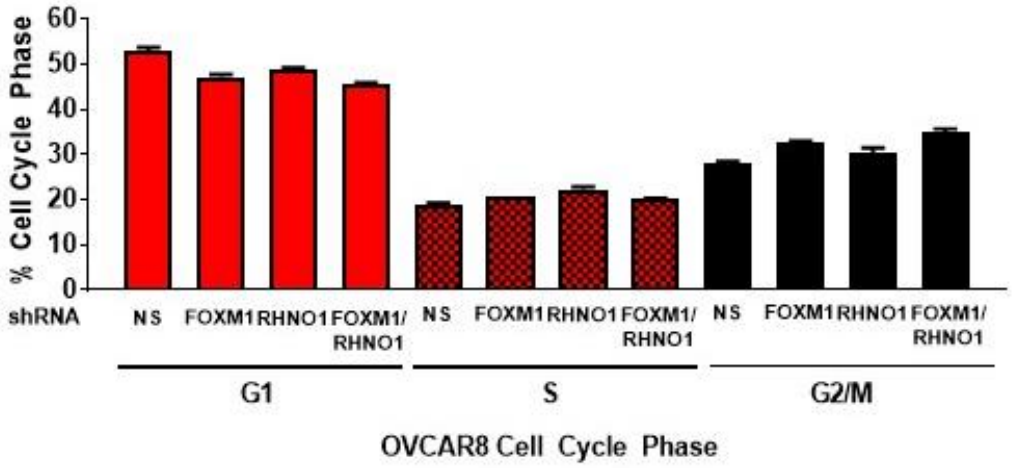

Figure 56. Cell cycle analysis of HGSC cells following knockdown of FOXM1 and/or RHNO1. OVCAR8 cells engineered for FOXM1 and/or RHNO1 knockout were seeded in the presence of doxycycline and grown for 72 hours to harvest cells for cell cycle analysis.

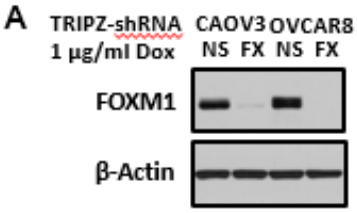

B

HiSeq 2500 DNA Analyzer (Illumina)
Triplicate replicates with 75 bp single reads

Sample name	Means reads ± SD (millions)
CAOV3-shNS	19.7 ± 3.3
CAOV3 -shFOXM1	22.1 ± 2.5
OVCAR8-shNS	21.5 ± 1.9
OVCAR8-shFOXM1	21.2 ± 0.8

Figure 57. RNA sequencing for HGSC cells with FOXM1 knockdown. CAOV3 and OVCAR8 cells with inducible non-targeting or FOXM1 shRNA were grown in the presence doxycycline for 48 hours and cells were harvested for RNA or protein. Sample were prepared in triplicate for each group. **A.** Western blot analysis of FOXM1 protein expression to confirm knockdown efficiency. **B.** RNA sequencing performance characteristics.

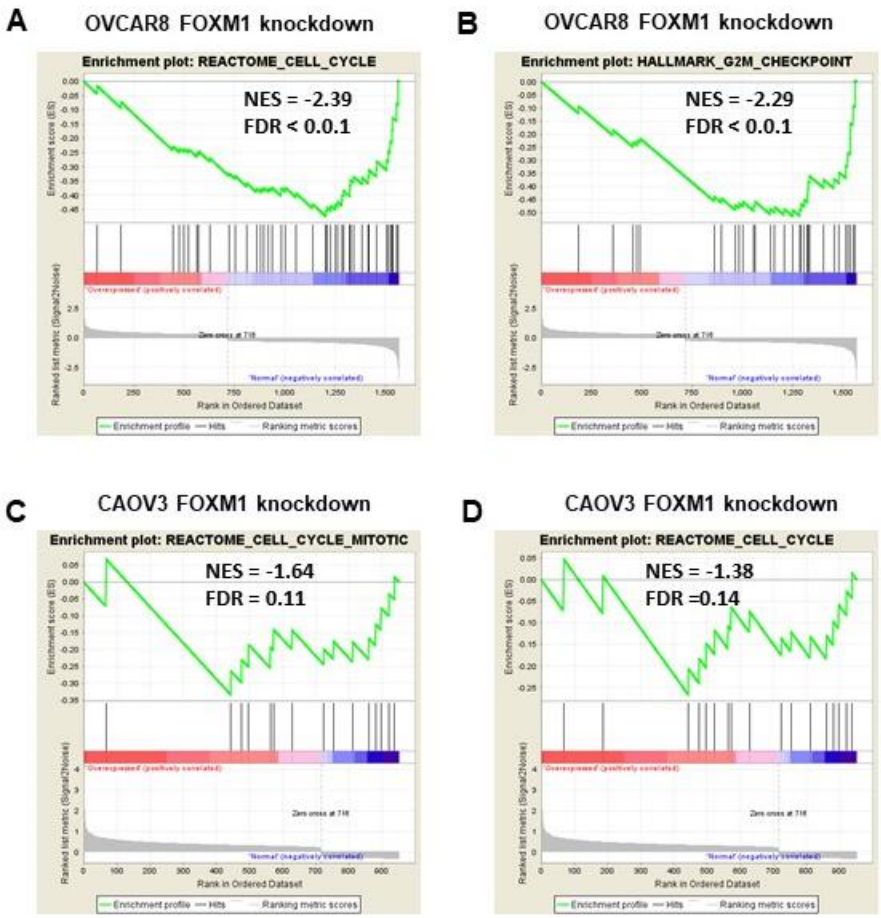

Figure 58. OVCAR8 and CAOV3 enriched pathway signatures. A-B. GSEA analysis of the top two hallmark pathways for OVCAR8 FOXM1 knockdown cells **A.** Cell Cycle and **B.** G, G2/M checkpoint**. C-D**. GSEA analysis of the top two hallmark pathways for CAOV3 FOXM1 knockdown cells **C.** Cell Cycle, mitotic and **D.** cell cycle. Enrichment analysis as a function of OVCAR8 and CAOV3 with knockdown of FOXM1 using RNA-seq expression data. Normalized enrichment score (NES), and false discovery rate q values (FDR) are shown.

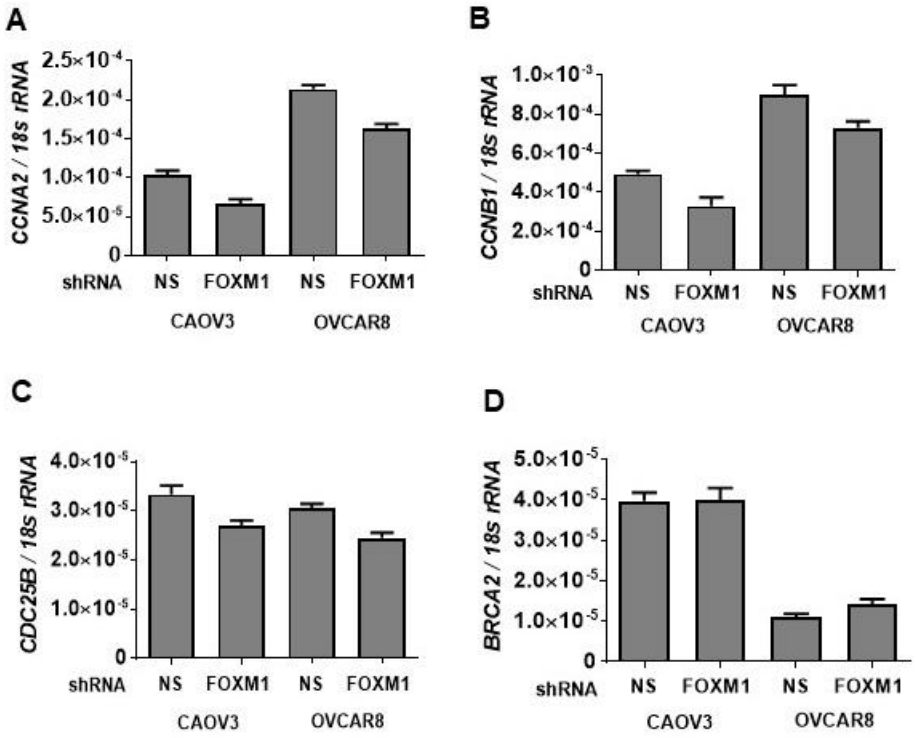

Figure 59. Validation of top differentially expressed genes from the RNA-seq analysis for HGSC cells with knockdown of FOXM1. A-D. A. *CCNA2* **B.** *CCNB1* **C.** *CDC25B* and **D.** *BRCA2* mRNA expression measured by RT-qPCR from CAOV3 and OVCAR8 cells expressing control or FOXM1 targeting shRNA. *BRCA2* did not show differential expression in the RNA-seq analysis, but instead was included used as a negative control.

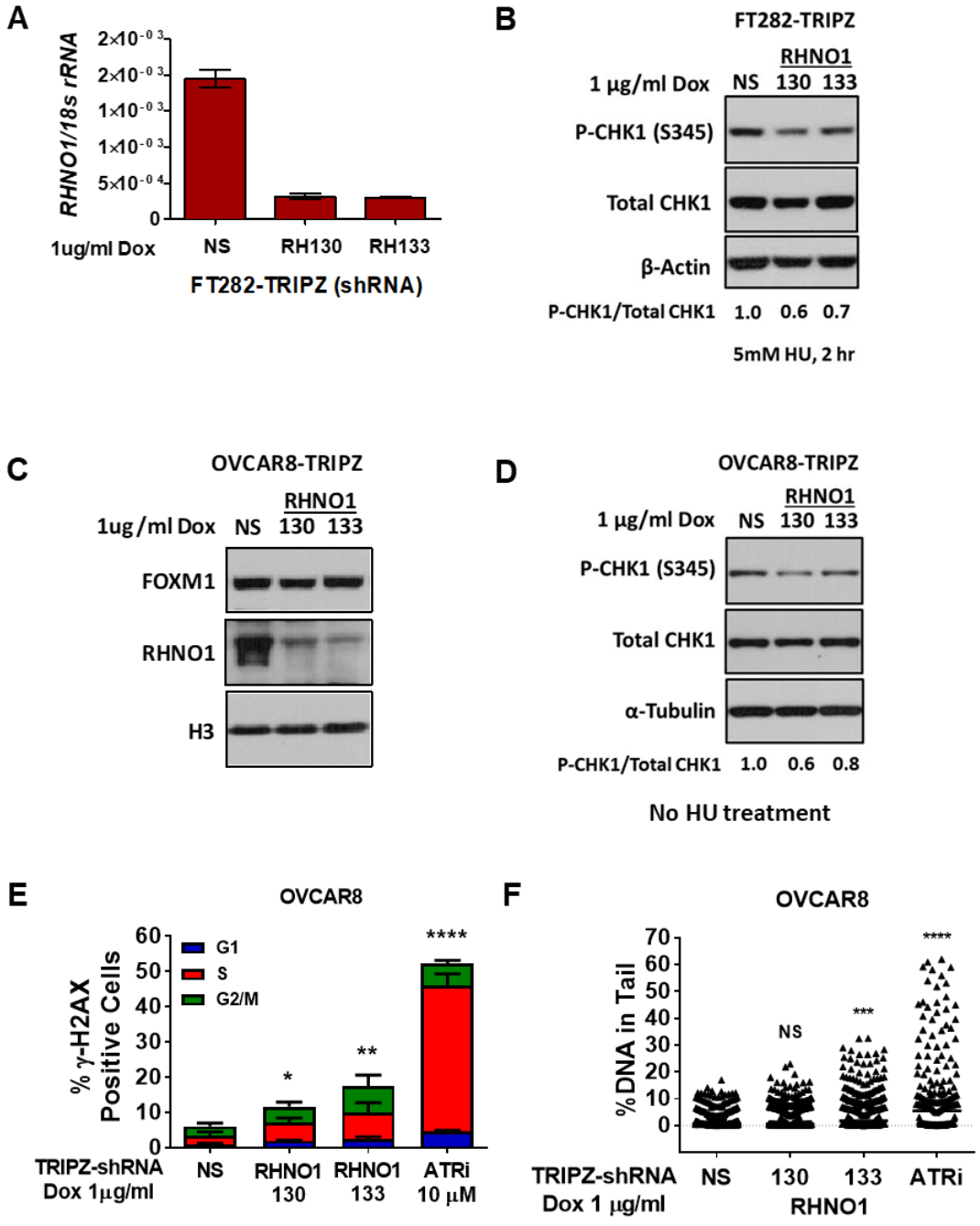
A
RHNO1/18s rRNA
2×10-03
2×10-03
1×10-03
1×10-03
5×10-04
0
1ug/ml Dox
NS
RH130
RH133
FT282-TRIPZ (shRNA)
B
FT282-TRIPZ
RHNO1
1 µg/ml Dox
NS 130 133
P-CHK1 (S345)
Total CHK1
β-Actin
P-CHK1/Total CHK1
1.0 0.6 0.7
5mM HU, 2 hr
C
OVCAR8-TRIPZ
RHNO1
1ug/ml Dox
NS 130 133
FOXM1
RHNO1
H3
D
OVCAR8-TRIPZ
RHNO1
1 µg/ml Dox
NS 130 133
P-CHK1 (S345)
Total CHK1
α-Tubulin
P-CHK1/Total CHK1
1.0 0.6 0.8
No HU treatment
E
OVCAR8
% γ-H2AX Positive Cells
60
50
40
30
20
10
0
G1
S
G2/M
*
**
****
TRIPZ-shRNA
Dox 1µg/ml
NS
RHNO1 130
RHNO1 133
ATRi 10 µM
F
OVCAR8
%DNA in Tail
70
60
50
40
30
20
10
0
NS
***
****
TRIPZ-shRNA
Dox 1 µg/ml
NS
130
133
ATRi
RHNO1

Figure 60.

Figure 60. RHNO1 promotes ATR-CHK1 signaling in FTE and HGSC cells. FT282 and OVCAR8 cells were engineered for doxycycline inducible RHNO1 knockdown. **A-B**. Inducible FT282 RHNO1 knockdown cells were seeded and grown in the presence of doxycycline for 72 hours to harvest RNA followed by **A.** RT-qPCR to confirm RHNO1 knockdown and protein followed **B.** Western blot analysis to measure the efficiency of ATR-CHK1 signaling. Cells for protein harvest received 2-hour treatment with 2 mM HU to induce DNA replication stress and ATR-CHK1 signaling. **C-D.** Inducible OVCAR8 RHNO1 knockdown cells were seeded and grown in the presence of doxycycline for 72 hours to harvest protein followed by Western blot analysis to **C.** confirm RHNO1 knockdown or **D.** measure the efficiency of ATR-CHK1 signaling at basal levels without HU treatment. **E-F**. Under the same conditions in C-D, Cells were harvested for the **E.** y-H2AX FACS analysis. ATRi was added at the indicated dose for 24 hours as a positive control. or **F.** Comet Assay. t test *P* value is shown. *P* value designation: **** < 0.0001, *** < 0.001, ** < 0.01, * < 0.05.

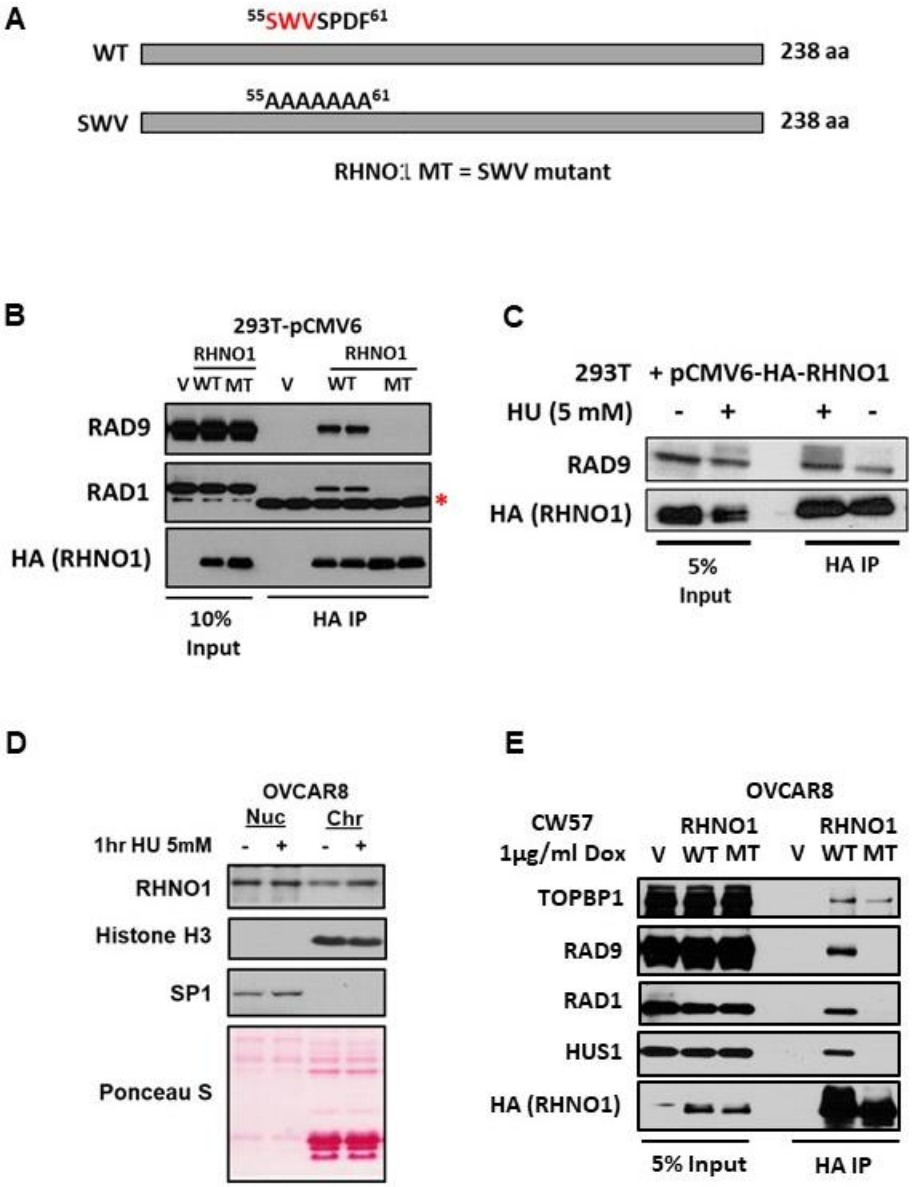
A
55SWVSPDF61
WT
238 aa
55AAAAAAA61
SWV
238 aa
RHNO1 MT = SWV mutant
B
293T-pCMV6
RHNO1
RHNO1
V WT MT
V
WT
MT
RAD9
RAD1
HA (RHNO1)
10% Input
HA IP
C
293T + pCMV6-HA-RHNO1
HU (5 mM) - + + -
RAD9
HA (RHNO1)
5% Input
HA IP
D
OVCAR8
Nuc
Chr
1hr HU 5mM - + - +
RHNO1
Histone H3
SP1
Ponceau S
E
OVCAR8
CW57
1μg/ml Dox
RHNO1
V WT MT
RHNO1
V WT MT
TOPBP1
RAD9
RAD1
HUS1
HA (RHNO1)
5% Input
HA IP

Figure 61.

Figure 61. RHNO1 interactions with 9-1-1 checkpoints proteins in 293T and OVCAR8 cells. A. Comparison **of** RHNO1 wild-type and SWV mutant proteins. The proteins are the same molecular weight, but they are different for residues 55-61. The residues at 55-61 were all converted to alanine for the SWV mutant, thus disrupting its ability to interact with 9-1-1 checkpoint proteins**. B.** 293T were transfected with empty vector, vector expressing HA tagged RHNO1 wild-type or SWV mutant. Protein was harvested 24 hours post transfection for co-immunoprecipitation and Western blot analysis. **C.** 293T cells were transfected with vector expressing HA tagged RHNO1 wild-type. Cells with treated with vehicle or 5 mM HU for 1 hour at 24 hours post transfection then protein was harvested for co-immunoprecipitation and Western blot analysis. **D.** OVCAR8 cells were seeded for growth for 24 hours then treated with vehicle or 5 mM HU for 1 hour then cells were harvest for subcellular fraction into soluble nuclear and chromatin bound protein followed by Western blot analysis to determine RHNO1 localization. Histone H3 was used as the chromatin control and Sp1 as the soluble nuclear control. **E.** OVCAR8 inducible RHNO1 knockdown cells were engineered for inducible expression of HA tagged RHNO1 wild-type or SWV mutant and grown in the presence of doxycycline for 72 hours then protein was harvested for co-immunoprecipitation and Western blot analysis.

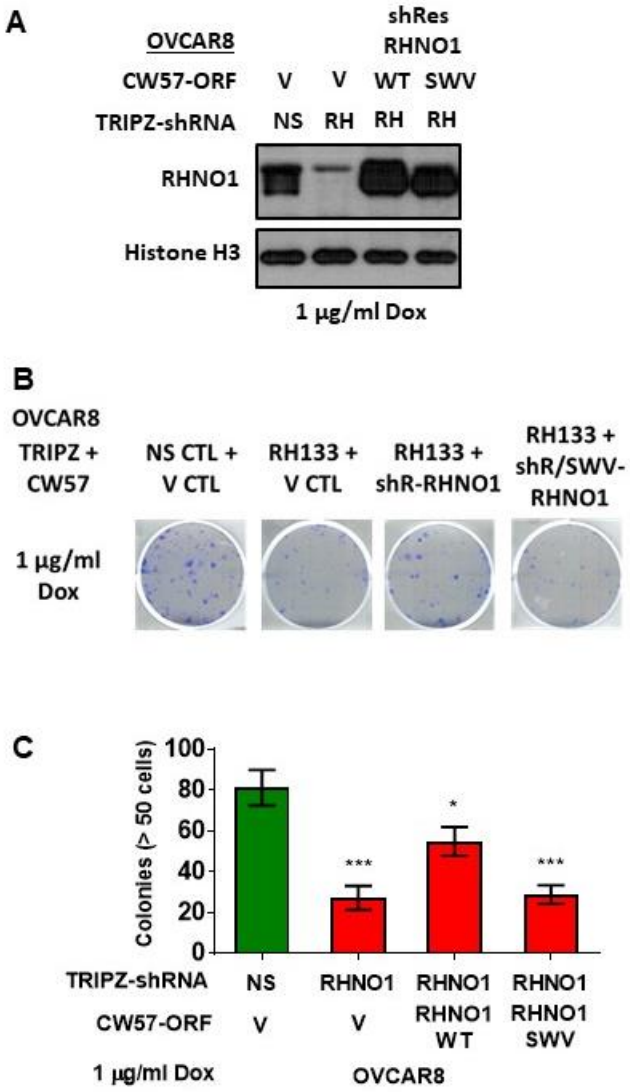
A
OVCAR8
shRes RHNO1
CW57-ORF V V WT SWV
TRIPZ-shRNA NS RH RH RH
RHNO1
Histone H3
1 µg/ml Dox
B
OVCAR8
TRIPZ + CW57
NS CTL + V CTL
RH133 + V CTL
RH133 + shR-RHNO1
RH133 + shR/SWV-RHNO1
1 µg/ml Dox
C
Colonies (> 50 cells)
100
80
60
40
20
0
***
*
***
TRIPZ-shRNA NS RHNO1 RHNO1 RHNO1
CW57-ORF V V RHNO1 WT RHNO1 SWV
1 µg/ml Dox
OVCAR8

Figure 62.

Figure 62. RHNO1 interaction with 9-1-1 checkpoint clamp is important for survival in HGSC cells. OVCAR8 inducible RHNO1 knockdown cells engineered for inducible expression of HA tagged RHNO1 wild-type or SWV mutant were seeded for protein or clonogenic survival. **A.** Cells were seeded in the presence of doxycycline and grown for 72 hours to harvest protein followed by Western blot to confirm knockdown efficiency**. B.** Cells were seeded into a 6-well dish, in triplicate, in the presence of doxycycline at a density of 500 cells. Media containing doxycycline was replenished every 48 hours. Clonogenic survival was measured at 12 days after the cells were fixed with methanol and stained with crystal violet. **C.** Colonies containing more than 50 cells were counted and clonogenic survival was quantified as an average of the replicates. NS = non-targeting shRNA. test P value is shown. P value designation: **** < 0.0001, *** < 0.001, ** < 0.01, * < 0.05.

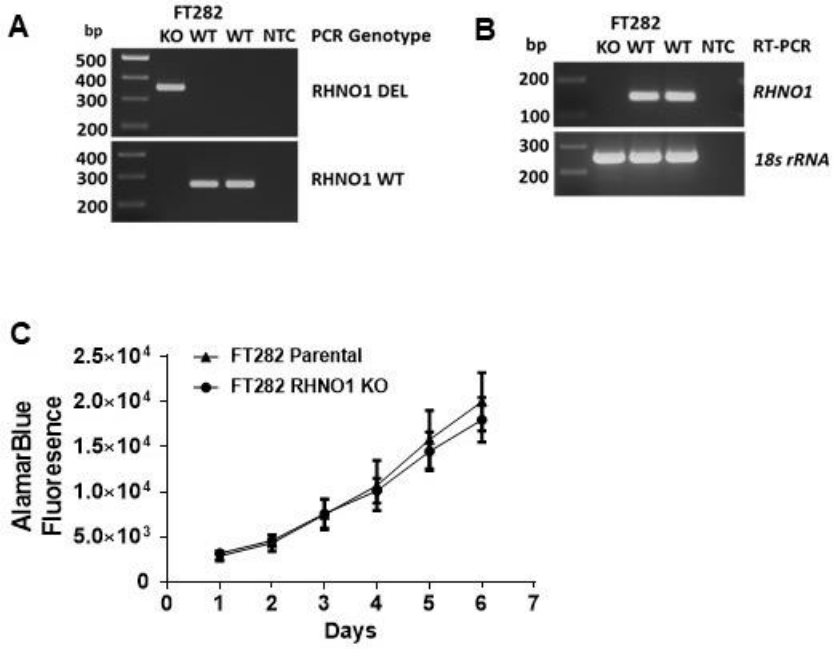

Figure 63. RHNO1 knockout in FTE cells does not impact cell viability. Homozygous deletion of RHNO1 in FT282 cells was achieved with CRISPR-Cas9 and guide RNAs that targeted near the start and stop codon. **A.** RHNO1 homozygous knockout was confirmed by **A.** PCR with genomic DNA and B. *RHNO1* mRNA expression measure by RT-PCR. **C.** FT282 parental and RHNO1 clonal knockout cells were seeded in quadruplicate and grown for a period of one-week. Cell viability was measured with the AlamarBlue assay every 24 hours.

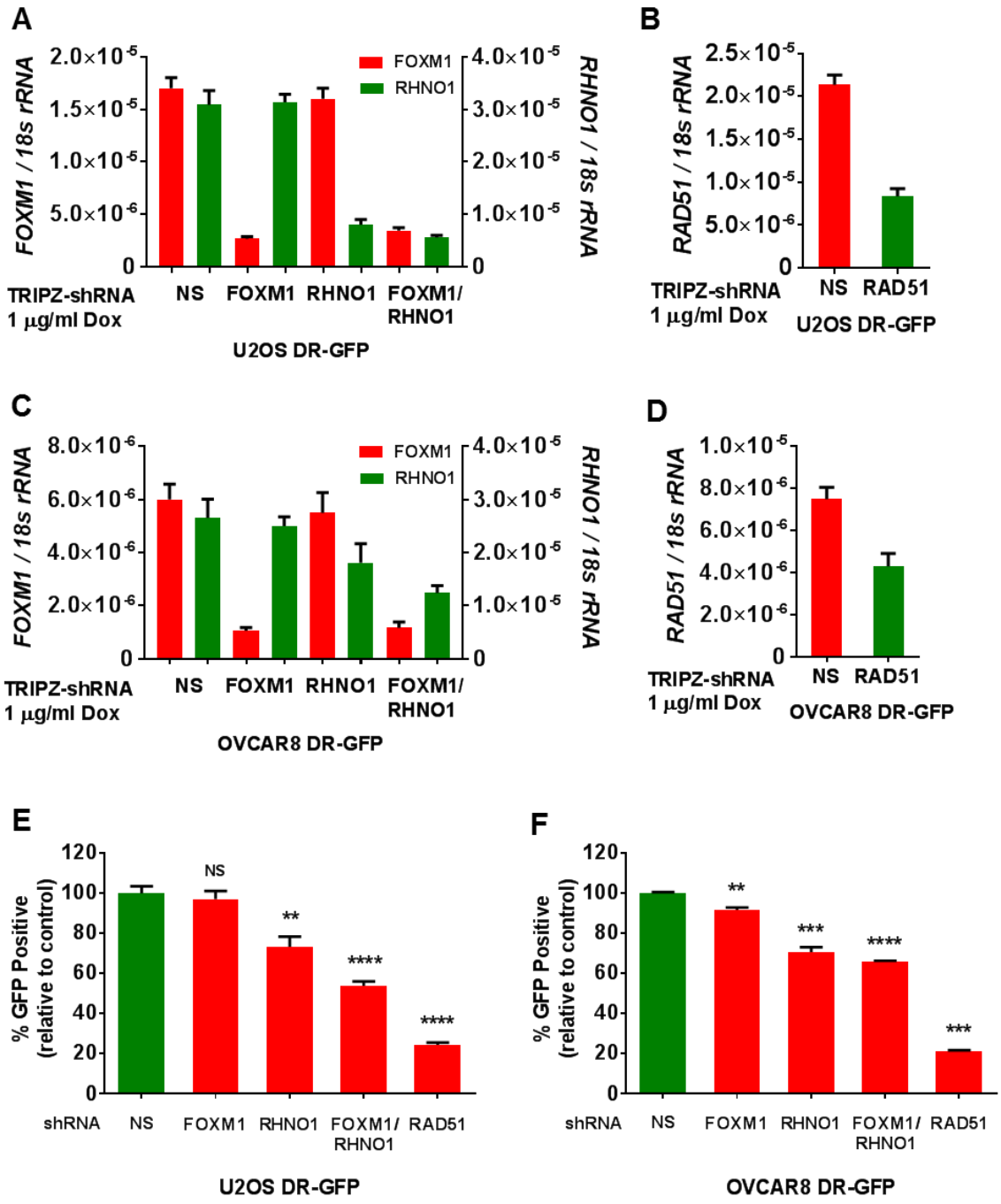
A
FOXM1 / 18s rRNA
RHNO1 / 18s rRNA
FOXM1
RHNO1
TRIPZ-shRNA
1 μg/ml Dox
NS
FOXM1
RHNO1
FOXM1/ RHNO1
U2OS DR-GFP
B
RAD51 / 18s rRNA
TRIPZ-shRNA
1 μg/ml Dox
NS
RAD51
U2OS DR-GFP
C
FOXM1 / 18s rRNA
RHNO1 / 18s rRNA
FOXM1
RHNO1
TRIPZ-shRNA
1 μg/ml Dox
NS
FOXM1
RHNO1
FOXM1/ RHNO1
OVCAR8 DR-GFP
D
RAD51 / 18s rRNA
TRIPZ-shRNA
1 μg/ml Dox
NS
RAD51
OVCAR8 DR-GFP
E
% GFP Positive (relative to control)
shRNA
NS
FOXM1
RHNO1
FOXM1/ RHNO1
RAD51
U2OS DR-GFP
F
% GFP Positive (relative to control)
shRNA
NS
FOXM1
RHNO1
FOXM1/ RHNO1
RAD51
OVCAR8 DR-GFP

Figure 64.

Figure 64. FOXM1 and RHNO1 bidirectional gene partners promote HR in U2OS and OVCAR8 cells. **A-D.** Cells were treated with doxycycline to induce shRNA expression and knockdown was confirmed by measuring **A and C.** *FOXM1* and *RHNO1* mRNA expression and **B and D.** *RAD51* mRNA expression by RT-qPCR. **E-F**. Following knockdown, the HR repair rate of I-SceI-induced DSBs was measured in **E.** U2OS and **F.** OVCAR8 DR-GFP cells. Each value is relative to the percentage of GFP-positive cells in I-SceI-transfected (U2OS) and transduced (OVCAR8) control cells. Results are shown as mean ± SE from three independent experiments; Student's *t*-test was used for comparisons. RAD51 knockdown was used as a positive control. All results are shown as mean ± SE from three independent replicates (*$P < 0.05$, **$P < 0.01$, ***$P < 0.005$).

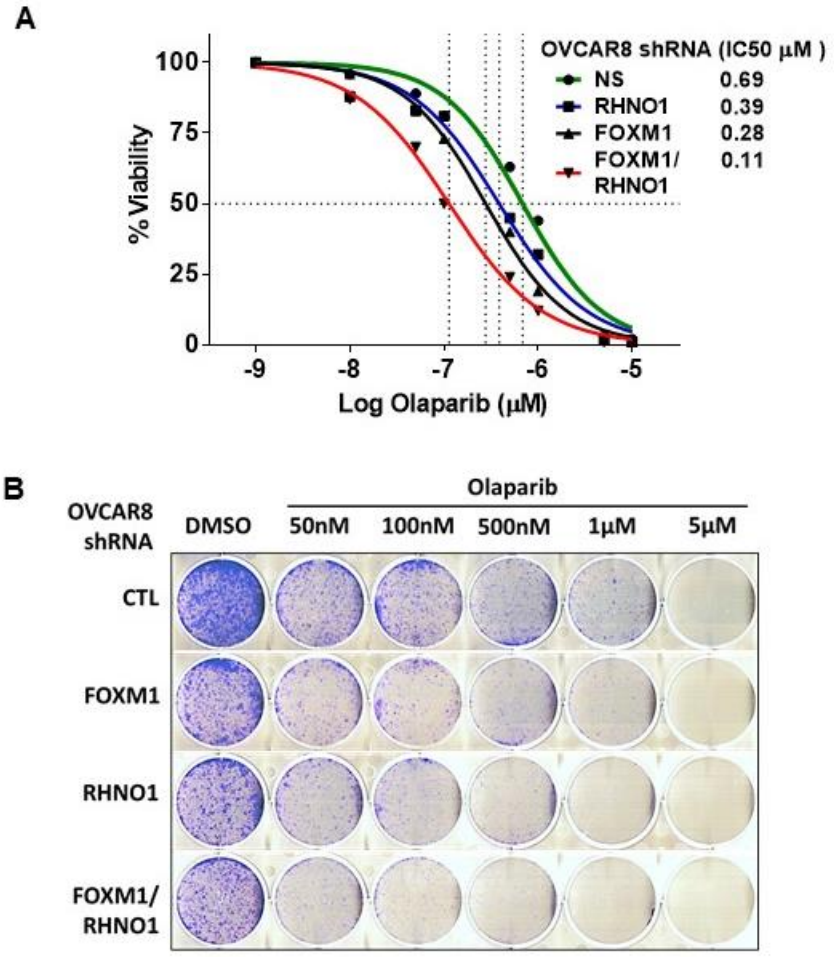
A
OVCAR8 shRNA (IC50 μM)
NS 0.69
RHNO1 0.39
FOXM1 0.28
FOXM1/ RHNO1 0.11
% Viability
100
75
50
25
0
-9
-8
-7
-6
-5
Log Olaparib (μM)
B
Olaparib
OVCAR8 shRNA
DMSO
50nM
100nM
500nM
1μM
5μM
CTL
FOXM1
RHNO1
FOXM1/ RHNO1

Figure 65.

Figure 65. FOXM1 and RHNO1 knockdown sensitizes OVCAR8 cells to olaparib. OVCAR8 cells engineered for FOXM1 and/or RHNO1 knockout were grown in the presence of doxycycline for 72 hours prior to seeding cells for olaparib IC50 or clonogenic survival. **A.** Cells were harvested then seeded in 96-well plates in quadruplicate in the presence of doxycycline at a density of 500 cells per well. Twenty-four hours later cells received media containing doxycycline and vehicle or olaparib, and this was repeated every 48 hours. Cell viability was measured at 8 days using AlamarBlue and the IC50 for olaparib was determined. **B**. Cells were harvested and seeded into a 6-well dish, in triplicate, in the presence of doxycycline at a density of 5,000 cells per well. Twenty-four hours later cells received media containing doxycycline and vehicle or olaparib, and this was repeated every 48 hours. Media containing doxycycline was replenished every 48 hours. After 8 days of growth, cells were fixed with methanol and stained with crystal violet. NS = non-targeting shRNA.

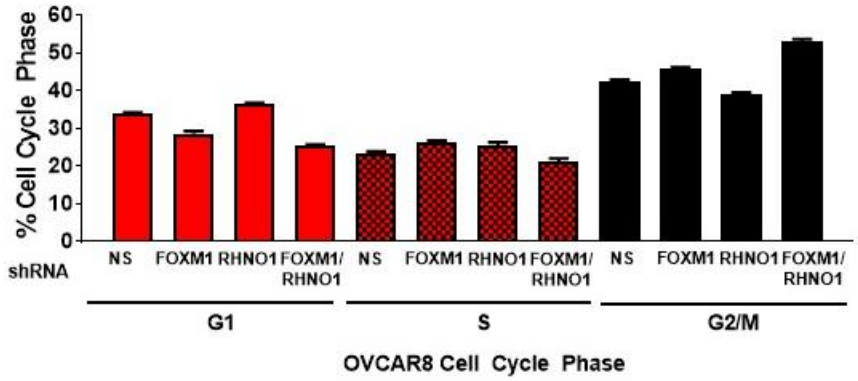

Figure 66. OVCAR8 FOXM1 and/or RHNO1 knockdown cells show increased cell cycle arrest following olaparib treatment. OVCAR8 FOXM1 and RHNO1 knockdown cells were treated with olaparib for 24 hours and the corresponding changes in Cell cycle analysis was were measured with PI staining.

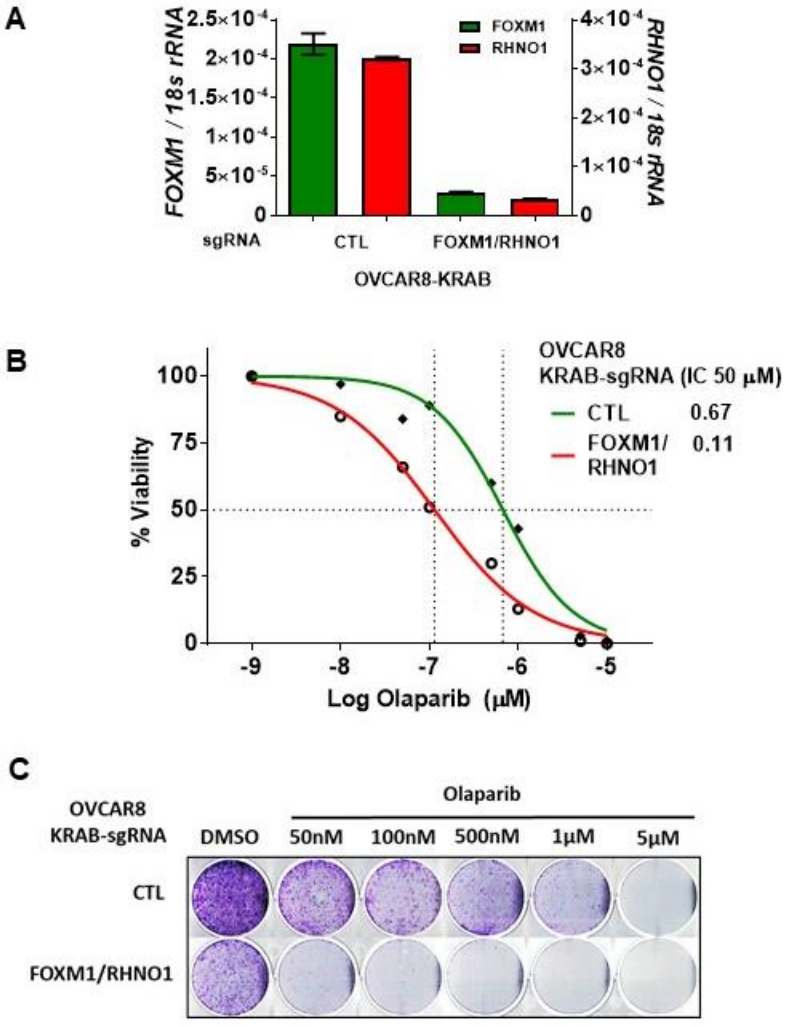
A
FOXM1 / 18s rRNA
RHNO1 / 18s rRNA
FOXM1
RHNO1
2.5×10⁻⁴
2×10⁻⁴
1.5×10⁻⁴
1×10⁻⁴
5×10⁻⁵
0
4×10⁻⁴
3×10⁻⁴
2×10⁻⁴
1×10⁻⁴
0
sgRNA
CTL
FOXM1/RHNO1
OVCAR8-KRAB
B
% Viability
100
75
50
25
0
-9
-8
-7
-6
-5
Log Olaparib (μM)
OVCAR8
KRAB-sgRNA (IC 50 μM)
CTL 0.67
FOXM1/ RHNO1 0.11
C
OVCAR8
KRAB-sgRNA
Olaparib
DMSO
50nM
100nM
500nM
1μM
5μM
CTL
FOXM1/RHNO1

Figure 67.

Figure 67. FOXM1/RHNO1 CRISPR inhibition sensitives OVCAR8 cells to olaparib treatment. A. OVCAR8 cells expressing KRAB transcriptional repressor and a guide RNA targeting the bidirectional promoter, and the corresponding changes in mRNA expression as measured by RT-qPCR. NT1 – non-targeting guide RNA. **B.** Cells were seeded in 96-well plates in quadruplicate at a density of 500 cells per well. Twenty-four hours later cells received media containing vehicle or olaparib, and this was repeated every 48 hours. Cell viability was measured at 8 days using AlamarBlue and the IC50 for olaparib was determined**. C**. Cells were seeded into a 6-well dish, in triplicate, at a density of 5000 cells per well. Twenty-four hours later cells received media containing vehicle or olaparib, and this was repeated every 48 hours. After 8 days of growth, cells were fixed with methanol and stained with crystal violet.

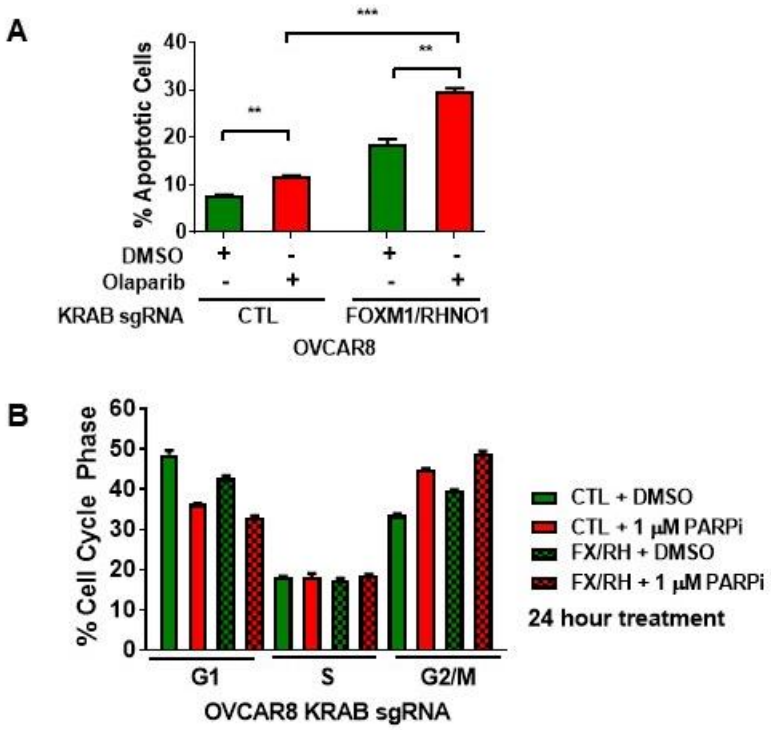

Figure 68. OVCAR8 FOXM1 and RHNO1 depleted cells show increased cell death and G2/M arrest after olaparib treatment. A-B. OVCAR8 cells expressing KRAB transcriptional repressor and a guide RNA targeting the bidirectional promoter were treated with olaparib for 24 hours and the corresponding changes in **A.** apoptosis were measured by Annexin V staining and FACS, and **B. c**ell cycle were measure measured with PI staining. t test *P* value is shown. *P* value designation: **** < 0.0001, *** < 0.001, ** < 0.01, * < 0.05.

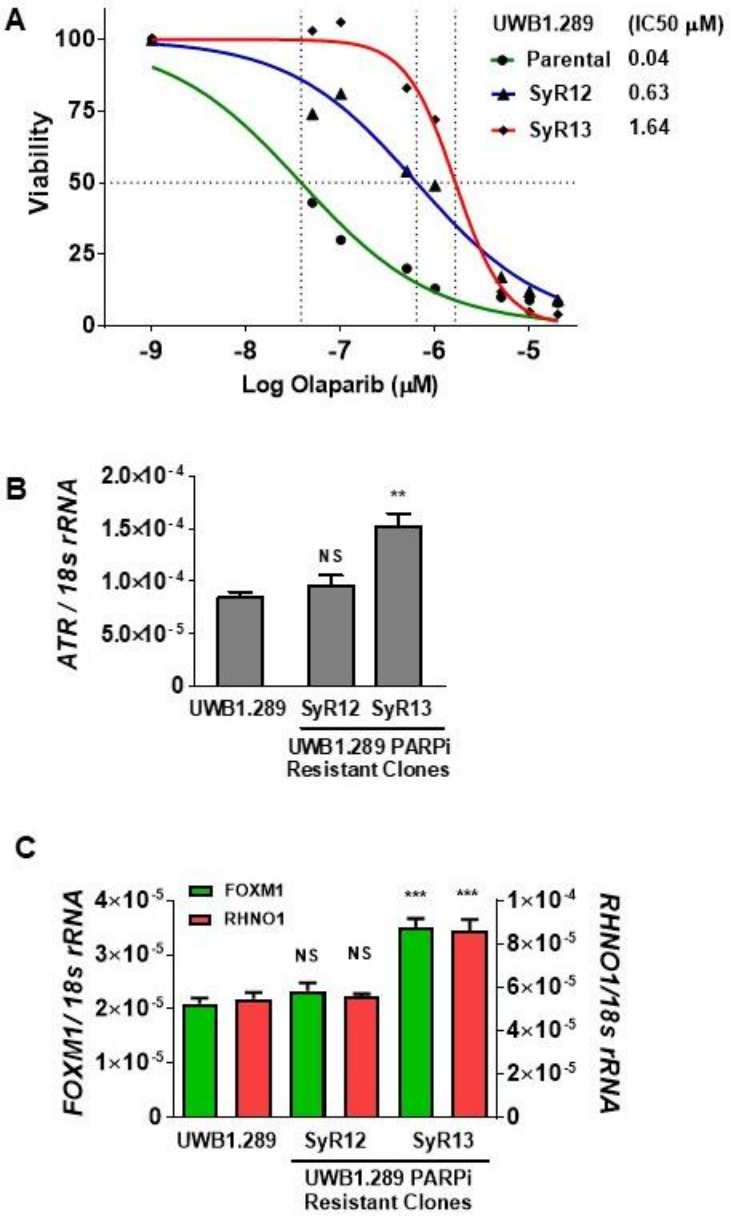
A
Viability
100
75
50
25
0
-9
-8
-7
-6
-5
Log Olaparib (μM)
UWB1.289 (IC50 μM)
Parental 0.04
SyR12 0.63
SyR13 1.64
B
ATR / 18s rRNA
2.0×10-4
1.5×10-4
1.0×10-4
5.0×10-5
0
NS
**
UWB1.289
SyR12
SyR13
UWB1.289 PARPi Resistant Clones
C
FOXM1/ 18s rRNA
RHNO1/18s rRNA
FOXM1
RHNO1
4×10-5
3×10-5
2×10-5
1×10-5
0
1×10-4
8×10-5
6×10-5
4×10-5
2×10-5
NS
NS
***
***
UWB1.289
SyR12
SyR13
UWB1.289 PARPi Resistant Clones

Figure 69.

Figure 69. Differential FOXM1 and RHNO1 expression and olaparib sensitivity for UWB1.289 parental cells and isogenic PARPi resistant clones. A. Cells were seeded in 96-well plates in quadruplicate at a density of 750 cells per well. Twenty-four hours later cells received media containing vehicle or olaparib, and this was repeated every 48 hours. Cell viability was measured at 8 days using AlamarBlue and the IC50 for olaparib was determined. **B-C.** Cells were seeded and grown for a period of 72 hours before RNA was harvested for RT-qPCR measurement of **B.** *ATR* mRNA expression and **C.** *FOXM1* and *RHNO1* mRNA expression. *t* test *P* value is shown. *P* value designation: **** < 0.0001, *** < 0.001, ** < 0.01, * < 0.05.

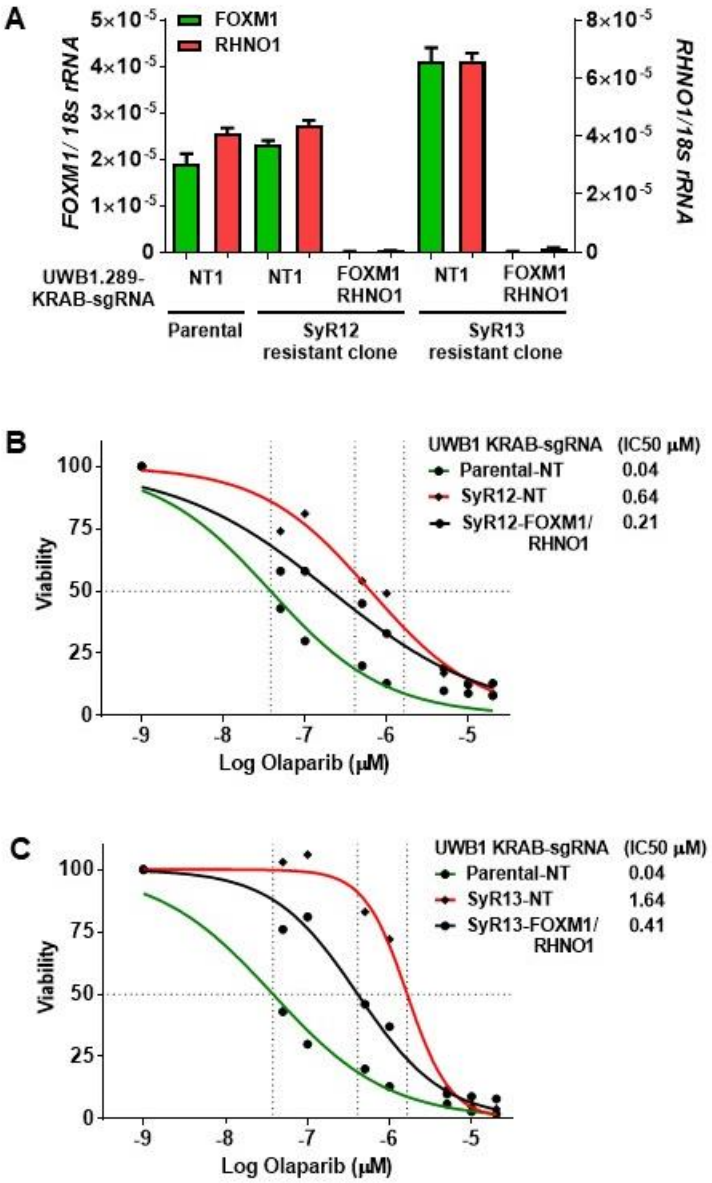
A
FOXM1
RHNO1
FOXM1/ 18s rRNA
RHNO1/18s rRNA
5×10-5
4×10-5
3×10-5
2×10-5
1×10-5
0
8×10-5
6×10-5
4×10-5
2×10-5
0
UWB1.289-KRAB-sgRNA
NT1
NT1
FOXM1 RHNO1
NT1
FOXM1 RHNO1
Parental
SyR12 resistant clone
SyR13 resistant clone
B
UWB1 KRAB-sgRNA (IC50 μM)
Parental-NT 0.04
SyR12-NT 0.64
SyR12-FOXM1/ RHNO1 0.21
Viability
100
75
50
25
0
-9
-8
-7
-6
-5
Log Olaparib (μM)
C
UWB1 KRAB-sgRNA (IC50 μM)
Parental-NT 0.04
SyR13-NT 1.64
SyR13-FOXM1/ RHNO1 0.41
Viability
100
75
50
25
0
-9
-8
-7
-6
-5
Log Olaparib (μM)

Figure 70.

Figure 70. Inhibition of FOXM1/RHNO1 in UWB1 resistant clones restores olaparib sensitivity. UWB1 parental and PARPi resistant cells were engineered to express KRAB transcriptional repressor and a control guide RNA or guide RNA targeting the bidirectional promoter. **A.** Cells were seeded and grown for 72 hours to harvest RNA followed by RT-qPCR to confirm knockdown efficiency**. B-C.** UWB1 parental KRAB and **B.** SyR12 KRAB or **C.** SyR13 KRAB cells were seeded in 96-well plates in quadruplicate at a density of 750 cells per well. Twenty-four hours later cells received media containing vehicle or olaparib, and this was repeated every 48 hours. Cell viability was measured at 8 days using AlamarBlue and the IC50 for olaparib was determined. NT1 – non-targeting guide RNA.

CHAPTER 6: DISCUSSION AND FUTURE DIRECTIONS

Genetic Determinants of FOXM1 Expression in HGSC

Several mechanisms have been reported to contribute to FOXM1 overexpression in cancer, including gene amplification, loss of negative regulation by p53, Rb, and FOXO3, and transcriptional activation by E2F and Myc (2,73-76,81,82). To date, the mechanisms underlying FOXM1 upregulation in HGSC have not been described, although FOXM1 pathway activation is extremely frequent in this malignancy. Here we demonstrate that, in HGSC, FOXM1 is upregulated at the transcriptional level by combined loss of Rb and p53, and show that *FOXM1* copy number gains correlate with increased FOXM1 expression in primary tumors and cell lines. Combinatorial loss of p53 and Rb in murine and human OSE cells synergistically induced FOXM1 expression, and murine ovarian cancer arising in a p53/Rb compound deletion model led to FOXM1 overexpression. In addition, we demonstrate that E2F1 contributes to FOXM1 overexpression in cell models, and closely correlates with FOXM1 expression in primary tumors. Genetic manipulation of the RB-E2F pathway in FTE cell models further supports a role for their regulation of FOXM1 expression in HGSC. Moreover, basal/TNBC breast cancer show similar patterns of *FOXM1* copy number gains as HGSC. Thus, our data establish p53 loss, RB-E2F deregulation and copy number gain as positive regulators, of FOXM1 expression in EOC. Consistent with our p53 data, it was recently shown that Nutlin 3 (an MDM2 inhibitor)-mediated p53 activation repressed FOXM1 in EOC cells (204).

Consistent with our findings, loss of Rb function leads to activation of E2F transcription factors (205), and two putative E2F sites have been identified in the *FOXM1* promoter (81). Second, the Rb-E2F pathway is regulated by p21, a potent negative regulator of cyclin-dependent kinases (CDKs) and a direct transcriptional target of p53.

Therefore, functional loss of p53 may relieve p21-mediated repression of E2F1, which in turn may promote FOXM1 expression. In agreement, prior work shows that p53-mediated repression of FOXM1 is partially p21-dependent (74,81). p53-mediated negative regulation of FOXM1 may also be independent of any effects on the Rb-E2F pathway, although this remains to be determined. In addition to p53, Rb, and E2F1, other relevant mechanisms of FOXM1 regulation involve Myc and FOXO3 (2,76). These may act independently or in concert with p53 and Rb loss, and require further study using EOC models.

Implications of FOXM1 Expression in HGSC

Importantly, a recent study showed increased FOXM1 IHC staining in STIC lesions, early HGSC precursor lesions, and that FOXM1 expression is maintained in invasive tumors (2). As TP53 mutations appear to be a ubiquitous early event in human HGSC, and Cyclin E1 overexpression occurs in STIC lesions (2,155), we speculate that during HGSC tumor progression, deregulation of the RB-E2F pathway and/or *FOXM1* amplification, coupled with the p53 impairment already present, leads to high level FOXM1 expression. Consistent with this model, our data indicate that FOXM1 expression is markedly elevated in late stage, high-grade disease. FOXM1 is not only expressed in STIC lesions and HGSC tumors, but also in FTE stem cells (2,206). These observations suggest that FOXM1 may have oncogenic potential that contributes both to early and late stages of HGSC progression. To test this hypothesis and determine if FOXM1 is important for HGSC development and/or progression, an HGSC mouse model should be engineered for inducible and temporal regulation of FOXM1 expression in the fallopian tube epithelium.

FOXM1 has three known splice variants: FOXM1a, b, and c, which encode proteins with varying activities (10). An earlier study showed that FOXM1c is the predominant isoform expressed in pancreatic cancer, while another study showed that FOXM1b is the major isoform expressed in other cancer types (79,207). FOXM1c has alternative exon A1; residues in this region can be phosphorylated by the RAF/MEK/MAPK signaling cascade, providing a distinction with FOXM1b (65). Considering the differential expression and functional potential of different FOXM1 isoforms, it is important to determine which variants are responsible for oncogenic activity in EOC. We performed a comprehensive analysis of *FOXM1* isoform expression in normal, HGSC and pan-cancer tissue and cell lines to determine isoform expression profile and if normal and cancer show differential isoform expression. We found that the predominant *FOXM1* isoform expressed in all contexts was FOXM1c. Furthermore, our cell cycle data suggests that FOXM1c, but not FOXM1b, drives cell cycle progression in hOSE cells. In agreement, FOXM1c promoted cell cycle progression in FTE cells. In contrast to the cell cycle phenotype, we found that all FOXM1 isoforms interacted with DNA replication proteins suggesting these isoforms may have important functions that are independent of their transcriptional activity. This is especially true for FOXM1a which is transcriptionally inactive. Alternatively, FOXM1 isoforms may complement each other to perform certain functions and possibly regulate each other through direct interaction, considering FOXM1 is capable of dimerizing (208,209). However, the knowledge of FOXM1 dimerization has been in the context of studies overexpressing a single isoform, FOXM1c and FOXM1b. In this setting, the homodimerization has been shown to repress transcriptional function until post-translational modifications relieve the protein-protein interaction, thus activating the protein (209,210). Furthermore, the functional role and regulation of dimerization may be cell context dependent based on the genetic background of the cell type, suggesting there might be differences between normal and cancer cells. Therefore, it remains unknown if

FOXM1 isoforms dimerize and if these interactions promote or inhibit function or give rise to a new function. Notably, a recent study discovered the expression of additional isoforms of FOXM1 in ovarian cancer and speculated that these isoforms may be constitutively active (211).

FOXM1 and CCNE1 and Genomic Instability in HGSC

Prior to this study, the role of FOXM1 in DNA replication stress and genomic instability had not been explored in HGSC, a disease characterized by FOXM1 overexpression and genomic instability. It was also unknown if FOXM1 promoted DNA replication stress in any context. Many phenotypes associate with genomic instability including increased proliferation, cell cycle progression and DNA replication stress, and we show that FOXM1 is associated with these phenotypes in HGSC. STIC lesions have both increased DNA damage and FOXM1 expression, suggesting they may be related. In the current study, we demonstrated a role for FOXM1 in cell cycle progression using primary and immortalized human HGSC precursor models and HGSC cell lines. Additionally, it is plausible that FOXM1 overexpression, combined with p53 gain of function mutations, may synergistically promote genomic instability in ovarian cancer. For example, FOXM1 upregulation induced genomic instability in normal human keratinocytes, and FOXM1 is a member of a conserved gene expression profile for genomic instability in human cancer (37,85,89). Furthermore, p53 gain of function mutations can positively regulate FOXM1 and correlate with higher levels of genomic instability as compared to p53 null mutations (204,212).

Interestingly, we observed a novel phenotype for FOXM1 where FOXM1 overexpression in FTE cells increased DNA fork rate suggesting a novel form of DNA replication stress unlike CCNE1 which decreased DNA fork rate. This phenotype appears

to be independent of FOXM1 transcriptional activity, but instead related to FOXM1 protein interacting with DNA replication proteins. However, this is speculative at this point and it requires additional studies to confirm this mechanism. Based on the data in our study and reports in the literature, it is possible that FOXM1 contributes to HGSC genesis and progression, through its promotion of genomic instability in STIC lesions, and promoting progression to HGSC. Notably, in our study, FOXM1 activation occurred downstream of Cyclin E1. We found that CCNE1 increased the transcriptional activity of FOXM1, promoted cell cycle progression and contributed to genomic instability. Cyclin E1 and FOXM1 are both expressed in STIC lesions, thus supporting a potential role for cooperativity in promoting genomic instability early in HGSC development (2,155).

FOXM1 and RHNO1 in HGSC Development and Progression

Our data thus far showed that FOXM1 and RHNO1 are frequently expressed in normal and cancer cells and tissues. Importantly, HGSC shows overexpression of both FOXM1 and RHNO1. The FOXM1/RHNO1 bidirectional promoter and copy number gains contribute to their frequent co-expression, but DNA methylation does not appear to regulate their expression. It remains unknown which transcription factors regulate the bidirectional promoter. Bidirectional promoters are overrepresented with following transcription factor motifs: GABPA, MYC, E2F1, E2F4, NRF-1, CCAAT, and YY1 (119). E2F1 appears to be a potential candidate for future studies related to the regulation of the bidirectional promoter based on our data showing a relationship between FOXM1 and E2F1 expression. In agreement, the bidirectional promoter has two E2F motifs. Additionally, FOXM1 is reported to regulate its own promoter through a positive feedback loop suggesting it may also regulate the bidirectional promoter, thus promote RHNO1

expression (213). However, we did not see a difference for RHNO1 expression in the RNA-seq analysis from FTE cells expressing FOXM1 or HGSC with FOXM1 knockdown.

We focused on FOXM1 and RHNO1 in the context of HGSC cell lines, specifically survival, genome stability and chemoresistance. Taken together, our data suggest a dual role for FOXM1: 1) promoting genomic instability in FTE cells, which suggest that FOXM1 promotes genomic instability early in HGSC development, contributing to the evolution of the disease, and 2) promoting genomic stability in HGSC cells, thus promoting survival and chemoresistance in tumors. Therefore, it is important to further differentiate and understand these phenotypes, but most importantly, to determine how RHNO1 contributes, *in vitro* and *in vivo*. FOXM1 has been studied for its ability to promote tumor formation in mouse models, and it was necessary but not sufficient for tumor formation, while RHNO1 has never been studied *in vivo*. Our data suggests cooperatives roles for FOXM1 and RHNO1 using *in vitro* models, therefore, *in vivo* studies should be further revealing. More broadly, bidirectional gene partners have never been studied *in vivo*, therefore, these experiments would provide much needed knowledge to expand the concept of cooperativity between bidirectional gene partners in oncogenesis

FOXM1 and RHNO1 in Chemoresistance and HR DNA Repair, and Potential for Therapeutic Targeting

We showed that FOXM1 and RHNO1 loss decreased homologous recombination DNA repair and sensitized HGSC cells to the PARP inhibitor olaparib. We observed that FOXM1 loss alone sensitized HGSC cells to PARP inhibitor, but surprisingly, our RNA-seq analysis did not reveal DNA repair genes as transcriptional targets of FOXM1. However, we observed that FOXM1 regulated genes involved in the G2/M checkpoint and in agreement, cell cycle analysis showed that FOXM1 loss increased the number of G2/M

cells. Furthermore, we observed that FOXM1 promoted DNA fork progression in FTE cells, a function that appears to be independent of its transcriptional activity. Therefore, we hypothesize that FOXM1 may be promoting chemoresistance in HGSC cells through protein interactions with DNA repair and chromatin modifying proteins, and not through its transcriptional activity. Further studies are needed to test this hypothesis.

Importantly, we observed that PARP inhibitor sensitization was greatest when both FOXM1 and RHNO1 were inhibited. These data support additional studies to determine if FOXM1 and RHNO1 loss will sensitive HGSC cells to other chemotherapeutic agents. Potential candidates for these studies include carboplatin and paclitaxel based on previous studies showing that FOXM1 promotes resistance to these drugs (199-201,214,215). CHK1 inhibitor has been shown to be synthetically lethal with ATR inhibitor, suggesting that RHNO1 loss may synergize with a CHK1 inhibitor (216). RHNO1 functions proximal to ATR, therefore, we would expect there to be synergy with a CHK1 inhibitor and potentially not an ATR inhibitor. We also observed a novel function for FOXM1 in promoting increased DNA fork rate so potentially inhibition of FOXM1 and RHNO1 in combination with CHK1 inhibition will show the greatest synergy.

Based on growing recognition of the oncogenic role of FOXM1 in cancer, there is great interest in developing drugs to target this protein. This is particularly true in HGSC, for which the current therapeutic regimens are inadequate. Until recently, FOXM1 targeting drugs, such as the thiazole antibiotics Siomycin A and Thiostrepton, were non-specific and had global effects on proteasome-dependent pathways (217,218). However, Gormally *et al*. recently reported the identification and characterization of a specific inhibitor of FOXM1, which they named FDI-6 (219). Importantly, FDI-6 specifically inhibited the DNA binding activity of FOXM1, but not other FOX family members, and inhibited cancer cell growth *in vitro*. However, FDI-6 will need further validation because there are

concerns about its specificity for FOXM1 only and not other forkhead family members specificity (220), and the potency will need improvement for *in vivo* treatment of FOXM1-dependent cancers. Regardless, the existence of a specific inhibitor of FOXM1 provides a new opportunity for translational studies of FOXM1-dependent cancers, including HGSC. Furthermore, there are currently no inhibitors of RHNO1. Therefore, ATR inhibitors could be used in lieu of RHNO1 inhibition to combine with FOXM1 inhibitors as a potentially feasible and novel treatment strategy for HGSC.

CONCLUSION

Our data identified genetic mechanisms that contribute to FOXM1 overexpression in HGSC. More importantly, we determined the functional consequences of FOXM1 overexpression in HGSC, showing that FOXM1 promotes cell cycle progression and alters DNA replication dynamics, thus providing a mechanistic link to its association with genomic instability. We identified FOXM1 activation downstream of Cyclin E1-induced DNA replication stress, which cooperatively promoted cell cycle progression, increased transcriptional activity and enriched the CIN70 gene expression signature. In agreement, HGSC tumors with copy number gain for both FOXM1 and CCNE1 showed increased genomic instability. Furthermore, for the first time, we investigated the contribution of FOXM1 and its bidirectional gene partner, RHNO1, in HGSC cell survival and chemoresistance, showing that FOXM1 and RHNO1 augment the phenotypes to a greater extent than either gene alone. Finally, taken together, our data support additional *in vitro* and *in vivo* studies focusing on the cooperativity of FOXM1 and RHNO1 bidirectional gene partners, to further understand their contribution to HGSC development, progression and survival.

LITERATURE CITED

1. Vaughan S, Coward JI, Bast RC, Jr., Berchuck A, Berek JS, Brenton JD*, et al.* Rethinking ovarian cancer: recommendations for improving outcomes. Nat Rev Cancer **2011**;11:719-25
2. Levanon K, Sapoznik S, Bahar-Shany K, Brand H, Shapira-Frommer R, Korach J*, et al.* FOXO3a loss is a frequent early event in high-grade pelvic serous carcinogenesis. Oncogene **2014**;33:4424-32
3. Quinet A, Carvajal-Maldonado D, Lemacon D, Vindigni A. DNA Fiber Analysis: Mind the Gap! Methods Enzymol **2017**;591:55-82
4. Karst AM, Drapkin R. Primary culture and immortalization of human fallopian tube secretory epithelial cells. Nat Protoc **2012**;7:1755-64
5. Lindsey-Boltz LA, Kemp MG, Capp C, Sancar A. RHINO forms a stoichiometric complex with the 9-1-1 checkpoint clamp and mediates ATR-Chk1 signaling. Cell Cycle **2015**;14:99-108
6. Siegel RL, Miller KD, Jemal A. Cancer statistics, 2018. CA Cancer J Clin **2018**;68:7-30
7. Siegel R, Ma J, Zou Z, Jemal A. Cancer statistics, 2014. CA: a cancer journal for clinicians **2014**;64:9-29
8. Romero I, Bast RC, Jr. Minireview: human ovarian cancer: biology, current management, and paths to personalizing therapy. Endocrinology **2012**;153:1593-602
9. Serov SF, Scully RE, Sobin LH. Histological typing of ovarian tumors. Geneva: World Health Organization1973.
10. Scully R, Xobin L. Histological typing of ovarian tumours. New York: Springer Berlin1999.
11. Prat J. Staging classification for cancer of the ovary, fallopian tube, and peritoneum. International journal of gynaecology and obstetrics: the official organ of the International Federation of Gynaecology and Obstetrics **2014**;124:1-5
12. Benedet JL, Bender H, Jones H, 3rd, Ngan HY, Pecorelli S. FIGO staging classifications and clinical practice guidelines in the management of gynecologic cancers. FIGO Committee on Gynecologic Oncology. International journal of gynaecology and obstetrics: the official organ of the International Federation of Gynaecology and Obstetrics **2000**;70:209-62
13. Cho KR, Shih Ie M. Ovarian cancer. Annual review of pathology **2009**;4:287-313
14. Malpica A, Deavers MT, Lu K, Bodurka DC, Atkinson EN, Gershenson DM*, et al.* Grading ovarian serous carcinoma using a two-tier system. The American journal of surgical pathology **2004**;28:496-504
15. Diaz-Padilla I, Malpica AL, Minig L, Chiva LM, Gershenson DM, Gonzalez-Martin A. Ovarian low-grade serous carcinoma: a comprehensive update. Gynecologic oncology **2012**;126:279-85
16. Roett MA, Evans P. Ovarian cancer: an overview. American family physician **2009**;80:609-16
17. Siegel R, Naishadham D, Jemal A. Cancer statistics, 2013. CA: a cancer journal for clinicians **2013**;63:11-30
18. Drake J. Diagnosis and management of the adnexal mass. American family physician **1998**;57:2471-6, 9-80
19. Yin BW, Lloyd KO. Molecular cloning of the CA125 ovarian cancer antigen: identification as a new mucin, MUC16. The Journal of biological chemistry **2001**;276:27371-5
20. Bast RC, Jr., Klug TL, St John E, Jenison E, Niloff JM, Lazarus H*, et al.* A

radioimmunoassay using a monoclonal antibody to monitor the course of epithelial ovarian cancer. The New England journal of medicine **1983**;309:883-7
21. Gynecologists ACoOa. The role of the generalist obstetrician-gynecologist in the early detection of ovarian cancer. Gynecologic oncology **2002**;87:237-9
22. Auersperg N, Wong AS, Choi KC, Kang SK, Leung PC. Ovarian surface epithelium: biology, endocrinology, and pathology. Endocrine reviews **2001**;22:255-88
23. Fathalla MF. Incessant ovulation--a factor in ovarian neoplasia? Lancet **1971**;2:163
24. Piek JM, van Diest PJ, Zweemer RP, Jansen JW, Poort-Keesom RJ, Menko FH*, et al.* Dysplastic changes in prophylactically removed Fallopian tubes of women predisposed to developing ovarian cancer. J Pathol **2001**;195:451-6
25. Erickson BK, Conner MG, Landen CN, Jr. The role of the fallopian tube in the origin of ovarian cancer. American journal of obstetrics and gynecology **2013**;209:409-14
26. Piek JM, Verheijen RH, Kenemans P, Massuger LF, Bulten H, van Diest PJ. BRCA1/2-related ovarian cancers are of tubal origin: a hypothesis. Gynecologic oncology **2003**;90:491
27. O'Shannessy DJ, Jackson SM, Twine NC, Hoffman BE, Dezso Z, Agoulnik SI*, et al.* Gene expression analyses support fallopian tube epithelium as the cell of origin of epithelial ovarian cancer. International journal of molecular sciences **2013**;14:13687-703
28. Klinkebiel D, Zhang W, Akers SN, Odunsi K, Karpf AR. DNA Methylome Analyses Implicate Fallopian Tube Epithelia as the Origin for High-Grade Serous Ovarian Cancer. Mol Cancer Res **2016**;14:787-94
29. Labidi-Galy SI, Papp E, Hallberg D, Niknafs N, Adleff V, Noe M*, et al.* High grade serous ovarian carcinomas originate in the fallopian tube. Nat Commun **2017**;8:1093
30. Cancer Genome Atlas Research N. Integrated genomic analyses of ovarian carcinoma. Nature **2011**;474:609-15
31. Ciriello G, Miller ML, Aksoy BA, Senbabaoglu Y, Schultz N, Sander C. Emerging landscape of oncogenic signatures across human cancers. Nat Genet **2013**;45:1127-33
32. Network CGA. Comprehensive molecular portraits of human breast tumours. Nature **2012**;490:61-70
33. Zack TI, Schumacher SE, Carter SL, Cherniack AD, Saksena G, Tabak B*, et al.* Pan-cancer patterns of somatic copy number alteration. Nat Genet **2013**;45:1134-40
34. Etemadmoghadam D, Weir BA, Au-Yeung G, Alsop K, Mitchell G, George J*, et al.* Synthetic lethality between CCNE1 amplification and loss of BRCA1. Proc Natl Acad Sci U S A **2013**;110:19489-94
35. Teixeira LK, Wang X, Li Y, Ekholm-Reed S, Wu X, Wang P*, et al.* Cyclin E deregulation promotes loss of specific genomic regions. Curr Biol **2015**;25:1327-33
36. Barger CJ, Zhang W, Hillman J, Stablewski AB, Higgins MJ, Vanderhyden BC*, et al.* Genetic determinants of FOXM1 overexpression in epithelial ovarian cancer and functional contribution to cell cycle progression. Oncotarget **2015**;6:27613-27
37. Carter SL, Eklund AC, Kohane IS, Harris LN, Szallasi Z. A signature of chromosomal instability inferred from gene expression profiles predicts clinical outcome in multiple human cancers. Nature genetics **2006**;38:1043-8
38. Gentles AJ, Newman AM, Liu CL, Bratman SV, Feng W, Kim D*, et al.* The

prognostic landscape of genes and infiltrating immune cells across human cancers. Nat Med **2015**;21:938-45
39. Dai J, Yang L, Wang J, Xiao Y, Ruan Q. Prognostic Value of FOXM1 in Patients with Malignant Solid Tumor: A Meta-Analysis and System Review. Dis Markers **2015**;2015:352478
40. Halasi M, Gartel AL. FOX(M1) news--it is cancer. Molecular cancer therapeutics **2013**;12:245-54
41. Bowtell DD, Bohm S, Ahmed AA, Aspuria PJ, Bast RC, Jr., Beral V*, et al.* Rethinking ovarian cancer II: reducing mortality from high-grade serous ovarian cancer. Nat Rev Cancer **2015**;15:668-79
42. Bowtell DD. The genesis and evolution of high-grade serous ovarian cancer. Nat Rev Cancer **2010**;10:803-8
43. Stuart GC, Kitchener H, Bacon M, duBois A, Friedlander M, Ledermann J*, et al.* 2010 Gynecologic Cancer InterGroup (GCIG) consensus statement on clinical trials in ovarian cancer: report from the Fourth Ovarian Cancer Consensus Conference. International journal of gynecological cancer : official journal of the International Gynecological Cancer Society **2011**;21:750-5
44. Vergote I, Trope CG, Amant F, Kristensen GB, Ehlen T, Johnson N*, et al.* Neoadjuvant chemotherapy or primary surgery in stage IIIC or IV ovarian cancer. The New England journal of medicine **2010**;363:943-53
45. Farmer H, McCabe N, Lord CJ, Tutt AN, Johnson DA, Richardson TB*, et al.* Targeting the DNA repair defect in BRCA mutant cells as a therapeutic strategy. Nature **2005**;434:917-21
46. Bryant HE, Schultz N, Thomas HD, Parker KM, Flower D, Lopez E*, et al.* Specific killing of BRCA2-deficient tumours with inhibitors of poly(ADP-ribose) polymerase. Nature **2005**;434:913-7
47. Kaelin WG. The concept of synthetic lethality in the context of anticancer therapy. Nat Rev Cancer **2005**;5:689-98
48. Lord CJ, Tutt AN, Ashworth A. Synthetic lethality and cancer therapy: lessons learned from the development of PARP inhibitors. Annu Rev Med **2015**;66:455-70
49. Lord CJ, Ashworth A. PARP inhibitors: Synthetic lethality in the clinic. Science **2017**;355:1152-8
50. Audeh MW, Carmichael J, Penson RT, Friedlander M, Powell B, Bell-McGuinn KM*, et al.* Oral poly(ADP-ribose) polymerase inhibitor olaparib in patients with BRCA1 or BRCA2 mutations and recurrent ovarian cancer: a proof-of-concept trial. Lancet **2010**;376:245-51
51. Fong PC, Boss DS, Yap TA, Tutt A, Wu P, Mergui-Roelvink M*, et al.* Inhibition of poly(ADP-ribose) polymerase in tumors from BRCA mutation carriers. N Engl J Med **2009**;361:123-34
52. Ledermann J, Harter P, Gourley C, Friedlander M, Vergote I, Rustin G*, et al.* Olaparib maintenance therapy in platinum-sensitive relapsed ovarian cancer. N Engl J Med **2012**;366:1382-92
53. Kaufman B, Shapira-Frommer R, Schmutzler RK, Audeh MW, Friedlander M, Balmaña J*, et al.* Olaparib monotherapy in patients with advanced cancer and a germline BRCA1/2 mutation. J Clin Oncol **2015**;33:244-50
54. Kim G, Ison G, McKee AE, Zhang H, Tang S, Gwise T*, et al.* FDA Approval Summary: Olaparib Monotherapy in Patients with Deleterious Germline BRCA-Mutated Advanced Ovarian Cancer Treated with Three or More Lines of Chemotherapy. Clin Cancer Res **2015**;21:4257-61
55. Bitler BG, Watson ZL, Wheeler LJ, Behbakht K. PARP inhibitors: Clinical utility and possibilities of overcoming resistance. Gynecol Oncol **2017**;147:695-704

56. Fojo T, Bates S. Mechanisms of resistance to PARP inhibitors--three and counting. Cancer Discov **2013**;3:20-3
57. Sonnenblick A, de Azambuja E, Azim HA, Piccart M. An update on PARP inhibitors--moving to the adjuvant setting. Nat Rev Clin Oncol **2015**;12:27-41
58. Westendorf JM, Rao PN, Gerace L. Cloning of cDNAs for M-phase phosphoproteins recognized by the MPM2 monoclonal antibody and determination of the phosphorylated epitope. Proc Natl Acad Sci U S A **1994**;91:714-8
59. Korver W, Roose J, Clevers H. The winged-helix transcription factor Trident is expressed in cycling cells. Nucleic Acids Res **1997**;25:1715-9
60. Myatt SS, Lam EW. The emerging roles of forkhead box (Fox) proteins in cancer. Nature reviews Cancer **2007**;7:847-59
61. Wierstra I, Alves J. Despite its strong transactivation domain, transcription factor FOXM1c is kept almost inactive by two different inhibitory domains. Biol Chem **2006**;387:963-76
62. Chen X, Muller GA, Quaas M, Fischer M, Han N, Stutchbury B*, et al.* The forkhead transcription factor FOXM1 controls cell cycle-dependent gene expression through an atypical chromatin binding mechanism. Molecular and cellular biology **2013**;33:227-36
63. Ye H, Kelly TF, Samadani U, Lim L, Rubio S, Overdier DG*, et al.* Hepatocyte nuclear factor 3/fork head homolog 11 is expressed in proliferating epithelial and mesenchymal cells of embryonic and adult tissues. Molecular and cellular biology **1997**;17:1626-41
64. Yao KM, Sha M, Lu Z, Wong GG. Molecular analysis of a novel winged helix protein, WIN. Expression pattern, DNA binding property, and alternative splicing within the DNA binding domain. J Biol Chem **1997**;272:19827-36
65. Ma RY, Tong TH, Cheung AM, Tsang AC, Leung WY, Yao KM. Raf/MEK/MAPK signaling stimulates the nuclear translocation and transactivating activity of FOXM1c. Journal of cell science **2005**;118:795-806
66. Wang IC, Chen YJ, Hughes D, Petrovic V, Major ML, Park HJ*, et al.* Forkhead box M1 regulates the transcriptional network of genes essential for mitotic progression and genes encoding the SCF (Skp2-Cks1) ubiquitin ligase. Mol Cell Biol **2005**;25:10875-94
67. Wonsey DR, Follettie MT. Loss of the forkhead transcription factor FoxM1 causes centrosome amplification and mitotic catastrophe. Cancer Res **2005**;65:5181-9
68. Laoukili J, Kooistra MR, Bras A, Kauw J, Kerkhoven RM, Morrison A*, et al.* FoxM1 is required for execution of the mitotic programme and chromosome stability. Nat Cell Biol **2005**;7:126-36
69. Krupczak-Hollis K, Wang X, Kalinichenko VV, Gusarova GA, Wang IC, Dennewitz MB*, et al.* The mouse Forkhead Box m1 transcription factor is essential for hepatoblast mitosis and development of intrahepatic bile ducts and vessels during liver morphogenesis. Dev Biol **2004**;276:74-88
70. Costa RH. FoxM1 dances with mitosis. Nat Cell Biol **2005**;7:108-10
71. Laoukili J, Alvarez-Fernandez M, Stahl M, Medema RH. FoxM1 is degraded at mitotic exit in a Cdh1-dependent manner. Cell Cycle **2008**;7:2720-6
72. Laoukili J, Stahl M, Medema RH. FoxM1: at the crossroads of ageing and cancer. Biochim Biophys Acta **2007**;1775:92-102
73. Pandit B, Halasi M, Gartel AL. p53 negatively regulates expression of FoxM1. Cell cycle **2009**;8:3425-7
74. Barsotti AM, Prives C. Pro-proliferative FoxM1 is a target of p53-mediated repression. Oncogene **2009**;28:4295-305
75. McGovern UB, Francis RE, Peck B, Guest SK, Wang J, Myatt SS*, et al.* Gefitinib

(Iressa) represses FOXM1 expression via FOXO3a in breast cancer. Molecular cancer therapeutics **2009**;8:582-91
76. Blanco-Bose WE, Murphy MJ, Ehninger A, Offner S, Dubey C, Huang W*, et al.* C-Myc and its target FoxM1 are critical downstream effectors of constitutive androstane receptor (CAR) mediated direct liver hyperplasia. Hepatology **2008**;48:1302-11
77. Mencalha AL, Binato R, Ferreira GM, Du Rocher B, Abdelhay E. Forkhead box M1 (FoxM1) gene is a new STAT3 transcriptional factor target and is essential for proliferation, survival and DNA repair of K562 cell line. PloS one **2012**;7:e48160
78. Teh MT, Wong ST, Neill GW, Ghali LR, Philpott MP, Quinn AG. FOXM1 is a downstream target of Gli1 in basal cell carcinomas. Cancer research **2002**;62:4773-80
79. Kong X, Li L, Li Z, Le X, Huang C, Jia Z*, et al.* Dysregulated expression of FOXM1 isoforms drives progression of pancreatic cancer. Cancer research **2013**;73:3987-96
80. Xia LM, Huang WJ, Wang B, Liu M, Zhang Q, Yan W*, et al.* Transcriptional up-regulation of FoxM1 in response to hypoxia is mediated by HIF-1. J Cell Biochem **2009**;106:247-56
81. Millour J, de Olano N, Horimoto Y, Monteiro LJ, Langer JK, Aligue R*, et al.* ATM and p53 regulate FOXM1 expression via E2F in breast cancer epirubicin treatment and resistance. Molecular cancer therapeutics **2011**;10:1046-58
82. Yu J, Deshmukh H, Payton JE, Dunham C, Scheithauer BW, Tihan T*, et al.* Array-based comparative genomic hybridization identifies CDK4 and FOXM1 alterations as independent predictors of survival in malignant peripheral nerve sheath tumor. Clin Cancer Res **2011**;17:1924-34
83. Korver W, Schilham MW, Moerer P, van den Hoff MJ, Dam K, Lamers WH*, et al.* Uncoupling of S phase and mitosis in cardiomyocytes and hepatocytes lacking the winged-helix transcription factor Trident. Curr Biol **1998**;8:1327-30
84. Kalin TV, Ustiyan V, Kalinichenko VV. Multiple faces of FoxM1 transcription factor: lessons from transgenic mouse models. Cell Cycle **2011**;10:396-405
85. Teh MT, Gemenetzidis E, Chaplin T, Young BD, Philpott MP. Upregulation of FOXM1 induces genomic instability in human epidermal keratinocytes. Mol Cancer **2010**;9:45
86. Liu Y, Gong Z, Sun L, Li X. FOXM1 and androgen receptor co-regulate CDC6 gene transcription and DNA replication in prostate cancer cells. Biochim Biophys Acta **2014**;1839:297-305
87. Anders L, Ke N, Hydbring P, Choi YJ, Widlund HR, Chick JM*, et al.* A systematic screen for CDK4/6 substrates links FOXM1 phosphorylation to senescence suppression in cancer cells. Cancer Cell **2011**;20:620-34
88. Kotsantis P, Petermann E, Boulton SJ. Mechanisms of Oncogene-Induced Replication Stress: Jigsaw Falling into Place. Cancer Discov **2018**
89. Gemenetzidis E, Bose A, Riaz AM, Chaplin T, Young BD, Ali M*, et al.* FOXM1 upregulation is an early event in human squamous cell carcinoma and it is enhanced by nicotine during malignant transformation. PLoS One **2009**;4:e4849
90. Molinuevo R, Freije A, de Pedro I, Stoll SW, Elder JT, Gandarillas A. FOXM1 allows human keratinocytes to bypass the oncogene-induced differentiation checkpoint in response to gain of MYC or loss of p53. Oncogene **2017**;36:956-65
91. Tan Y, Raychaudhuri P, Costa RH. Chk2 mediates stabilization of the FoxM1 transcription factor to stimulate expression of DNA repair genes. Mol Cell Biol **2007**;27:1007-16
92. Macheret M, Halazonetis TD. DNA replication stress as a hallmark of cancer. Annu

Rev Pathol **2015**;10:425-48
93. Gaillard H, García-Muse T, Aguilera A. Replication stress and cancer. Nat Rev Cancer **2015**;15:276-89
94. Dobbelstein M, Sørensen CS. Exploiting replicative stress to treat cancer. Nat Rev Drug Discov **2015**;14:405-23
95. Costantino L, Sotiriou SK, Rantala JK, Magin S, Mladenov E, Helleday T*, et al.* Break-induced replication repair of damaged forks induces genomic duplications in human cells. Science **2014**;343:88-91
96. Arlt MF, Wilson TE, Glover TW. Replication stress and mechanisms of CNV formation. Curr Opin Genet Dev **2012**;22:204-10
97. Halazonetis TD, Gorgoulis VG, Bartek J. An oncogene-induced DNA damage model for cancer development. Science **2008**;319:1352-5
98. Abbas T, Keaton MA, Dutta A. Genomic instability in cancer. Cold Spring Harb Perspect Biol **2013**;5:a012914
99. Cimprich KA, Cortez D. ATR: an essential regulator of genome integrity. Nat Rev Mol Cell Biol **2008**;9:616-27
100. Cotta-Ramusino C, McDonald ER, 3rd, Hurov K, Sowa ME, Harper JW, Elledge SJ. A DNA damage response screen identifies RHINO, a 9-1-1 and TopBP1 interacting protein required for ATR signaling. Science **2011**;332:1313-7
101. Kousholt AN, Menzel T, Sorensen CS. Pathways for genome integrity in G2 phase of the cell cycle. Biomolecules **2012**;2:579-607
102. Zhang Y, Hunter T. Roles of Chk1 in cell biology and cancer therapy. International journal of cancer Journal international du cancer **2014**;134:1013-23
103. Jackson SP, Helleday T. DNA REPAIR. Drugging DNA repair. Science **2016**;352:1178-9
104. Buisson R, Boisvert JL, Benes CH, Zou L. Distinct but Concerted Roles of ATR, DNA-PK, and Chk1 in Countering Replication Stress during S Phase. Mol Cell **2015**;59:1011-24
105. Karnitz LM, Zou L. Molecular Pathways: Targeting ATR in Cancer Therapy. Clin Cancer Res **2015**
106. O'Connor MJ. Targeting the DNA Damage Response in Cancer. Mol Cell **2015**;60:547-60
107. Fang B. Development of synthetic lethality anticancer therapeutics. J Med Chem **2014**;57:7859-73
108. Huntoon CJ, Flatten KS, Wahner Hendrickson AE, Huehls AM, Sutor SL, Kaufmann SH*, et al.* ATR inhibition broadly sensitizes ovarian cancer cells to chemotherapy independent of BRCA status. Cancer Res **2013**;73:3683-91
109. Weber AM, Ryan AJ. ATM and ATR as therapeutic targets in cancer. Pharmacol Ther **2015**;149:124-38
110. Ma CX, Janetka JW, Piwnica-Worms H. Death by releasing the breaks: CHK1 inhibitors as cancer therapeutics. Trends Mol Med **2011**;17:88-96
111. Negrini S, Gorgoulis VG, Halazonetis TD. Genomic instability--an evolving hallmark of cancer. Nat Rev Mol Cell Biol **2010**;11:220-8
112. Adachi N, Lieber MR. Bidirectional gene organization: a common architectural feature of the human genome. Cell **2002**;109:807-9
113. Takai D, Jones PA. Origins of bidirectional promoters: computational analyses of intergenic distance in the human genome. Mol Biol Evol **2004**;21:463-7
114. Trinklein ND, Aldred SF, Hartman SJ, Schroeder DI, Otillar RP, Myers RM. An abundance of bidirectional promoters in the human genome. Genome Res **2004**;14:62-6
115. Yang M, Elnitski L. Orthology-driven mapping of bidirectional promoters in human

and mouse genomes. BMC Bioinformatics **2014**;15 Suppl 17:S1
116. Yang MQ, Taylor J, Elnitski L. Comparative analyses of bidirectional promoters in vertebrates. BMC Bioinformatics **2008**;9 Suppl 6:S9
117. Wakano C, Byun JS, Di LJ, Gardner K. The dual lives of bidirectional promoters. Biochim Biophys Acta **2012**;1819:688-93
118. Bornelov S, Komorowski J, Wadelius C. Different distribution of histone modifications in genes with unidirectional and bidirectional transcription and a role of CTCF and cohesin in directing transcription. BMC Genomics **2015**;16:300
119. Lin JM, Collins PJ, Trinklein ND, Fu Y, Xi H, Myers RM*, et al.* Transcription factor binding and modified histones in human bidirectional promoters. Genome Res **2007**;17:818-27
120. Yang MQ, Koehly LM, Elnitski LL. Comprehensive annotation of bidirectional promoters identifies co-regulation among breast and ovarian cancer genes. PLoS Comput Biol **2007**;3:e72
121. Matsuoka S, Ballif BA, Smogorzewska A, McDonald ER, 3rd, Hurov KE, Luo J*, et al.* ATM and ATR substrate analysis reveals extensive protein networks responsive to DNA damage. Science **2007**;316:1160-6
122. Kim JW, Fukukawa C, Ueda K, Nishidate T, Katagiri T, Nakamura Y. Involvement of C12orf32 overexpression in breast carcinogenesis. Int J Oncol **2010**;37:861-7
123. Liu Q, Guntuku S, Cui XS, Matsuoka S, Cortez D, Tamai K*, et al.* Chk1 is an essential kinase that is regulated by Atr and required for the G(2)/M DNA damage checkpoint. Genes Dev **2000**;14:1448-59
124. Serov SF, Scully RE, Sobin LH. Histological typing of ovarian tumours [by] S. F. Serov [and] R. E. Scully in collaboration with L. H. Sobin and pathologists in ten countries. Geneva,: World Health Organization; 1973. 56 p. p.
125. Li NF, Broad S, Lu YJ, Yang JS, Watson R, Hagemann T*, et al.* Human ovarian surface epithelial cells immortalized with hTERT maintain functional pRb and p53 expression. Cell Prolif **2007**;40:780-94
126. Bast RC, Jr., Hennessy B, Mills GB. The biology of ovarian cancer: new opportunities for translation. Nature reviews Cancer **2009**;9:415-28
127. Gunn A, Bennardo N, Cheng A, Stark JM. Correct end use during end joining of multiple chromosomal double strand breaks is influenced by repair protein RAD50, DNA-dependent protein kinase DNA-PKcs, and transcription context. J Biol Chem **2011**;286:42470-82
128. Gunn A, Stark JM. I-SceI-based assays to examine distinct repair outcomes of mammalian chromosomal double strand breaks. Methods Mol Biol **2012**;920:379-91
129. Subramanian A, Tamayo P, Mootha VK, Mukherjee S, Ebert BL, Gillette MA*, et al.* Gene set enrichment analysis: a knowledge-based approach for interpreting genome-wide expression profiles. Proc Natl Acad Sci U S A **2005**;102:15545-50
130. Fang P, Madden JA, Neums L, Moulder KR, Forrest ML, Chien J. Olaparib-induced Adaptive Response is Disrupted by FOXM1 Targeting which Enhances Sensitivity to PARP Inhibition. Mol Cancer Res **2018**
131. Pierce AJ, Johnson RD, Thompson LH, Jasin M. XRCC3 promotes homology-directed repair of DNA damage in mammalian cells. Genes Dev **1999**;13:2633-8
132. Sanders DA, Gormally MV, Marsico G, Beraldi D, Tannahill D, Balasubramanian S. FOXM1 binds directly to non-consensus sequences in the human genome. Genome Biol **2015**;16:130
133. Flesken-Nikitin A, Choi KC, Eng JP, Shmidt EN, Nikitin AY. Induction of carcinogenesis by concurrent inactivation of p53 and Rb1 in the mouse ovarian surface epithelium. Cancer research **2003**;63:3459-63

134. Ye J, Coulouris G, Zaretskaya I, Cutcutache I, Rozen S, Madden TL. Primer-BLAST: a tool to design target-specific primers for polymerase chain reaction. BMC Bioinformatics **2012**;13:134
135. Schneider CA, Rasband WS, Eliceiri KW. NIH Image to ImageJ: 25 years of image analysis. Nat Methods **2012**;9:671-5
136. Iorio F, Knijnenburg TA, Vis DJ, Bignell GR, Menden MP, Schubert M*, et al.* A Landscape of Pharmacogenomic Interactions in Cancer. Cell **2016**;166:740-54
137. Reinhold WC, Sunshine M, Liu H, Varma S, Kohn KW, Morris J*, et al.* CellMiner: a web-based suite of genomic and pharmacologic tools to explore transcript and drug patterns in the NCI-60 cell line set. Cancer research **2012**;72:3499-511
138. Shankavaram UT, Varma S, Kane D, Sunshine M, Chary KK, Reinhold WC*, et al.* CellMiner: a relational database and query tool for the NCI-60 cancer cell lines. BMC Genomics **2009**;10:277
139. Clark SJ, Harrison J, Paul CL, Frommer M. High sensitivity mapping of methylated cytosines. Nucleic acids research **1994**;22:2990-7
140. MethPrimer.
141. Kent WJ, Sugnet CW, Furey TS, Roskin KM, Pringle TH, Zahler AM*, et al.* The human genome browser at UCSC. Genome Res **2002**;12:996-1006
142. Jackson DA, Pombo A. Replicon clusters are stable units of chromosome structure: evidence that nuclear organization contributes to the efficient activation and propagation of S phase in human cells. J Cell Biol **1998**;140:1285-95
143. Ray Chaudhuri A, Hashimoto Y, Herrador R, Neelsen KJ, Fachinetti D, Bermejo R*, et al.* Topoisomerase I poisoning results in PARP-mediated replication fork reversal. Nat Struct Mol Biol **2012**;19:417-23
144. Li J, Lu Y, Akbani R, Ju Z, Roebuck PL, Liu W*, et al.* TCPA: a resource for cancer functional proteomics data. Nat Methods **2013**;10:1046-7
145. Li J, Akbani R, Zhao W, Lu Y, Weinstein JN, Mills GB*, et al.* Explore, Visualize, and Analyze Functional Cancer Proteomic Data Using the Cancer Proteome Atlas. Cancer Res **2017**;77:e51-e4
146. Beroukhim R, Getz G, Nghiemphu L, Barretina J, Hsueh T, Linhart D*, et al.* Assessing the significance of chromosomal aberrations in cancer: methodology and application to glioma. Proceedings of the National Academy of Sciences of the United States of America **2007**;104:20007-12
147. Haber AL, Biton M, Rogel N, Herbst RH, Shekhar K, Smillie C*, et al.* A single-cell survey of the small intestinal epithelium. Nature **2017**;551:333-9
148. Tirosh I, Izar B, Prakadan SM, Wadsworth MH, Treacy D, Trombetta JJ*, et al.* Dissecting the multicellular ecosystem of metastatic melanoma by single-cell RNA-seq. Science **2016**;352:189-96
149. Winterhoff BJ, Maile M, Mitra AK, Sebe A, Bazzaro M, Geller MA*, et al.* Single cell sequencing reveals heterogeneity within ovarian cancer epithelium and cancer associated stromal cells. Gynecol Oncol **2017**;144:598-606
150. Li WV, Li JJ. An accurate and robust imputation method scImpute for single-cell RNA-seq data. Nat Commun **2018**;9:997
151. Consortium EP. An integrated encyclopedia of DNA elements in the human genome. Nature **2012**;489:57-74
152. Miotto B, Ji Z, Struhl K. Selectivity of ORC binding sites and the relation to replication timing, fragile sites, and deletions in cancers. Proc Natl Acad Sci U S A **2016**;113:E4810-9
153. Stavrovskaya ED, Niranjan T, Fertig EJ, Wheelan SJ, Favorov AV, Mironov AA. StereoGene: rapid estimation of genome-wide correlation of continuous or interval feature data. Bioinformatics **2017**;33:3158-65

154. Kuo KT, Guan B, Feng Y, Mao TL, Chen X, Jinawath N*, et al.* Analysis of DNA copy number alterations in ovarian serous tumors identifies new molecular genetic changes in low-grade and high-grade carcinomas. Cancer research **2009**;69:4036-42
155. Karst AM, Jones PM, Vena N, Ligon AH, Liu JF, Hirsch MS*, et al.* Cyclin E1 deregulation occurs early in secretory cell transformation to promote formation of fallopian tube-derived high-grade serous ovarian cancers. Cancer Res **2014**;74:1141-52
156. Akbani R, Ng PK, Werner HM, Shahmoradgoli M, Zhang F, Ju Z*, et al.* A pan-cancer proteomic perspective on The Cancer Genome Atlas. Nat Commun **2014**;5:3887
157. Vivian J, Rao AA, Nothaft FA, Ketchum C, Armstrong J, Novak A*, et al.* Toil enables reproducible, open source, big biomedical data analyses. Nat Biotechnol **2017**;35:314-6
158. Woloszynska-Read A, James SR, Link PA, Yu J, Odunsi K, Karpf AR. DNA methylation-dependent regulation of BORIS/CTCFL expression in ovarian cancer. Cancer immunity **2007**;7:21
159. Woloszynska-Read A, Zhang W, Yu J, Link PA, Mhawech-Fauceglia P, Collamat G*, et al.* Coordinated cancer germline antigen promoter and global DNA hypomethylation in ovarian cancer: association with the BORIS/CTCF expression ratio and advanced stage. Clinical cancer research : an official journal of the American Association for Cancer Research **2011**;17:2170-80
160. Domcke S, Sinha R, Levine DA, Sander C, Schultz N. Evaluating cell lines as tumour models by comparison of genomic profiles. Nature communications **2013**;4:2126
161. McCloskey CW, Goldberg RL, Carter LE, Gamwell LF, Al-Hujaily EM, Collins O*, et al.* A new spontaneously transformed syngeneic model of high-grade serous ovarian cancer with a tumor-initiating cell population. Frontiers in oncology **2014**;4:53
162. Garson K, Gamwell LF, Pitre EM, Vanderhyden BC. Technical challenges and limitations of current mouse models of ovarian cancer. Journal of ovarian research **2012**;5:39
163. Clark-Knowles KV, Senterman MK, Collins O, Vanderhyden BC. Conditional inactivation of Brca1, p53 and Rb in mouse ovaries results in the development of leiomyosarcomas. PloS one **2009**;4:e8534
164. Nicolay BN, Danielian PS, Kottakis F, Lapek JD, Sanidas I, Miles WO*, et al.* Proteomic analysis of pRb loss highlights a signature of decreased mitochondrial oxidative phosphorylation. Genes Dev **2015**;29:1875-89
165. Sanjana NE, Shalem O, Zhang F. Improved vectors and genome-wide libraries for CRISPR screening. Nat Methods **2014**;11:783-4
166. Leung TW, Lin SS, Tsang AC, Tong CS, Ching JC, Leung WY*, et al.* Over-expression of FoxM1 stimulates cyclin B1 expression. FEBS letters **2001**;507:59-66
167. Wang Z, Banerjee S, Kong D, Li Y, Sarkar FH. Down-regulation of Forkhead Box M1 transcription factor leads to the inhibition of invasion and angiogenesis of pancreatic cancer cells. Cancer research **2007**;67:8293-300
168. Chan DW, Yu SY, Chiu PM, Yao KM, Liu VW, Cheung AN*, et al.* Over-expression of FOXM1 transcription factor is associated with cervical cancer progression and pathogenesis. The Journal of pathology **2008**;215:245-52
169. Zeman MK, Cimprich KA. Causes and consequences of replication stress. Nat Cell Biol **2014**;16:2-9

170. Littler DR, Alvarez-Fernández M, Stein A, Hibbert RG, Heidebrecht T, Aloy P*, et al.* Structure of the FoxM1 DNA-recognition domain bound to a promoter sequence. Nucleic Acids Res **2010**;38:4527-38
171. Chen YJ, Dominguez-Brauer C, Wang Z, Asara JM, Costa RH, Tyner AL*, et al.* A conserved phosphorylation site within the forkhead domain of FoxM1B is required for its activation by cyclin-CDK1. J Biol Chem **2009**;284:30695-707
172. Neelsen KJ, Zanini IM, Herrador R, Lopes M. Oncogenes induce genotoxic stress by mitotic processing of unusual replication intermediates. J Cell Biol **2013**;200:699-708
173. Bianco JN, Poli J, Saksouk J, Bacal J, Silva MJ, Yoshida K*, et al.* Analysis of DNA replication profiles in budding yeast and mammalian cells using DNA combing. Methods **2012**;57:149-57
174. Bartkova J, Rezaei N, Liontos M, Karakaidos P, Kletsas D, Issaeva N*, et al.* Oncogene-induced senescence is part of the tumorigenesis barrier imposed by DNA damage checkpoints. Nature **2006**;444:633-7
175. Jones RM, Mortusewicz O, Afzal I, Lorvellec M, García P, Helleday T*, et al.* Increased replication initiation and conflicts with transcription underlie Cyclin E-induced replication stress. Oncogene **2013**;32:3744-53
176. Singhal G, Leo E, Setty SK, Pommier Y, Thimmapaya B. Adenovirus E1A oncogene induces rereplication of cellular DNA and alters DNA replication dynamics. J Virol **2013**;87:8767-78
177. Deutzmann A, Ganz M, Schönenberger F, Vervoorts J, Kappes F, Ferrando-May E. The human oncoprotein and chromatin architectural factor DEK counteracts DNA replication stress. Oncogene **2015**;34:4270-7
178. Rimmelé P, Komatsu J, Hupé P, Roulin C, Barillot E, Dutreix M*, et al.* Spi-1/PU.1 oncogene accelerates DNA replication fork elongation and promotes genetic instability in the absence of DNA breakage. Cancer Res **2010**;70:6757-66
179. Sincennes MC, Humbert M, Grondin B, Lisi V, Veiga DF, Haman A*, et al.* The LMO2 oncogene regulates DNA replication in hematopoietic cells. Proc Natl Acad Sci U S A **2016**;113:1393-8
180. Hills SA, Diffley JF. DNA replication and oncogene-induced replicative stress. Curr Biol **2014**;24:R435-44
181. Dominguez-Sola D, Gautier J. MYC and the control of DNA replication. Cold Spring Harb Perspect Med **2014**;4
182. Kurat CF, Yeeles JTP, Patel H, Early A, Diffley JFX. Chromatin Controls DNA Replication Origin Selection, Lagging-Strand Synthesis, and Replication Fork Rates. Mol Cell **2017**;65:117-30
183. Tibes R, Qiu Y, Lu Y, Hennessy B, Andreeff M, Mills GB*, et al.* Reverse phase protein array: validation of a novel proteomic technology and utility for analysis of primary leukemia specimens and hematopoietic stem cells. Mol Cancer Ther **2006**;5:2512-21
184. Li X, Wang W, Wang J, Malovannaya A, Xi Y, Li W*, et al.* Proteomic analyses reveal distinct chromatin-associated and soluble transcription factor complexes. Mol Syst Biol **2015**;11:775
185. Carr JR, Kiefer MM, Park HJ, Li J, Wang Z, Fontanarosa J*, et al.* FoxM1 regulates mammary luminal cell fate. Cell Rep **2012**;1:715-29
186. Wierstra I, Alves J. FOXM1c is activated by cyclin E/Cdk2, cyclin A/Cdk2, and cyclin A/Cdk1, but repressed by GSK-3alpha. Biochem Biophys Res Commun **2006**;348:99-108
187. Wierstra I, Alves J. Transcription factor FOXM1c is repressed by RB and activated by cyclin D1/Cdk4. Biol Chem **2006**;387:949-62

188. Wierstra I, Alves J. Cyclin E/Cdk2, P/CAF, and E1A regulate the transactivation of the c-myc promoter by FOXM1. Biochem Biophys Res Commun **2008**;368:107-15
189. Antequera F. Structure, function and evolution of CpG island promoters. Cell Mol Life Sci **2003**;60:1647-58
190. Chen Y, Li Y, Wei J, Li YY. Transcriptional regulation and spatial interactions of head-to-head genes. BMC genomics **2014**;15:519
191. Barger CJ, Zhang W, Hillman J, Stablewski AB, Higgins MJ, Vanderhyden BC*, et al.* Genetic determinants of FOXM1 overexpression in epithelial ovarian cancer and functional contribution to cell cycle progression. Oncotarget **2015**
192. Shu J, Jelinek J, Chang H, Shen L, Qin T, Chung W*, et al.* Silencing of bidirectional promoters by DNA methylation in tumorigenesis. Cancer Res **2006**;66:5077-84
193. Joung J, Konermann S, Gootenberg JS, Abudayyeh OO, Platt RJ, Brigham MD*, et al.* Genome-scale CRISPR-Cas9 knockout and transcriptional activation screening. Nat Protoc **2017**;12:828-63
194. Thakore PI, D'Ippolito AM, Song L, Safi A, Shivakumar NK, Kabadi AM*, et al.* Highly specific epigenome editing by CRISPR-Cas9 repressors for silencing of distal regulatory elements. Nat Methods **2015**;12:1143-9
195. Maachani UB, Shankavaram U, Kramp T, Tofilon PJ, Camphausen K, Tandle AT. FOXM1 and STAT3 interaction confers radioresistance in glioblastoma cells. Oncotarget **2016**;7:77365-77
196. Park YY, Jung SY, Jennings NB, Rodriguez-Aguayo C, Peng G, Lee SR*, et al.* FOXM1 mediates Dox resistance in breast cancer by enhancing DNA repair. Carcinogenesis **2012**;33:1843-53
197. Monteiro LJ, Khongkow P, Kongsema M, Morris JR, Man C, Weekes D*, et al.* The Forkhead Box M1 protein regulates BRIP1 expression and DNA damage repair in epirubicin treatment. Oncogene **2013**;32:4634-45
198. Khongkow P, Karunarathna U, Khongkow M, Gong C, Gomes AR, Yagüe E*, et al.* FOXM1 targets NBS1 to regulate DNA damage-induced senescence and epirubicin resistance. Oncogene **2014**;33:4144-55
199. Kwok JM, Peck B, Monteiro LJ, Schwenen HD, Millour J, Coombes RC*, et al.* FOXM1 confers acquired cisplatin resistance in breast cancer cells. Mol Cancer Res **2010**;8:24-34
200. Tassi RA, Todeschini P, Siegel ER, Calza S, Cappella P, Ardighieri L*, et al.* FOXM1 expression is significantly associated with chemotherapy resistance and adverse prognosis in non-serous epithelial ovarian cancer patients. J Exp Clin Cancer Res **2017**;36:63
201. Nestal de Moraes G, Delbue D, Silva KL, Robaina MC, Khongkow P, Gomes AR*, et al.* FOXM1 targets XIAP and Survivin to modulate breast cancer survival and chemoresistance. Cell Signal **2015**;27:2496-505
202. Yazinski SA, Comaills V, Buisson R, Genois MM, Nguyen HD, Ho CK*, et al.* ATR inhibition disrupts rewired homologous recombination and fork protection pathways in PARP inhibitor-resistant BRCA-deficient cancer cells. Genes Dev **2017**;31:318-32
203. Evers B, Drost R, Schut E, de Bruin M, van der Burg E, Derksen PW*, et al.* Selective inhibition of BRCA2-deficient mammary tumor cell growth by AZD2281 and cisplatin. Clin Cancer Res **2008**;14:3916-25
204. Zhang X, Cheng L, Minn K, Madan R, Godwin AK, Shridhar V*, et al.* Targeting of mutant p53-induced FoxM1 with thiostrepton induces cytotoxicity and enhances carboplatin sensitivity in cancer cells. Oncotarget **2014**;5:11365-80
205. Harbour JW, Dean DC. The Rb/E2F pathway: expanding roles and emerging paradigms. Genes Dev **2000**;14:2393-409

206. Yamamoto Y, Ning G, Howitt BE, Mehra K, Wu L, Wang X*, et al.* In vitro and in vivo correlates of physiological and neoplastic human Fallopian tube stem cells. J Pathol **2016**;238:519-30
207. Lam AK, Ngan AW, Leung MH, Kwok DC, Liu VW, Chan DW*, et al.* FOXM1b, which is present at elevated levels in cancer cells, has a greater transforming potential than FOXM1c. Frontiers in oncology **2013**;3:11
208. Schimmel J, Eifler K, Sigurðsson JO, Cuijpers SA, Hendriks IA, Verlaan-de Vries M*, et al.* Uncovering SUMOylation dynamics during cell-cycle progression reveals FoxM1 as a key mitotic SUMO target protein. Mol Cell **2014**;53:1053-66
209. Laoukili J, Alvarez M, Meijer LA, Stahl M, Mohammed S, Kleij L*, et al.* Activation of FoxM1 during G2 requires cyclin A/Cdk-dependent relief of autorepression by the FoxM1 N-terminal domain. Mol Cell Biol **2008**;28:3076-87
210. Schimmel J, Eifler K, Sigurethsson JO, Cuijpers SA, Hendriks IA, Verlaan-de Vries M*, et al.* Uncovering SUMOylation dynamics during cell-cycle progression reveals FoxM1 as a key mitotic SUMO target protein. Mol Cell **2014**;53:1053-66
211. Barrett CL, DeBoever C, Jepsen K, Saenz CC, Carson DA, Frazer KA. Systematic transcriptome analysis reveals tumor-specific isoforms for ovarian cancer diagnosis and therapy. Proceedings of the National Academy of Sciences of the United States of America **2015**;112:E3050-7
212. Hanel W, Moll UM. Links between mutant p53 and genomic instability. J Cell Biochem **2012**;113:433-9
213. Halasi M, Gartel AL. A novel mode of FoxM1 regulation: positive auto-regulatory loop. Cell Cycle **2009**;8:1966-7
214. Wang Y, Wen L, Zhao SH, Ai ZH, Guo JZ, Liu WC. FoxM1 expression is significantly associated with cisplatin-based chemotherapy resistance and poor prognosis in advanced non-small cell lung cancer patients. Lung Cancer **2013**;79:173-9
215. Carr JR, Park HJ, Wang Z, Kiefer MM, Raychaudhuri P. FoxM1 mediates resistance to herceptin and paclitaxel. Cancer Res **2010**;70:5054-63
216. Sanjiv K, Hagenkort A, Calderón-Montaño JM, Koolmeister T, Reaper PM, Mortusewicz O*, et al.* Cancer-Specific Synthetic Lethality between ATR and CHK1 Kinase Activities. Cell Rep **2016**;17:3407-16
217. Wang M, Gartel AL. Micelle-encapsulated thiostrepton as an effective nanomedicine for inhibiting tumor growth and for suppressing FOXM1 in human xenografts. Molecular cancer therapeutics **2011**;10:2287-97
218. Radhakrishnan SK, Bhat UG, Hughes DE, Wang IC, Costa RH, Gartel AL. Identification of a chemical inhibitor of the oncogenic transcription factor forkhead box M1. Cancer research **2006**;66:9731-5
219. Gormally MV, Dexheimer TS, Marsico G, Sanders DA, Lowe C, Matak-Vinkovic D*, et al.* Suppression of the FOXM1 transcriptional programme via novel small molecule inhibition. Nature communications **2014**;5:5165
220. Kalinichenko VV, Kalin TV. Is there potential to target FOXM1 for 'undruggable' lung cancers? Expert Opin Ther Targets **2015**:1-3